Storage Physics and Noise Mechanism in Heat-Assisted Magnetic Recording

Submitted in partial fulfillment of the requirements for

the degree of

Doctor of Philosophy

in

Electrical and Computer Engineering

Hai Li

B.S., Applied Physics, Huazhong University of Science and Technology
M.S., Electrical and Computer Engineering, Carnegie Mellon University

Carnegie Mellon University
Pittsburgh, PA

September, 2016

Acknowledgement

In the past five years of my Ph.D. journey, many people have offered me constructive guidance and sincere help.

First, I would like to express my sincere appreciation to my advisor, Prof. Jian-Gang (Jimmy) Zhu, who has offered full-hearted help and insightful guidance. He has been paying attention to my research actively and always ready to advise me. I am grateful for him offering me splendid opportunities to explore research as well as trusting me to conquer the challenges. Without his advice, encouragement and inspiration, not would this thesis work be possible. He is also a great example of the researcher with constant passion, enthusiasm, and commitment to excellence, which influence me deeply.

Also, I am highly thankful to my other committee members: Professor David E. Laughlin, Professor James A. Bain and Dr. Michael Alex. Their constructive suggestions and feedback through my entire Ph.D. greatly help enrich and strengthen the thesis work. Their multi-disciplinary background stimulates me to investigate the research topic from various novel angles.

Meanwhile, I would like to express my sincere thanks to Professor David N. Lambeth, who taught me the first magnetic course at CMU and provided great spiritual inspiration. I would also like to thank both Professor David N. Lambeth and Professor Tamal Mukherjee for taking me as teaching assistant for the capstone course and providing helpful instructions.

I would like to deliver my sincere gratitude to Dr. Michael Alex for offering the great internship opportunity at Western Digital Corporation and greatly helping validation of the recording physics theorem via spin stand testing experiments. During the internship, the kind help from Mr. Jimmy Bui, Dr. Bodgan Valcu, Dr. Fenghua Zong, Dr. Boris Livshitz, Dr. Hua Yuan, Dr. Daniel Lottis, Dr. Antony Ajan and Dr. Gerardo Bertero are also highly appreciated.

For constant help through my Ph.D. research, I would like to send my sincere gratitude to Dr. Yiming Wang. His advice and insights greatly help me overcome the energy barriers of research.

I would like to thank Carnegie Mellon University, Department of Electrical and Computer Engineering, Data Storage Systems Center (DSSC) and its industrial sponsors for generous financial support throughout my Ph.D.

Friends have been great sources of support and companionship. They are my friends as well as my teachers. In particular, I would like to thank the following friends in Pittsburgh, Dr. David Bromberg, Dr. Abhishek A. Sharma, Dr. Vignesh Sundar, Dr. Hoan Ho, Dr. En Yang, Dr. B.S.D.Ch.S. Varaprasad, Dr. Darmindra Arumugam, Dr. Andreas Kulovits, Dr. Daniel Morris, Dr. Masaki Furuta, Dr. Steven Granz, Dr. Yuan-Fu (Efrem) Huang, Dr. Baoan Liu, Dr. Jiawei Shi, Dr. Li Li, Dr. Shan Hua, Dr. Miaolei Yan, Dr. Siyang Xu, Xiaoyu Bai, Zhengkun Dai, Huan Chen, Yuwei Qin, Tong Mo, Jinglin Xu, Min Xu, Jinxu Bai, Chang Yang, Yunlu Li, Jingyu Wang, Guangshuo Liu, Jiang He, Haichao Xu, Dr. Jiannan Ouyang, Dr. Zitao Liu, Boyu Sun, Wenhao Chen, Xia Miao, Ankita Mangal, Shivram Kashyap. It has been such a pleasure to go through the Ph.D. with you guys. For friends not in Pittsburgh, the distance never weakens your support. I would like to thank, Yang Yang, Dr. Lisi Xie, Lusi Wu, Chenwei Pan, Kun Fan, Xin Jiang, Kun Fan, Xiao Liu, Renpeng Fang, Dr. Liang Liu, Yibing Liu, Dr. Yanzhao Lai, Dr. Xiaohang Li. There are still so many friends out there. Even if not listed here, your consistent help is always there. I want to thank you all for your help and support.

Especially, I thank my dear girlfriend Fangyuan Cao for trusting and accompanying me. She makes me a better me.

Definitely, I thank my family, especially my dear parents, Mr. Luming Li and Mrs. Yonglin Gong. Their unlimited love, unconditional care, and absolute trust are my sources of inspiration and origins of motivation. They make me stand where I am today.

Abstract

In this dissertation, through systematic thermal coupled micromagnetic modeling using the Landau-Lifshitz-Bloch equation (LLB), the full recording process is simulated to capture the underlying physics and noise mechanism for the leading candidate of next generation storage, heat-assisted magnetic recording (HAMR).

To build up fundamental understanding, HAMR recording physics and transition bits characteristics are discussed in detail. Specifically, incomplete switching and erase-after-write are proposed and analyzed at low head field and high head field, respectively. Based upon this, multiple aspects of the HAMR system are investigated, which show similar head field dependence. Overall, system performance tightly correlates with a single term: recording time window. Several seemingly paradoxical observations can be explained by the theorem above.

With this fundamental understanding, various HAMR medium properties are analyzed and compared to identify the most important parameters. The theorem manages to not only describe the impact of the well know noise, like H_k variation but also to predict several new noise origins, like T_c variation and T variation. For each type of noise, the physics origin and its impact on the recording performance are analyzed. Potential solutions are also discussed.

To further validate this theorem and apply it to realistic scenarios, a series of spin stand testing as well as system optimization modeling are conducted. The major representative behaviors predicted in our simulation have all been observed in industrial labs. The model and theorem also suggest a way to modify current system specifications, which could be applied in design iterations. Additionally, for the new noise T_c variation as well as the temperature dependence of H_k, the model is utilized to justify and optimize measurement methodology before the setup of the testing platform. Furthermore, the well-known transition front curvature has been systematically analyzed in terms of storage density impact. Using the understanding of recording physics, a novel solution has been proposed to completely eliminate curvature issue.

Table of Contents

Contents

List of Figures

1. Introduction

1.1 Background and Motivation

As big data and cloud computing expand, so too does the demand for ultra-large volume data storage. Every day, 2.5 quintillion bytes of data are created. In fact, 90% of the data in the world today has been created in the last two years alone [1], [2]. A great portion of the data is stored in hard disk drives (HDDs). In 2012, the hard disk industry shipped 569 million hard disk drives with an average capacity of 702 GB per drive [3]. However, increasing the number of drives would not solve the issue of insufficient storage volume due to cost and energy consumption. Since its invention in the late 1970s [4], [5], there has been a large ongoing effort to increase the storage density of HDDs.

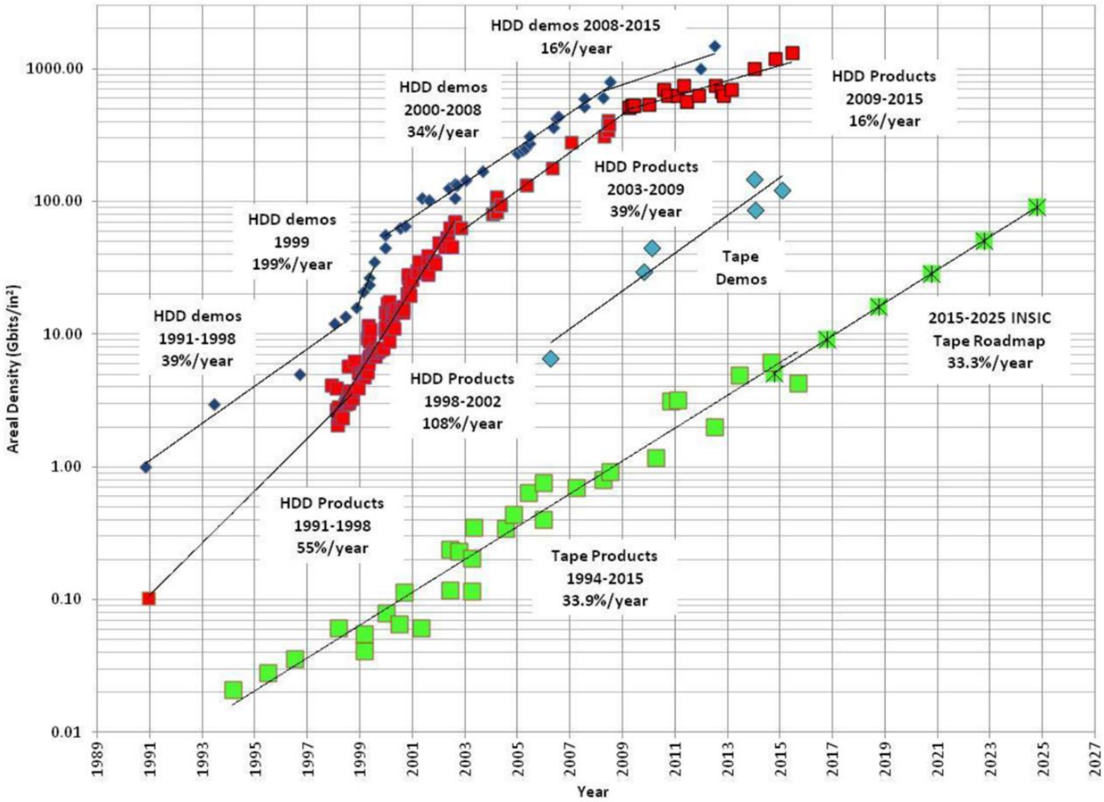

Figure 1.1 Areal density of hard disk drive (HDD) and tape storage [6]**.**

Figure 1.1 shows the historic roadmap for the hard disk drive (HDD) in comparison with tape storage. Although the areal density of tape recording is one order lower than that of HDDs, tape-based storage is still widely employed as an alternative technology. Tape storage continues developing to preserve the cost advantage over HDD in several applications [6]. For recent HDD demos and HDD products from 2008 to 2015, areal density growth has been approximately 16% per year. Whereas for tape products, from 1994 to 2015, the areal density has demonstrated 33.9% growth. For tape demos from 2006 to 2015, the areal density growth is even higher. From the areal density evolution rate, it can be observed that the tape storage enjoys a faster increasing rate, while the growing rate of HDD has started to slow down and saturate.

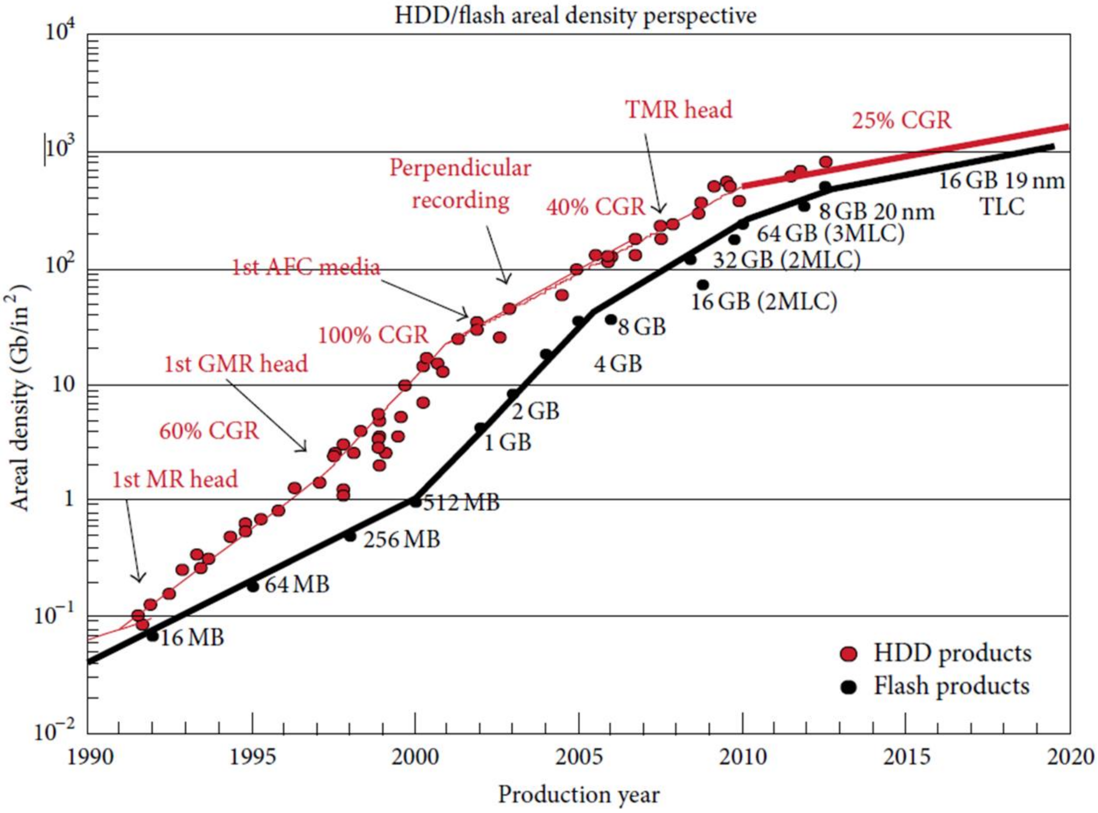

Figure 1.2 Areal density roadmap for hard disk drive (HDD) and flash-based solid state drive (SSD) [7].

On the other hand, with increasing demand for data accessing speed and system performance, flash-based solid state drives (SSDs) are proving to be fierce competition for conventional HDDs. Figure 1.2 shows the historic roadmap for both HDDs and flash. Compared to HDD technology, the flash was introduced slightly later. In terms of areal density, flash has been actively catching up with that of HDDs. Recently, Seagate has demonstrated a 60 TB flash [8]. To this point, the relative areal density difference between flash and HDD is quite small. But the cost difference is still large and HDD is less expensive than SSD. Meanwhile, both technologies have begun to show a saturation of areal density growth rate due to different technical reasons. Especially for mobile and laptop applications, recent flash SSDs have gradually taken quite a large portion of the market with their fast response and increasingly larger capacity. Meanwhile, hybrid drives, which combine HDDs and SSDs, have started to emerge.

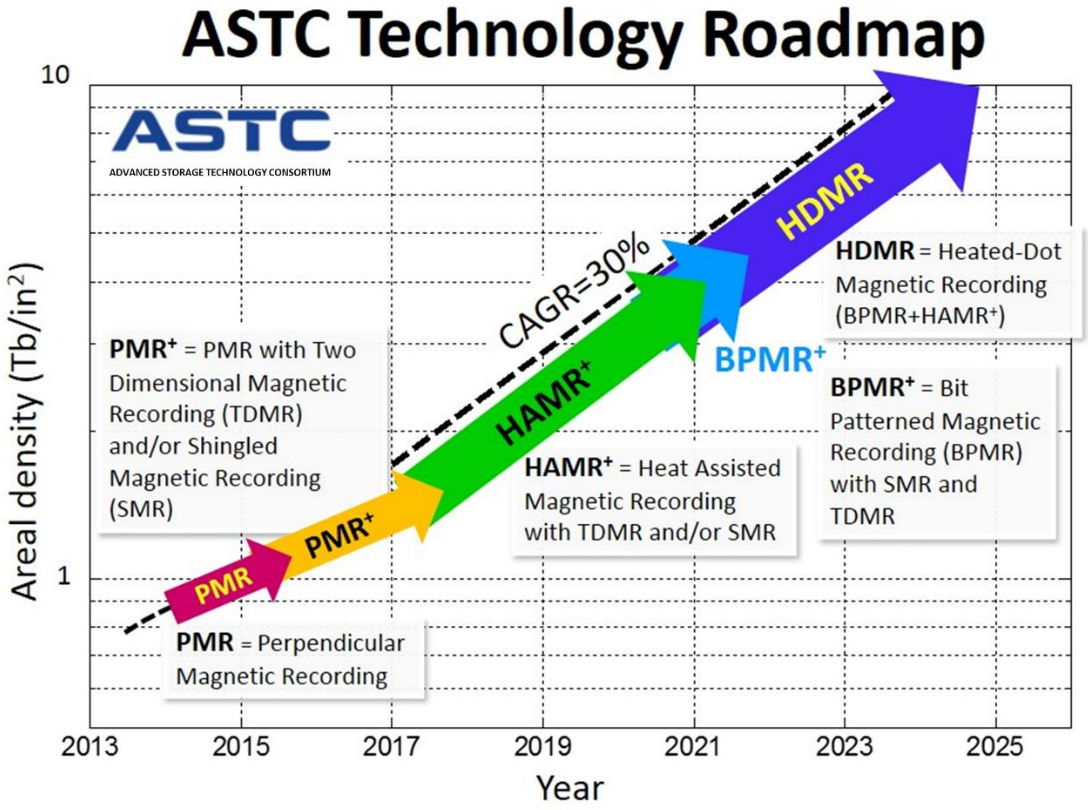

Figure 1.3 Advanced Storage Technology Consortium (ASTC) roadmap for the future hard disk drive areal density [9].

To keep the future HDD technology evolving, a roadmap has been plotted as shown in Figure 1.3 during the recent Advanced Storage Technology Consortium (ASTC). The roadmap suggests heat-assisted magnetic recording (HAMR) will soon replace conventional perpendicular magnetic recording (PMR). The first few generations of HAMR based HDDs are expected to reach 2 Tb/in^2 by 2019. Around 2020, bit patterned magnetic recording (BPMR) is expected to enter the market along with shingled magnetic recording (SMR) and two-dimensional magnetic recording (TDMR). To realize extremely high density approaching, or even surpassing, 10 Tb/in^2, heated-dot magnetic recording, a combination of BPMR and HAMR would be employed.

From the analysis above, it is clear that HDD faces great challenges from its competitors. As a huge amount of data is generated and needs to be stored every day, advancement and progress for HAMR, the leading candidate for next generation storage, are needed. This Ph.D. thesis work is motived by the above-listed reasons.

1.2 Perpendicular Magnetic Recording

After the introduction of perpendicular magnetic recording (PMR) concept back in the 1970s [4], [5], it took two decades for the commercialization of hard disk drive (HDD). The PMR technology started to embrace the market after 2000, before which longitudinal magnetic recording (LMR) was the dominant technology for HDD. In PMR, the magnetization is of out-of-plane direction, while the magnetization of LMR lies in the thin film plane. Due to several technical challenges and fundamental limit, the LMR density stopped increasing when it reached 100 Gb/in^2 in 2000. Later PMR based HDD gradually took over the market around 2005 [10].

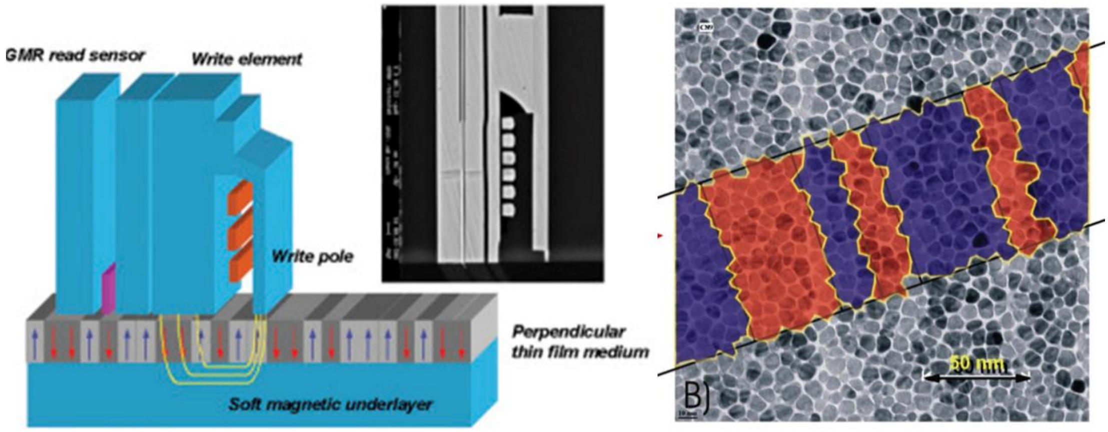

Figure 1.4 Perpendicular magnetic recording scheme (left) along with the microscopic image of the writer cross section [11]**. Typical magnetization pattern is shown on the right, where blue and red color relate to downward or upward magnetization state, respectively** [12]**.**

Figure 1.4 shows the schematic of perpendicular magnetic recording. The magnetic moment in the medium is perpendicular to the Co-alloy film plane, because of the strong perpendicular magnetocrystalline anisotropy. The head field is concentrated between the bottom of the write pole and the top of the soft magnetic underlayer [11]. During recording, the writer moves with respect to the recording medium. By switching the head field polarity periodically, the magnetization of the medium will change to up or down states accordingly, which correspond to the information bits [12]. The right graph in the figure is the microscopic image of granular PMR medium. The blue and red colors represent the negative or positive magnetization state, respectively.

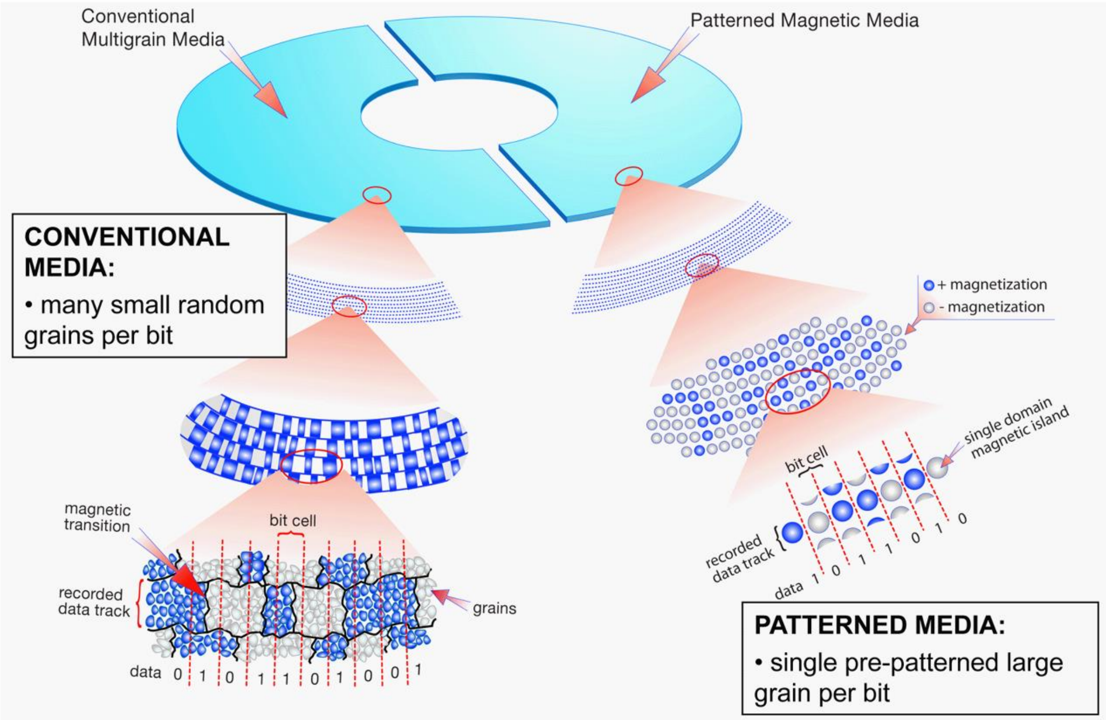

Figure 1.5 Schematic of the conventional granular medium and patterned medium [12].

Figure 1.5 shows the relationship between the disk, track, bit, and microstructure of both continuous granular medium and bit patterned medium [12]. For the HDD disk shown in the top, it consists many circular tracks, called recording tracks, with gradually changing radius. Zooming in the recording tracks with magnetic force microscope, it can be seen that each recording track consists of many small areas with different magnetization state. Between these small regions with positive or negative magnetization states are transitions, which enable storage of information bits. Until this scale, both the continuous granular medium and bit patterned medium are very similar. When medium are looked at the even closer distance, it is noticed that a bit in granular medium consists of many smaller grains segregated by non-magnetic boundary material. Whereas for the patterned media, each bit is a relatively larger grain. For current conventional PMR medium, the granular structure is still dominant since the sputtering process is more costly effective and better studied. In later discussion, the study will also be more focused on the continuous granular recording medium for heat-assisted magnetic recording.

1.3 Magnetic Recording Trilemma

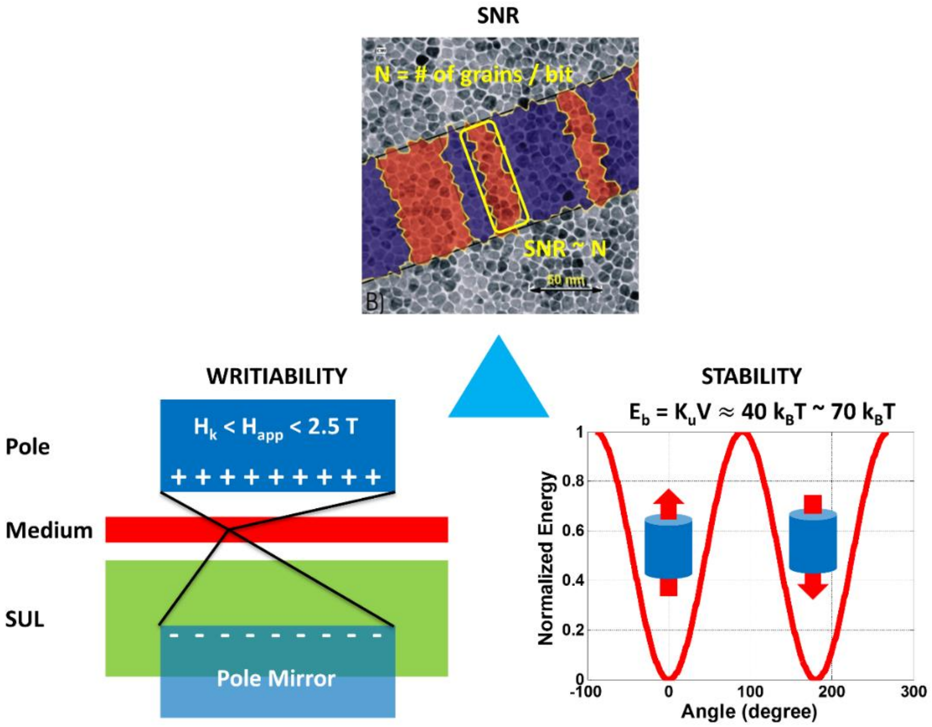

Figure 1.6 Magnetic recording trilemma [12], [13].

Figure 1.6 illustrates the trilemma originating from multiple requirements in the magnetic recording. As shown in the top graph, information is represented by several magnetic grains within each bit sitting on the thin film of a recording disk. To accommodate more bits, the area of each bit has to shrink. It is critical to maintain the number of grains per bit since the signal-to-noise ratio (SNR) is proportional to grains number [13]. Therefore, to maintain sufficient SNR and increase storage density simultaneously, the size of grains have to be scaled down. This is the consideration from the SNR aspect.

The stability issue is illustrated in the bottom right graph. The energy profile of a magnetic grain with uniaxial anisotropy is plotted. Between the magnetically positive or negative states, there is an energy barrier to overcome. The energy barrier, E_b, is the product of the anisotropy constant, K_u, and the grain volume, V. When a sufficiently strong field is applied, the energy barrier will disappear and magnetization state can be changed. Once the external field is removed, the original energy profile will be restored and the magnetization state is protected by the energy barrier. However, it is possible for the magnetization state to change even without an external field. This is because the grains are constantly experiencing the thermal agitation. The probability for a grain to switch depends on the ratio of the energy barrier, $E_b = K_uV$, and the thermal energy k_BT, where the k_B is the Boltzmann constant and T is the environment temperature. For instance, to make sure the grain is magnetically stable for 10 years, the ratio needs to be higher than 40. For longer maintenance, the ratio needs to be larger. This fundamental limit is also known as superparamagnetism [14] or the thermal stability issue.

To guarantee large thermal stability and use smaller grains for higher storage density, the anisotropy constant has to be enhanced. However, writability will become another issue as shown in the bottom left graph. In PMR recording, the applied head field has to be larger than the medium coercivity to change the magnetization state of the medium. The applied head field from both the main pole and soft underlayer (SUL) is proportional to the saturation magnetization, M_s. In nature, the highest magnetization value of discovered materials is around 1980 emu/cc and the resulting field is $4\pi M_s = 2.5\ T$. Additionally, since the main pole tip of writer must be small to provide a narrow track, the recording field strength is lower than 1 T [15]. This means that the medium with too high K_u would not be able to be written with the magnetic writer.

From these three aspects, it can be seen that the further scaling of PMR will be challenging and fundamentally limited. From several studies, it is widely agreed that the PMR areal density would not reach far beyond 1 Tb/in^2 [16]–[18].

1.4 Heat Assisted Magnetic Recording

As shown in the recording trilemma, to accommodate more data on the same disk area, the grain size has to shrink. While to assure the thermal stability, which is indicated by the product of anisotropy constant K_u, and grain volume V, higher K_u material, like FePt, is supposed to replace current CoCrPt. However, there are limited M_s for materials. Consequently, the applied head field can't ever increase.

In recent years, quite a few novel recording schemes and techniques have been proposed and studied intensively to realize recording beyond 1 Tb/in^2. The primary recording techniques are as follows, Heat-Assisted Magnetic Recording (HAMR) [19]–[24], Microwave-Assisted Magnetic Recording (MAMR) [25]–[29], Bit Pattern Magnetic Recording (BPMR) [30]–[37], Shingled Magnetic Recording (SMR) [38]–[42], Two-Dimensional Magnetic Recording (TDMR) [42]–[47], Pulsed HAMR [48]–[52], Acoustic Assisted Magnetic Recording (AAMR) [53]–[57], Exchange Coupled Composite Media (ECC) [58]–[62], Discrete Track Media (DTM) [63]–[67], Percolated Perpendicular Media (PPM) [68]–[72] and so on. Among these new features or new schemes, the heat-assisted magnetic recording has been widely agreed to be the leading candidate for the next generation storage. HAMR is believed to have extremely high effective field gradient to create sharp transitions at ultra-high storage density, and a great portion of the conventional PMR scheme can be kept.

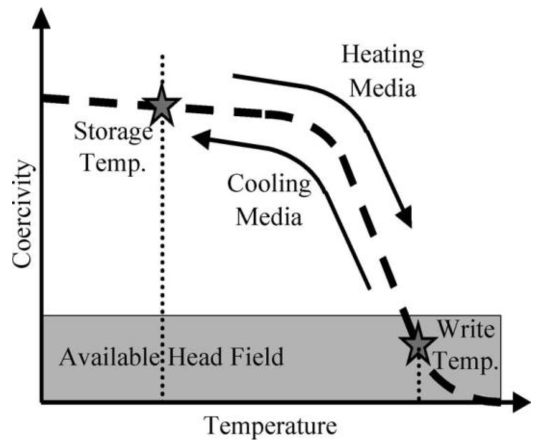

Figure 1.7 Heat-Assisted Magnetic Recording mechanism [19].

In HAMR scenario as shown in Figure 1.7, the local heating is employed to temporarily decrease the anisotropy field of grains below the applied head field. After changing the magnetic state, the heating is shifted away. Then the grains would maintain their states under the applied field during the cooling process. Specifically for heating, the near-field transducer has been invented to make local heating below the diffraction limit. Therefore, the bit size reduces to tens of nanometers. Despite the novel mechanism to overcome the recording trilemma and further extend the storage capability, there has been active research on HAMR for decades and quite a few challenges have to be overcome before the commercialization of HAMR based HDD products [12], [22], [40], [73]–[75].

1.5 Thesis Outline

In this dissertation, micromagnetic modeling coupled with finite-element analysis has been conducted systematically to study HAMR. Multiple primary aspects of HAMR system have been analyzed in detail and the corresponding results are organized as follows.

In Chapter 1, a brief introduction and motivation for HDD is given. The hard disk drive (HDD) trilemma and the basic idea of HAMR recording are discussed as well.

In chapter 2, the major governing equations of the simulation are explained. For purpose of comparison, both the Landau-Lifshitz-Gilbert equation and Laudan-Lifshitz-Bloch equations are discussed. Regarding effective field, various field terms are explained in terms of energy.

In chapter 3, the very fundamental recording physics and noise behaviors are laid out. Different aspects, such as disk velocity, thermal gradient, room temperature Hk, and so on are addressed. One important concept, the recording time window, is also proposed, and it turns out to correlate closely with system performance.

In chapter 4, based on the understanding and theorem above in chapter 3, several medium properties are examined to sort out the dominant ones. Both physical reasons and typical characteristics are presented for comparison, which leads to relevant measurement of the critical one, T_c variation in the following chapter. On the other hand, in-plane grains are medium defects, which could not be prevented from writing optimization and behave as embedded noise. A statistical method is proposed to distinguish the embedded noise of defects and random noise of improper writing.

In chapter 5, a series of spin stand testing results are given to validate the simulation predictions of basic noise behaviors as well as the head field dependence of system performance. As all the primary system parameters relate to the recording time window, the disk rotational velocity, medium anisotropy field as well as a specific industrial head field design are taken for instances. Their recording impacts are looked at in terms of recording time window. Since T_c variation directly leads to the recording time window variation, it could result in significant performance degradation. The simulation has been conducted before experimental measurement. Apart from T_c variation, the temperature dependence of H_k is also obtained by applying external field. Considering that major part of the simulations in this work unifies the quasi-Gaussian thermal profile along crosstrack, this section will also discuss the areal density impact of the well-known transition curvature. Meanwhile, a solution will be given to overcome this well-known transition curvature issue.

In chapter 6, the entire dissertation will be summarized.

2. Micromagnetic Modeling

In this chapter, an introduction is given for the micromagnetic modeling. The governing equation is the critical key to capture the desired magnetic dynamics. Conventionally, the Landau-Lifshitz-Gilbert (LLG) equation has been intensively utilized for micromagnetic simulation [23], [76]–[78]. However, in the HAMR scheme, the temperature induced magnetization change adds another degree of freedom, which motivates Landau-Lifshitz-Bloch (LLB) equation. Here the conventional LLG equation is presented first and the LLB equation will be discussed for comparison.

2.1 Landau-Lifshitz-Gilbert Equation

Based upon the Gilbert Equation (2.1), the magnetic dynamics of single macro spin consists of precession and damping processes, which correspond to the first and the second term on the right-hand side of the equation. For the procession, the magnetization would precess with respect to the field $\vec{H}$ direction, while for the damping, the magnetization would gradually rotate towards the field $\vec{H}$ direction. Because of the cross product, both terms are perpendicular to the magnetization.

$$\frac{d\overrightarrow{M}}{dt} = -\gamma\overrightarrow{M}\times\overrightarrow{H} + \frac{\alpha}{M_s}\overrightarrow{M}\times\frac{d\overrightarrow{M}}{dt} \tag{2.1}$$

Where $\vec{M}$ is the magnetization of macro spin, t is the evolution time, γ ($= 1.76 \times 10^7$ Oe^{-1}s^{-1}) is the gyromagnetic ratio, M_S is the saturation magnetization, α is the intrinsic damping constant, and $\vec{H}$ is the total effective field, which will be explained later in detail.

Application of cross product of $\vec{M}$ to both side and simplification will lead to Equation (2.2), the Landau-Lifshitz-Gilbert equation. Similar to (2.1), both terms on the right hand side of equation are cross product, which makes the change of $\vec{M}$ always perpendicular to itself. Therefore, the magnitude of the magnetization is kept constant, even if the external temperature changes drastically.

$$\frac{d\vec{M}}{dt} = -\frac{\gamma}{1+\alpha^2}\vec{M}\times\vec{H} - \frac{\alpha}{(1+\alpha^2)M_s}\vec{M}\times\left(\vec{M}\times\vec{H}\right) \quad \textbf{(2.2)}$$

Equation (2.2) is the explicit form of LLG equation, with which the dynamics of macrospin can be calculated with a varying or fixed time step. In conventional magnetic recording scheme, both α and M_S are constant, therefore, the only undefined term is the effective field $\vec{H}$ which will be discussed later. This LLG equation manages to actually describe or predict quite a few magnetic behaviors in nanoscale mostly at room temperature. However, the temperature changes and, the relevant impacts are not fully included in LLG equation, which is a critical issue since the recording heating and cooling process happens at temperature ranges near as well as beyond the Curie temperature.

2.2 Landau-Lifshitz-Bloch Equation

As mentioned in section 2.1, the conventional LLG equation have both precession and damping torques perpendicular to the magnetization, which makes the magnetization magnitude constant. However, when the environment temperature is elevated, the thermal agitation would make the spin vibrate significantly. Therefore the average saturation magnetization would shrink with temperature increase. So the LLG equation would not be able to describe the elongation or shrinkage of the magnetization in heating and cooling procedures, respectively.

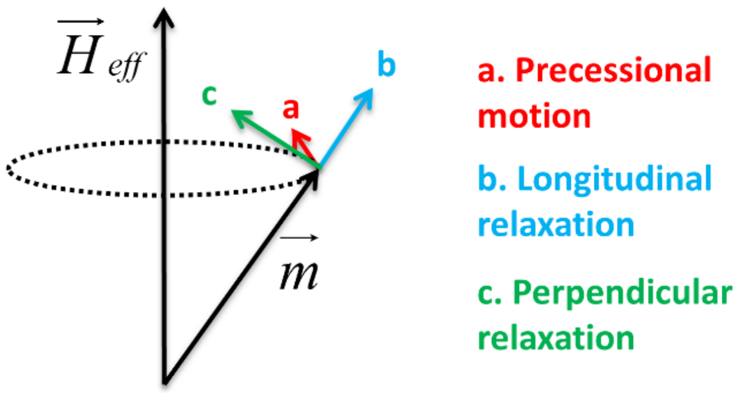

Figure 2.1 Representative directions of precession, longitudinal and perpendicular torque terms in Landau-Lifshitz-Bloch (LLB) equation.

To better capture the magnetic dynamics, the Landau-Lifshitz-Bloch (LLB) equation has been proposed as Equation (2.3) [79], [80]. Compared to the LLG equation above, one primary difference is the second term, the longitudinal relaxation term. This term is the dot product of the magnetic field and magnetization vector, which makes it parallel to the magnetization vector. It is also supposed to tune the magnitude of magnetization due to temperature changes. The representative directions of the torque terms in LLB equation are shown in figure 2.1.

$$\frac{d\vec{m}}{dt} = -\gamma \vec{m} \times \vec{H}_{eff} + \gamma \alpha_{\parallel} \frac{\left(\vec{m} \cdot \vec{H}_{eff}\right)\vec{m}}{m^2} - \gamma \alpha_{\perp} \frac{\vec{m} \times \left(\vec{m} \times \vec{H}_{eff}\right)}{m^2} \qquad \textbf{(2.3)}$$

There are two less noticeable aspects worthy of further attention. On one hand, the two damping parameters in the second and third terms have different subscripts, which corresponds to the longitudinal damping and transverse damping. On the other hand, instead of being a constant, each of them follows a specific temperature dependence described in Equation (2.4), and is also a function of intrinsic damping α and Curie temperature T_c. As is shown, the longitudinal damping would increase with temperature while the transverse damping would decrease at elevated temperature. This suggests that the longitudinal relaxation process would be enhanced at high temperature, while the transverse relaxation would become weakened.

$$\alpha_{\parallel} = \alpha \frac{2T}{3T_c}, \alpha_{\perp} = \alpha \left(1 - \frac{T}{3T_c}\right) \qquad \textbf{(2.4)}$$

The effective field term H_{eff} not only contains the same terms as H_{eff} in LLG, but also includes additional equivalent field which is also functions of temperature. The specific equation is shown in (2.5).

$$\vec{H}_{eff} = \vec{H}_{eff-LLG} + \begin{cases} \dfrac{1}{2\chi_{\parallel}}\left(1 - \dfrac{m^2}{m_e^2}\right)\vec{m}, & T \le T_c \\ \dfrac{3k_B T_c}{\mu_0}\left(1 - \dfrac{T}{T_c} - \dfrac{3}{5}m^2\right)\vec{m}, & T > T_c \end{cases} \qquad \textbf{(2.5)}$$

Where $\chi_{\parallel}$ indicates longitudinal susceptibility at zero field condition, m_e is the zero-field-equilibrium spin polarization in the mean field approximation condition, m is the magnitude of magnetization, k_B is the Boltzmann constant, T_c is the Curie temperature and μ_0 is the spin magnetic momentum. It should be noted that the effective field follows different formula below and above Curie temperature, respectively.

The original derivation of LLB equation starts with the Fokker-Plank distribution and tries to use the macrospin description to approximate the precise atomistic description of each atom [79].

2.3 Energy and Field Terms

In both LLG and LLB equations, the effective field term $\vec{H}_{eff}$ consists of several similar field terms, while the effective field in LLB has several additional terms. Through the iterative simulation process, the effective field term must be updated at each step for every grain of interest. Based upon the classical magnetism theorem, the magnetic energy terms are given in this section. Each individual field term will be derived from the relevant energy term as well.

2.3.1 Crystalline Anisotropy Energy

For perpendicular magnetic recording medium, the grains are made to have uniaxial crystalline anisotropy. This is realized with the $L1_0$ crystal structure of FePt. The uniaxial anisotropy energy density follows the Equation (2.6).

$$E_{anis}(i) = K_u(i)\sin^2\theta_i = K_u(i)\left[1-\left(\vec{k}_i\cdot\vec{m}_i\right)\right] \qquad \textbf{(2.6)}$$

Where $K_u(i)$ indicates the anisotropy constant for ith grain, θ_i is the angle between the easy axis and the spin magnetization directions. Symbol $\vec{k}_i$ denotes unit vector of easy axis and $\vec{m}_i$ denotes unit vector of magnetization. To get the anisotropy field, the energy term only need to be differentiated with respect to magnetization vector and multiplied with -1. The anisotropy field is as Equation (2.7).

$$\vec{H}_{anis}(i) = -\frac{\partial E_{anis}(i)}{\partial \vec{M}_i} = \frac{2K_u}{M_s}(i)\left(\vec{k}_i \cdot \vec{m}_i\right)\vec{k}_i \quad \textbf{(2.7)}$$

2.3.2 Exchange Energy

In the state of the art perpendicular magnetic recording medium, there are two major types of exchange coupling interactions. The first one is lateral exchange coupling between the grains, although the oxide in between is supposed to decouple the grains. This type of coupling happens between the same ferromagnetic materials via the grain boundary. The second one is the vertical exchange coupling between the layers. This type of coupling happens mainly between different ferromagnetic materials. There is usually exchange coupling break layer between the upper and lower layers to carefully tune the vertical coupling strength as well. In the bulk magnetic theory, the adjacent spin neighbors would have exchange energy as (2.8).

$$\vec{E}_{ex}(i) = A_{ex}\left[\left(\frac{\partial m_x}{\partial x}\right)^2 + \left(\frac{\partial m_y}{\partial y}\right)^2 + \left(\frac{\partial m_z}{\partial z}\right)^2\right] \quad \textbf{(2.8)}$$

Where A_{ex} is the exchange stiffness, $m_{x,y,z}$ are orthogonal components of normalized magnetization vector, and x, y, z are the three degrees of freedom.

Because of the granular structure of the medium, the continuous format of (2.8) can be discretized into (2.9).

$$\vec{E}_{ex}(i) = -\frac{A_{ex}}{M_s^2 a^2}\vec{M}_i \cdot \sum_{n.n.}\vec{M}_j \quad \textbf{(2.9)}$$

Where a is the grain pitch size, M_s is the saturation magnetization, $\vec{M_i}$ is for the grain of interest, and $\vec{M_j}$ are for the nearest neighbors. By applying differentiation with respect to magnetization, the relevant exchange field can be obtained as (2.10).

$$\vec{H}_{ex}(i) = -\frac{\partial E_{ex}(i)}{\partial \vec{M}_i} = \frac{2A_{ex}}{M_s a^2}\vec{M}_i \cdot \sum_{n.n.}\vec{M}_j \quad \textbf{(2.10)}$$

For the vertical exchange coupling between different materials, the exchange coupling energy follows the Equation of (2.11).

$$\vec{E}_{ex}(i) = -\frac{\sigma S}{V_i}\left(\vec{m}_i \cdot \vec{m}_j\right) \quad \textbf{(2.11)}$$

Where σ is the interfacial exchange stiffness, S is the interface area and V_i is the grain volume of interest. Similar as before, differentiation of the energy term gives the corresponding field term as (2.12).

$$\vec{H}_{ex}(i) = -\frac{\partial E_{ex}(i)}{\partial \vec{M}_i} = \frac{\sigma}{M_s(i) \cdot t_i}\vec{M}_j \quad \textbf{(2.12)}$$

Where M_s is the saturation magnetization, t is the layer thickness where i-th grain stands.

2.3.3 Magneto Static Energy

According to the classical electromagnetism, both the volume charge and the surface charge will generate the field. Here, the charge refers to the magnetic charge. This type of magneto interaction happens between each pair of grains in the system, regardless of their distance. The Equation to calculate the field is given as (2.13).

$$\vec{H}_{demag}(i) = \iiint \nabla \cdot \vec{M}_j \frac{\vec{r}_{ij}}{r_{ij}^3} d^3\vec{r}_j - \iint \vec{n} \cdot \vec{M}_j \frac{\vec{r}_{ij}}{r_{ij}^3} d\vec{r}_j \quad \textbf{(2.13)}$$

Where $\vec{M}_j$ is the magnetization vector of the j-th grain, $\vec{r}_{ij}$ is the displacement vector from i-th grain to j-th grain, $\vec{n}$ is the surface normal vector. The first and second terms on the right hand side relate to the field originated from volume magnetic change and surface magnetic charge, respectively. In our model, since it's assumed that the magnetization is uniform within each of the grain, there would be no volume magnetic charge due to volume magnetization change. Then the Equation of demagnetization field can be simplified as (2.14).

$$\vec{H}_{demag}(i) = -\iint \vec{n} \cdot \vec{M}_j \frac{\vec{r}_{ij}}{r_{ij}^3} d\vec{r}_j = -\sum_j \vec{D}_{ij} \cdot \vec{M}_j \quad \textbf{(2.14)}$$

Where $\vec{D}_{ij}$ is the tensor matrix of magneto-static interaction which is a function of geometry only. In this simulation, the side surfaces of grains are rectangular. While the top or bottom surfaces of grains could be various polygons. These polygons are generally split into multiple squares and triangles. With the formulas derived from [81], the demagnetization factor can be calculated separately and summed up together.

2.3.4 Zeeman Energy

The Zeeman energy basically originates from the externally applied field, which is generated from the recording head component here. It follows the standard magnetic energy density formula as (2.15).

$$E_{zeeman}(i) = -\overrightarrow{M}_i \cdot \overrightarrow{H}_a(i) \tag{2.15}$$

With simple differentiation, the Zeeman field can be obtained as (2.16).

$$\overrightarrow{H}_{zeeman}(i) = -\frac{\partial E_{zeeman}(i)}{\partial \overrightarrow{M}_i} = \overrightarrow{H}_a(i) \tag{2.16}$$

2.3.5 Thermal Agitation

Originating from the fluctuation dissipation theorem in thermal dynamics, the field is three dimensional independent and random. The amplitude of each component follows a Gaussian distribution with variance as Equation (2.17).

$$\left\langle \overrightarrow{H}_{Thermal_{(x,y,z)}} \right\rangle^2 = \frac{2k_B T\alpha}{VM_s\gamma\Delta t} \tag{2.17}$$

Where α is intrinsic damping, V is the volume of grain, k_B is Boltzmann constant, T is temperature, Δt is the time step of simulation. During the heating and cooling process, besides the temperature change, the saturation magnetization will also change. Therefore, the thermal agitation field would have different amplitude.

To this moment, there are still active discussions on whether there is better type or format of the thermal agitation or even entire LLB equations. For instance in [82], one of the three independent field components is replaced with a three-dimensional spatially random torque. Through comparison, the switching distributions turn out to be noticeably different, especially near the Curie temperature, for two types of LLB equations. But the essential impact on simulation results and underlying physical behaviors still remain in the fog. From the following discussion, it can be seen that many primary and special HAMR recording behaviors and noise mechanisms are essentially related or caused by the thermal agitation noise. The thermal noise intensity, temperature dependence of parameters, format of field or torque and so on would consequently affect the description of the thermal noise greatly. Hence the accurate depiction of the HAMR recording physics would definitely require rigorous theorem of thermal agitation along with the LLB or better physics disciplines. The corresponding fundamental physics experiments would be critical and necessary to justify the right theorem as well.

2.4 Typical Setting

In this part, the typical setting of the simulation specifications will be discussed. Since the technology keeps advancing, some settings are modified based upon better understanding, measurement results or the improvement of the HDD components. While it should be mentioned that the results in following chapters remain to be representative, to our best knowledge and experience. For some particular setting variations, it will be discussed in relevant sections.

In the simulation, the setup primarily consists of two parts, the head component, and the recording medium. For the head component, in most of the following simulation cases, the magnetic head field is assumed to be uniform throughout the entire medium, with 45 degrees with respect to the out-of-plane direction of the recording medium. The primary reason is that the thermal spot generated by the near-field transducer (NFT) is much smaller than the magnetic field profile. Hence the magnetic field would be quasi-uniform within the hot region of the thermal profile. Meanwhile, the NFT could not be put at the same downtrack position as the magnetic writer main pole, which may affect the main pole magnetic dynamics and also cause coupling between NFT and main pole to lower NFT efficiency [20], [83], [84]. Hence, the angle between the field direction and the out-of-plane direction tends to be nonzero. In the preliminary simulation study of angle effect, using the model of this thesis, smaller angle is found to benefit the recording performance. More vertical field direction helps maintain spin orientation against thermal agitation and also avoid erase-after-write. This also matches the experimental observation from Western Digital spin stand testing [85], where smaller offset leads to more vertical head field vector. The head field is assumed to have exponential rise and fall behaviors, with the rise time constant equal to 0.2 nanosecond. During the recording process, the polarity of the magnetic field is switched periodically to write the information bits in the so-called 1T pattern.

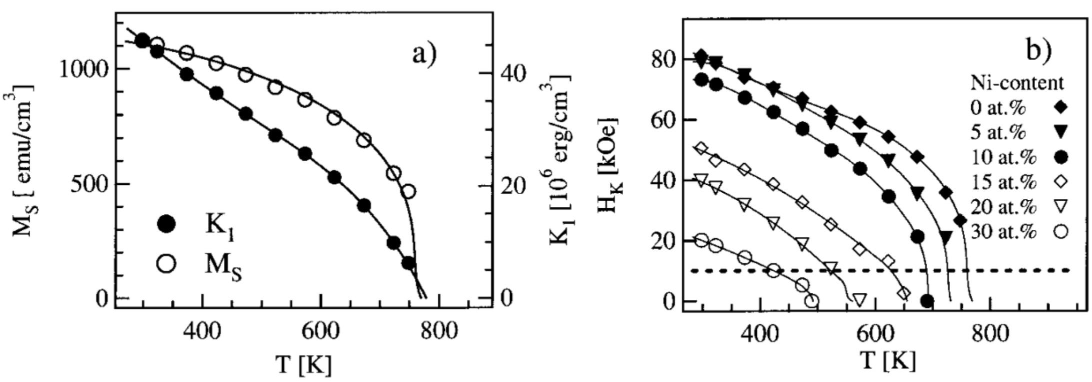

Figure 2.2 Experimental observation of saturation magnetization M_s and anisotropy field H_k versus temperature [86]**. Various doping amounts of the Ni are conveyed to modify the temperature dependence of the medium properties.**

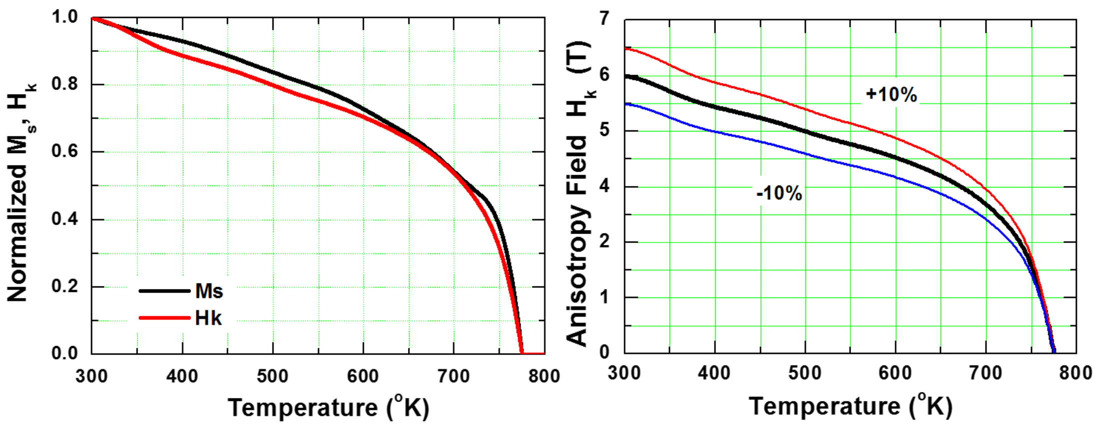

Figure 2.3 Normalized M_s / H_k versus temperature (left) and H_k variation at all the temperatures below Curie temperature, T_c (right). The H_k distribution is induced by vertical scaling of the H_k vs. T curve so that the standard deviation is kept the same at all the temperatures. Similarly, the H_k vs. T curve could be scaled horizontally to induce the T_c variation, which is not shown here.

For the recording medium, the primary magnetic parameters are set as follows:

geometry wise, FePt-$L1_0$ thin film with magnetic grains segregated by nonmagnetic grain boundaries are generated during the initialization process. Since the magnetostatic interaction is primarily dependent upon the geometry of the grains, the proper grain shapes and distribution are needed to mimic realistic medium. Utilizing the Voronoi method with Lubachevsky-Stillinger random grain packing algorithm [87][88], a single layer assembly of magnetic grains with the quasi-Gaussian distribution of grain areas is generated to mimic realistic FePt $L1_0$ based HAMR media [89][90][91]. The thickness of the nonmagnetic grain boundary is set to be 10% of the center-to-center distance between adjacent grains. Zero lateral intergranular exchange is induced if not mentioned. The medium thickness is set to be 10 nm. The magnetization of each grain is assumed to be uniform within the grain so that it is represented by a single magnetization vector. Each grain has its crystalline anisotropy easy axis pointing out-of-plane direction, with small variation. The orientation of all grain easy axes follows a Gaussian distribution. The typical standard deviation of easy axis distribution is $\sigma_{\Delta\theta} = 3^{\circ}$. The temperature dependence of FePt saturation magnetization and anisotropy follows the experimental measurement reported in [92] as Figure 2.2. It should be mentioned that in this reference, the Ni has also been doped into the FePt medium to modify the temperature dependence of magnetic properties. Simultaneously, the doping of Ni could also lead to the change of H_k value, T_c value and so on. Averaging thermally induced spin dispersion [93]–[95], the relation between the anisotropy and saturation magnetization in FePt-$L1_0$ thin film can be shown to follow the Equation (2.18).

$$\frac{K_u(T)}{K_u(0)} = \left[\frac{M_s(T)}{M_s(0)}\right]^n \tag{2.18}$$

Where n is set to be 2 for each grain unless stated otherwise. With the higher value of index n, it can be noticed that the anisotropy would decay much faster versus environment temperature, which results in a shallower dH_k/dT slope near Curie temperature. Based upon the setting of anisotropy, K_u, and saturation magnetization, M_s, the anisotropy field $H_k = 2K_u/M_s$ is assumed to follow a Gaussian distribution with a standard deviation of $\sigma_{H_k} = 10\%$ at all the temperatures below the Curie temperature T_c. As shown in Figure 2.3, during simulation, the H_k and M_s versus T curves are scaled vertically to guarantee same standard deviation of H_k, and scaled horizontally to guarantee T_c standard deviation at all the temperatures. The mean value of the grain anisotropy field is $H_k = 60kOe$ for most of early simulation regarding recording physics. With technology evolving forward, anisotropy field is enhanced to around 90 kOe in later chapters. The Curie temperature is kept to be constant of $775K^{\circ}$ for all the grains if not mentioned. The saturation magnetization M_s is set to be 750 emu/cm^3 for all the grains at room temperature unless stated otherwise [92].

It should be noted that in practical situations, the real parameters above may vary significantly especially for smaller grains, as the surface-volume-ratio would increase to induce obvious surface effect, and the control of variation would be more challenging. At this point, the accurate characterization techniques are still necessary to develop, while the direct measurements of these parameters are crucial for a better description of the physical system.

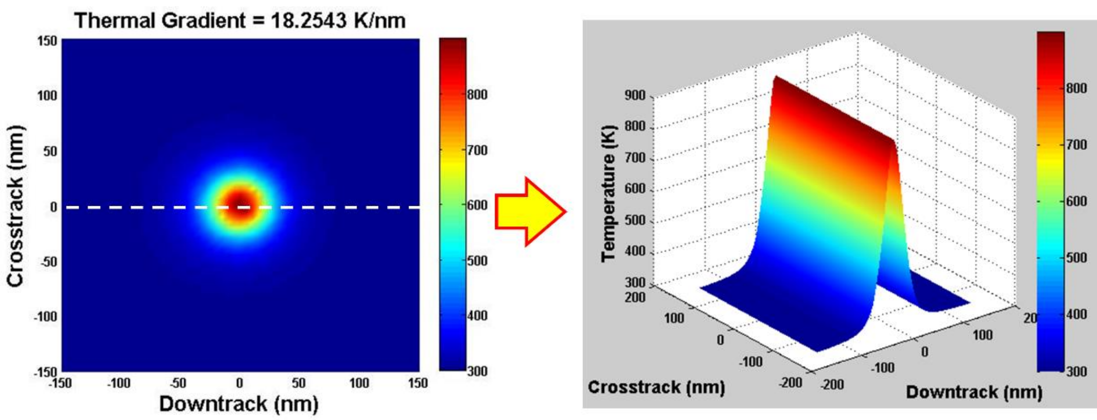

Figure 2.4 Typical thermal profile generated with COMSOL™ and its simplified version, which is used as the input for the micromagnetic modeling.

Following the introduction of the magnetic specifications for both head and medium, here the thermal settings in the modeling will be covered. To obtain an accurate and idealistic thermal profile requires a full understanding of both the thermal head properties as well as the recording medium thermal properties. Present NFT head designs offer various different thermal profiles with series of degrees of freedom [84][96]. Despite multiple specific NFT designs, a quasi-Gaussian heat flux is used as the heating source in the simulation. To avoid dealing with the granular structure of the thin film, stacks of the continuous thin film are used to mimic the recording medium structure in the modeling. The thermal properties are set similar to those in [97]. Both heating source and thermal conducting medium are set in COMSOL™ commercial software package, which uses the finite element method (FEM) to calculate the thermal profile in this simplified heating scenario. A typical thermal profile generated in this method is shown in the left graph in Figure 2.4. For purpose of simplification, the thermal profile is unified along the crosstrack direction. The resulted thermal profile is then generated as the right graph in Figure 2.4. With this modification, the thermal gradient is kept the same along the crosstrack direction. Then this edited thermal profile is used as the input for following micromagnetic simulation. It should be mentioned for most cases, the peak temperature of the thermal profile is set to be $900^{\circ}K$ to ensure optimal transition sharpness with sufficient thermal gradient. If the peak temperature of thermal profile is too low, the thermal gradient at the recording temperature would tend to vanish to zero and no transition could be generated. The thermal gradient (TG) here is around 18K/nm, which would be changed by lateral scaling of downtrack dimension later to obtain different TG values. In recent report of the thermal gradient or even thermal profile measurement [98], [99], the current thermal gradient is still between 6 K/nm and 10 K/nm. In this thesis, it can be seen that the thermal gradient has been tuned between 3 K/nm and 18 K/nm to analyze the relevant affects and tradeoffs.

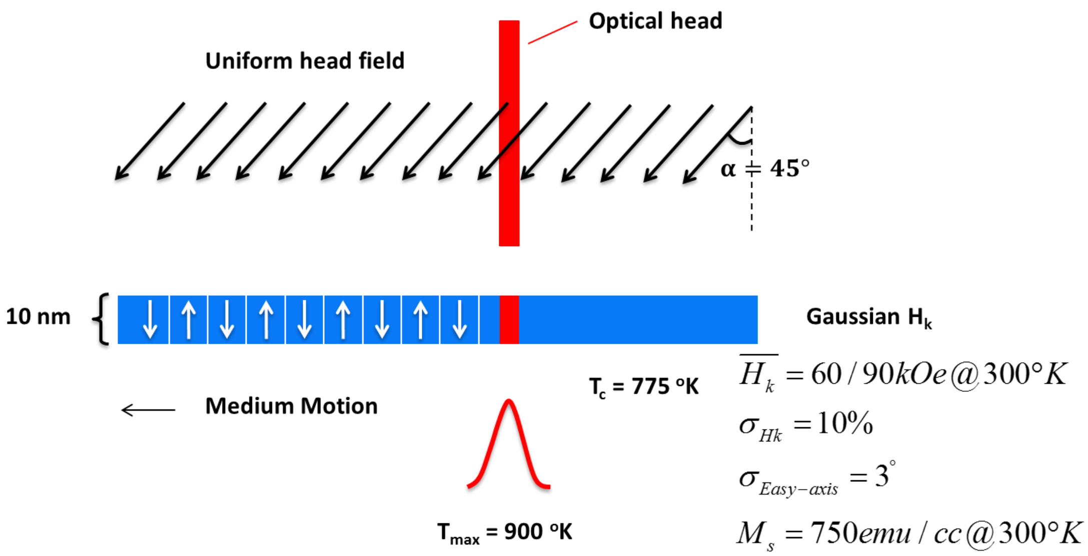

Figure 2.5 Typical recording scheme in the HAMR modeling. The field is uniform all over the medium with 45 degrees with respect to the out-of-plane direction. The writer is moving towards right direction relative to the recording medium.

Additionally, the relative positions and motions of head component and the recording medium are also critical. In current PMR product, the spacing between the air bearing surface (ABS, the lower surface of the writer main pole) and the lubricant top surface of the medium is only a few nanometers. This is to maximally enhance the amplitude and gradient of the head field, which would quickly decay at a position further away from the ABS. The recent Helium filled PMR HDD is partially relying on this advantage as the aerodynamic of lighter Helium atoms allows closer ABS-medium spacing. While in this thesis, both the field and thermal profile are set to be uniform along the depth. Hence the ABS-medium spacing is not a major concern. While to take advantage of the composite medium, like ECC medium, it is definitely necessary to consider the depth variation of the field and temperature profiles.

Regarding the relative motion, the disk rotation velocity is usually evaluated in a unit of rotation per minute (RPM). Generally, when the variation of the rotational velocity is considered, it could be induced from two aspects. One is to simply change the motor rotation speed and another is to consider the linear velocity at the inner track circle or the outer track circle of the disk. For the motor speed, the popular settings are 5400, 7200 and up to 15000 RPM [100]. But to employ higher rotation speed motor would cause issues, such as power consumption and the mechanical reliability and so on. This is also limiting the data rate for the HDD products. For the recording on disk track circles with various diameters, it always has to be considered. For 3.5-inch disk, the velocities at inner tracks and outer tracks could vary significantly. For a 2-inch drive with 5400 RPM, the head disk relative velocity equals to 15 m/s and this is also the default value in this modeling. Besides, to get relative wide bit length and standard comparison, most of the recording is conducted with 1000 kilo flux change per inch (KFCI) or 1 million flux change per inch (MFCI).

To summarize the information above, the typical setting and HAMR recording scheme is shown in Figure 2.5.

2.5 Signal-to-Noise Ratio

To evaluate the recording quality, signal-to-noise ratio (SNR) is critical and commonly refer to. In real recording systems, there are multiple steps to post process the read-out signal, and the specific sensitivity function of the reader sensor has to be characterized. To avoid dealing with various different signal processing algorithms, channel designs or the reader characterizations, this model calculates the SNR value using a rectangular reader having a sensitivity of step function. The raw read-back signal is mostly presented and no additional post-processing is conducted if not mentioned.

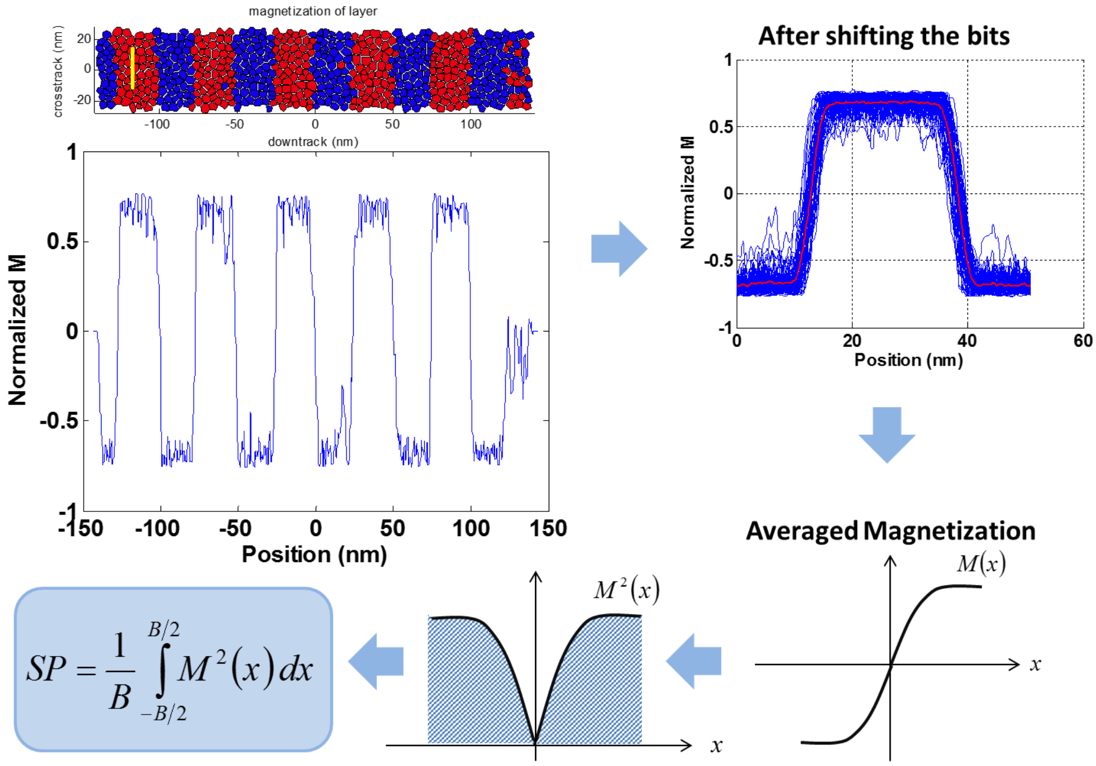

Figure 2.6 The steps to extract the signal power from recording pattern.

Figure 2.6 shows the procedures to extract the signal power from the recording pattern. After the writing process is complete, a narrow rectangular window of 0.1nm downtrack width and 6-grain crosstrack width is utilized to sweep along the downtrack. The step size is set to be 0.1nm to obtain extremely high resolution. The read out magnetization at each step is defined by the overlap area between the reading window and the magnetic grains, multiplied by the vertical magnetization component. Hence, sweeping along the downtrack would give a raw read-back waveform. Those spikes within each bit are because the pseudo reader here has extremely high resolution and the corresponding downtrack position has the relatively larger amount of the nonmagnetic oxide boundary materials. Since the recording is conducted with the 1T pattern, the transition profiles shown as a bunch of blue noisy curves can be shifted together as the top right graph. By averaging each downtrack position, the mean signal is obtained as the red curve in the graph. Ideally, the recorded signal should be a quasi-square waveform. After previous steps, applying square of the mean signal at each downtrack position, integrating over the period length, and normalizing with period length, would eventually give the signal power of the read out waveform. As suggested by work of several groups [22], [101]–[103], the noise mainly consists of the DC noise and the jitter noise. The remnant or DC noise may make the amplitude of square pulse lower and the jitter noise may make the transition less sharp and broadened.

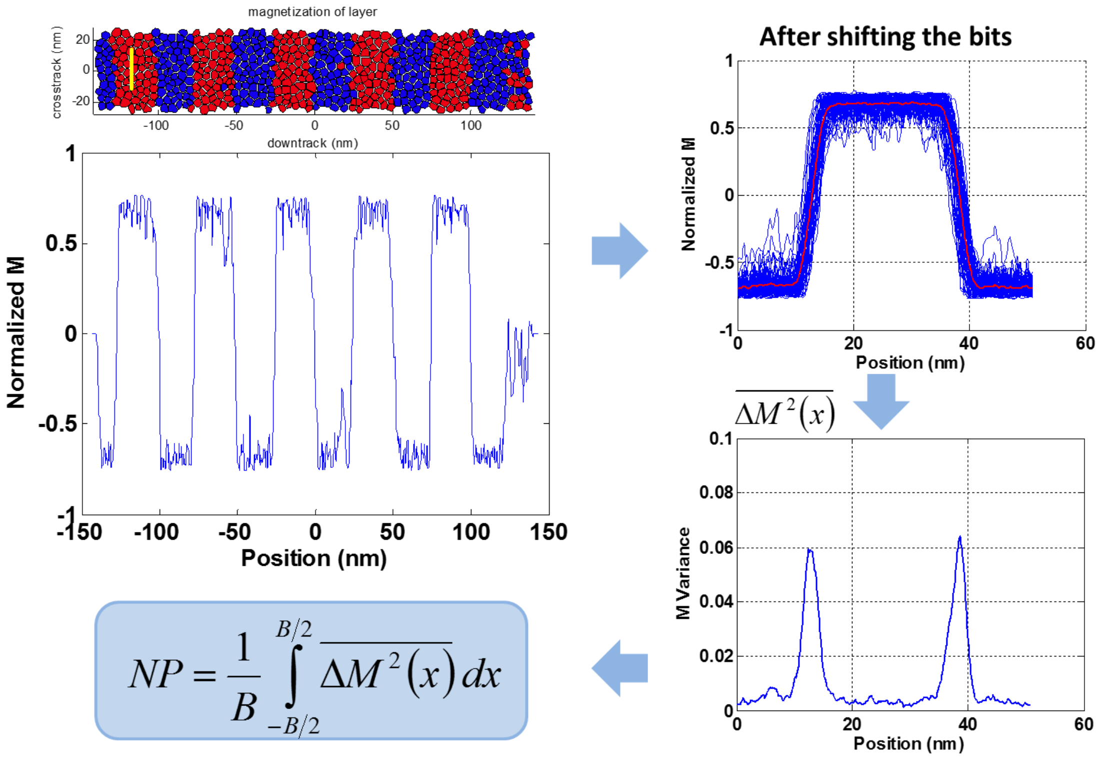

Figure 2.7 The steps to extract the noise power from recording pattern.

Similar to the steps of signal power extraction, the transition profiles are shifted together. Instead of averaging, the bunch of curves are used to calculate the variance along the downtrack. Then taking the integration of variance along bit length and dividing bit length will give the noise power. The jitter noise is supposed to correlate with the spikes in the variance plot. For the DC noise, the variance in the middle of bits may still remain fairly low, even if DC noise is quite high.

With the signal power and noise power obtained, the logarithmic ratio of them would give the signal-to-noise ratio (SNR) as Equation (2.19) in a unit of decibel (dB).

$$\mathit{Signal\ to\ Noise\ Ratio} = 10\log_{10}\left(\frac{\mathit{Signal\ Power}}{\mathit{Noise\ Power}}\right) \tag{2.19}$$

3. Recording Physics

In this chapter, the fundamental recording physics, and the underlying noise mechanism will be covered. The formation and characteristics of magnetic transitions created in granular FePt-L1_0 film media by thermal profiles generated by near-field transducer will be analyzed. The medium SNR performance dependence on grain sizes or pitches is the focus. In the conventional perpendicular magnetic recording, people keep scaling down the grain pitch size so that there would be less zigzag at the transitions, which leads to higher medium SNR and higher areal density. However, in the HAMR scheme, the situation is more complicated.

3.1 Size Effect on Recording Field Dependence

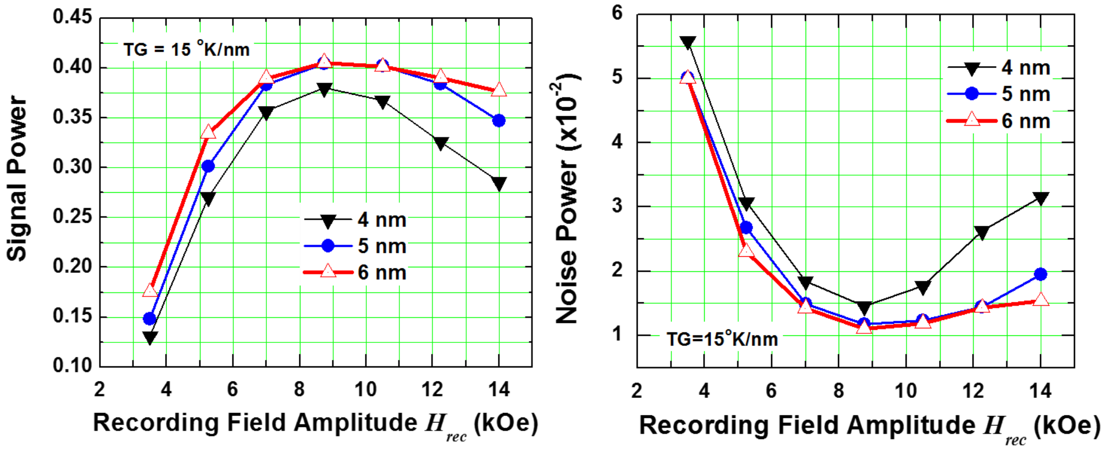

Figure 3.1 Signal power and noise power as a function of the recording field amplitude with three different grain pitch sizes [104], [105]**, 4 nm, 5 nm and 6 nm, respectively.**

Figure 3.1 shows the calculated signal power and noise power as a function of the recording head field amplitude for three different grain pitch sizes. For each of the grain pitch size, there is an obvious applied field dependence of both signal power and noise power. Besides, there is specific optimal field value to get highest signal power and lowest noise power at the same time. Below the optimal applied head field, with lower applied field amplitude, the signal power will be lower and noise power will be higher. On the other hand, beyond the optimal head field, with higher applied field amplitude, the signal power will reduce and noise power will increase. It should be mentioned that the thermal gradient here is fixed at 15K/nm, yet this type of behavior is representative.

Similar behaviors with certain variations can be observed in different system specifications, but the primary field dependence and relevant trends still remain the same. Meanwhile, it should be noted that for the three different grain pitch sizes here, the optimal SNR value is relatively higher for the larger grain size. As is well known, in conventional PMR, the smaller granular medium is supposed to provide superior performance, since the finer grains would form sharper transitions with less jaggedness. However, here, the smaller grain pitch size shows poorer recording quality. To justify this counterintuitive observation, closer observation is conducted as follows.

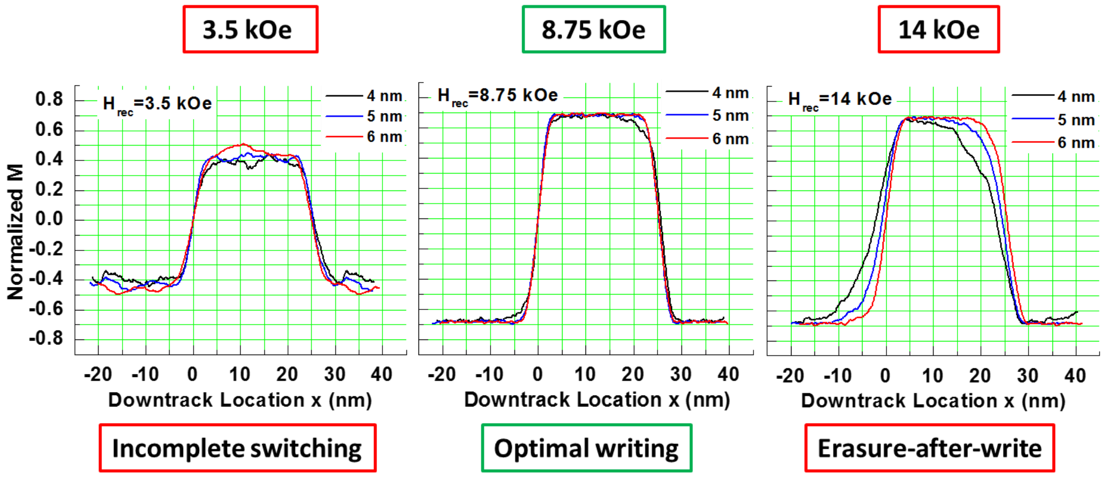

Figure 3.2 Transition profiles at low, optimal or high applied field values, which have incomplete switching noise, optimal recording, and erase-after-write noise, respectively.

In Figure 3.2, three recorded transition profiles of three different grain pitch sizes of 4 / 5 / 6 nm, at low field (3.5 kOe), optimal field (8.75 kOe) and high field (14 kOe) values are shown together. Ideally, the recorded transition profile should be standard square waveforms. It is the DC noise and jitter noise that make the transition profile deviate from the square wave. In Figure 3.2, the transition profile at optimal field value is the one closest to the standard waveform. Among the three, this profile has been saturated to similarly high magnetization level. Very slight degradation at the tail of each transition bit could be noticed for the 4 nm grain pitch size, while the 5 nm or 6 nm are of almost no noticeable defects.

When the field is at a low value of 3.5 kOe, the magnetization level of the transition profile is far from saturation level of 8.75 kOe case. This is because, during the recording process, the magnetic grains would be heated beyond Curie temperature, T_c, first and then cool down to room temperature again. Since the magnetic state cannot be maintained when the temperature is beyond T_c, the heating process will clear the information and only cooling process will allow the information bit to be written. Because the applied field from the writing component is limited and the FePt recording medium has very high anisotropy field, H_k, the recording process has to happen at high temperature to lower H_k, so that the head field is strong enough to change and maintain the magnetic state of grains. However, during cooling, when the temperature is lower than but still close to T_c, the magnetization is relatively low and the temperature is high. Therefore, the resulting thermal agitation field would be very intensive. This would make the magnetic state of grains very unstable. Additionally, if the applied field value is not that high, the recorded bit would not be magnetized or maintained as expected. Only a portion of all the grains would be switched properly in this case. This type of noise is named as incomplete switching noise. It can be seen that this type of noise would make the initial writing quality degrade, while no after effect is following it.

In contrast, when the applied head field is higher than the optimal field value, it can be noticed that the magnetization level is similar to the optimal field case. At the end of each bit, the degradation is noticed for all three grain pitch sizes. This degradation is more severe when the downtrack position is closer to the transition and the degradation decays when the position is further away from the transition. The underlying reason for this type of noise is because after finishing writing of the first bit, the polarity of the magnetic head field would be switched to record the consequent bit. As shown in typical setting of the modeling, the thermal profile of the recording is quasi-Gaussian along the downtrack position, with extension of tail. Therefore, when the writing of the second bit starts, the cooling of the previous bit is not complete. The thermal profile tail can extend to the previous bit. At this time, with the switched head field, the grains in the previous bit would have a probability to switch to the other direction. So this type of noise is called erase-after-write noise. Through the explanation above, it can be noticed that this noise is related to both the switched head field and the thermal profile. Besides, whether the medium is hard or stable enough also has impact on the erasure noise. Since the grains closer to the transition would have higher temperatures during the erasure, they would be more vulnerable to suffer from the erase-after-write noise. This is why the noise is most severe at the transition and gradually decays away from the transition position. Another aspect worth attention is that this noise happens after the initial writing process is complete, which makes this type noise an after effect.

Apart from the discussion above, it should be pointed out that among the three graphs in Figure 3.2, the degradation is always more severe for smaller grain pitch size. Similar to the previous signal power and noise power plot suggests, this is counter-intuitive. In conventional perpendicular magnetic recording scheme, the smaller grain pitch would make the transition much sharper, so the medium SNR value would be greatly enhanced. Here the observation in HAMR scheme is the opposite, and the intrinsic reason is because as the grain size is smaller and smaller, the thermal agitation field, which is inversely proportional to the grain volume, would be stronger. Both the incomplete switching noise and the erase-after-write noise are thermal induced noise. Therefore, with smaller grains in the recording medium, both types of noise would be more significant as thermal agitation increases. When the grain size is below a certain limit, the increased thermal noise would cancel the geometry induced SNR benefit from smaller grains. Then the SNR gain would even be replaced by the SNR reduction. This is the reason why this counterintuitive behavior is observed. Regarding the grain pitch limited SNR, further analysis will be given after discussion of the recording pattern characteristics and the dynamic recording process. The essential origin of these noise sources will later also be validated to be the thermal agitation.

To better understand the head field amplitude dependence, the recording magnetization patterns are analyzed as shown in Figure 3.3. The representative magnetization patterns of recorded transitions under same field values in Figure 3.2 are shown here. (a), (b) and (c) correspond to the low field, optimal field, and high field, respectively. With low head field, in graph (a), the basic recording pattern can vaguely be observed after writing process. But many randomly flipped grains exist within each of the information bit. As mentioned before, this is due to the insufficient head field amplitude, which is not strong enough to maintain the magnetization orientation during the cooling process. Because this process happens during writing, many grains are not flipped as expected, which is the reason why the magnetization level in Figure 3.1 is lower, when head field is 3.5 kOe. It can be also noticed that the magnetization patterns with smaller grain size have more randomly flipped grains. This further validates the observation that the smaller grain medium has more noise in this case.

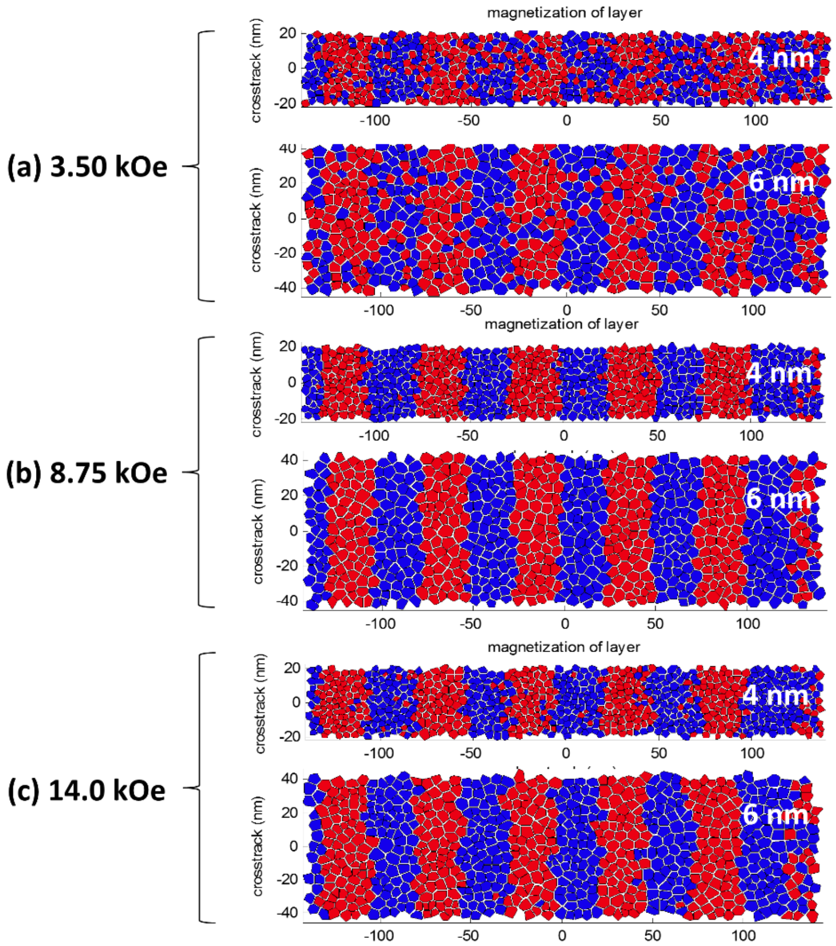

Figure 3.3 Magnetization recording patterns under low field (a. 3.5 kOe), optimal field (b. 8.75 kOe) and higher field (c. 14.0 kOe). Both small (4 nm) and large (6 nm) grain size are shown for comparison.

For the high head field case in graph (c), the applied field is much higher than the optimal field value. For this case, the writing process is properly conducted with sufficient head field value. However, when the writing of the consequent bit starts, the switched head field would be also applied to the previous bit, which has not completely cooled down yet. This would result in the partial erasure of the previous bit. In the graph group (c), the randomly flipped grains can be observed to concentrate near the end or tail of the bits, instead of everywhere. The closer to the transition, the more random flipped grains can be seen. Also, compared to the large grain medium, the medium with smaller grain pitch size show more noise grains embedded, which is due to higher thermal agitation field. While in graph group (b), the head field amplitude is around the optimal value. It can be seen that the grains within each bit are mostly switched properly and the transition sharpness is primarily defined by the grain geometry. No significant amount of the randomly flipped grains can be observed. This would help make the transition profiles approach ideal square waveform.

To further validate the formation and characteristics of the noise behaviors above, magnetic dynamics of a single grain is tracked through the entire recording process as shown in Figure 3.4. Similar to Figure 3.1, three groups of graphs are shown in turn, which correspond to low, optimal and high field cases, respectively. In each group of graphs, the top one is the recording magnetization pattern and the bottom one is the z component or the out-of-plane magnetization component versus the recording time.

For low field case, the grain labeled by the yellow arrow is supposed to be pointing upward after recording. From the time evolution of the out of plane magnetization component, it can be seen the grain is initialized to point downward at the very beginning. From 0 nanosecond (ns) to around 7.6 ns, the temperature gradually increases and the magnetization shrinks accordingly. Between 7.8 ns to 9 ns, the temperature is beyond Curie temperature and therefore the magnetization magnitude approaches to zero. After 9 ns, the magnetization starts to recover and this indicates the temperature is below Cure temperature and the cooling process starts. For this specific grain, the head field during the cooling process should be positive, while the magnetization is always negative and points into the plane. So after the entire writing process, the magnetization is still negative and did not switch as expected. Quite a few grains like this would cause the overall incomplete switching noise as a result from insufficient head field value. Meanwhile, looking closely at the z component vs. time curve, numerous tiny spikes can be observed. This is supposed to be caused by the thermal agitation field, which would make the spin rotate and vibrate randomly. From

7.8 to 9 ns, the spikes magnitude seems to be larger than other time ranges, which is because the temperature is beyond T_c, thus induceing higher agitation field.

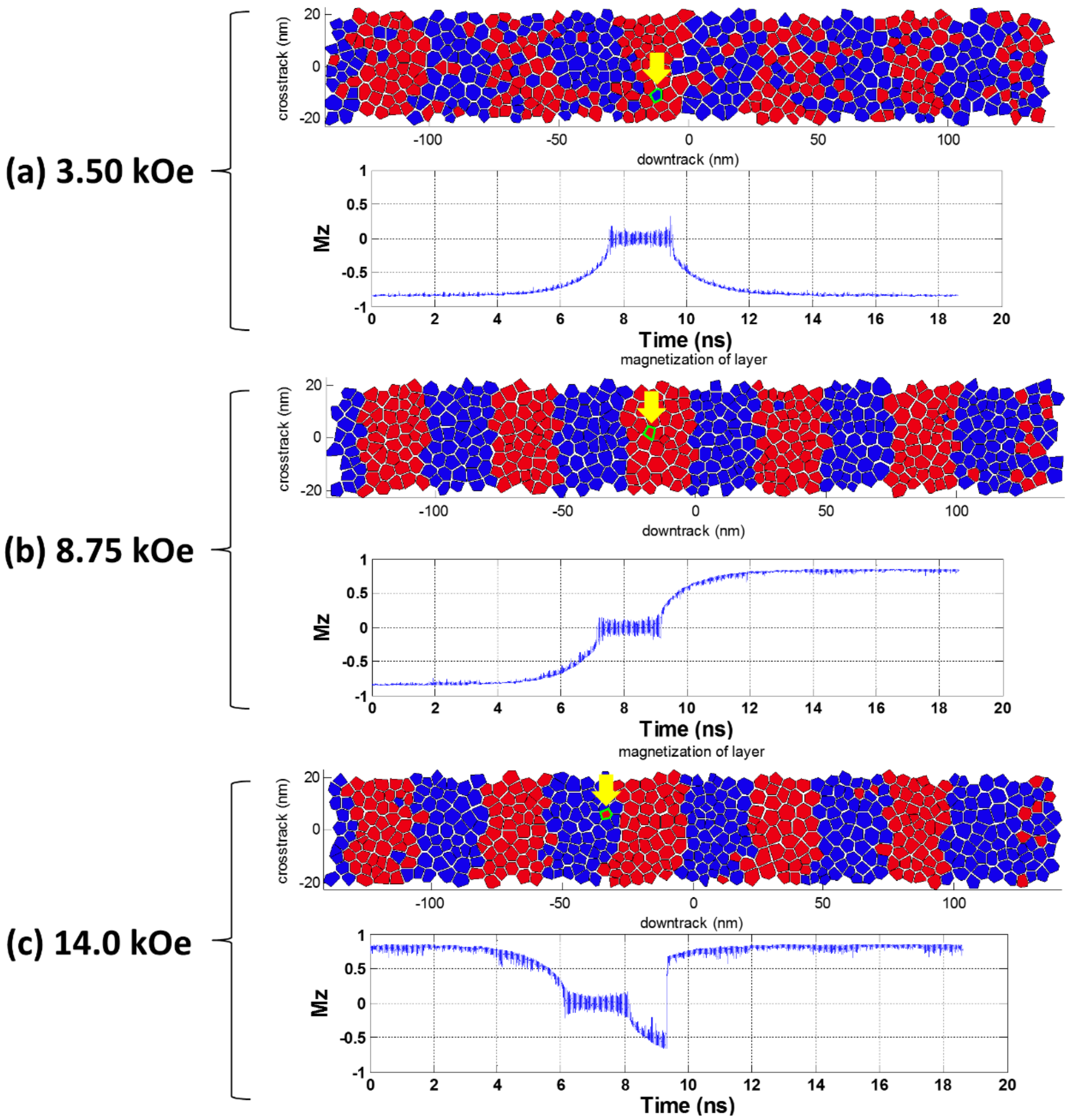

Figure 3.4 Switching process tracking of a single grain in the recording medium through the entire recording process. The incomplete-switching, successful switching and erase-after-write happens under low (a. 3.5 kOe), optimal (b. 8.75 kOe) and high head field (c. 14.0 kOe) magnitude correspondingly.

In graph group (c), the writing is conducted with the high field. The grain labeled by yellow arrow here is supposed to be blue (in a blue bit) and has negative magnetization to point into the plane. From the time evolution of magnetization, it can be seen that from 0 ns to 6.1 ns, the temperature gradually increases and magnetization shrinks simultaneously. From 6.1 ns to 8 ns, the magnetization is nearly zero, which suggests that the temperature is beyond the T_c. After 8 ns, the magnetization is nonzero and starts to recover. From 8 ns to 9.4 ns, it can be noticed that the magnetization is negative, but after 9.4 ns, the magnetization changes its polarity quickly and points upward instead. This is because the switched head field makes this specific grain flip before this grain completely cools down. Similar grains can also be seen at the edges of other transitions. This type of grains makes the transition blurred and is categorized as erase-after-write noise. Meanwhile, it can be noted that there are several ranges where the spike magnitude is larger. These ranges relate to the period when the field polarity is opposite to the magnetization. Since the opposite field tilts the spin and consequently the thermal agitation field would disturb the spin more easily and cause more noise.

For purpose of comparison, the writing with optimal head field is shown in group (b) in Figure 3.4. For this specific grain, the magnetization is initially set to be negative. During the writing process, the magnetization is positive and gradually recover without sudden change. Since the grains are mostly switched as the expected orientation, the information bits are created rigorously and would lead to high SNR.

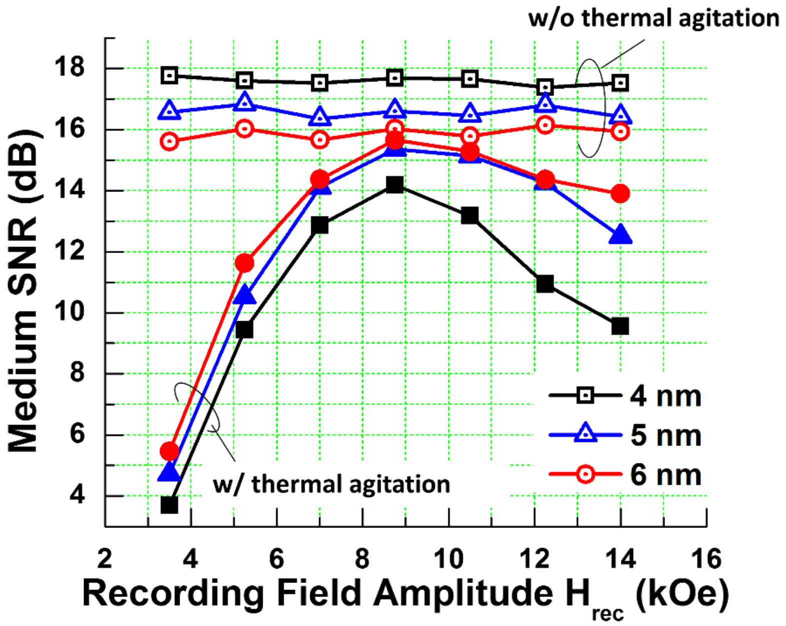

Figure 3.5 Recording field amplitude dependence of the recording medium SNR using three different grain pitch sizes, with or without thermal agitation field.

As mentioned, the smaller grain pitch medium has more noise in the cases above, and it is believed to be caused by higher thermal agitation with smaller grain volume.

To further identify this physics origin, the same recording process is also conducted with the thermal agitation field term turned off in the simulation. The comparative results are shown in Figure 3.5. The results indicate that the curves with thermal agitation field, have overall SNR values lower than those without thermal noise. Meanwhile, with thermal agitation, an obvious head field dependence can be observed, while the SNR values are independent of the applied head field when thermal agitation is off. On the other hand, for the curves with thermal agitation, the 4 nm grain pitch gives lowest SNR value. Without thermal noise, the 4 nm grain pitch will have higher SNR instead, which coincides with expected results. Therefore, these observations prove that the field dependence and the size effect are originally caused by the thermal agitation. The smaller the grain pitch, the more significant the difference between cases with, or without thermal noise, the stronger field dependence of SNR.

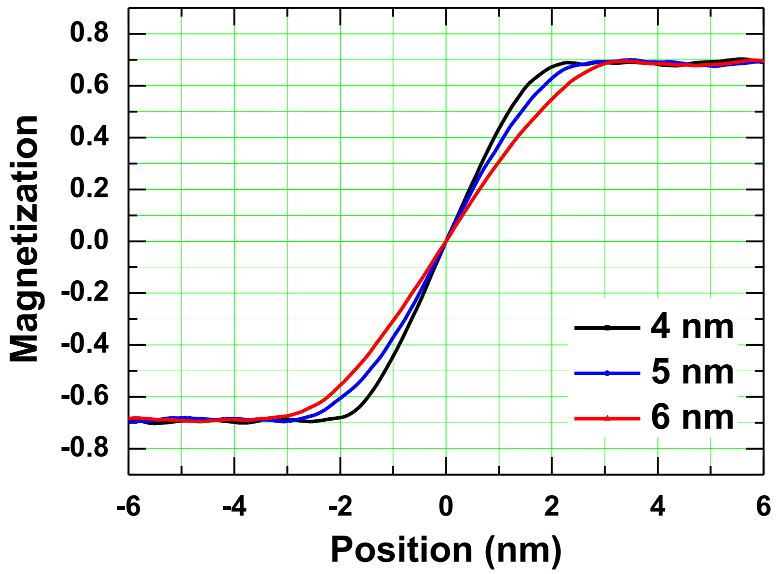

Figure 3.6 Recording transition profile along downtrack position with various grain pitch sizes.

Figure 3.6 shows the transition profiles along downtrack position of three different grain pitch sizes without thermal agitation field. In HAMR scheme, the effective field gradient is the product of the anisotropy field temperature gradient, dH_k/dT, and the thermal gradient, dT/dx as Equation (3.1).

$$\frac{dH_{eff}}{dx} = \frac{dH_k}{dT} \cdot \frac{dT}{dx} \quad \textbf{(3.1)}$$

Assuming the value of dH_k/dT is 600 Oe/K and dT/dx is 15 K/nm, their product will give 9000 Oe/nm. This is much larger than that in the conventional PMR scheme, where the effective field gradient is usually below 1000 Oe/nm [106], [107]. The effective field gradient in HAMR is so high that the transition sharpness is limited by the grain pitch size. Without the thermal agitation, the smaller grain medium would have sharper transitions, which is the case in Figure 3.6.

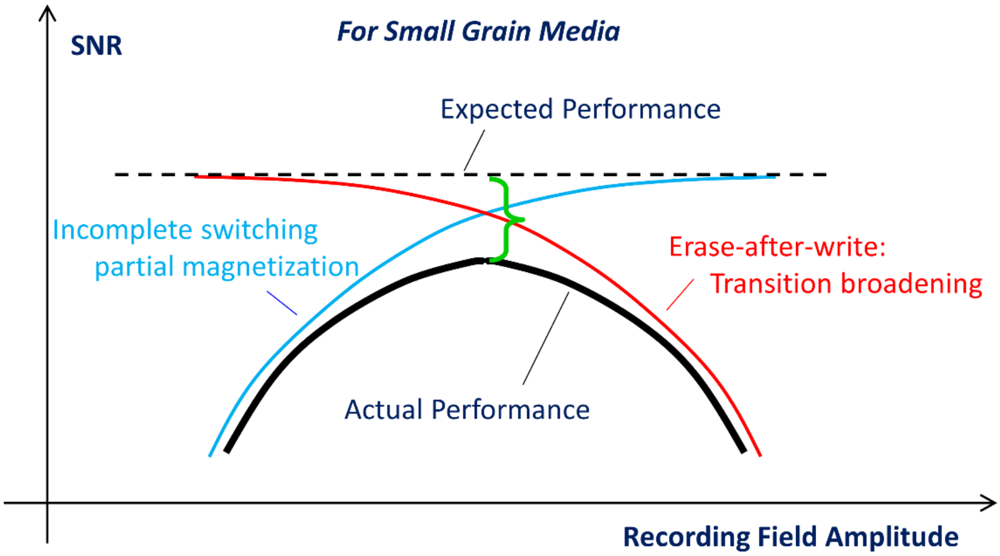

Figure 3.7 Schematic of the thermally induced noise, incomplete switching, and erase-after-write.

To summarize the thermally induced incomplete switching and erase-after-write, a schematic is shown in Figure 3.7. As shown here, these two types of noise mainly can be observed in the small grain medium. The smaller the grain, the more severe these noises. As the applied recording field increases from low to high value, the partial magnetization due to incomplete switching is gradually minimized, but there is no clear point when this is reduced completely. In contrast, when the applied recording field decreases from high value to low value, the transition broadening due to erase-after-write is gradually minimized, but there is not a clear boundary where erasure is totally prevented. If ideal recording quality without thermally induced noise is represented by the dashed line in the figure, the actual performance would be lower than the ideal performance, due to the combinational effect of both incomplete switching and erase-after-write. Such combinational noise also gives this head field amplitude dependence of recording performance. This type of behavior is very representative and typical in HAMR scheme, but some variations of different degrees should be expected. More detailed analysis of different scenarios will be discussed in later sections.

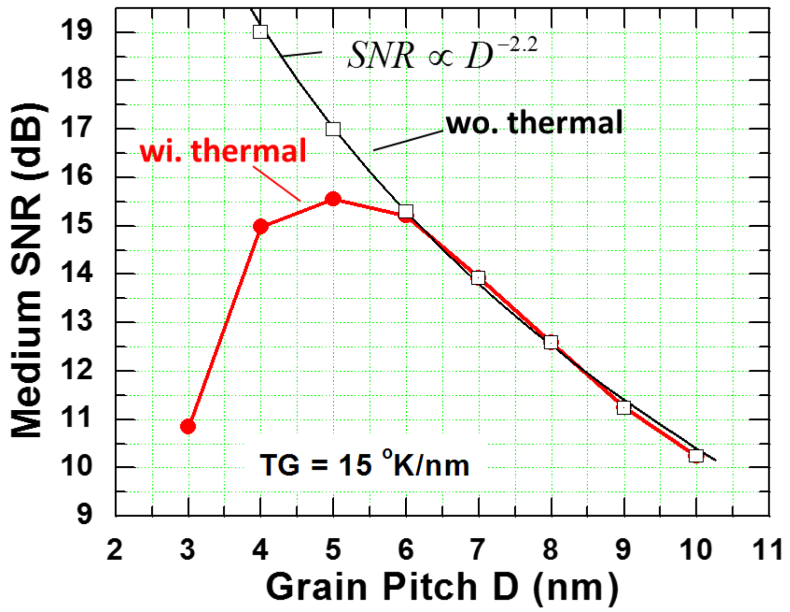

Figure 3.8 Optimal SNR value as a function of the grain pitch size, D (the grain center-to-center distance), with (red) or without (black) thermal agitation field term. The SNR without thermal noise follows a function of $D^{-2.2}$.

Now that it can be noticed that in the cases above, the smaller grain has worse performance. While for relatively large grain, the thermal agitation should be much slighter and recording should behave more similarly as PMR scheme. Then the question is where the turning point appears. To answer this, the field dependence for a series of grain pitch sizes have been calculated to obtain the optimal SNR value correspondingly. The obtained optimal SNR is replotted as a function of the grain pitch size as shown in Figure 3.8. The square symbols and the black curves refer to the cases with thermal agitation field term switched off. It should be mentioned that the SNR values shown here in Figure 3.8 have been obtained by considering the same track width of 30 nm. The results indicate that when the grain pitch is larger or equal to 6 nm, the SNR values with or without thermal agitation is the same. This also suggests that the optimal SNR or grain pitch limited SNR has been reached. However, when the grain pitch is lower than 5 nm, the smaller grain pitch gives significantly lower SNR value. For the specific setting here, the turning point happens to be 5 nm grain pitch. Apart from this, when the grain pitch is below 6 nm, the SNR value with thermal agitation starts to deviate from the SNR without thermal noise. This means that the SNR is below the grain pitch limited SNR and degrades due to the more severe thermal induced noise, like incomplete switching and erase-after-write. These thermally induced noises have canceled the SNR gain from scaling down of grain size and become dominant. Besides, for the black curve, the medium SNR is approximately proportional to $D^{-2.2}$, where D is the grain pitch size. With smaller grain pitch, the SNR monotonically increases. This matches up with the statement that the SNR is proportional to the number of grains within each bit [19].

In this section, the thermally induced incomplete switching and erase-after-write have been discussed and the underlying physical origin is validated to be the thermal agitation. These effects together lead to the head field dependence, which makes the real optimal SNR lower than ideal no-thermal SNR, especially when grain size deeply scales down. This phenomenon fundamentally limits the conventional way of enhancing storage density just with smaller grain medium.

In practice, it would be critical to construct the grain pitch dependence of the real SNR to precisely locate the deviation point similar to Figure 3.8. This allows people to make sure whether the SNR gain from grain scaling down would not be completely canceled by the thermal noise. From the thermal agitation aspect, it can be noticed that the random field amplitude is mainly dependent upon the temperature, damping, saturation magnetization and grain volume. Lowering the recording temperature and increasing the grain saturation magnetization may help suppress the thermal noise. At the same time, to lower the recording temperature may result in the thermal gradient decrease, which may have SNR penalty (shown later). To tune the saturation magnetization, the chemical composition of the medium may have to be changed, which may affect other medium properties. Regarding the damping constant, active research have been going on to characterize or manipulate it. While the magnetic torque is also a function of the intrinsic damping constant. With larger damping, the thermal noise would be less but the dynamics may be faster. Through several preliminary simulation studies using model described in this thesis, the change of intrinsic damping between 0.01 and 0.2 does not significantly vary the recording performance. This suggests that these two effects may cancel each other greatly. While for the grain volume, although people try to employ smaller grain to make transition shaper, the following increases in thermal noise may cancel the gain. This also suggests that the recording may be enhanced with small or even no decrease of grain size.

After the optimal SNR vs. grain pitch size is constructed and the next question would be to understand how to manipulate the SNR vs. grain pitch curve, so that the deviation from ideal no-thermal SNR would happen at smaller grain pitch.

3.2 Recording Time Window

In section 3.1, the thermally induced incomplete switching and erase-after-write noises have been introduced along with the resulting field dependence and deviation from ideal SNR, especially for smaller grains. However, this is actually only one facet of the recording physics. Through careful examination of the recording behaviors in many different setups, it has been discovered that there is a single quantity, recording time window, which tightly correlates with the system performance and will be discussed in this section.

Figure 3.9 shows the combined figure of both anisotropy field H_k versus temperature (rotated counterclockwise 90 degrees, on the left) and the temperature versus downtrack position (on the right). Since the applied head field region is much larger than the region of the thermal profile generated by NFT, here the head field is assumed to be a constant value. The effective field, H_{eff}, can be calculated from this value with Stoner-Wohlfarth model [108]. By projecting this value onto H_k vs. T curve, a corresponding temperature can be found. Below this temperature, the head field is lower than the anisotropy field and recording should not happen, thus this temperature is named as recording temperature, T_{rec}. By projecting both T_{rec} and T_c onto the thermal profile, two spatial positions along downtrack direction can be obtained. The cooling and recording process is supposed to happen within this range. As the disk is rotating at a specific velocity, v, dividing the spatial range with v would give the time range. Since for each grain, this time period allows for recording, it is named as recording time window (RTW). The equation on the right-hand side in Figure 3.9 gives the method to calculate the RTW. It indicates that the RTW is a function of the H_k vs. T curve, head field, Curie temperature, thermal profile, and disk rotational speed. Later, it can be observed that the system performance tightly correlates with the RTW.

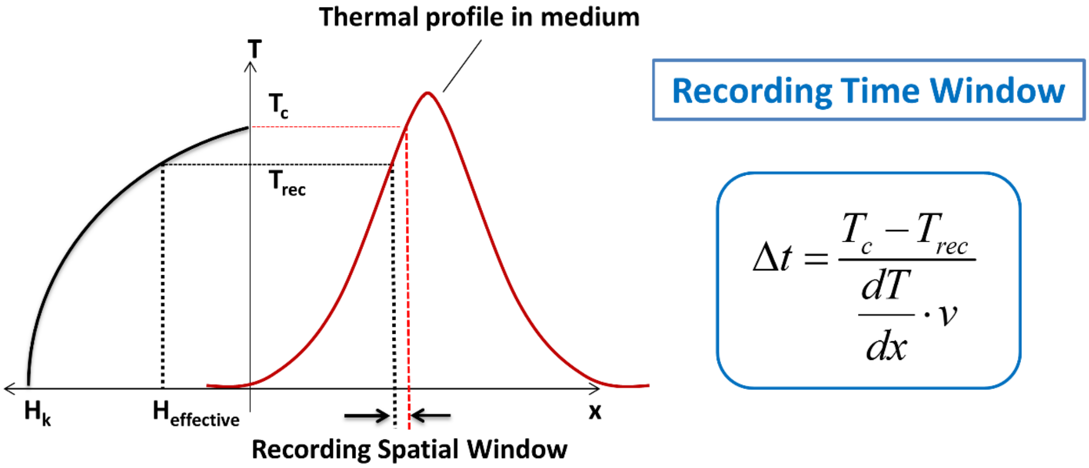

Figure 3.9 Schematic of the definition for the recording time window, where x is the downtrack position.

Looking back at the previous field dependence of the recording performance, RTW could be utilized to help explain the behavior. From Figure 3.9, it can be seen that low / high field value would lead to short / long RTW. Since the switching of spin would have to take a certain amount of time, it is critical to make sure that the time provided during recording is sufficient. If the time provided is too short, the spin could not complete switching. If the time provided is too long, the spin may be quite unstable after the spin switches completely. Therefore, it can be interpreted that the low field causes limited RTW and results in the incomplete switching, while the high field causes redundant RTW and results in the erase-after-write. At the optimal field value, the RTW would be just right for spins to switch. When the recording conditions, like medium properties, thermal agitation intensity and so on change, the ideal RTW may vary slightly. The degrees of the incomplete switching and erase-after-write may vary as well, but the primary trend and field dependence still remains. To maximize the HAMR system performance, it is necessary to find the exact time for the spin of grains to complete switch. As the industry has been making efforts to take advantage of the smaller grain medium, which may induce more property variation and enhancement of thermal noise, to understand and measure the spin dynamics and required RTW would become increasingly important.

This additional consideration is quite special for HAMR application, compared to the conventional PMR scheme. As in PMR, the entire recording is conducted at room temperature, where thermal noise is much milder and has a lower impact on the recording. The magnetic dynamics of the grain spins are almost completely deterministic. The spin trajectory projections in this section have quite intensive oscillation or noise spikes, especially in a high-temperature bath. This thermal noise makes the spin magnetic dynamics much more nonlinear and nondeterministic.

Assuming that the HAMR recording system is properly designed and fabricated, this ideal spin RTW may eventually become a fundamental physical limit for the data rate. The input or output rate beyond this switching speed may lead to the degradation, like incomplete switching. At this time, to employ the nonlinearity of magnetic dynamics and ultra-fast switching properties might be a potential solution to surpass this spin dynamic limit. But for now, even the magnetic dynamics of the writer may be still relatively slow to provide such high speed of magnetic field polarity switching.

3.3 Disk Velocity

As indicated by the equation in section 3.2, the recording time window is a strong function of velocity. Therefore, a straightforward way to tune the RTW without modifying the system settings would be to change the disk velocity.

Figure 3.10 shows the medium SNR versus head field amplitude with different disk rotational velocity values. It can be noted that both curves have similar field dependence, while the obvious shift of the curves can be seen. At the low field side, the case with slower velocity has higher medium SNR value. This is because the low field would lead to incomplete switching noise, since the RTW is relatively narrow for this case. With slower disk rotation, the RTW would be longer and allow better magnetization process and enhance the SNR. On the other hand, when the field is much higher than the optimal value, the recording primarily suffers from the erase-after-write noise. This is because the redundant RTW would make the recorded grains expose to the switched field. Therefore, when the disk is rotating much faster, this redundant exposure time would be effectively narrowed, so that the erasure is greatly avoided and SNR would increase.

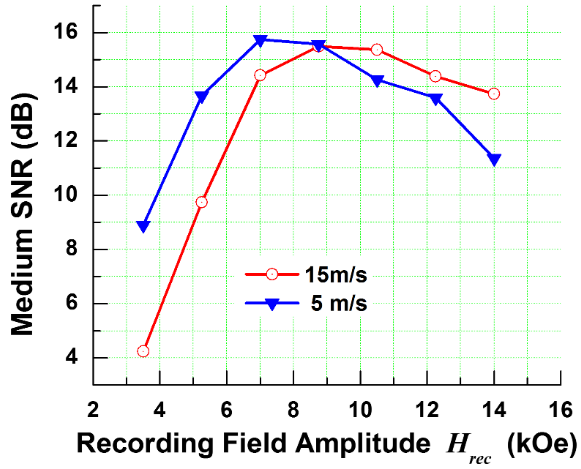

Figure 3.10 Medium SNR versus the recording field amplitude with different disk rotational speed, 5 m/s (blue) and 15 m/s (red), respectively.

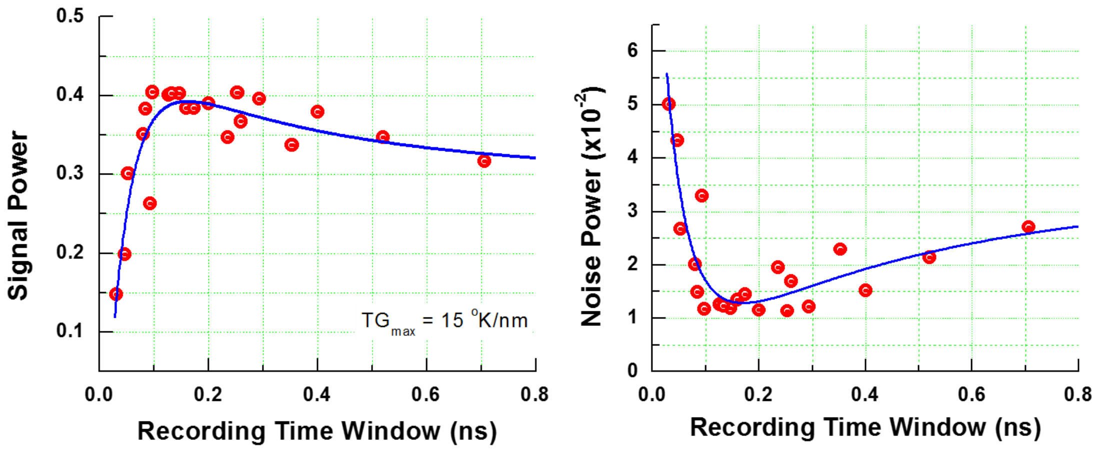

Figure 3.11 Signal power and noise power as a function of recording time window for different disk velocities while keeping other parameters the same. The optimal RTW is between 100 ps and 200 ps here.

From these results, it can be seen that the tuning of velocity would greatly impact the medium SNR. In Figure 3.11, the corresponding signal and noise power with different velocity values and the same other parameters are plotted together in terms of RTW. The left graph and the right graph relates to the signal power and noise power, respectively. The results indicate that the correlation between the system performance and the RTW is relatively tight. When RTW is too short, the signal power is low while noise power is high. Similarly, when the RTW is too long, the signal power decreases and noise power increases due to the erasure. It should be noted that there is an optimal value of RTW and in this case, it is around 100 ps to 200 ps. This optimal RTW is close to the value from a different perspective and method like in [109]. This strong correlation between performance and RTW is very critical and useful since the complicated HAMR system can now be interpreted in the same single term and optimized. This also provides guidance on towards which direction the primary parameters should be tuned. Further application and validation will be given later.

From the investigation of disk rotational velocity, it is validated that the system performance does tightly correlate with RTW. Currently, the disk RPM primarily ranges from 5400 to 15000. Besides, with the same disk velocity, the inner track circle, and outer track circle would have very different velocities. Therefore, while maintaining the proper parameters of other aspects, the modulation of RPM should also be included to compensate the change of RPM or track circle radius.

It should also be noted that for the realistic situation, when the velocity is modified, the aerodynamics of the writer would be affected as well. For instance, with higher linear velocity, the spacing between ABS and the medium top surface tends to increase. Hence the head field strength felt by the medium would decay and the field angle will also change. Since the optical writer, or the NFT, would also be further from the medium, the thermal profile shape may also change. To maintain the writer flying height and orientation, there is active research going on about the thermal-flying-height-control (TFC) [110]–[112]. However, even if the relative distance and orientation are kept the same with different rotational velocities, the nanoscale heat transfer at the head-medium-interface may still vary. This would result in the thermal profile change. Since the heating temperature, thermal gradient and so on would also greatly affect the RTW, it is critical to have a full understanding of the nanoscale heat transfer. In terms of the thermal reliability of the recording system, the different heating mechanisms may also alter the robustness and efficiency of the NFT as well as the protection layers, like the lubricant and the overcoats. More aggressive heating may make the lubricant evaporate or even have chemical properties change at a faster rate. The overcoat may also more easily suffer from thermal challenges, mechanical attack, chemical corrosions and so on. To summarize, when tuning or maintaining the ideal disk velocity, the other system parameters should also be carefully looked at to avoid abrupt change from happening.

3.4 Thermal Gradient

From the equation of RTW, the thermal gradient would also directly change the RTW value. Meanwhile, in Figure 3.8, a deviation from the optimal SNR can be seen and how to make this deviation appear at smaller grain is a critical question. Here, the thermal gradient of the heating profile is adjusted to see its impact on the recording quality. The recording thermal gradient (TG) here refers to the dT/dx near recording temperature in the thermal profile at the cooling side.

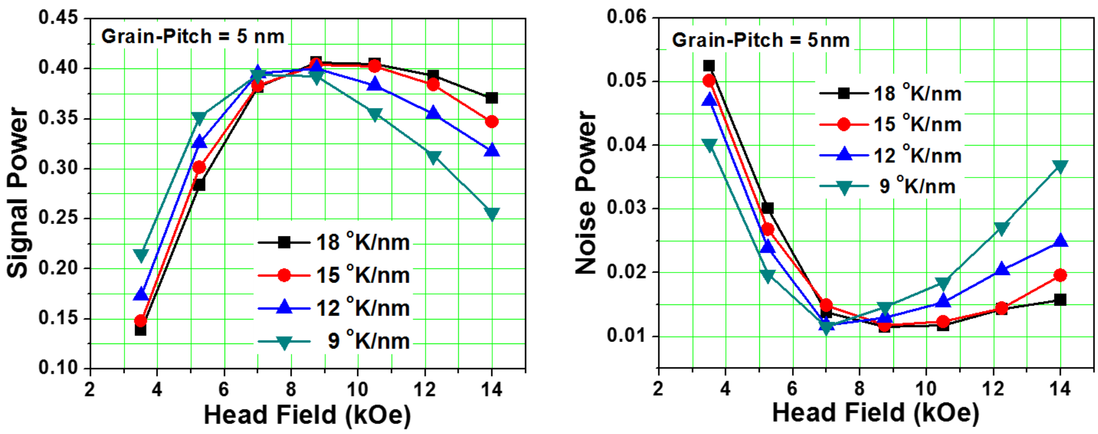

Figure 3.12 Signal power (left) and noise power (right) as a function of the head field with various thermal gradients for 5 nm grain medium.

Figure 3.12 shows the signal power and noise power versus the head field value. The recording has been conducted with 4 different maximal thermal gradients, 9, 12, 15, 18 K/nm. The results suggest that with different thermal gradient, the general trend of the curve remains similar. The signal power increases with head field, reaches the maximum and then decreases with the head field. While the noise power decreases with head field, reaches the minimum and then increases with the head field, accordingly. Besides, on the low field side, the higher thermal gradient gives lower signal power and higher noise power. It is because that the recording already suffers from the insufficient RTW and increasing of TG would make the RTW even shorter. Then the incomplete switching noise would be more severe. On the high field side, the higher thermal gradient gives better performance. This is because that the higher field case would suffer from the erase-after-write, which is caused by the redundant RTW. By increasing the TG, the RTW would be narrowed so that the exposure to erasure is reduced. Additionally, comparing the optimal value of each curve would suggest that the optimal SNR is gradually increasing when the thermal gradient is enhanced. Therefore, further increasing the TG is necessary to keep increasing the optimal SNR value. As mentioned, the incomplete switching happens during the initial writing process, while the erase-after-write would happen after the initial writing is complete. The initial writing could be done properly with different TG, although the higher TG requires higher head field. But higher TG would greatly help alleviate the erase-after-write. So optimal SNR is higher with higher TG. To this point, there is also experimental work going on to measure the realistic thermal profile and its thermal gradient value tends to be between 5 K/nm and 10 K/nm [98], [99].

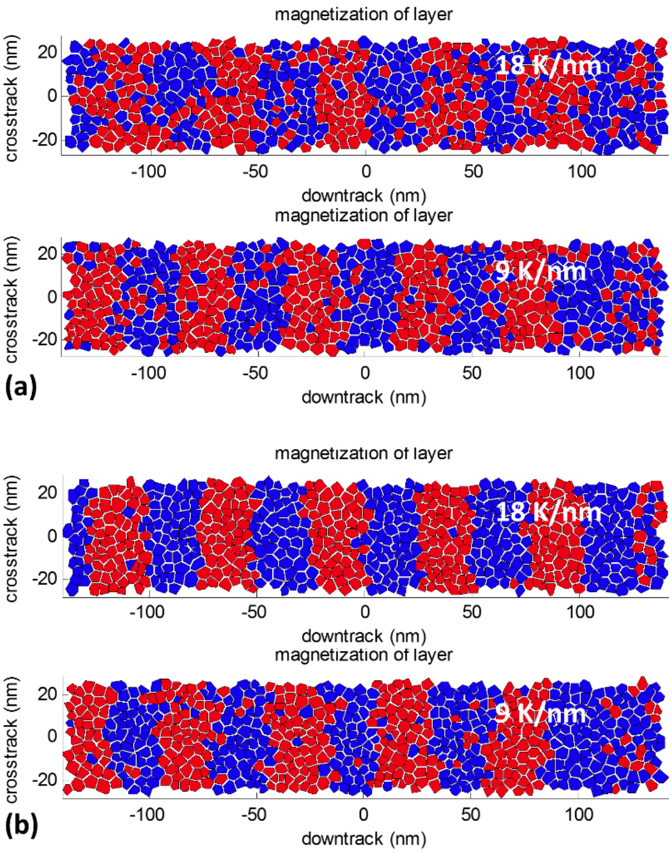

Figure 3.13 Representative magnetization patterns recorded with two different thermal gradients (18 K/nm and 9 K/nm) at (a) low recording field with H_{rec} = 3.5 kOe and (b) high recording field with H_{rec} = 14 kOe.

Figure 3.13 shows representative magnetization patterns at lower (a) or higher (b) than the optimal values in the same recording medium, where grain pitch is 5 nm, for two distinctively different thermal gradient values, TG = 18 K/nm (upper) and TG = 9 K/nm (lower). Although the incomplete magnetization at the low field amplitude is evident for both cases of different thermal gradients, the incompleteness of magnetization is more severe for the higher TG value than that with the lower one. Whereas at the higher field amplitude, H_{rec} = 14 kOe, it is the other way around: higher thermal gradient would significantly limit the transition-broadening-after-write while for the lower thermal gradient case, the broadening is very much evident.

For HAMR, the sharpness of a bit transition is related to the effective field gradient, which is the product of dH_k/dT and dT/dx. For FePt-$L1_0$, the dH_k/dT is very high, over 700 Oe/K, therefore, a relatively low thermal gradient, on the order of a few degree Kelvin, would already be sufficient to create grain pitch limited transition. However, the thermally induced transition broadening after its creation has more to do with the thermal gradient alone.

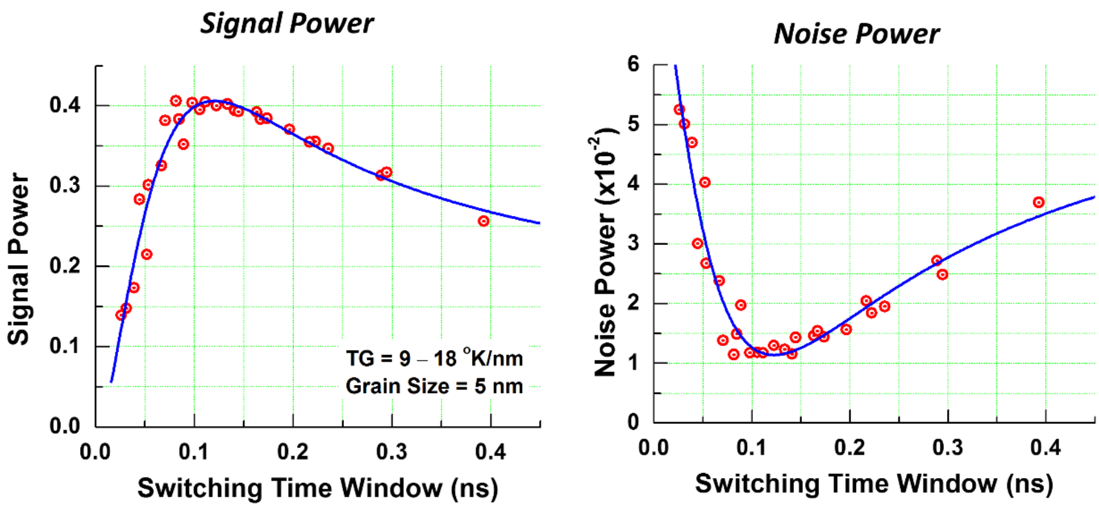

Figure 3.14 Signal power and noise power versus the switching time window using the previous data points with various thermal gradients, 9, 12, 15, 18 K/nm. For each thermal profile with different TG, seven field values ranging from 3.5 to 14 kOe were used for writing.

Similar to the study of the velocity, after the SNR versus head field is obtained, the data points are replotted in terms of RTW as shown in the Figure 3.14. The data points in the figure are gathered from the signal power and noise power dependence on recording field amplitude at four different recording thermal gradients: TG = 18, 15, 12, 9 K/nm. There is a clear and tight correlation between the performance and the RTW. It again indicates that the RTW is a key factor in determining transition noise. Similarly, the optimal RTW here is between 100 picoseconds (ps) and 200 picoseconds. When RTW is below the optimum, the degradation of the performance is very steep, while the performance reduction is more gradual when RTW is higher than optimum. Now that the system performance tightly correlates with the RTW, it indicates that any mechanisms to change RTW will be likely to cause medium noise, especially when RTW is lower than the optimum.

As indicated by the previous result, especially for small grain, the recording field amplitude is required to be sufficient so that the incomplete switching is avoided. While a not-so-high thermal gradient would make erase-after-write very severe at large recording field. To increase the optimal SNR at the optimal field would need to use higher thermal gradient.

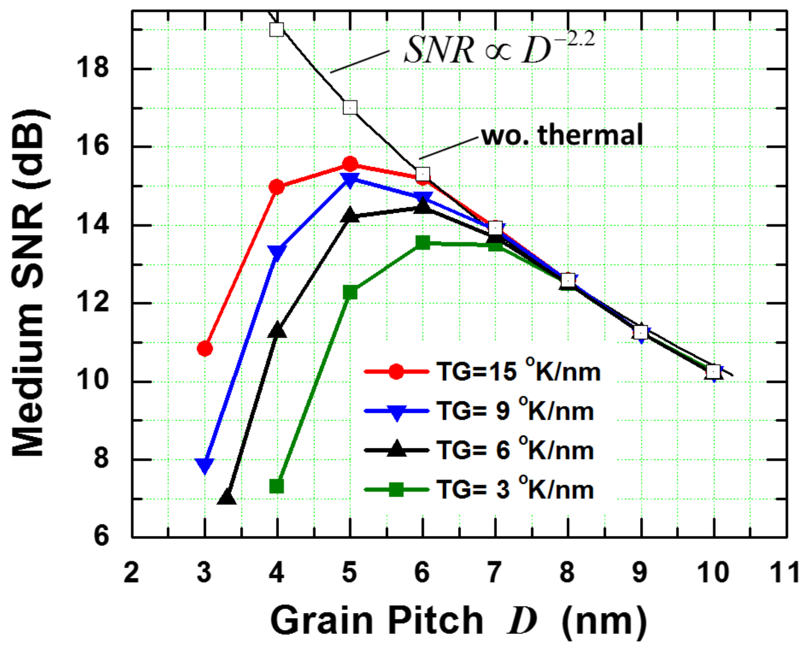

Figure 3.15 The optimal medium SNR versus grain pitch with different thermal gradient value. For each SNR value, the field value is optimized. The open square symbol stands for the case without thermal noise and is also shown here for comparison. Here read track width is fixed at 30 nm for all the grain sizes.

After calculation of the medium SNR versus recording head field, each case would give a specific optimal SNR value. By repetition of this process for different grain pitch and different thermal gradient values, the optimal SNR value can be plotted as a function of grain pitch under different thermal gradient as shown in Figure 3.15. It should be noted here the read width is fixed to be 30 nm for all grain pitch sizes. The open square symbol represents for the SNR without thermal agitation noise with 15 K/nm thermal gradient. This is basically limited by the grain pitch size. The fitting for the nonthermal case here results from two effects, a) SNR is proportional to the number of grains across track with fixed track width [19], b) decreasing grain pitch would make transition sharper so that signal power increases and noise power decreases. With the thermal agitation, the SNR starts to deviate from the non-thermal optimal SNR (limited by grain pitch), when the grain size is below 7 nm. Meanwhile, with higher thermal gradient, this onset of deviation will appear at smaller grain. For instance, when the thermal gradient is 15 K/nm, which is much higher than current realistic value, the deviation happens below 6 nm. Therefore, more potential of HAMR can be utilized with a higher thermal gradient.

The results here indicate that a sufficiently high thermal gradient is crucial for obtaining the grain pitch limited SNR, especially for small grain medium. This requires thermal gradient to be much higher than that needed for obtaining a high effective field gradient. Although 3 K/nm thermal gradient with 500 Oe/K dH_k/dT would have a product of 1500 Oe/nm effective field gradient, which is much higher than the PMR standard. To avoid erase-after-write and enhance optimal SNR, the system would still require the thermal gradient to be even higher.

To realize higher thermal gradient, it is necessary to carefully design the medium thermal properties, NFT, head-medium-interface (HMI) as well as the coupling between these components. For instance, to have a higher thermal gradient and narrow track, the hot spot should be well confined. It may be possible to tune the lateral and vertical thermal conductivity of medium. For instance, higher vertical thermal conductivity may make the primary heat flux flow vertically without too much lateral heating. Meanwhile, it should be noted that in this way, the medium magnetic properties along with grain distribution may vary together. The other direction is to engineer the heating components. Consequently, the heat flux should quickly dump into the medium and its heat sink underneath. However, the good heat dissipation would make the medium more difficult to heat up and more laser power consumption is required. As the current energy absorption efficiency for the NFT heating is still around 10% or even less, more wasted energy would tend to give more thermal burden to the recording components. Some following issue, like the NFT protrusion [113] or misshape [114] would also happen and needs consideration. Additionally, for the current quasi-circular thermal profile near the track edge, the recording temperature would approach to the peak temperature, which is suboptimal recording condition, since the thermal gradient would vanish to zero. Further discussion will be given in the curvature section in chapter 5.

3.5 Room Temperature H_k

In previous sections, simulations are primarily conducted on the recording medium with H_k equal to 60 kOe, since the early FePt-$L1_0$ medium has similar H_k. With technology progresses, the medium H_k steadily climbs up making optimization vary as well. Below is an example of recording using medium with different anisotropy field values.

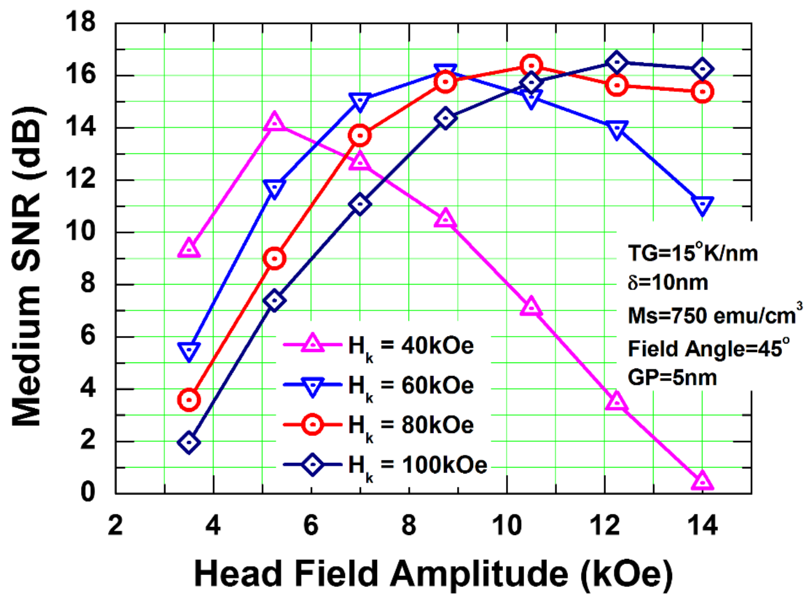

Figure 3.16 Medium SNR versus head field amplitude with different recording medium of various anisotropy field H_k, 40, 60, 80 and 100 kOe.

As shown in Figure 3.16, medium SNR changes as a function of head field for medium with different H_k, ranging from 40 kOe, 60 kOe, 80 kOe to 100 kOe. At the low field side, softer medium gives better performance while the opposite happens at the high field side. Meanwhile, the optimal field value shifts upward when harder medium is utilized. Additionally, the harder medium will also enjoy higher SNR value at optimum. RTW can be used to interpret these: with higher H_k and the same effective head field, the corresponding recording temperature would shift towards the Curie temperature. Consequently, the temperature range which allows for the recording would shrink. Then the value of RTW for the recording to happen would be lower. In the insufficient field case, incomplete switching would be more severe, while in the high field case, erase-after-write can be alleviated greatly with shorter exposure to a switched field. Incomplete switching noise makes the initial writing improper, while the erase-after-write blurs the well-written transition. For hard magnetic medium, the optimal head field could be higher to assure proper initial writing. Because hard medium has robust energy barrier, so that erase-after-write is still slight. Then hard medium gives higher optimal SNR value.

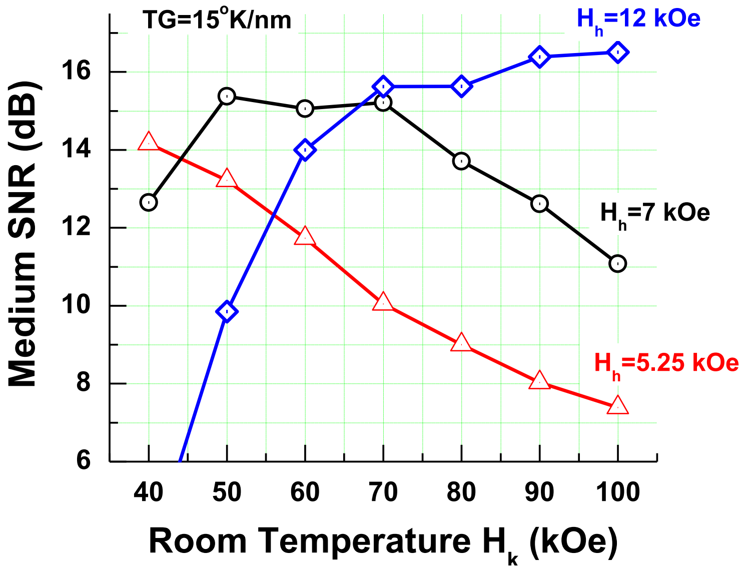

Figure 3.17 Medium SNR versus room temperature anisotropy field, H_k, under different head field values.

The corresponding SNR values at 5.25, 7 and 12.25 kOe in Figure 3.16 are extracted to replot the medium SNR as a function of room temperature H_k as shown in Figure 3.17. When the head field is as low as 5.25 kOe, the medium with H_k of 40 kOe gives decent SNR. As medium H_k becomes higher and higher, SNR significantly decreases. With head field equals to 7 kOe, the recording medium SNR would first increase with H_k value, saturates around 50 kOe and then starts to decrease with even higher H_k value. When even higher head field is utilized, the medium SNR monotonically increases as medium H_k climbs up. These results indicate that with higher head field, the medium with higher H_k value could be employed to take advantage of higher SNR value. The reason behind this conclusion is that harder recording medium has shorter RTW and requires larger head field to broaden RTW for good recording quality. Since hard medium is very robust for erase-after-write, it would give better overall performance.

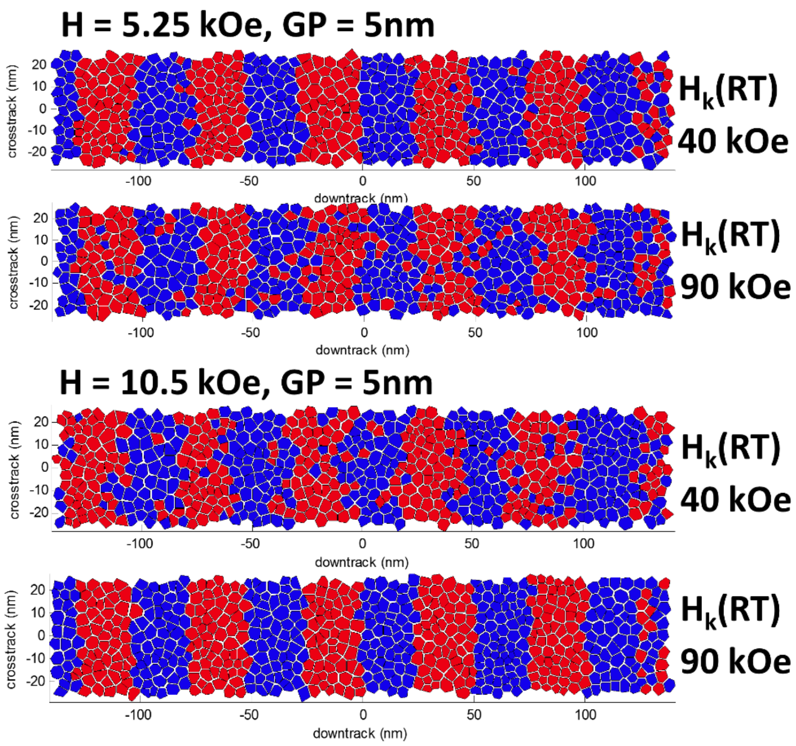

Figure 3.18 Magnetization pattern at low (5.25 kOe) and high field (10.5 kOe) value for medium with different room temperature anisotropy field, H_k.

Shown in the Figure 3.18 are the representative recording magnetization at low and high field values. Here the two different head field values are 5.25kOe and 10.5kOe respectively and the two room temperature anisotropy field values are 40kOe and 90kOe. When the head field is 5.25kOe, the medium of 40kOe H_k shows much better recording performance while the 90kOe medium is not fully magnetized. The reason is that the medium with higher H_k value now has very limited recording time window to conduct switching of spins. For softer medium, the time window is already sufficient since the slope of H_k vs. T curve is relatively shallower, which makes the recording temperature far away enough from the T_c. On the other hand, when the head field is 10.5 kOe, the hard medium now have a decent recording time window to finish the switching process and reach good recording quality. However, the soft medium will have redundant RTW, which makes the recorded bit unstable and suffer from the erasure. Therefore, the recording of soft medium greatly degrades from the erase-after-write phenomenon.

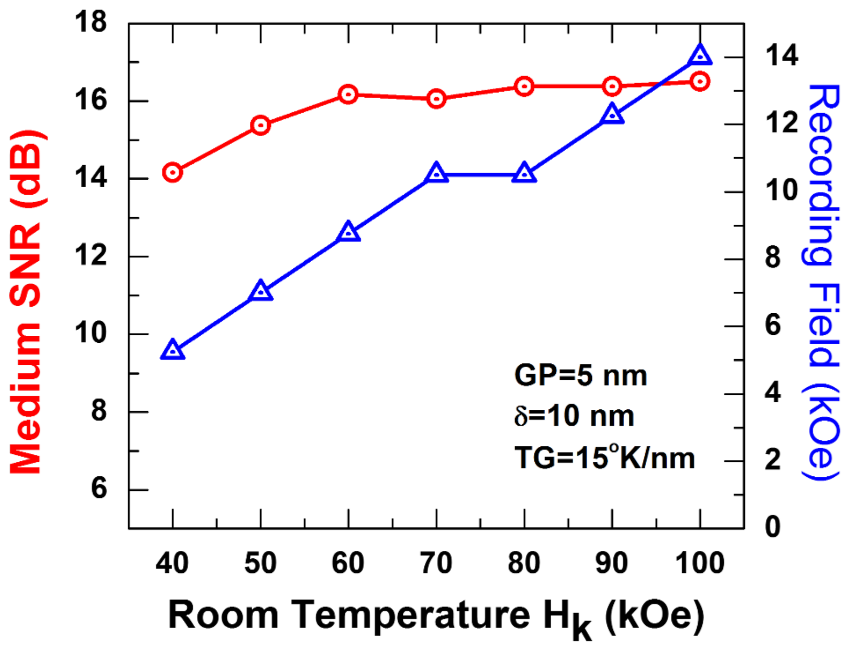

Figure 3.19 Medium SNR and required optimal head field as a function of recording medium anisotropy field, H_k. The grains size is 5 nm, thickness δ is 10nm and thermal gradient is 15 K/nm.

To better show the medium anisotropy field dependence of SNR as well as the required head field, the data above has been replotted into Figure 3.19. The results indicate that with harder and harder medium, the optimal medium SNR value will gradually increase. Simultaneously, the required head field will also increase, which is another challenge. For instance, the soft underlayer (SUL) becomes more and more necessary to partially satisfy this requirement of high head field. SUL layer not only mirrors the magnetic field from writer component, but may also induce new types of noise. Meanwhile, the fabrication process may have to be re-optimized or re-designed to maintain medium properties after SUL insertion [115]. Regarding the field profile, with the SUL inserted, it should be noted that the angle between field vector and out-of-plane direction would also decrease, which may help suppress the erase-after-write.

Since the optimal SNR value would gradually increase with the medium room temperature $H_{k,}$ the optimized SNR is plotted as a function of various grain pitch for medium with different H_k values as shown in Figure 3.20. Here the medium thickness of 6 nm is used, because in less aggressive medium design, the thickness would be less to avoid stacked particles [116], which introduces extra noise. Magnetization value is set to be 1000 emu/cc here, which would offset the thermal noise increase due to thickness reduction. Similar to the Figure 3.15, for relatively large grain size, the medium SNR would increase as grain size shrinks. However, when grain size becomes lower than a certain level, the medium SNR would start to decrease instead. Compared to the medium SNR without thermal agitation (the black open symbol), SNR with thermal noise deviates and is obviously lower, especially for smaller grain sizes. Therefore, to achieve higher density, harder medium should be employed at the cost of writing with higher field. It is also important to note that since many aspects of the system could also affect the RTW, other parameters could be utilized to avoid the usage of too high field. Essentially, to obtain the proper RTW for all the grains of recording medium is the critical focus.

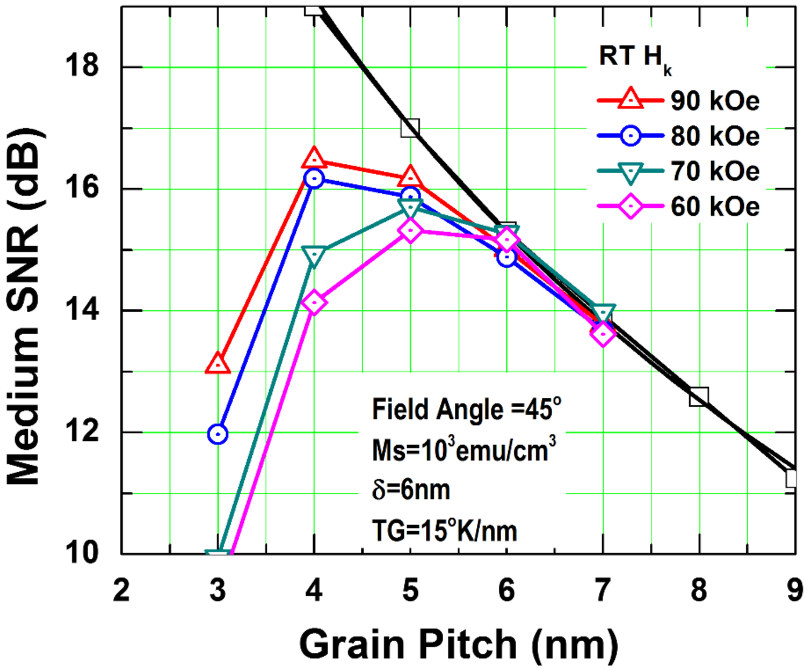

Figure 3.20 Optimal medium SNR versus grain pitch for different room temperature anisotropy field H_k. The head field angle is 45 degrees, the saturation magnetization at room temperature is 1000 emu/cc, the medium thickness is 6 nm and the thermal gradient is 15 K/nm.

From the analysis of medium with various room temperature H_k values, it is proved that higher H_k medium does offer better SNR, since it is more robust during the cooling process and has less erase-after-write. Single crystal [117], one-on-one growth [118], better fabrication conditions [119] or novel underlayer may be helpful to further enhance the medium H_k value. However, it is critical to realize that to fully take advantage of the high H_k medium, it would be essential to apply sufficiently high head field so that the incomplete switching noise is avoided. But to achieve this, for ultra-high H_k medium, it may become more necessary to utilize the SUL. As mentioned, this may simultaneously degrade the medium quality or require extra optimization of the fabrication process or even medium structures. A side advantage of using SUL is to make the head field vector more vertical and help avoid erase-after-write. While regarding the increasing of the room temperature H_k for medium, it would also be interesting to check whether the other medium properties change or not, like the H_k temperature dependence, M_s and so on. If the H_k manages to reach the theoretical H_k value of 120 kOe [120], the required head field would also have to be significant. From these discussions, it can be seen that although the HAMR scheme is originally proposed to relax the writability issue of recording trilemma, it would still require pretty large recording head field, which is counterintuitive.

3.6 H_k Temperature Dependence

Looking at the definition of RTW in the previous chapter, it can be noticed that the H_k vs. T curve with a shallower slope would make the T_{rec} further away from the T_c, and vice versa. This indicates that the slope of H_k curve or the H_k temperature would change RTW directly and is supposed to affect the recording performance significantly. This section is targeted at discussing the impact of H_k temperature dependence, especially in the aspects of field requirement and laser power consumption.

Figure 3.21 shows the normalized anisotropy field as a function of the temperature for different index n. As shown in the formula above the graph, index n could tune the temperature dependence of anisotropy. Meanwhile, by changing index n, the room temperature anisotropy field and Curie temperature still remain unchanged. With a larger index n, the slope of H_k will be shallower. The right graph shows the dH_k/dT versus index n at head field and effective field values. The typical field value of 1T and room temperature H_k of 90kOe are used to obtain the slope. Since for most simulations, the applied head field is 45 degrees from the vertical axis, the effective field is double amount of the field magnitude based upon Stoner-Wohlfarth model [121]. Therefore, the dH_k/dT is lower for the effective field curve in the right graph, since it is away from the Curie temperature. The data indicates that the slope significantly decreases from 1300 Oe/K to 200 Oe/K when higher index n is used. Meanwhile, the reduction of dH_k/dT is larger for smaller n and is smaller for larger index n. On the other hand, regarding the method to change index x, the Figure 2.2 [92] gives a hint, which is to introduce new types of atoms to modulate the lattice structure, like the nickel and and so on. It should be noticed that in [92], too much mixture of the new atom would make both the anisotropy field and Curie temperature change significantly as well. Therefore, to focus on the H_k temperature dependence, relatively small mixture is considered. So in the following discussion, the medium with index of 2, 2.5 and 3 are investigated and compared.

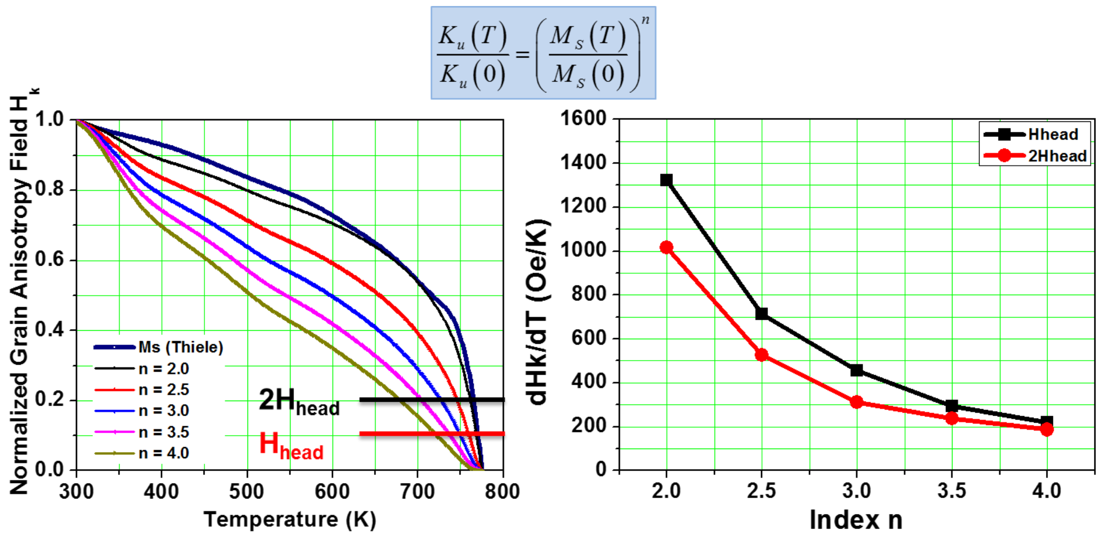

Figure 3.21 Normalized anisotropy field versus temperature with different index n values and the right graph shows the dH_k/dT versus index n values. The dH_k/dT is obtained with 1T head field and room temperature H_k is 90kOe for typical settings.

Using the medium with index of 2, 2.5 and 3, the recording has been conducted to obtain the medium SNR values under a series of head field values as shown in Figure 3.22. The results indicate that each medium has different head field dependence. For the medium with index of 2, the medium SNR first increases, then almost saturates around 10.5 kOe and starts to drop beyond 12.25 kOe. For the medium with index of 2.5, the SNR also increases first, but saturates at lower field of 7 kOe and starts to decrease beyond 8.75 kOe. On the other hand, the medium of index 3 almost has maximal SNR at 5.25kOe and the SNR obviously decreases for higher field. These results indicate that the optimal head field varies with various index n. For higher index value, the optimal field value would be lowered. For the system design, the head field magnitude is limited and the introduction of the SUL would induce other types of noise sources. So, utilization of medium with higher index n would help relax the requirement of the writing head field, writing component design as well as the medium design.

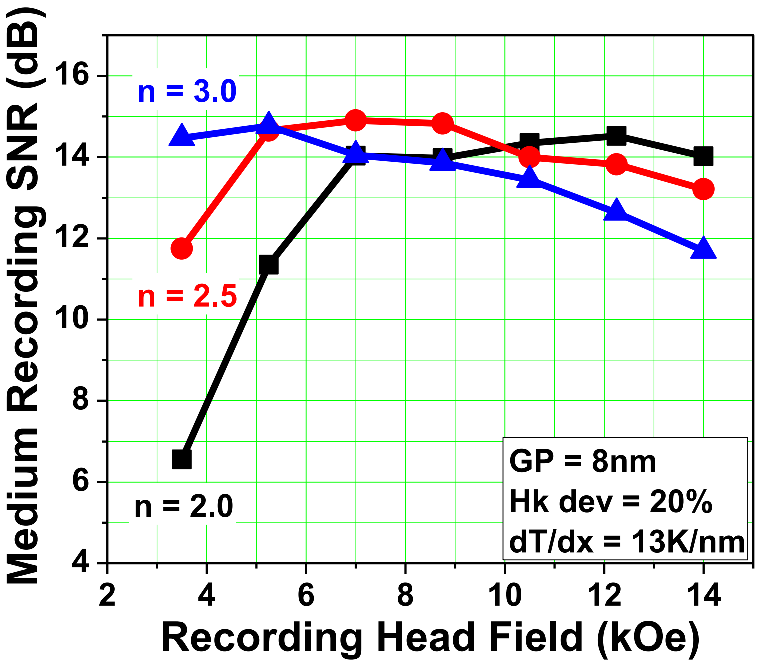

Figure 3.22 Medium SNR versus head field for different index n values and the same other settings [122].

For the writing noise, the recording patterns would be helpful to analyze the noise mechanism. As shown in the Figure 3.23, the recording patterns at the low head field are presented on the right-hand side. The medium with 3, 2.5 and 2 are from top to bottom. For the medium with index of 3, the writing is properly conducted without obvious noise. For the medium with index of 2.5, a couple of randomly flipped grains can be seen embedded in the information bits. For the medium with index of 2, quite a few grains are not switched properly. All these noise grains are mostly caused by the incomplete switching here due to the insufficient field. For medium with index of 2, the dH_k/dT is the highest and the recording temperature is the closest to the T_c, which makes the RTW too limited for switching. While for the medium with index of 3, the medium is softer at temperatures close to T_c and have broader RTW for recording and thus better performance.

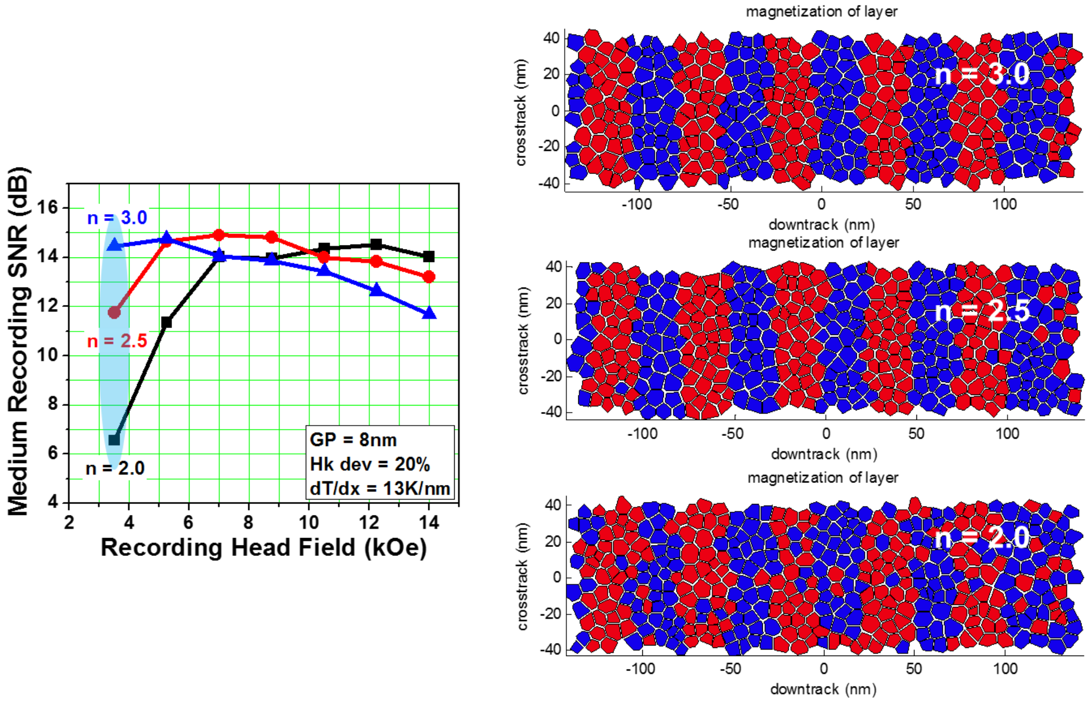

Figure 3.23 Medium SNR as a function of the head field (on the left-hand side) and the recording patterns at the low field side are shown on the right-hand side. The patterns are shown from top to bottom for index values of 3, 2.5 and 2, respectively.

Figure 3.24 shows the recording patterns at high field side for medium with different index values. In the case of index 2, the medium has only one grain switched not as expected in the first bit. For the medium with index of 2.5, a few more grains can be seen in the bits. The medium of index 3 has even more grains flipped incorrectly. One common aspect is that all the noise grains are located near the transition, specifically at the end of the bits. This is a clear indication that the noise here is caused by the erase-after-write. For the medium with a small index, the anisotropy field near the T_c would be higher so that the medium is more robust against the erase-after-write. In terms of the RTW, the medium with small index value would have T_{rec} closer to the T_c, which makes the RTW relatively shorter. As the erase-after-write is caused by the redundant

RTW, medium with lower index could help shorten the RTW and prevent the exposure to switched head field. Oppositely, for the medium with higher index n value, the H_k near T_c would be lower and the medium is more vulnerable to erase-after-write noise.

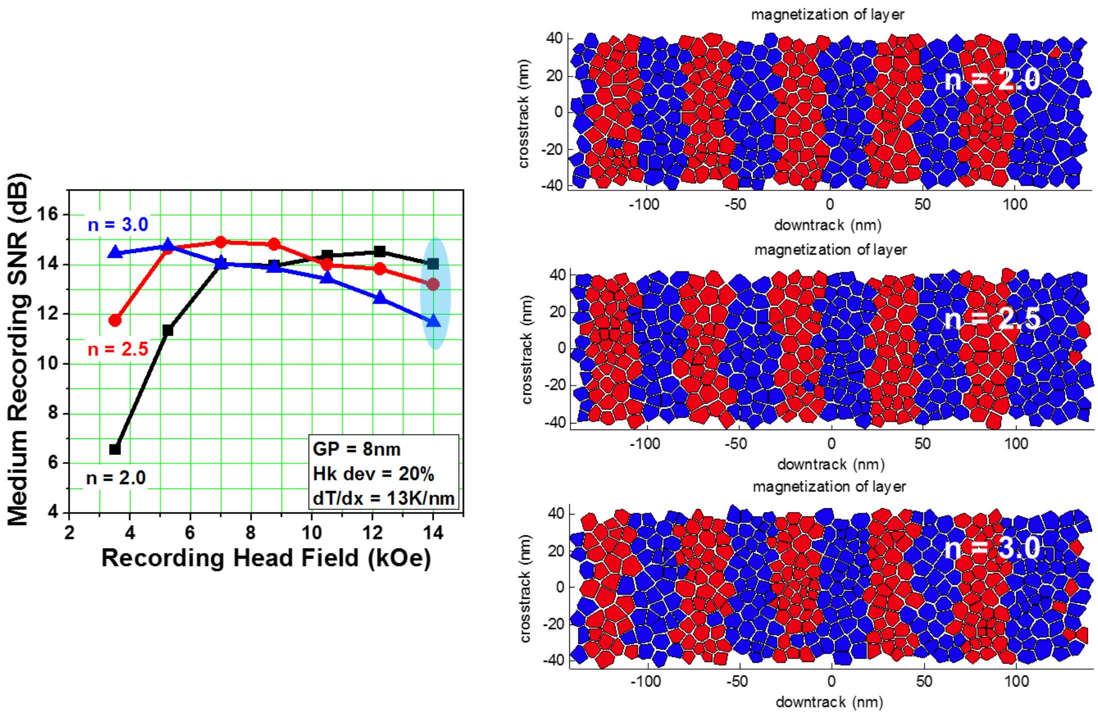

Figure 3.24 Medium SNR as a function of the head field (on the left-hand side) and the recording patterns at the high field side are shown on the right-hand side. The patterns are shown from top to bottom for index of 2, 2.5 and 3, respectively

As shown in the discussion above, the medium index n would have a great impact on the head field dependence of SNR as well as the optimal SNR value. Figure 3.25 shows the optimal SNR value versus grain pitch size for medium with different index n values. Similar as before, the reading width here is set to be 30 nm for all the cases. For the grain pitch above 6 nm, no noticeable deviation are noticed between the case with thermal agitation and the case with grain pitch limited SNR. When the grain pitch is below 5 nm, the SNR values is obviously lower than the ideal SNR. Additionally, for the medium with index of 2, even when the grain pitch is as small as 4 nm, the medium SNR still increases with smaller grain pitch. While for medium with index 4, the medium SNR stops to grow with smaller grain pitch until 4 nm and then starts to decrease. The deviation from ideal no-thermal SNR is also larger for case of index 4. As previously pointed out, the combination of incomplete switching and erase-after-write affects recording. But the incomplete switching can be avoided by using sufficiently high head field, while the erase-after-write can be greatly prevented with harder medium. For medium with smaller index n, the H_k near T_c would be relatively higher, which makes medium robust against erasure. Therefore, overall speaking, harder medium would help enhance the medium SNR and take advantage of smaller grain pitch. But higher head field would have to be applied and this leads to other system design challenges.

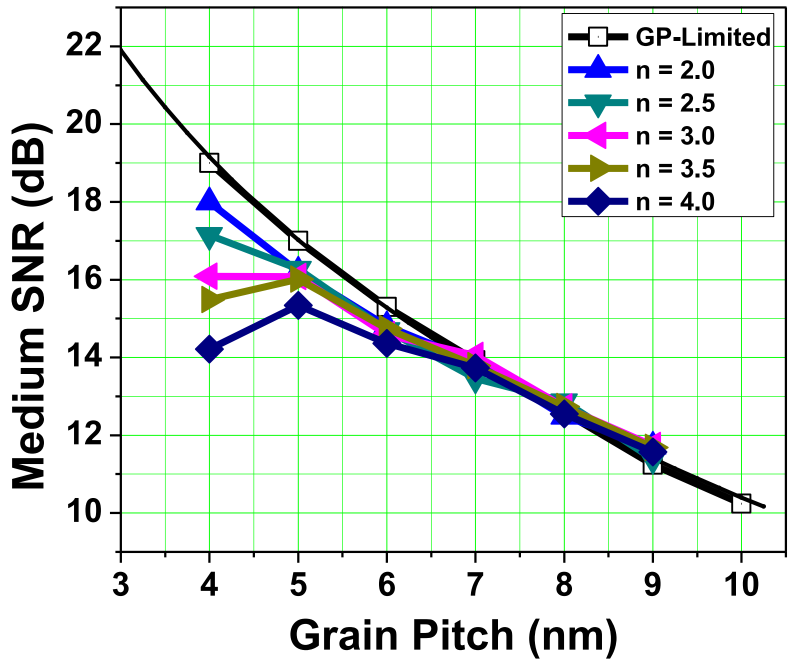

Figure 3.25 Optimal SNR value as a function of the grain pitch for medium with index from 2.0 to 4.0. The reading width is kept to be 30 nm for all the cases. The same previous grain pitch limited SNR is plotted together to compare with the data of various index n values.

Regarding the field requirement, a schematic is shown in Figure 3.26 to illustrate. For the same magnetic grains of recording medium, the optimal recording time window should be the same as shown in the plot. With the same T_c, this RTW would define the same value of T_{rec} for medium with different temperature dependences of anisotropy field or different index n here. For the medium with shallower dH_k/dT slope (with larger index n value), the corresponding T_{rec} would lead to lower H_{eff}. This explains the previous observation that the medium with larger index n would help relax the requirement of head field and only needs a relatively lower head field to achieve proper recording quality. In other words, for medium with different H_k versus T curves, the head field is tuned to obtain the optimal RTW. This is also an example where one aspect

(H_k vs. T curve) of HAMR is tuned to relax the challenging requirement of another aspect (head field amplitude).

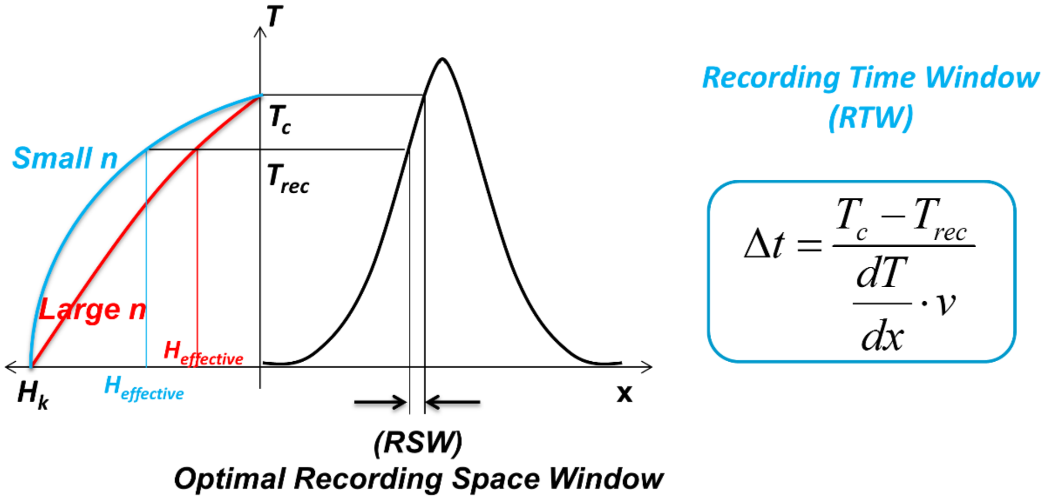

Figure 3.26 Schematic of the head field requirement using the concept of recording time window. The blue curve refers to the medium of small index n and higher dH_k/dT slope, while the red curve relates to the medium of larger index n and lower dH_k/dT slope.

In previous sections, it has been observed that the system performance has a tight correlation with the RTW. Here the RTW of each data points in Figure 3.24 has been calculated and replotted in Figure 3.27. The symbol has been kept consistent between left and right graph. Again, the data points exhibit a strong correlation and the SNR is observed to increase first, saturate around 0.2 ns (200 ps) and then start to decrease as the RTW value increases. From the color of the data points (black, red and blue correspond to medium of index 2.0, 2.5 and 3.0, respectively), it is noticed that the medium with index of 2.0 primarily has SNR values on the increasing part of the curve. This suggests that this type of medium primarily suffers from the incomplete switching due to the insufficient RTW. On the other hand, for the medium with index of 3.0, the data points mostly concentrate on the decreasing part of the curve in the right graph. The indication is that this type of medium primarily suffers from the erase-after-write due to the redundant RTW. For the medium of index 2.5, the data points distribute over the optimal RTW and SNR. This type of plot helps provide guidance for the system design since it tells the range of RTW that can be covered by the current design. If the design mostly has incomplete switching induced noise, the system could be tuned to the direction of increasing RTW, and vice versa. In Chapter 5, one example will be given to evaluate a generic industrial design using the RTW analysis for detailed discussion to provide the direction of system modification.

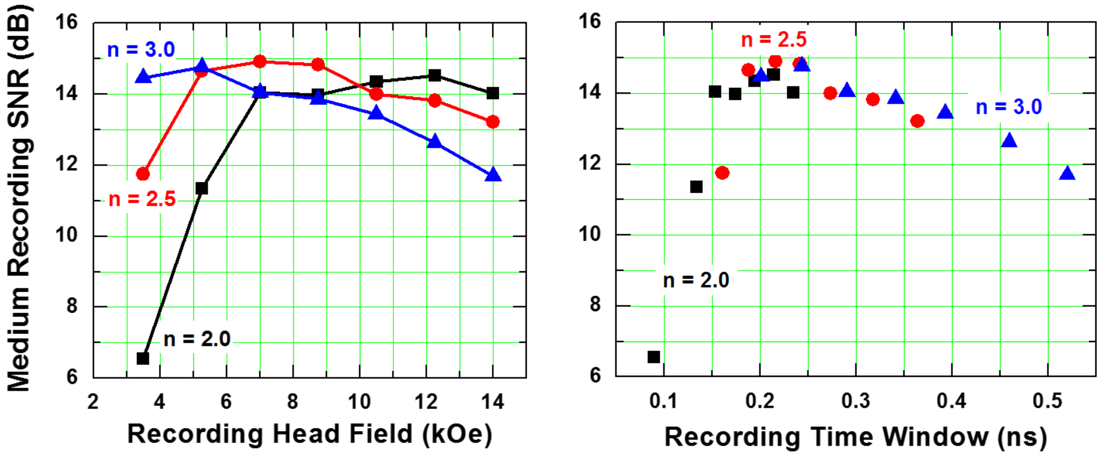

Figure 3.27 Medium Recording SNR versus head field (left graph) and recording time window (right graph). The black, red and blue points correspond to medium of index 2.0, 2.5 and 3.0, respectively.

On the other hand, the temperature dependence of the anisotropy field would also make the H_k value near the T_c be very different. For the shallower H_k vs. T curve, the recording, therefore, could happen at a lower temperature. If the peak temperature is lower, this lower recording temperature would still correlate with a decent thermal gradient. On the contrary, steep dH_k/dT would make the recording happen close to T_c, and suboptimal peak temperature would make the corresponding thermal gradient vanish a lot, which degrades recording. Specifically, the medium of index 3.0 would have lower H_k value near T_c and this may help relax the power consumption. Figure 3.28 shows the medium SNR as a function of the peak temperature. In practice, the heating power often is below the value required to maximize the SNR so that written track width is limited. Here the impact to SNR when heating power is suboptimal is investigated. In Figure 3.28, when the peak temperature is close to or above 900 K (16% > T_c), similar SNR is obtained for the media with all three index n values. When the peak temperature is below optimal, SNR for the medium with n = 3 is higher than that with n = 2. The SNR difference is greater when the peak temperature is lower, i.e. the SNR for medium with lower n value falls more rapidly. For a decent value of SNR as labeled out by the dashed line, the corresponding recording patterns are shown on the right-hand side. The recording patterns look similar to deliver same SNR value. On the other hand, in the left graph, it can be noticed that the medium with index equal to 3.0 would need lower recording peak temperature to reach this SNR. For medium with index 2.0, the required peak temperature would be much higher. For HAMR system, reliability is a critical issue and heating procedure induces a lot of design challenges. Therefore, medium with larger index n would help relax the heating requirement and alleviate the burden for the thermal issue, which greatly enhances the HAMR thermal reliability.

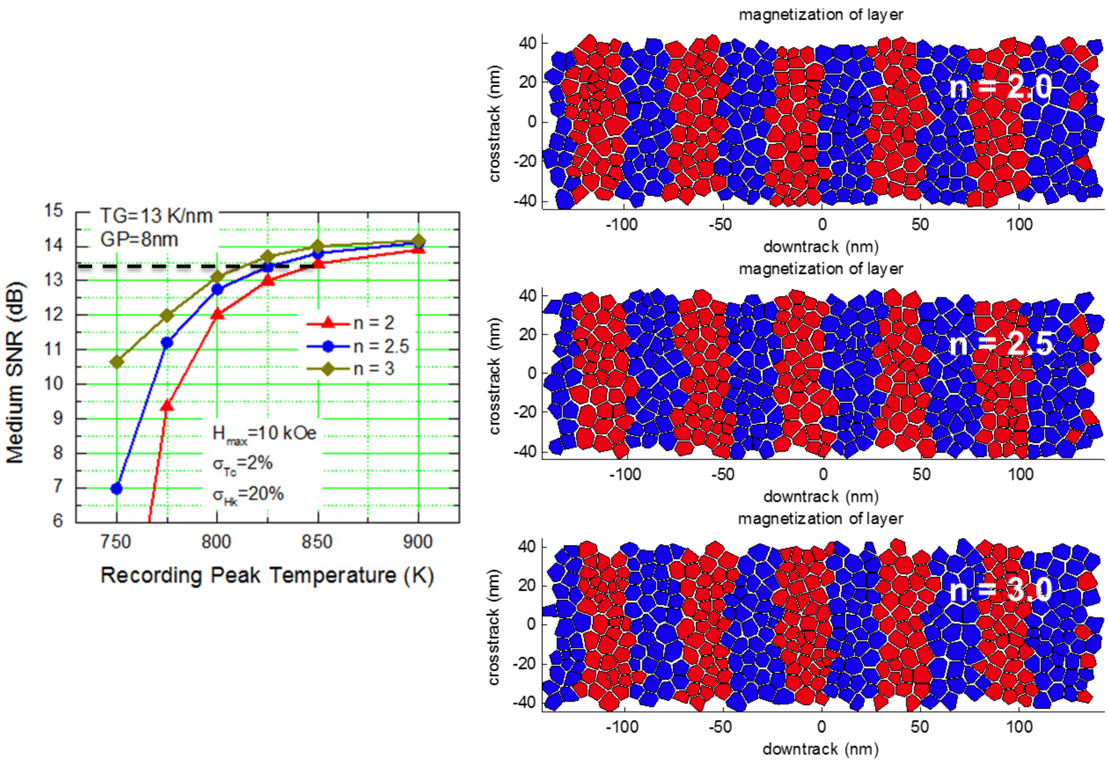

Figure 3.28 Calculated medium recording SNR as a function of peak temperature of the recording thermal profile. The head field amplitude is optimized for each data point with an upper limit of 10 kOe. The dashed line refers to a decent SNR value to intersect with three curves and obtain the require head field of each medium type. The corresponding recording patterns are given on the right-hand side.

The SNR dependence on index n at suboptimal heating in Figure 3.28 could be explained via the correlation between recording head field amplitude and RTW as shown in Figure 3.29. The left graph shows the medium SNR as a function of the recording head field for medium with index values of 2.0, 2.5 and 3.0. Here the peak temperature is selected to be Curie temperature (775K). For the medium with n = 3.0, the SNR saturates around 9 kOe, while for medium with n = 2.0, even when head field is 14 kOe, the SNR still has not saturated. These results indicate that when the heating is suboptimal, higher head field amplitude is needed, so that the thermal gradient at the recording temperature would not vanish too much. For each of the data point, the relevant RTW is calculated to obtain the right graph. Apart from the tight correlation, it should also be noted that the optimal RTW shifts to 0.8 ns, which is much higher than previous 0.1-0.2 ns optimal RTW. For the medium of index 2.0, even when head field is 14 kOe, the RTW is still 25% narrower than the optimum. Only for medium with n equal to 3.0, the data distribution covers the optimal RTW.

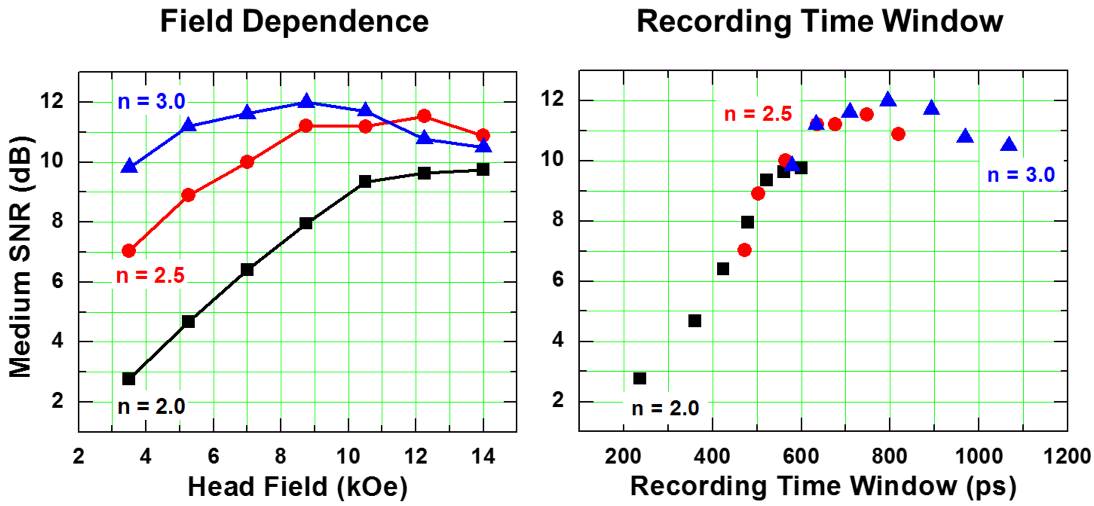

Figure 3.29 Medium SNR of the recording with peak temperature in the media equal to the Curie temperature (775 K). Left: SNR as a function of recording field amplitude. Right: the same data plotted as a function of RTW.

From the H_k temperature dependence, it can be seen that the shallower H_k vs. T curve would help relax the requirement of head field as well as the thermal peak temperature. While how to specifically manipulate the H_k vs. T curve would need more research. Although [86] suggests that the additional type of atom helps modify the temperature dependence, the temperature dependence could not vary significantly, since the room temperature H_k, M_s as well as other properties may vary accordingly. However, it may be possible to simply enhance the H_k to approach the theoretical value first, so that there would be more margin to induce other types of atom and tune the temperature dependence. Another indication from the RTW is that since the RTW also greatly relies on the H_k vs. T curve shape, each of the grain may have different H_k vs.

T curves. Therefore, the recording behavior may consequently have noise due to the H_k vs. T variation. This in a way could be decomposed into the H_k variation and T_c variation as shown in the following chapter. Whereas it would still be meaningful to measure the variation of the H_k temperature dependence variation, especially between the recording effective field and zero field. On the other hand, it is true that according to the mean field theory [108], [121], the M_s and H_k would have the relation as in the formula in Figure 3.21. For deeply scaled FePt grains, a higher surface-to-volume would ensure that the surficial atoms have more non-uniformity of the field from other atoms. Consequently, the realistic temperature dependence and the relation between H_k and M_s would deviate from the mean field theory prediction, which is worthwhile of experimental characterization. One experimental example and the detailed methodology is discussed in chapter 5. Despite practical challenges, higher resolution at grain level measurement may give a better description of medium properties.

3.7 Conclusion

In this chapter, the thermally induced recording physics, and fundamental noise mechanism are introduced. The combinational effect of the incomplete switching and erase-after-write results in the obvious head field dependence of recording medium SNR, especially for small grain pitch size medium. In PMR, smaller grain pitch would lead to sharper transition, higher SNR, and larger storage volume. While in HAMR scheme, due to the thermally induced noise, the recording performance would deviate from expectation. In other words, even with smaller grain medium, the performance may be worse. To take advantage of the potential of small grain medium, it would be necessary to tune for higher H_k, higher thermal gradient and so on.

The concept of recording time window has been proposed and it is found to tightly correlate with the system performance. Importantly, this concept manages to integrate almost all the primary aspects and parameters of HAMR system into a unified measurement, so that the RTW analysis provide guidance and understanding for system design.

As velocity, thermal gradient, H_k, temperature dependence of H_k and so on greatly affect RTW, their impact on the recording performance are investigated individually. The results indicate that all these parameters could be tuned to provide ideal RTW. Considering realistic system design and fabrication challenge, relaxed aspects could be manipulated to compensate for the tightened parameters, while the overall system performance is still ideal.

In later chapters, several systematic modeling and experimentation will be given to further validate and give application examples of this theorem.

4. Medium Properties

In chapter 3, the fundamental recording physics and storage noise mechanisms are covered to ensure a good understanding of HAMR process. Besides the combinational effect of incomplete switching and erase-after-write, recording time window (RTW) has been proposed and it turns out that RTW has a strong correlation with the system performance. This chapter is based on the previous understanding and shed light upon the mechanism and the impact of the noise sources originated from a series of medium properties. In the granular magnetic medium, the grains are not uniform and have different variations. Even in future bit pattern recording, each recording bit may consist of one or a few magnetic dots and such variations become less. But the noise induced by these non-uniformities would still exist and affect performance.

4.1 H_k Variation

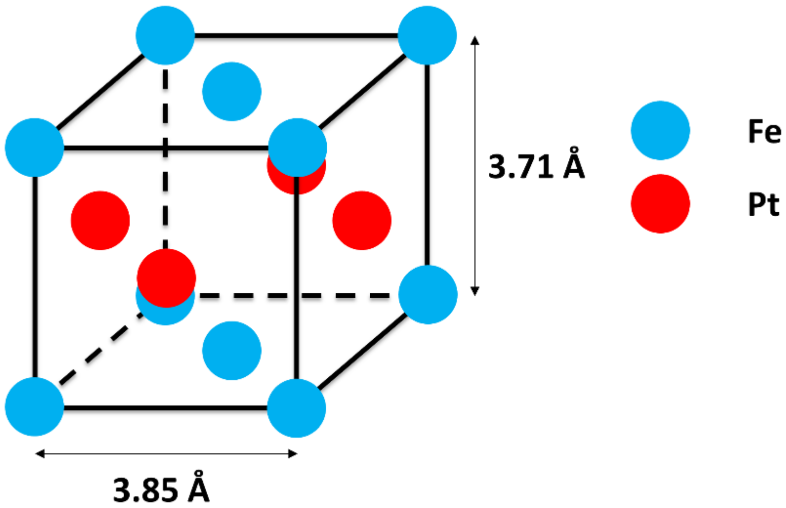

Figure 4.1 Schematic of unit cell for FePt L1$_0$ structure in HAMR medium. The spheres of blue and red correspond to the Fe and Pt atoms, respectively [123].

In FePt L1$_0$ medium for HAMR recording, the uniaxial anisotropy results from the ordering of the Fe and Pt atoms in L1$_0$ format as shown in the schematic of Figure 4.1. The anisotropic alignment of atoms with spatial symmetry gives the spins orientation preference, which is the magnetocrystalline anisotropy. However, in real recording medium, two identical grains can almost never be found. Microscopically, the atom stacking could vary from grain to grain due to the imperfection of the fabrication process and mixed defects. Figure 4.2 shows a set of typical transmission electron microscopy (TEM) images for recent FePt HAMR medium. The left graph and the right graphs are the top view of the FePt medium and the zoom-in side view pictures of the individual grains with layers underneath, which typically include, from top to bottom, the seed layer, heat sink and soft underlayer (SUL). The top view of the medium suggests that the grains over the medium are obviously non-uniform in shape and the grains are segregated by the boundaries which are made of oxide. As indicated by the figure, each grain has very different geometries and aspect ratios. Since the surface atoms of grain own different anisotropy compared to that of bulk material, the random geometry also lead to variation of anisotropy.

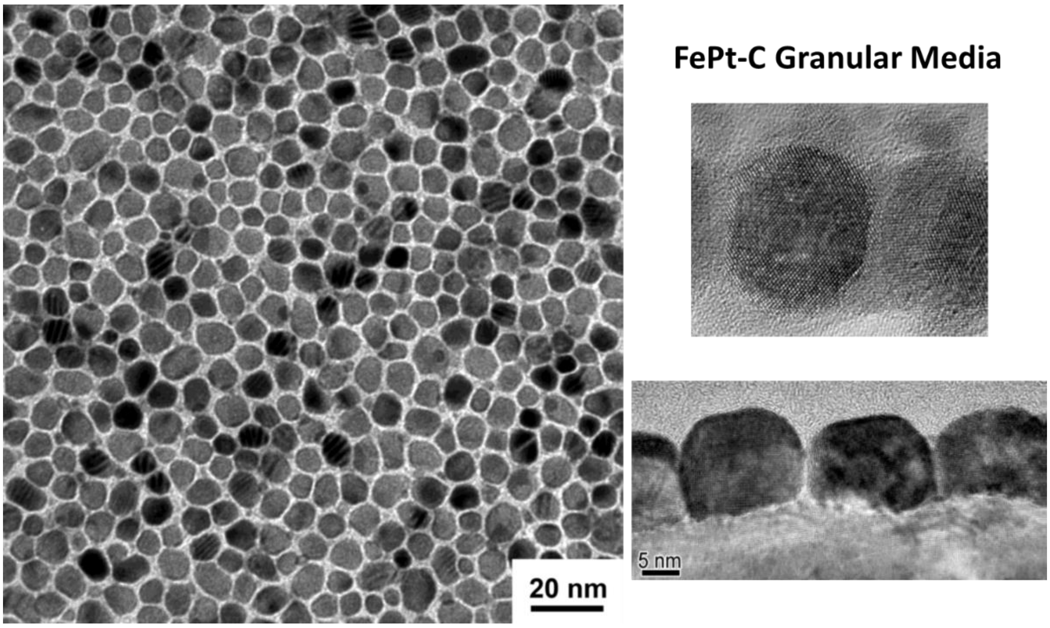

Figure 4.2 TEM images of recent FePt recording medium and the magnetic grains. The left graph is the top view of the granular medium, the right two graphs are the zoom-in cross section of individual grains with the seed layer, heat sink and so on. (Courtesy of Prof. Jimmy Zhu)

To mimic the variation of anisotropy field, a Gaussian distribution is assumed for the H_k value. To assure the same standard deviation at all temperature values, as shown in Figure 4.3, the H_k versus T curve is vertically scaled up and down. For this case, it can be noticed that the Curie temperature for each H_k vs. T curve is the same. On the other hand, the absolute H_k variation is more significant at relatively lower temperature values.

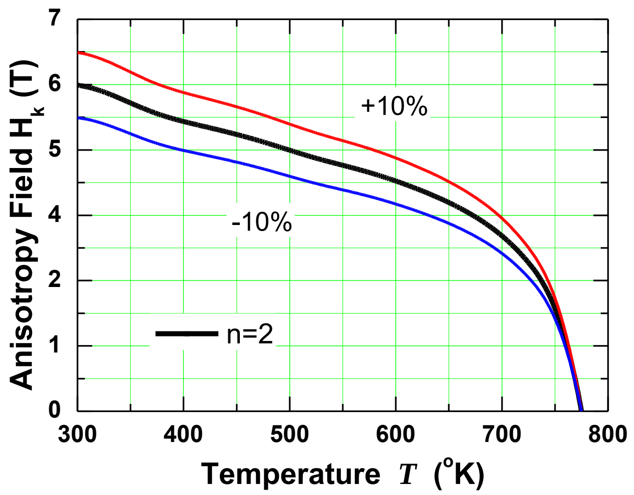

Figure 4.3 Anisotropy field H_k with Gaussian variation at all the temperatures. The standard deviation of H_k is the same at each temperature with vertical scaling.

Adding H_k variation in the simulator, similar recording processes are conducted to obtain the medium SNR as a function of the recording head field as shown in Figure 4.4. Here two different H_k variations, 1% and 10%, are compared under two TG values, 3 K/nm and 6 K/nm. The low and high thermal gradient are shown in the left and right graph, respectively. In this case, the mean grain pitch is 5 nm with a mean boundary thickness of 0.5 nm and the thickness of the medium is 10 nm. The H_k follows a Gaussian distribution similar to the previous description with different standard deviation. Since the effective field gradient is the product of the thermal gradient and the H_k temperature slope, it could be very high, especially when the temperature is close to T_c. Therefore, even if the H_k distribution changes the RTW, this change could be greatly suppressed by the high effective field gradient.

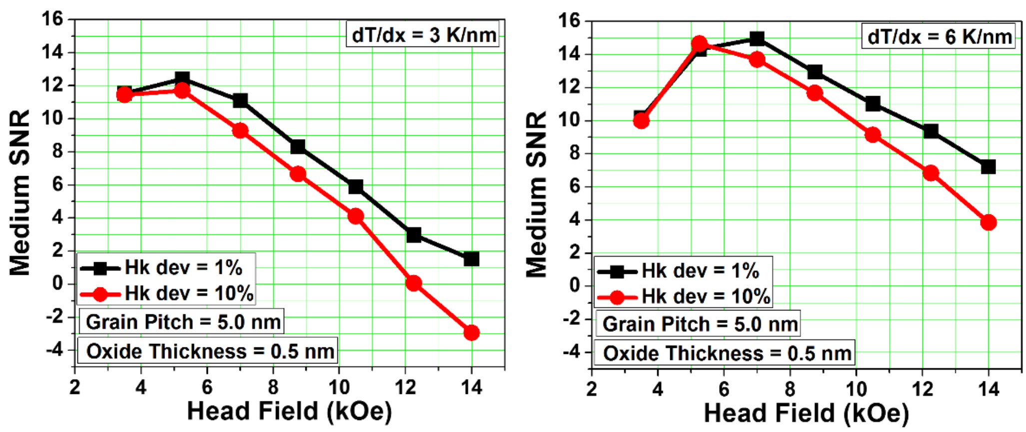

Figure 4.4 Medium SNR versus the head field for different H_k variation values under different thermal gradients, 3 K/nm and 6 K/nm. The grain pitch here is 5 nm with oxide boundary thickness equal to 0.5 nm.

As shown in Figure 4.4, for both graphs, there exists an optimum recording field amplitude. In chapter 3, it has been discussed that the degradation at low and high fields is caused by the incomplete switching and erase-after-write, respectively. When the field is at optimal value, the SNR values of two H_k variations look very similar, although the case with higher H_k variation has slightly lower SNR. It is more obvious that the SNR reduction mainly happens on the higher field side. This suggests that the H_k variation primarily leads to noise in terms of erase-after-write. Additionally, it can be noticed that the case with higher thermal gradient has less impact from H_k variation. It is also critical to realize that the non-optimized head field would have much stronger impact on SNR than that from a moderate H_k distribution.

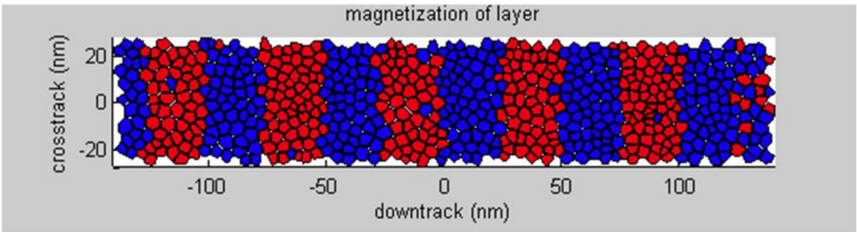

Figure 4.5 Magnetization pattern with 20% H_k variation under 15 K/nm thermal gradient.

In Figure 4.5, a magnetization pattern with 20% H_k variation under 15 K/nm thermal gradient is shown. Although the thermal gradient is much higher than the current value, the 20% H_k variation still shows a few randomly flipped grains at the end of bits, which is a clear footprint of the erase-after-write noise. This further validates the reason of SNR dropping at the high field side in Figure 4.4.

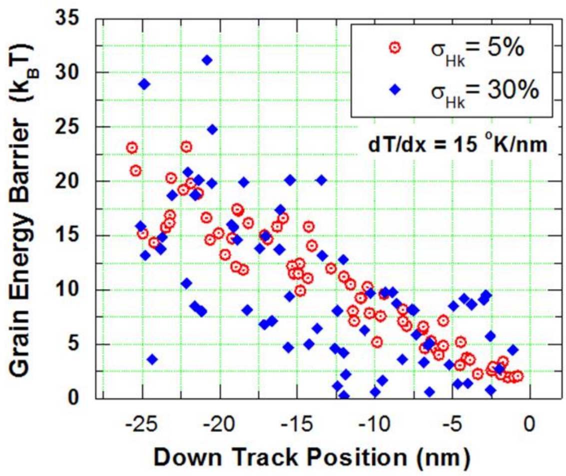

Figure 4.6 Minimum energy barrier of grains right after a transition is written, along downtrack position with different H_k variations.

To better understand the origin of H_k variation, Figure 4.6 plots the minimum energy barriers of the grains right after a transition is written, i.e., the moment when the head field reaches 100% (since its minimum energy barrier) of the saturation value after it is reversed. The energy barrier is calculated by Stoner-Wohlfarth model with effective field extracted from recording process. In the graph, the x = 0 indicates the transition position along downtrack. It should be mentioned that the thermal spot is moving towards the positive x direction. For both H_k variations, at more negative downtrack position, since it is further away from the transition (x = 0 nm), the temperature is supposed to be lower as the cooling process has happened for a longer time period. Consequently, the grain energy barrier starts to recover at more negative position linearly. On the other hand, it is obvious that the data points with 30% H_k variation are of much broader dispersion. Ideally, without any H_k variation, the energy barrier will tightly correlate with the downtrack position. This H_k variation induces the dispersion of the energy barrier (similar to blue dots) so that some grain would have energy barrier lower than the ideal value (close to red dots). These grains would be more vulnerable to the erase-after-write and cause more erasure noise. This explains why the field dependence of medium SNR mainly suffers at the high field side, when there is H_k variation noise.

Since the H_k distribution used to be known in PMR CoCrPt medium, the industry has been trying to enhance the grain properties for the HAMR recording medium [60], [116], [124]. Microscopically, the substrate or seed layer could have defects and nontrivial surface roughness in practical, which would be passed on to the FePt magnetic layer sitting on top of them. Besides, the mainstream seed layer of MgO for FePt medium is typically polycrystalline instead of single crystal, since the cost needs to be controlled. Hence, there exists crystal boundary between the MgO grains and the FePt sitting on the MgO crystal boundary would be affected to degrade H_k. In terms of the sputtering condition, since the fabrication condition is not perfectly identical for each grain, the chemical composition, and lattice alignment would also vary from grain to grain to cause H_k variation. Additionally, the annealing of the FePt should happen at relatively high temperature, the other contacting materials would diffuse into the FePt to induce H_k variation as well. Although the rapid thermal annealing (RTA) [125], [126] is employed, the fast heating process within the FePt could still be non-uniform to make H_k vary from grain to grain. On the other hand, the grain geometry distribution in granular medium is challenging to control. Since part of the crystalline anisotropy is contributed by the surficial anisotropy, the geometry distribution would also lead to H_k distribution. Considering these, apart from optimization of fabrication processes, the bit patterned medium [30], templated growth [35] or nanoscale imprint [127] may greatly narrow H_k distribution, at the cost of potentially more expensive fabrication or more challenging deposition / etching technique.

Despite these reasons to cause H_k variation, it should be kept in mind that the H_k variation mainly leads to the erase-after-write with relatively high head field. By selecting the optimal head field, the erase-after-write could be greatly avoided, hence H_k distribution impact could be suppressed as well. Meanwhile, using higher mean H_k recording medium under higher thermal gradient with faster disk velocity may also prevent the erase-after-write due to H_k distribution from affecting.

4.2 T_c Variation

As discussed in the 4.1, the atoms alignment, fabrication defects, geometry variation and so on would not only cause H_k variation, but also Curie temperature variation, i.e. T_c variation. Additionally, in the RTW definition formula, the RTW is explicitly depending upon the T_c value. As the HAMR recording performance tightly correlates with RTW, the T_c variation would also lead to a significant variation of RTW, which obviously degrades the performance. In this section, a series of simulation with Gaussian distributions of Curie temperature have been conducted.

Figure 4.7 shows the schematic of the T_c variation. To assure that the standard deviation of T_c distribution at all temperatures are the same, the H_k versus T curve is laterally scaled left or right, randomly. It can be noted that the absolute T_c variation is more significant when temperature is closer to T_c.

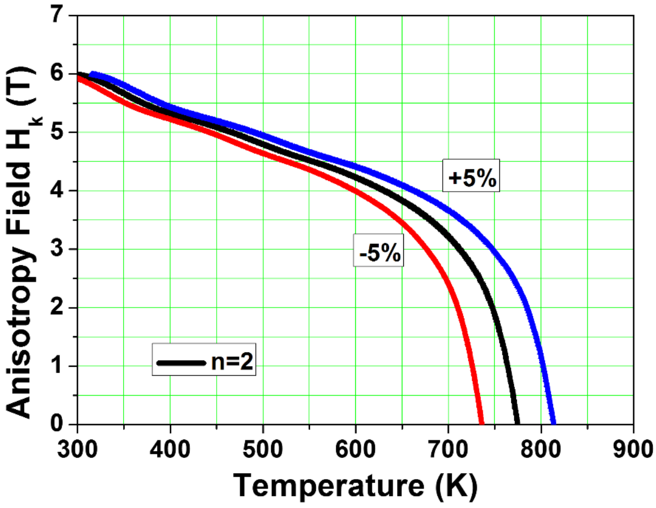

Figure 4.7 Schematic of the H_k versus T curve with T_c variation by lateral scaling. The standard T_c deviation is kept the same at all the temperatures.

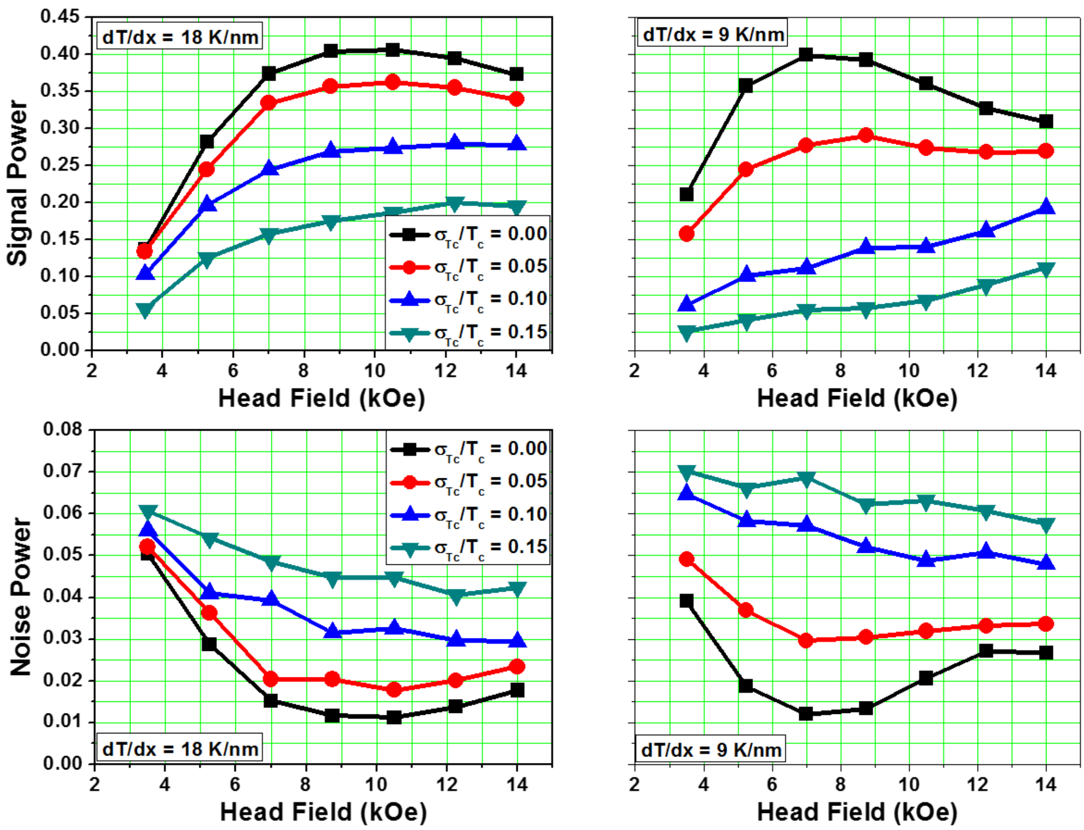

Figure 4.8 Signal power and noise power as a function of the recording head field with various T_c variations (0%, 5%, 10% and 15 %) under different thermal gradient values (18 K/nm and 9 K/nm) [128].

Figure 4.8 shows the medium signal power and noise power as a function of the head field amplitude with various T_c variations under two different thermal gradient. The upper and lower row of graphs relate to the signal power and noise power, respectively, while the left and right column of graphs relate to the 18 K/nm and 9 K/nm thermal gradient, respectively. Both signal power and noise power here show significant field dependence. The signal power first increases, saturates and then starts to decreases as head field increases, while the noise power is the opposite. On the other hand, the results indicate that the introduction of T_c variation obviously degrades the recording performance for all the cases. With larger T_c variation, the field dependence of the signal power or noise power is also less. Comparing the cases with different thermal gradient values, it can be noticed that the higher thermal gradient gives better overall recording quality. Meanwhile, the results suggest that even with only 5% T_c variation, the signal power could greatly decrease and the noise power greatly increases. As in current recording medium, the distribution of the grain properties could easily surpass this variation, which would result in significant SNR drop. Further comparison with the impact of H_k will be discussed in the following.

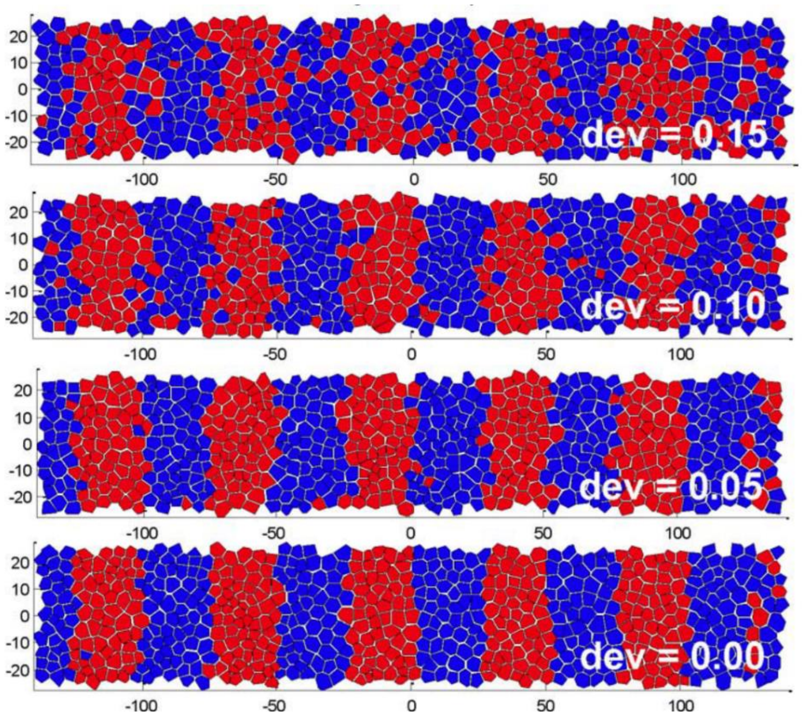

Figure 4.9 Recording magnetization with various T_c variation values, 0%, 5%, 10% and 15% respectively.

Figure 4.9 shows the representative recording patterns with different T_c variation values. The four graphs from top to bottom relate to 15%, 10%, 5% and 0%, respectively. The results indicate that obviously the patterns with higher T_c variation would have much more randomly flipped grains. It should be mentioned that looking at the recording dynamics (static version is shown here, animation available upon request), it can be seen that these noisy grains would not change once writing is complete. In other words, these T_c distribution induced noise affects the initial writing. Meanwhile, the randomly flipped grains are primarily located near the recording transitions, while the middle regions of recording bit are properly magnetized. Only when the T_c variation is too large, would the noise start to extend into the recording bits. This indicates that the T_c variation induced noise mainly behaves as the transition jitter. In later parts, the transition jitter of T_c variation and H_k variation would be compared. When the linear density is approaching higher and higher value, the transitions would be closer and their jitter noise would start to dominate. Hence, the T_c variation would make the performance degrade faster with linear density. To enable ultra-high volume storage, it is critical to suppress the T_c variation to a very low level.

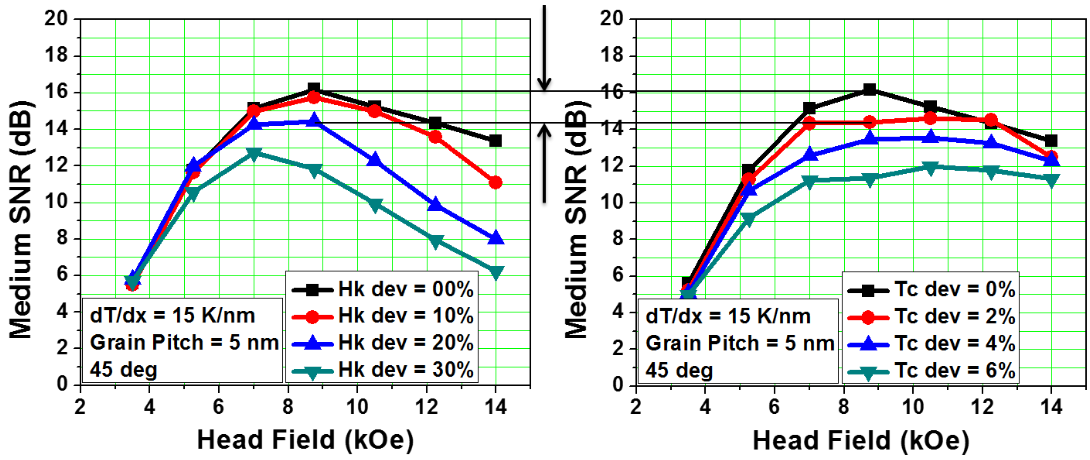

Figure 4.10 Medium SNR versus head field with H_k variation or T_c variation.

Next, it is interesting to compare the impact of the H_k variation and T_c variation. The medium SNR versus head field with various H_k or T_c standard deviation are compared in Figure 4.10. Apart from the field dependence similar to the previous discussion, this comparison focuses on the SNR reduction induced by two types of noise. Without any variation, the SNR saturates at optimal field value in both cases. While to reach the same amount of SNR drop (labeled by the two horizontal lines), it is necessary to induce as much as 20% H_k variation or only 2% T_c variation.

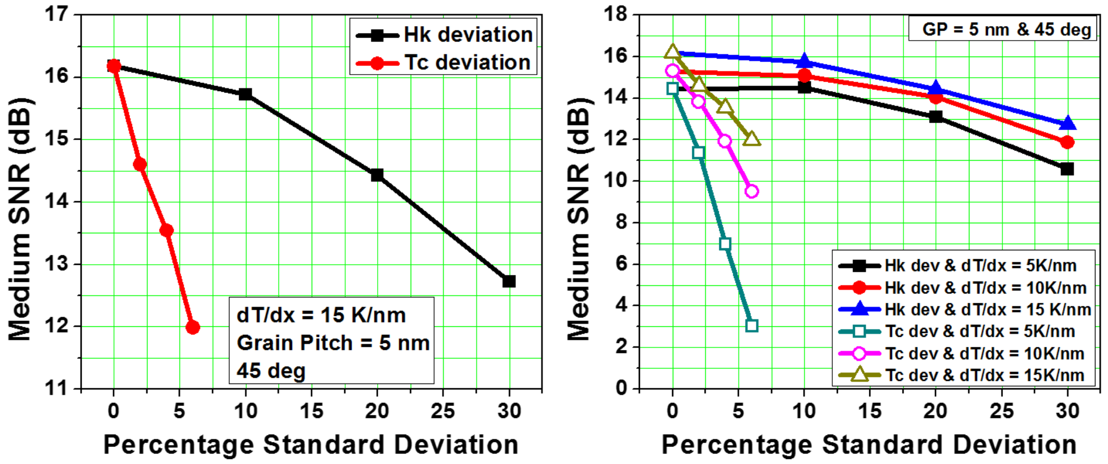

Figure 4.11 Medium SNR versus percentage standard deviation with various thermal gradient values, 5K/nm, 10K/nm and 15 K/nm [129]**.**

By extracting the maximal SNR value of each curve at the optimal field, the medium SNR could be plotted versus percentage standard deviation of either H_k variation or T_c variation, as shown in the left graph of Figure 4.11. Repeating this process for various thermal gradients, the right graph could be obtained. The resulting SNR for the two different causes has significantly different dependences in terms of sensitivity to the sigma value, which is the standard deviation. For the H_k variation case, the SNR degradation is substantially less in comparison to that caused by T_c variation, which is mainly because of high dH_k/dT values near recording temperature. On the contrary, the SNR degrades significantly with just a few percent of sigma T_c, especially when the thermal gradient is not extremely high.

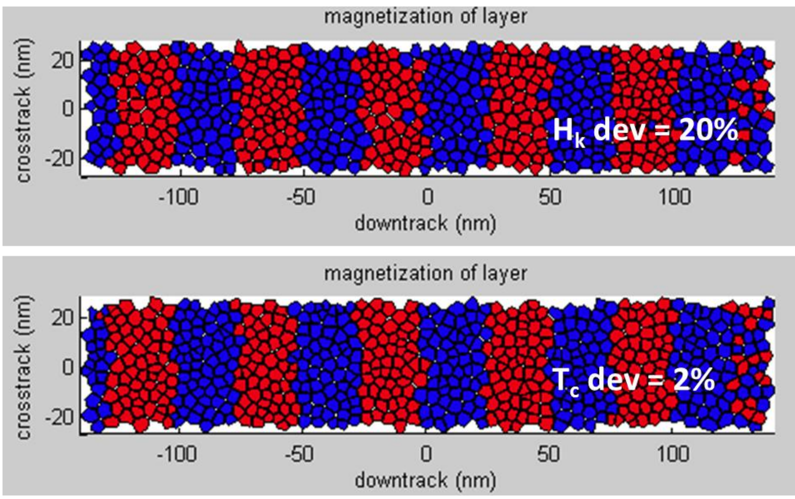

Figure 4.12 Recording magnetization patterns with 20% H_k variation (upper) or 2% T_c variation (lower).

The resulted recording patterns with two types of noise, H_k and T_c, are shown in the

Figure 4.12. Examining the detailed recording process, it can be noted that the increasing H_k variation leads to severe erase-after-write, while erase-after-write hardly changes with increasing T_c variation. For the recording patterns shown here, the case with 20% H_k variation has randomly flipped grain near the end of the transition bit. While the case with 2% T_c variation have almost all the grains within the bit switched properly. However, these two situations have very similar SNR value. To understand it, comparative analysis of the transition bit profile and bit variance will provide a good foundation for an explanation.

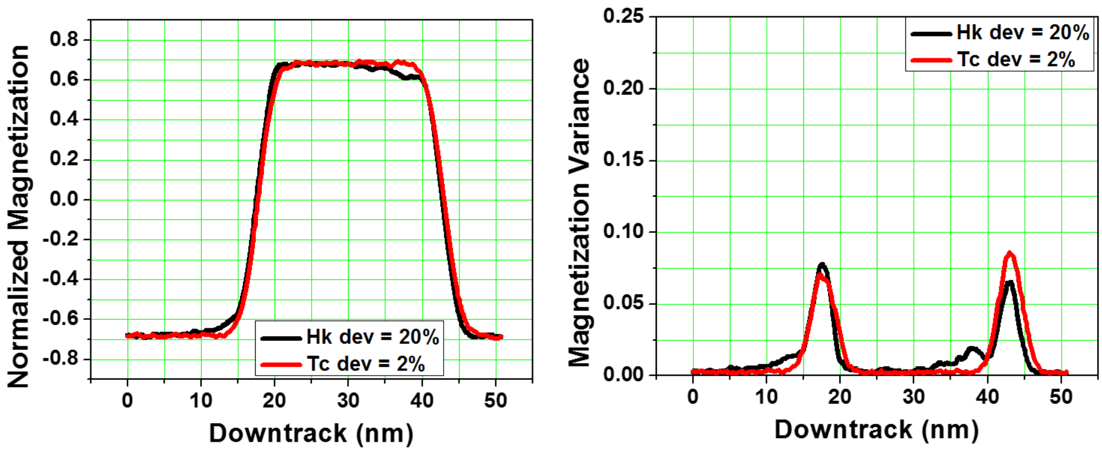

Figure 4.13 Normalized magnetization (left graph) and magnetization variance (right graph) along downtrack position with 20% H_k variation or 2% T_c variation.

Figure 4.13 shows the normalized magnetization and magnetization variance along downtrack position with 20% H_k variation or 2% T_c variation. The magnetization and variance are shown in the left and right graph, respectively. In the left graph, the magnetization has noticeable degradation at the end of the bit, which is caused by erase-after-write. However, in previous SNR figure, it can be seen that the 20% H_k case and 2% T_c case share similar SNR. This can be explained with the right graph of magnetization variance. For the H_k variation, the variance would extend to previous bit, which indicates erase-after-write. While the T_c variation case has broader variance peak, which suggests that the transition jitter is more significant. Meanwhile, the symmetrical behavior of the variance peak is considered as a signature of the T_c variation. This could be utilized in the experimental waveform measurement via spin stand testing, which will be shown in chapter 5.

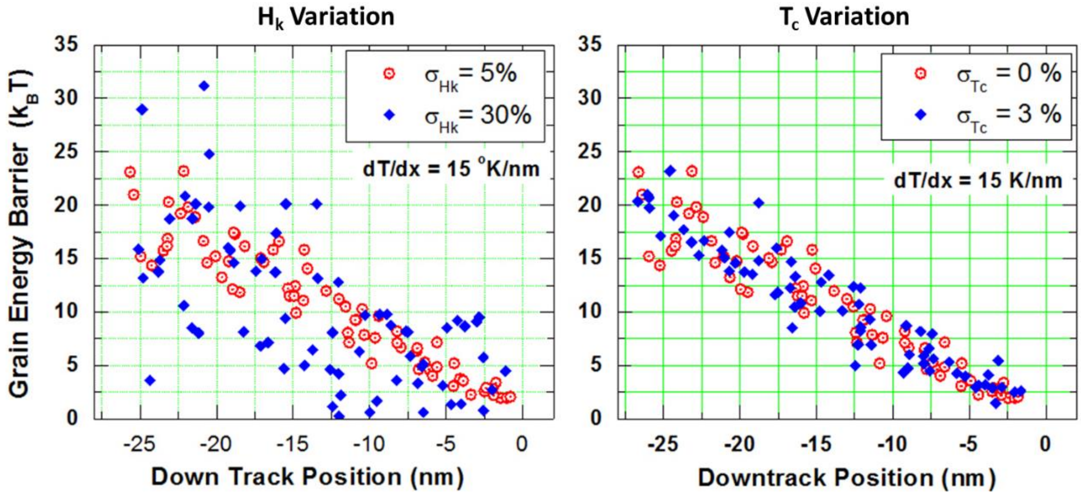

Figure 4.14 Minimum energy barrier of grains right after a transition is written, along down track with various H_k (left) or T_c variations (right).

To further understand the causes and impact of H_k and T_c noise, Figure 4.14 compares the minimum energy barrier of grains right after a transition is written, which is the moment when the head field reaches 100% (since it is minimum energy barrier) of the saturation value. The left and right graphs relate to the situation with H_k variation or T_c variation, respectively. Here x = 0 refers to the center of the transition in the downtrack direction. It should be noted that the thermal profile moves towards positive x-direction. The results indicate that a broader H_k distribution would yield a larger dispersion of the energy barriers, which result in more grains having very low energy barrier, and hence, more severe thermal reversal, or erasure. While for the T_c variation, the energy barrier does not change significantly with 3% standard deviation. Here the T_c variation is set to be 3% because of two reasons: on one hand, the 3% T_c variation is already able to induce obvious SNR reduction in the simulation; on the other hand, in the experimental measurement shown in later chapters, the T_c variation in current recording medium is around 3 - 4%. From this analysis, the results indicate that the H_k variation mainly manifests as the energy barrier dispersion, while T_c variation induces no obvious change in minimum energy barrier.

As mentioned, the T_c variation would lead to randomly flipped grains near the transition area, which increase the jitter noise. Figure 4.15 shows the transition center position jitter as a function of SNR for H_k and T_c variations, where the small SNR values are resulted from greater variation values. The blue and red curve relate to T_c

variation and H_k variation, respectively. The results indicate that for the same SNR values, the transition jitter caused by T_c variation is significantly greater than that by H_k variation.

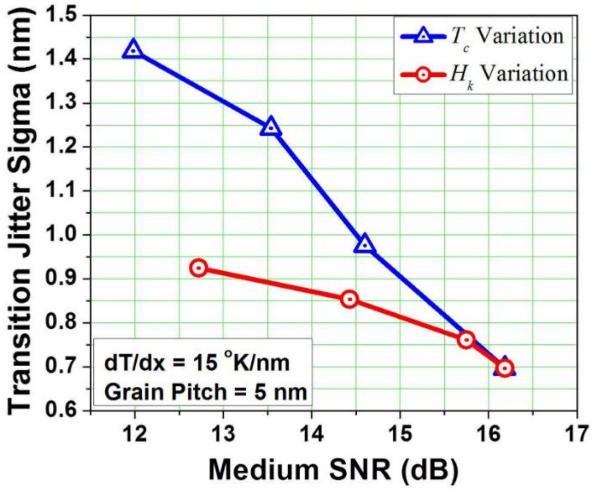

Figure 4.15 Transition jitter versus medium SNR with H_k or T_c variation noises.

As the linear density climbs up to reach extremely high storage density, there would be more and more transitions. From the analysis above, the T_c variation tends to primarily induce transition oriented noise, which suggests that the impact of SNR with T_c noise would be more significant. Figure 4.16 plots the medium SNR as a function of linear density for either 30% H_k variation or 5% T_c variation. The results indicate when the linear density is about 1000 KFCI, which has 25nm bit length, both cases share similar SNR. With higher density and shorter bit length, the case with T_c variation would decrease much more quickly, which validates the impact of T_c noise.

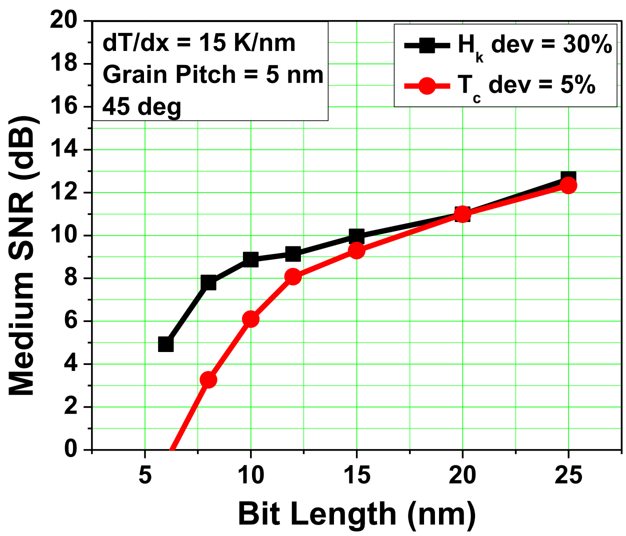

Figure 4.16 Medium SNR versus bit length with either 30% H_k variation or 5% T_c variation.

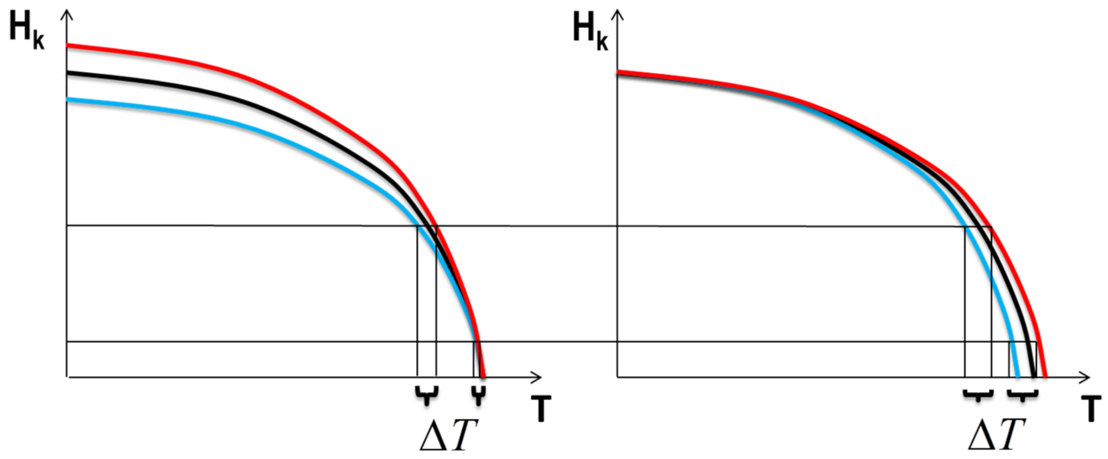

Figure 4.17 H_k versus T curve with H_k variation (left graph) or T_c variation (right graph). The delta T would correlate with the transition jitter or where the transitions are going to form along downtrack.

To analyze these behaviors together, a schematic is shown in Figure 4.17. The two horizontal lines refer to relatively high and low effective field values. At the intersection of those H_k versus T curves, the corresponding recording temperatures could be found. The ΔT in the graphs labels the recording temperature variation induced by the two types of noise. The results here indicate that with H_k variation noise, the delta T could be larger only when the field is higher and average recording temperature is much lower than Curie temperature. On the other hand, with T_c variation noise, the recording temperature variation is equally significant near Curie temperature. Meanwhile, here the H_k variation and T_c variation at temperature that is relatively far away from T_c are similar, but the induced recording temperature variation near T_c is much more significant for the T_c variation case. It has been shown that the recording performance tightly correlates with the recording time window, which is a strong function of recording temperature. Therefore, the temperature variation induced by T_c variation will greatly affect the medium SNR.

In conventional PMR, the T_c variation is never an issue. Since the proposal of T_c distribution in [128], efforts have been made to evaluate the T_c distribution in the recent medium [130]–[132], which suggest 3 to 4 percent of the standard deviation. From the mean field approximation (MFA) [108], [121], the Curie temperature is related to the exchange coupling between the atoms. Due to larger surface-volume-ratio and finite dimension, the thin film is supposed to have more surface atoms, which has less or different exchange coupling from adjacent atoms. As shown in the [131], [133], the Curie temperature becomes a stronger function of the grain volume, especially for smaller grains. Since people have been trying to take advantage of the smaller grains, the corresponding T_c variation due to the grain size distribution would be more evident compared to current FePt medium. Similar to the discussion at the end of the H_k variation section, substrate, seed layer defects, fabrication non-uniformity and so on would also vary the T_c of each grain. The BPM, the templated growth or nanoscale imprint may also help narrow down the T_c distribution, at the cost of fabrication obstacles.

But it should also be noted that from the calculation above, the T_c variation tends to flatten out the field dependence of the recording performance. Tuning the applied head field is seemingly not changing the SNR reduction due to T_c variation. This is because the T_c noise impact is induced at the very initial writing and different writing condition does alleviate its effects. Therefore, T_c distribution mainly relies on the medium fabrication quality, while H_k distribution could be suppressed via selection of optimal head field and so on. It is true that the higher thermal gradient also helps eliminate the T_c variation impact. But considering the advancement of the NFT design, to provide much higher thermal gradient is challenging and takes time. Hence, overall speaking, the elimination of the T_c variation via better medium fabrication, would be a more viable and complete solution for this type of noise. T_c variation is also a key and special noise origin for extremely high-density HAMR application.

4.3 Temperature Variation

Before further discussion of a new type of noise origin, it is helpful to look at the heating mechanism in HAMR scheme. Different from the previous H_k or T_c variation noise, this new type of noise originates from the thermal aspect instead of from the magnetic properties. Since heating is dependent upon heating source, bulk or interface of thermal conductor and so on, many aspects may cause the heating in variation.

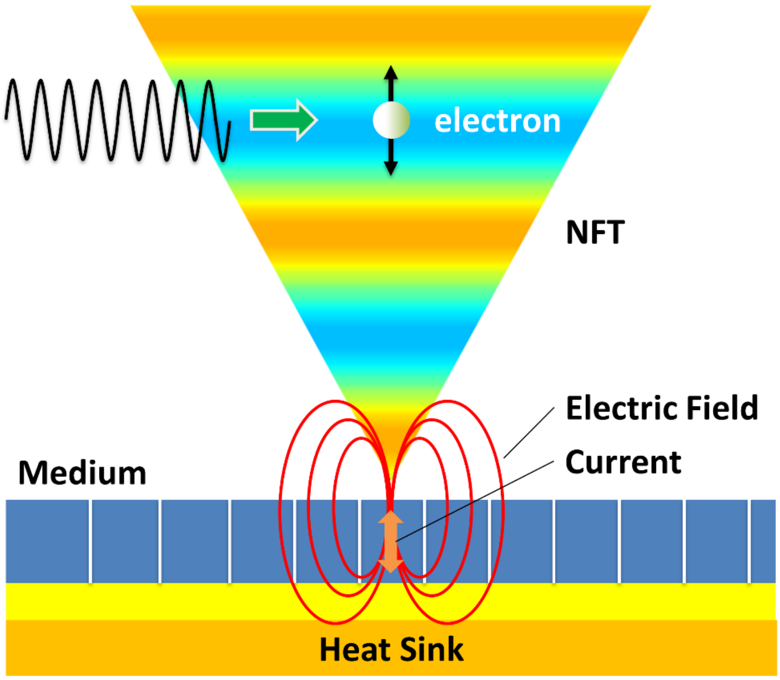

Figure 4.18 Schematic of the heating mechanism using near field transducer.

Figure 4.18 shows the schematic of the near-field transducer (NFT) tip suspended above the recording medium. As the near field transducer tip is metallic (gold) in a few classical designs, the incident light (labeled by the black sinusoidal wave) will make the electrons within the tip start to oscillate correspondingly. The oscillation will propagate towards the very bottom tip head and the wavy color indicates the electron oscillation wave. Because of the electron oscillation, the tip will hence generate oscillatory electric field, which will penetrate into the recording medium (the blue layer with oxide boundary labeled by the white line in the graph). As the current recording medium is made of FePt metallic film, the electrons within the recording medium will also follow the electric field and oscillate. Therefore, there will be induction current within the grains underneath or close to the NFT tip head. The induction heating will rapidly heat up the medium grains above T_C. Besides, during the recording process, the head will move relative to the medium. So when the NFT shifts away from the grain, the previously heated grain will pass the heat downwards to the heat sink via seed layer. On one hand, the heat sink is made of good heat conducting material so that the heat from the recording layer will be quickly dissipated. On the other hand, when the NFT tries to heat up the medium layer, the good heat sink may also make the medium power hungry and not easy to heat up. In realistic design, a good balance point needs to be found. Additionally, the mainstream seed layer underneath the recording layer is currently made of MgO, which is not a very good heat conductor. This leads to an additional degree of complexity for thermal design.

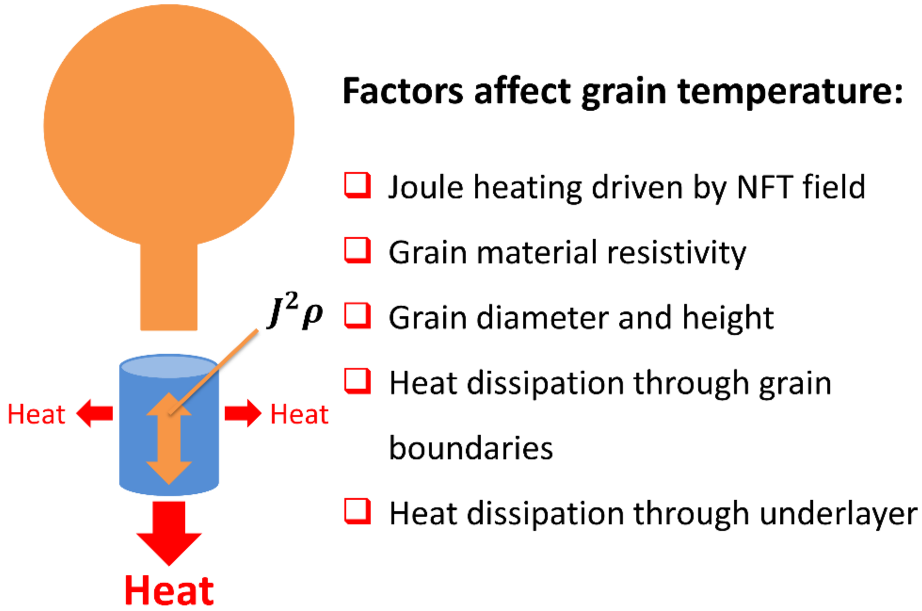

Figure 4.19 Schematic of the lollipop shape NFT [20], **along with the factors affecting grain temperature during heating process.**

Based upon the basic heating mechanism with NFT, several factors affecting the heating procedure should be considered and are shown in Figure 4.19. Since the dimension of the NFT could not be infinitely large and uniformly distant from the medium, the generated oscillatory electric field would not be uniform, even in local small region. This would make the heating power vary at different positions. Both the grain size distribution and the thickness variation could make the grain geometry vary from grain to grain. The geometry variation would have different surface-to-volume area. Besides, as pointed out previously, the grain atoms alignment inside grain could not be perfect, which would also make the material thermal resistivity vary. In terms of thermal resistance, which is a function of the cross section area and thickness, the geometry would also induce heating variation. Meanwhile, the boundary between the grains would also be of different quality. Considering that the boundary thermal resistance is a major portion in heat transfer problem [134], this will be specially addressed in a later section. Similar to the oxide boundary, the current seed layer MgO will also behave as the thermal barrier during the heating and cooling process. The contact variation between the FePt and the seed layer will affect the heating capability as well. Apart from these, assuring the power stability of the laser and controlling for the performance cost ratio, will be the additional challenges in system design.

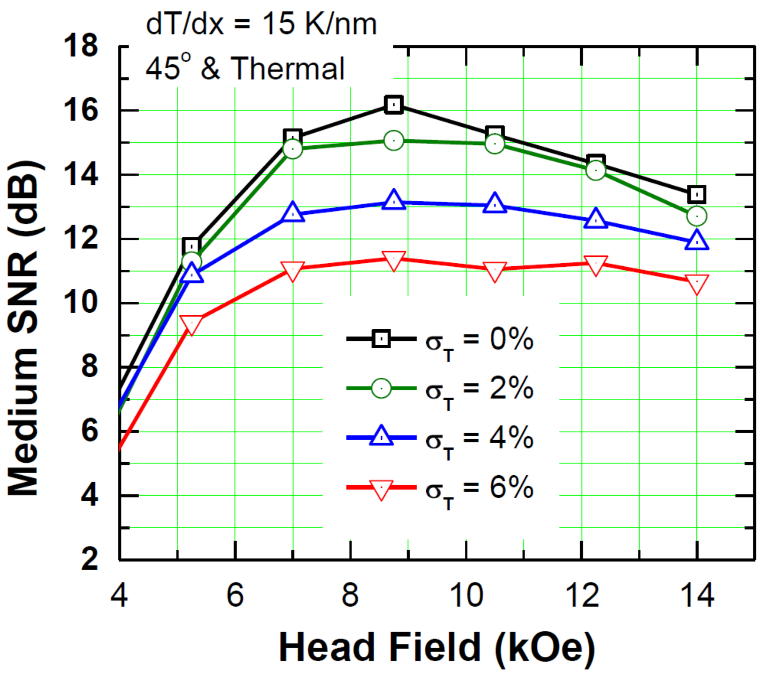

Figure 4.20 Medium SNR as a function of the head field with various temperature variation [135]**, 0%, 2%, 4% and 6%, respectively.**

To simplify the heating variation problem and obtain the estimation of the performance degradation, a Gaussian distribution of the temperature variation is generated and randomly assigned to each of the grains. The recording process has been conducted on the medium with various temperature variations and the results are shown in Figure 4.20. Here temperature variation distribution ranges from 0% to 6%. With zero heating variation, there exists an optimal head field to saturate SNR value, since too low or too high field would increase incomplete switching or erase-after-write, respectively. With nonzero temperature variation, the SNR at the optimal field value starts to decrease with increasing σ_T. With 6% of σ_T, the SNR could drop nearly 5 dB compared to the zero heating variation case. Meanwhile, the introduction of heating variation makes the field dependence much less obvious.

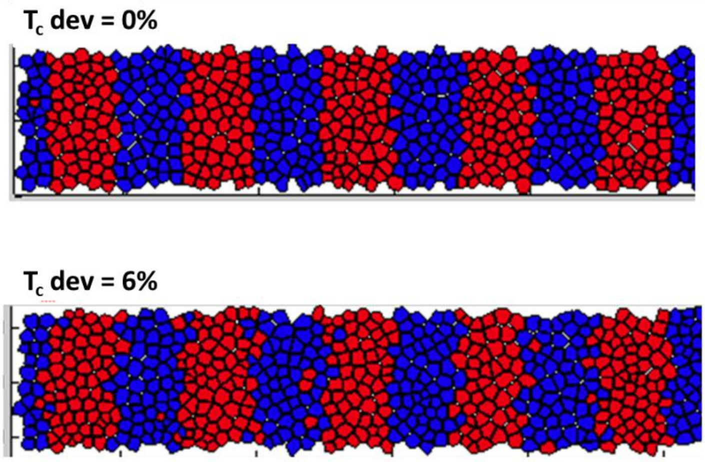

Figure 4.21 Simulated magnetization patterns of recording with a recording thermal gradient of 15 K/nm and a grain pitch of 5 nm.

To better understand the impact of the heating variation, the representative magnetization patterns are shown in the Figure 4.21 for 0% (top) and 6% (bottom) T variation. For the case without heating variation, the transitions are relatively straight, due to the extremely high effective field gradient. While for the case with 6% T variation, the transition boundaries start to become significantly jagged. The grain-to-grain temperature variation causes the magnetization of the grains to switch either "earlier" or "later" in the downtrack direction, which yields the jaggedness along the transition boundaries.

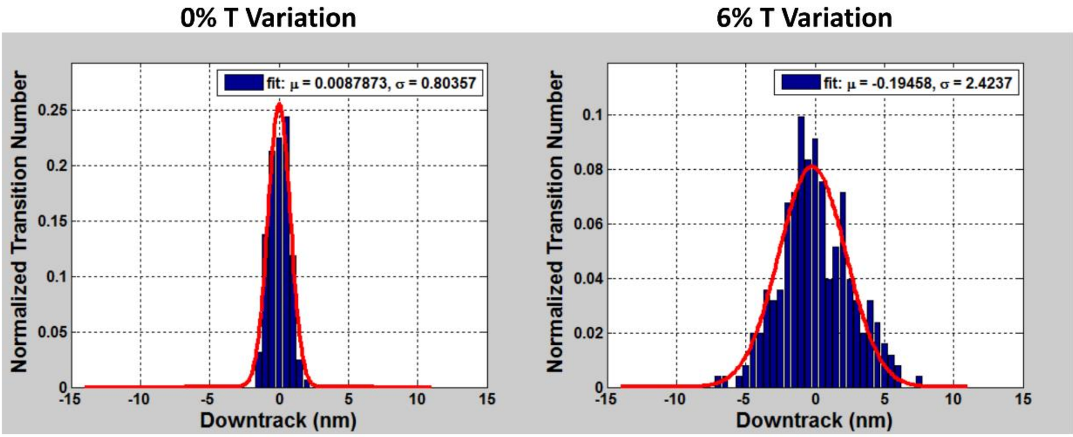

Figure 4.22 Histogram of the transition center position for cases with 0% (left) or 6% (right) grain-to-grain temperature variation.

Since the jaggedness is mainly near the transition area, which will cause the broadening of transition and behavior as jitter noise. For quantitative analysis, the transition center positions for both cases are recorded and plotted in terms of histogram as shown in Figure 4.22. The results clearly show that with 6% grain-to-grain temperature variation, the distribution of transition center is greatly broadened. Specifically, the standard deviation of 0% T variation is only about 0.8 nm, while that with 6% T variation is around 2.4 nm.

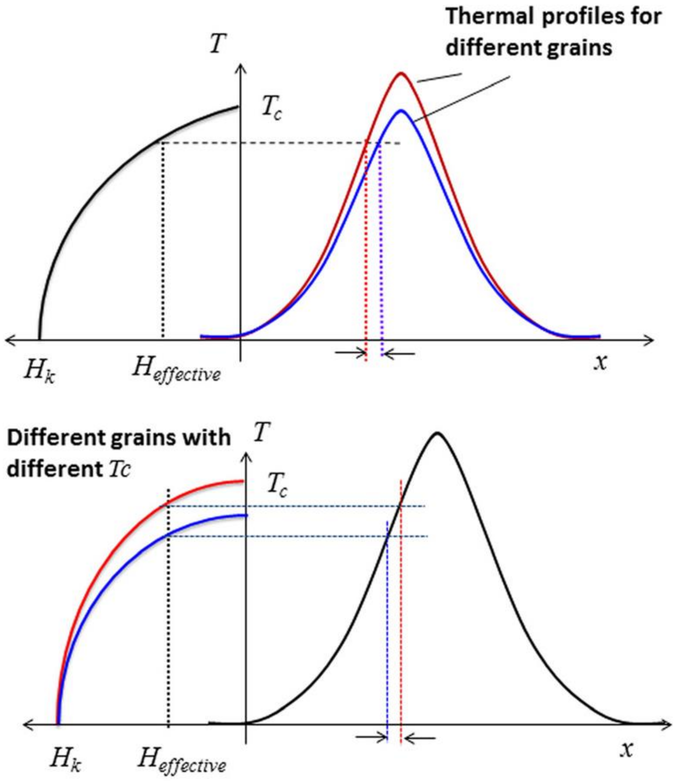

Figure 4.23 Schematic of the recording impact with T_c variation (top) or T variation (bottom).

As the SNR impact of T variation is quite significant, it would be interesting to compare it with the previously proposed T_c variation noise. To illustrate their noise mechanism, the H_k versus T curve is plotted with the thermal profile for both types of noise sources in Figure 4.23. In the T variation case (top graph), since heating varies from grain to grain, two different thermal profiles are shown together. With specific effective field value, the same recording temperature is determined for both thermal profiles. With the thermal profiles, two different downtrack positions could be defined. The difference of the downtrack position is also a difference of coordinates for transitions to form. On the other hand, for the T_c variation case (bottom graph), since the T_c varies from grain to grain, two different H_k versus T curves are shown together. With the same effective field, the two different recording temperatures are determined.

Since each grain experiences the same thermal profile, with two recording temperatures, two downtrack positions can also be defined. Their difference would cause the transition jitter. From this analysis, the T_c and T variation share very similar noise mechanism and can both affect the position to form transition. Therefore, both types of noise would greatly impact the recording medium SNR.

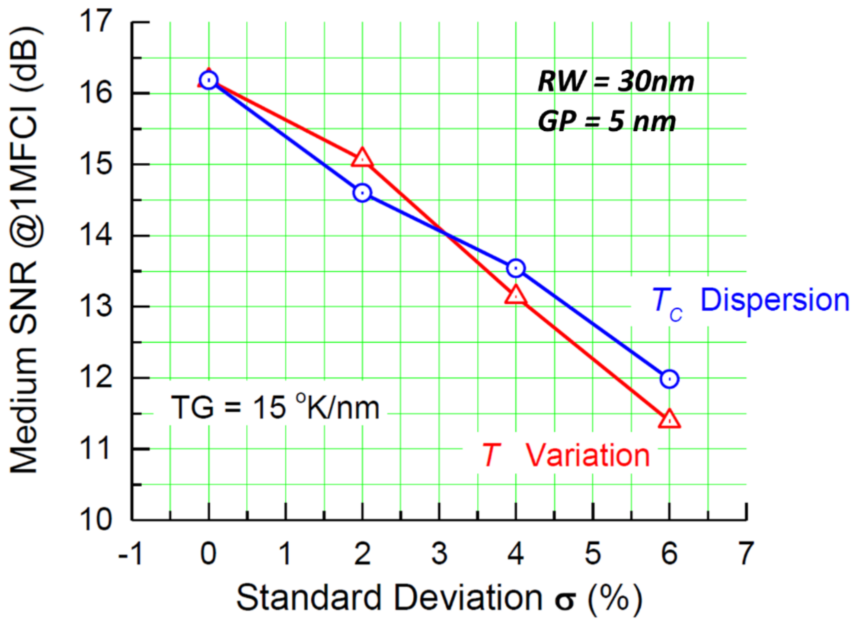

Figure 4.24 Optimal medium SNR at 1MFCI as a function of percentage standard deviation of T_c or T variation. The reading width is kept at 30 nm, the grain pitch here is 5 nm and the thermal gradient is set to be 15 K/nm.

To validate that the impact of T_c variation and T variation is similar, the optimal SNR value versus the percentage standard deviation is shown in Figure 4.24. The results indicate that both types of noise sources greatly affect the medium recording SNR. With higher standard deviation, the SNR drops significantly and quasi-linearly. With only 6% of variation, the SNR nearly decreases from 16 dB to 12 dB. Therefore, in real system design, it is crucial to control the distribution of both noises. In section 4.5, the grain boundary thickness distribution will be discussed and its induced temperature variation will be covered.

Through the discussion, it can be seen that the behavior and the noise mechanism is quite similar to that of the T_c distribution. Experimentally, recent work [136] has been done to measure the T_c distribution and T distribution for recent recording medium. The measured T_c and T distribution standard deviations are about 3-4% and 2-4%, respectively. This T variation originates from the thermal properties of the system, medium properties, optical writer as well as head-medium interface should be considered. Regarding the medium properties, similar to the H_k and T_c variation, one way is to optimize the sputtering condition or select better seed layer and substrate, which is expected to lower the roughness and make the grain geometry distribute more uniformly. Besides, in most medium optimizations, although multiple grain boundary materials have been investigated, they mostly are viewed in terms of the magnetic properties. Therefore, it would be also worthwhile to optimize the grain boundary with thermal or with thermal and magnetic properties considered together. Meanwhile, more uniform internal and contact thermal resistivity should be engineered to lower heating variation. The other option is to grow medium via bit patterning, nanoimprint or templated growth, despite the fabrication and cost challenges. This approach would transform the recording scheme into the heated-dot magnetic recording (HDMR) over granular medium HAMR. While in the extreme case, all the grains are of the same geometry without any variation, sitting on smooth seed layer.

However, the NFT heating is another issue. As the thermal spot decays from peak temperature to room temperature within scale of the track width, the heating is quite non-uniform. Essentially, the electrical field from the NFT tip also quickly decays at positions that are further away. To make the electrical field more uniform in the spot range, the NFT should be closer to medium, and the medium should also dump the heat at the same rate. But the flying capability may start to be a more evident issue. An additional approach would be to insert the plasmonic underlayer (PUL) [20], [137] to enhance the NFT heating. While the laser power is assumed to be relatively stable, a balance needs to be reached between the cost and the laser power stability.

To this point, the specific heat transfer at the head-medium-interface is still not quite clear. At the same time, people try to fill in the Helium [138], [139] and use graphene as new overcoat [140], which would add more degrees of freedom in both heat transfer and mechanical aspects.

Overall, T variation has a similarly significant impact as the T_c variation. As T variation can come from more properties of medium, head, and head-medium-interface, more optimization and study are necessary to eventually narrow down the T distribution.

4.4 Intergranular Exchange

In the current recording medium, the FePt grains are separated by the oxide boundary so that the grains could switch individually. However, in the real medium, there still exists some non-zero exchange coupling between grains, which makes the grains coherently switch and transition become broadened. Therefore, exchange coupling is usually regarded as the noise to degrade SNR, especially in current PMR recording. In this section, the impact of the quasi-uniform exchange coupling between the grains will be investigated and the exchange coupling variation will be discussed in section 4.5 together with the heating variation.

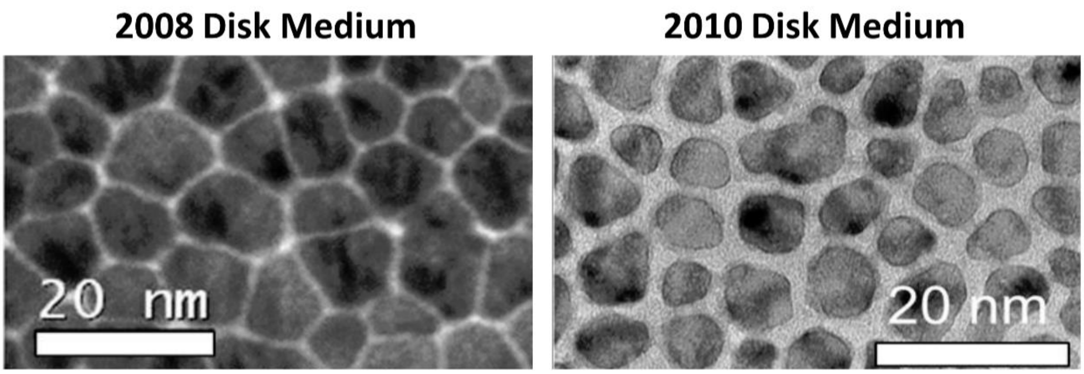

Figure 4.25 TEM micrographs of commercial PMR media from 2008 (left) and 2010 (right) on the same scale (Courtesy: Prof. Jimmy Zhu).

Figure 4.25 shows the TEM micrographs of commercial PMR media from 2008 (left) and 2010 (right). The dark region relates to the CoCrPt grains and the white region relates to the oxide boundary. The images suggest that a thicker oxide is being utilized in more recent medium, which is believed to better avoid the exchange coupling between the grains.

To quantitatively evaluate the oxide thickness dependence of the exchange coupling stiffness, previous work [141] suggests a general exponential dependence as shown in the Figure 4.26. It can be seen that until the grain boundary is thick enough, the exchange coupling field is negligible. Besides, when the boundary is relatively thin, the distribution of boundary thickness would cause wider exchange coupling field distribution. In the following discussion, the exchange coupling will be set in terms of the boundary oxide thickness with this exponential dependence.

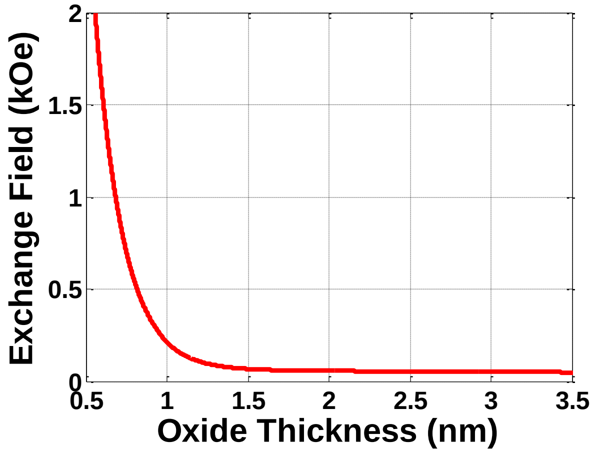

Figure 4.26 Experimental measurement of the exchange coupling stiffness versus different oxide boundary thickness [141]**.**

On the other hand, in previous discussion of HAMR physics, the recording quality suffers from the combinational effect of incomplete switching and erase-after-write at low and high field, respectively. One thing in common of incomplete switching and erase-after-write is that they both behave with the instability of the magnetic grains. Specifically, for incomplete switching, the thermal noise makes quite a few grains unstable and not able to maintain the expected magnetization direction. While for the erase-after-write, the thermal noise along with switched head field makes some vulnerable grains switch after proper initial writing. Considering that the exchange coupling may help stabilize the grains via the coupling field from adjacent neighbor grains, these low / high field induced thermal noise might get alleviated.

To investigate the impact of exchange coupling, the simulation starts with the various quasi-uniform exchange strengths for all the grains. The Figure 4.27 shows the medium SNR versus head field with three boundary thickness values 1.200 nm, 0.683 nm and 0.556 nm, which correspond to exchange field calculated with intergranular exchange constant (A) equal to 0.0e-6, 0.1e-6 and 0.2e-6 erg/cm, respectively, since here the Gaussian-like distribution of grain boundary thickness is assumed. To mimic the spatially uniform case, we set the standard deviation of the granular boundary thickness to be 0.01 nm. For these three cases in both signal power (left) and noise power (right) plot, obvious field dependence can be observed. With adequate exchange coupling (A ~ 0.1e-6 erg/cm), the signal power at low fields becomes significantly higher than cases where A = 0 erg/cm and A = 0.2e-6 erg/cm. This is because the moderate exchange coupling helps the Zeeman energy against thermal agitation field. At high fields, the exchange coupling also helps resist the thermally activated erase-after-write. However, when the exchange is too intensive, the recording performance will significantly degrade.

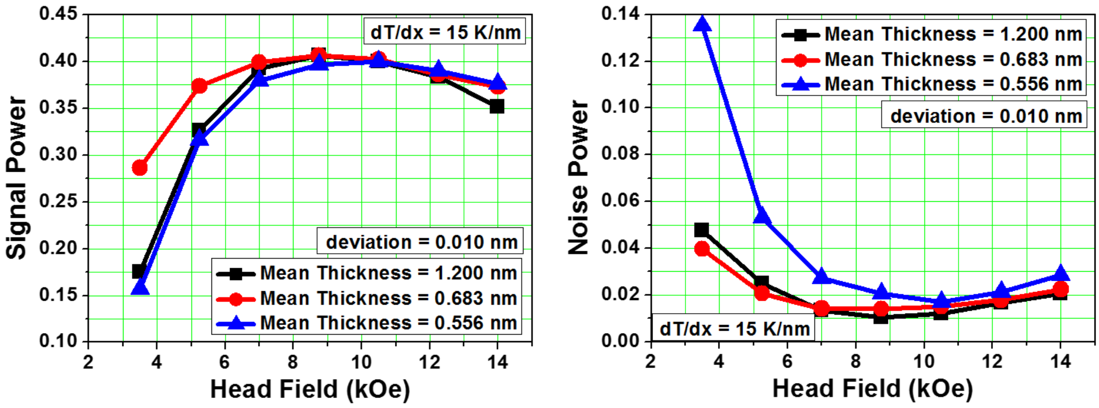

Figure 4.27 Medium SNR as a function of the head field for different boundary thickness values. The three boundary thickness values selected here are 1.200 nm, 0.683 nm, and 0.556 nm, which correspond to exchange field calculated with intergranular exchange constant (A) equal to 0.0e-6, 0.1e-6 and 0.2e-6 erg/cm, respectively. The standard deviation of the boundary thickness is set to be 0.1 nm.

For a better understanding of the noise behavior and recording quality, the representative recording patterns at the low field are shown in the Figure 4.28. The top, middle and bottom graphs correspond to the cases with oxide thickness of 1.200 nm, 0.683 nm, and 0.558 nm, respectively at 3.5 kOe. For the top case, the boundary thickness is relatively large and the exchange coupling is almost zero. The thermal agitation and narrow RTW make the switching hard to complete and therefore result in randomly distributed grains that are not flipped. With the assistance of adequate exchange coupling, the situation is greatly improved, since the neighbor grains would help the central grain switch via exchange field and suppress the impact of thermal agitation. However, when the exchange coupling is too strong with thin oxide boundary thickness, the grains couple together and could be viewed as larger grains, which increases the transition jaggedness and noise.

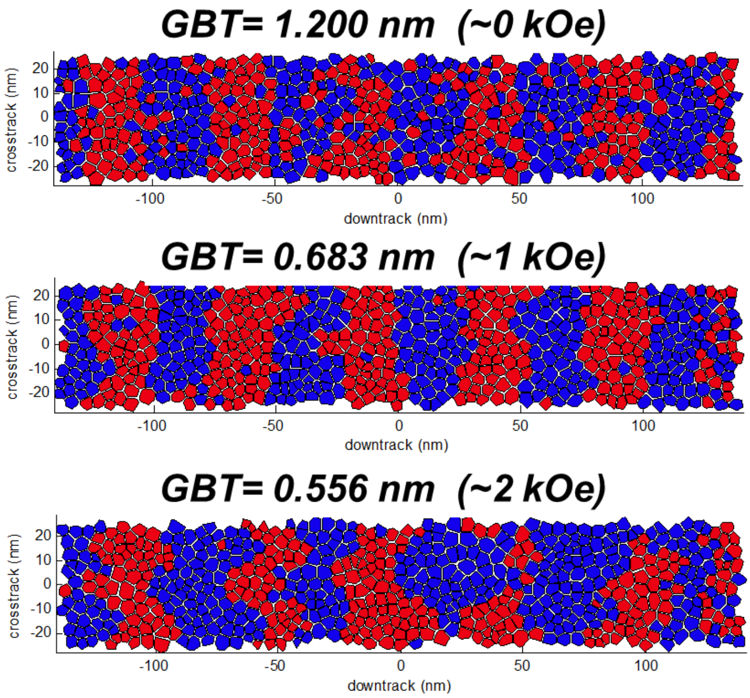

Figure 4.28 Recording patterns for various exchange coupling strengths with a head field of 3.5 kOe. Grain boundary thickness is abbreviated as GBT. The mean GBT is 1.200, 0.68 and 0.556 nm, which correspond to 0 kOe, 1 kOe, and 2 kOe, respectively.

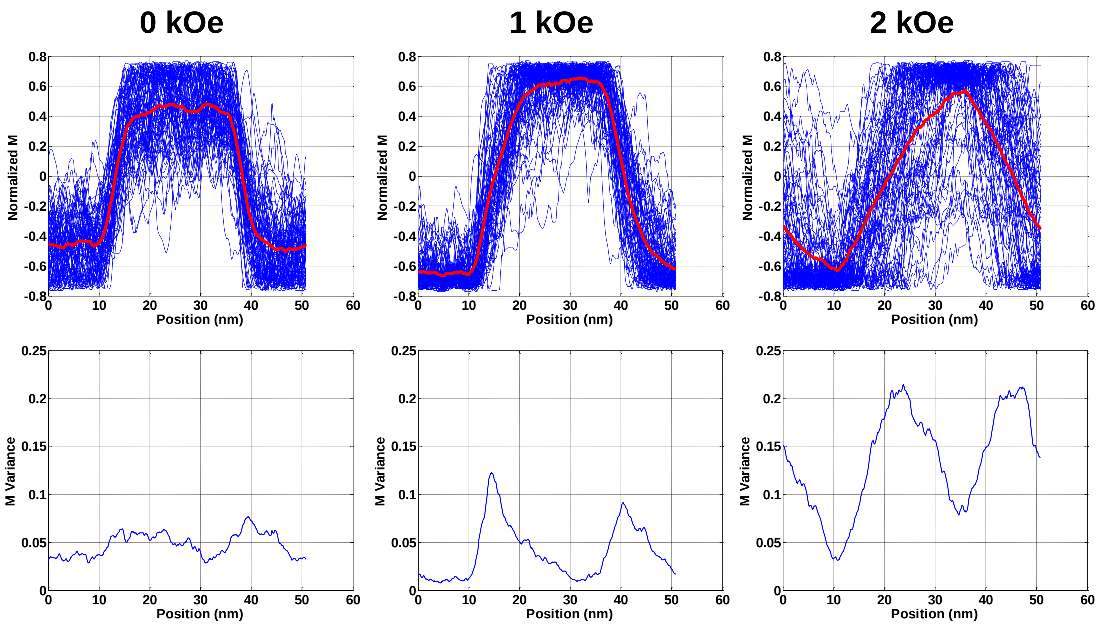

Figure 4.29 Average signal and variance of magnetization for various exchange coupling fields with a head field of 3.5 kOe. The exchange coupling field values are 0 kOe (1.200 nm), 1 kOe (0.68 nm) and 2 kOe (0.556 nm) from left to right, respectively. The upper row is the normalized magnetization while the lower row is the magnetization variance.

The average bit profile and the corresponding variance with a head field of 3.5 kOe are plotted in Figure 4.29. The upper row contains the average transition profiles out of 80 samples and the lower row contains the corresponding variance. When no exchange is incorporated, the average magnetization signal (red curve) is hard to saturate and high noise (variance) can be seen even away from the transitions. With slight exchange coupling induced, the magnetization magnitude is obviously elevated and the noise variance is redistributed, where the variance is more concentrated near the transitions. However, when the exchange further increases, the jittering increases to a great extent and noise variance also increases at all the downtrack positions.

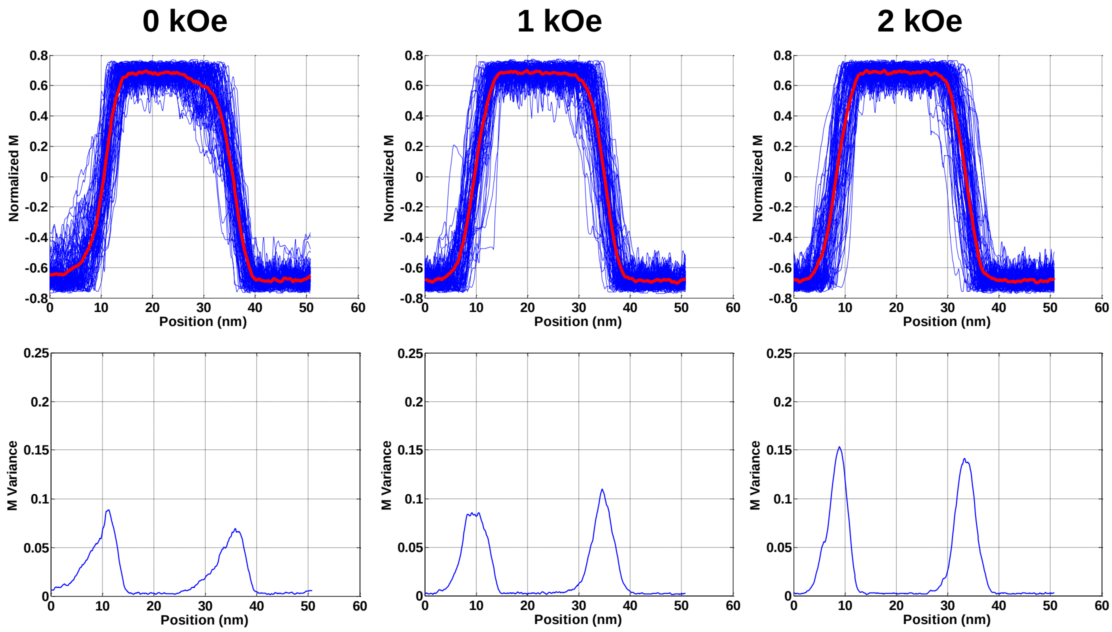

Figure 4.30 Average signal power and variance noise power for various exchange coupling fields for a head field of 14.0 kOe. The exchange coupling field values are 0 kOe, 1 kOe and 2 kOe from left to right, respectively. The upper row is the normalized magnetization while the lower row is the magnetization variance.

Similar to the Figure 4.29, the average magnetization signal and the noise variance at 14.0 kOe with various exchange coupling fields are shown in Figure 4.30 for the purpose of comparison. When there is almost no exchange, the degradation appears at the end of each recording bit, which is caused by erase-after-write when the next bit is being written. With small exchange coupling, this erasure is greatly suppressed, so the average signal profile approaches a square wave. This is the reason why the signal power increases in Figure 4.27. However, the variance is also increasing with the exchange strength. It is because the exchange makes it more difficult to have the grains form sharp transitions. Therefore, more transition jittering is induced and this is the so-called transformation of the noise format.

From this discussion, it can be seen that the quasi-uniform exchange coupling would be helpful to suppress the thermally induced noise. Essentially, the thermally induced noise make grains unstable, and the exchange coupling between the adjacent grain neighbors make the grains coherent and more stable. In practice, to induce proper strength of the exchange coupling, the average boundary thickness should be carefully selected. What is more important is to control the boundary thickness to be uniform all over the medium, which will be shown in the following section. Besides, in most of the recent medium research, efforts have been focused on the nonmagnetic materials. Considering the benefit from the exchange coupling, the magnetic boundary materials may be a new direction to approach. Since in the conventional PMR medium, the exchange coupled composite (ECC) medium achieves great areal density by carefully tuning both the lateral and vertical exchange coupling strength. To better take advantage of exchange coupling in HAMR medium, it would also be necessary to consider the lateral and vertical exchange together.

4.5 Grain Boundary Thickness Variation

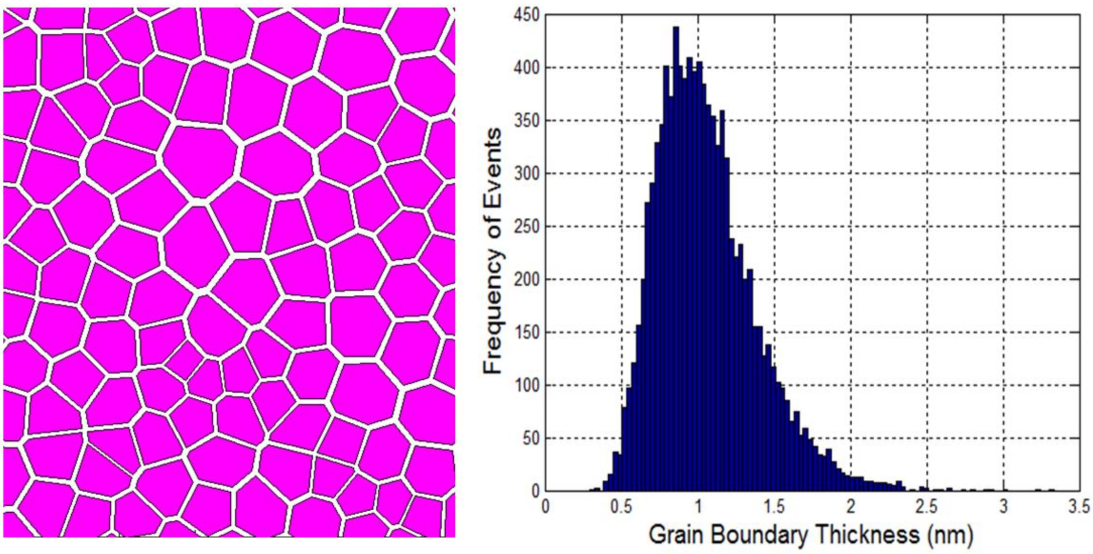

Figure 4.31 Grain geometry along with the boundary oxide (left graph) generated with Lubachevsky-Stillinger Method [87] **and the histogram of the oxide boundary thickness (right graph).**

Now with a better understanding of the role of both the Gaussian heating distribution and the quasi-uniform exchange coupling, the impact of the grain boundary thickness variation will be discussed. According to the exchange field vs. oxide boundary thickness, 1 nm thickness almost gets rid of the granular exchange coupling, so here the mean oxide boundary thickness is also set to be about 1 nm.

Firstly, for the heating variation, as mentioned previously, the heating variation could be induced by the distribution of the boundary, since the contact as well as the geometry could both affect the thermal resistance. Figure 4.31 shows the top view of the granular structure with the oxide boundary in the HAMR recording generated with Lubachevsky-Stillinger method [87], [142]. The oxide boundary is set to be 10% of the grain center-to-center distance on each side and the resulting histogram of oxide thickness is shown on the right for reference. The boundary thickness histogram here follows a log-normal distribution.

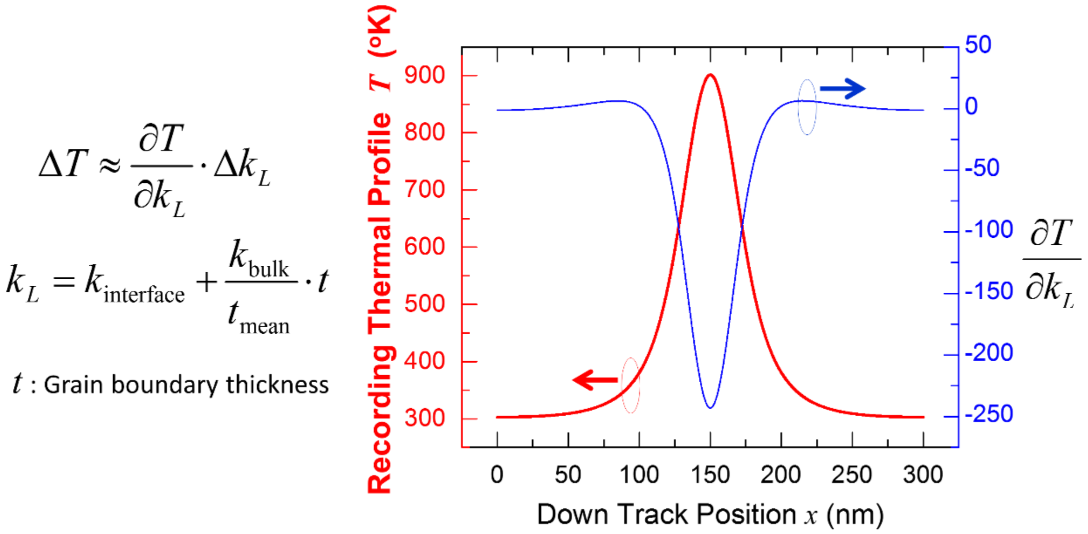

Figure 4.32 Calculated recording thermal profile (red) for a given ratio of perpendicular in lateral thermal conductivity ratio (red, left axis). Numerically calculated partial derivative of a thermal profile by making small change over the lateral thermal conductivity (blue, right axis).

Figure 4.32 shows the thermal profile along with T/k_L along downtrack position. The partial derivative of the recording thermal profile against lateral thermal conductivity k_L is calculated numerically using COMSOL™ on a laterally uniform film with lateral thermal conductivity k_L. Here the thermal resistance consists of both the interface and bulk thermal resistance. After thermal profiles with various k_L values are calculated, the change of temperature versus k_L could be obtained and the differentiation gives the dT/dk_L. As shown by the formulas on the left-hand side, the bulk proportion is linearly scaled with the oxide boundary thickness.

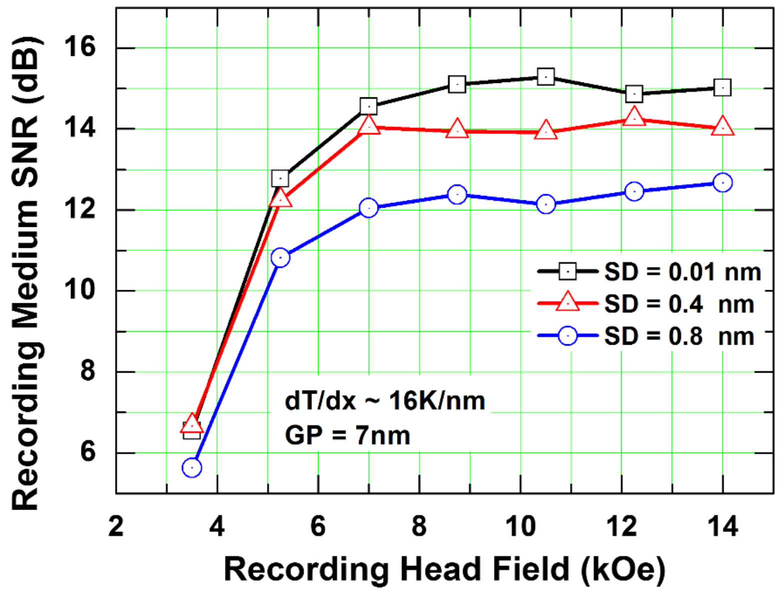

Figure 4.33 Recording medium SNR versus applied head field amplitude with various standard deviation (SD) for oxide boundary thickness distribution. SD is set to be 0.01 nm, 0.4 nm, and 0.8 nm, respectively. The grain pitch is 7 nm and the thermal gradient is 16 K/nm for this case.

With the previously generated distribution of grain boundary thickness, medium SNR versus head field amplitude using various standard deviation, 0.01 nm, 0.4 nm and 0.8 nm are calculated and shown in Figure 4.33. The three curves have obvious field dependence at low field side due to incomplete switching. While at higher field, the field dependence of SNR starts to flatten out, which is the similar impact of previous heating variation. Meanwhile, it can be seen that only half nanometer of SD could induce 1 dB SNR drop. This behavior also indicates that the noise characteristics and properties are exactly the same as that caused by grain Curie temperature distribution and are dominated by transition jitter.

After investigating the heating variation induced by the oxide boundary thickness distribution, the induced granular exchange coupling is discussed as follows.

Here, the mean oxide boundary thickness is set to be 0.683 nm since the previous quasi-uniform exchange coupling with this thickness seems to help suppress the noise and enhance the recording performance. The standard deviation are assumed to be 0.01, 0.10, 0.20, 0.30 nm. Figure 4.34 presents the signal power and noise power versus head field for different exchange distribution. Both signal and noise power indicate that there is an optimum head field around 8.75 kOe. However, any coupling distribution always degrades the signal power and increases the noise power at all the field values. Although the thermal gradient is set to be 15 K/nm here, which would make the effective field gradient extremely high, the resulted transition jitter is quite significant with large exchange coupling variation.

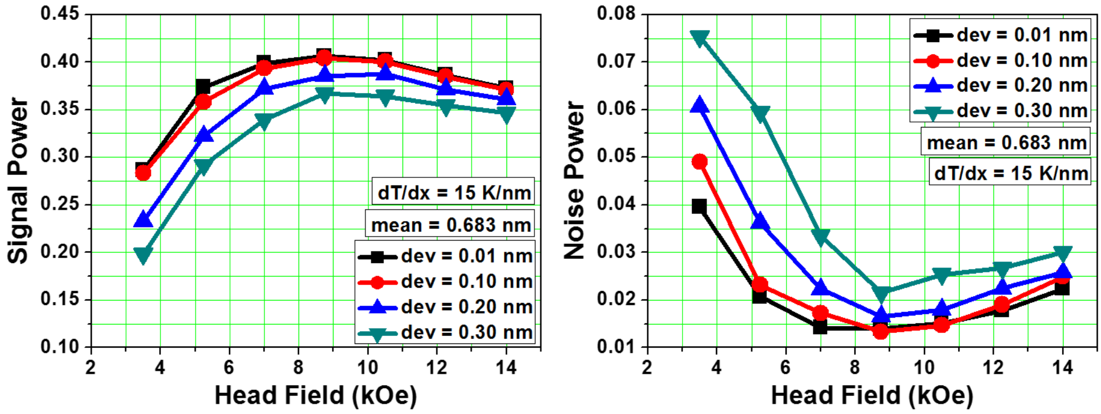

Figure 4.34 Field dependence of medium signal power and noise power for various exchange coupling distribution.

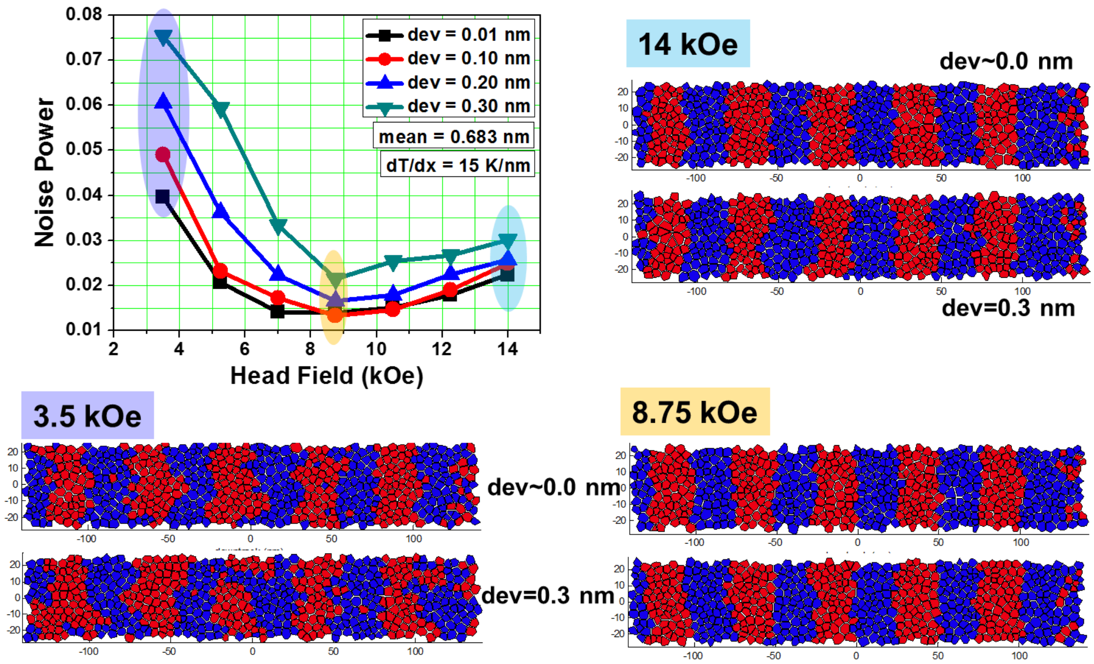

Figure 4.35 Representative magnetization patterns at low (3.5 kOe), optimal (8.75 kOe) and high (14 kOe) field values with boundary thickness standard deviation equals to 0.0 and 0.3 nm, respectively.

The magnetization patterns with 0.01 nm and 0.3 nm standard deviation at low (3.5 kOe), optimal (8.75 kOe) and high field (14 kOe) are shown in Figure 4.35. For the cases with 0.01 nm standard deviation, the decently sharp transitions could be obtained at the optimal head field of 8.75 kOe. While with a standard deviation of 0.3 nm at 8.75 kOe, the transition starts to have obvious jaggedness, which becomes jittering. With 3.5 kOe head field, some recording bits or parts of bits are still coherent, while some parts of bits become partially magnetized. This is believed to be caused by the non-uniform exchange coupling, where lower exchange cannot manage to stick the grains to rotate together. With 14 kOe head field, for a similar reason, at some areas, the exchange is not sufficient to avoid the erase-after-write. Consequently, the erasure is more severe near the bit tails. Overall, the broadening of exchange coupling generally weakens the advantage brought by the uniform exchange and may even induce extra noise.

From this section, the impact of the oxide boundary thickness distribution has been investigated in both thermal and magnetic perspectives. The analysis suggests that grain boundary thickness would lead to the T variation as well as exchange coupling distribution, both of which are detrimental to the recording performance. In practice, one option may be to utilize relatively thick grain boundary medium, similar to the medium of year 2010 in Figure 4.25. This basically removes the impact of the exchange coupling, while the impact of the thermal variation needs further study. The interface between the FePt and the boundary material needs to be closely looked at and engineered as well. Besides, the thick grain boundary would make the area of the magnetic material shrink, which would reduce the magnetic signal during read back. The other option may be to skip the granular structure and use the dot medium via lithography, nanoimprint, templated growth using block copolymer and so on. This medium may remove the grain boundary. Hence, the exchange coupling could be ignored. For the thermal issue, since air is not a good thermal conductor, the heating may be better confined to the magnetic island, which also reduces the laser power consumption and enhances NFT reliability. Whereas in this case, the island pitch size would be the track width, which suggests that the thermal spot generated from NFT must be well controlled. The side issues like the island position or size variation need to be taken into account [12], [31], [62] as well.

4.6 Embedded Noisy Grains

In the previous discussion of noise sources in chapter 4, all of them have head field or thermal gradient dependence to a certain degree. Within this section, the embedded noise grains will be discussed and this type of noise always exists in the recording procedure, no matter how the writing is conducted.

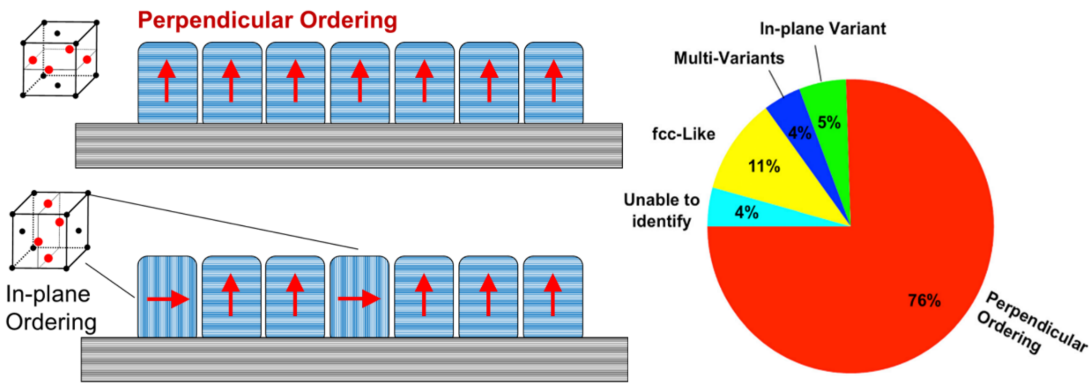

Figure 4.36 Schematic of the comparison for out-plane (vertical arrow) and in-plane (horizontal arrow) grains within recording medium. The grain-to-grain TEM image analysis delivers the proportion pie chart on the right-hand side [118]**.**

Figure 4.36 shows the schematic of the in-plane FePt grains on the left-hand side along with the pie chart on the right-hand side. In the recent design of FePt, the MgO is usually used as the seed layer underneath the FePt thin film. However, the MgO is mostly polycrystalline, which has quite a few grain boundaries. To obtain the perpendicular magnetic anisotropy, the FePt needs to grow on the MgO epitaxially with lattice matched. Due to the existence of the MgO boundary, the FePt grains spanning over the MgO boundary tends to have easy axis not perpendicular or even multi-variant behavior. Having the FePt grow one on one or simply using single crystal MgO substrate may solve the problem, and active research is still going on. For the pie chart on the right-hand side is obtained by looking at a bunch of grain TEM image and then histograms of each proportion are plotted. The pie chart indicates that the in-plane and multi-variant grains take up to 15% of all the FePt grains in the recording medium [118]. Without perpendicular anisotropy, these multi-variants will cause media noise, which is independent of the recording conditions. Spatially, these affected grains would appear at the same location for each writing process.

On the other hand, the previously proposed incomplete switching process would have poor recording quality even with perfect medium. Specifically, the insufficient head field is not able to maintain the orientation of each grain, which results in randomly flipped grains. This is a random process and the grains not flipped properly would appear all over the place and vary in each writing process. Since there are also noises coming from the erase-after-write and H_k / T_c / T variation, in the following discussion, the DC writing is applied to prevent the transition from forming and avoid entanglement of other types of noise. Therefore, only incomplete switching and embedded noisy grains are evaluated here.

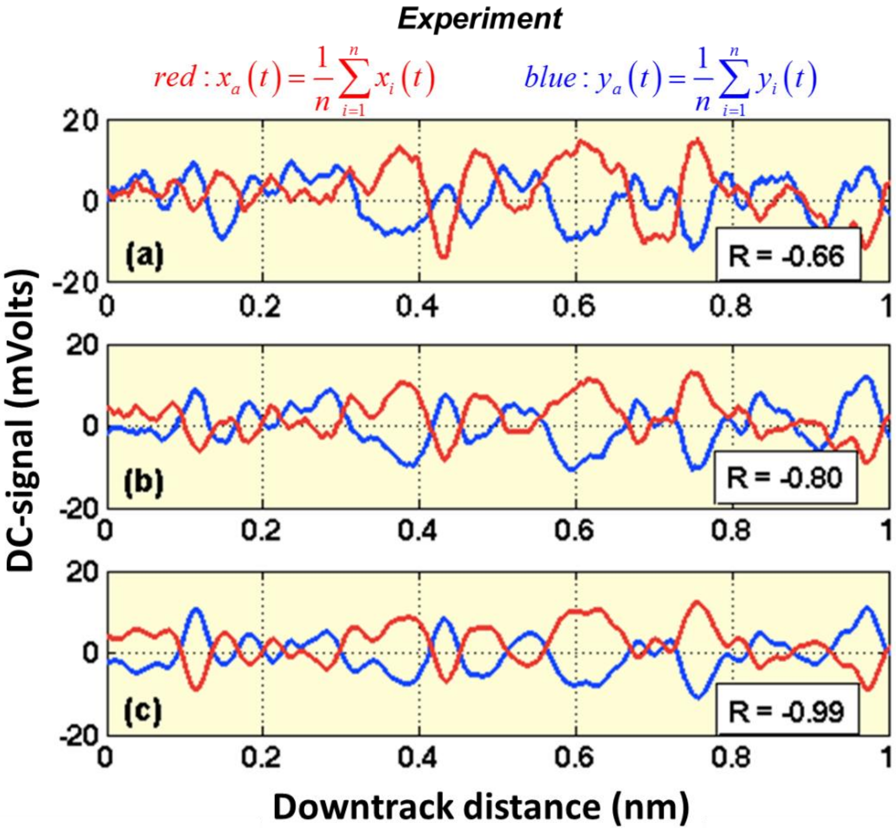

Figure 4.37 Average waveforms written with positive (red) and negative (blue) DC writing on spin stand testing. The three graphs from top to bottom relate to average waveform numbers of 1, 3 and 100. The corresponding correlation coefficient is shown in the top right corner of each graph.

To quantitatively evaluate the relative weight of the random noise (incomplete switching) and the fixed noise (embedded noisy grains), multiple DC writings with opposite polarities have been applied to calculate the correlation coefficient [143], [144]. Figure 4.37 shows the average waveform written with positive (red) and negative (blue) DC writing using various numbers of waveforms to average, 1, 3 and 100 from top to bottom. For each of the curves here, the average DC signal has been taken away to keep the noise component only. For the first graph of the raw noise waveform, it can be observed that some parts of the two waveforms show symmetrical behavior, while some parts look totally random. Hence, the correlation coefficient R is only about -0.66. With three waveforms averaged out in the second graph, obviously more symmetrical behavior could be observed at various downtrack locations and the correlation coefficient immediately becomes to -0.8. When 100 waveforms are collected and then averaged, the resulting mean waveforms are exactly mirror image of each other and the correlation coefficient is -0.99. These processing results indicate that as more waveforms are accumulated to average, the randomness within the waveform could be effectively removed. Consequently, the remaining average waveforms of positive and negative writings presents almost perfectly symmetrical and deterministic behaviors.

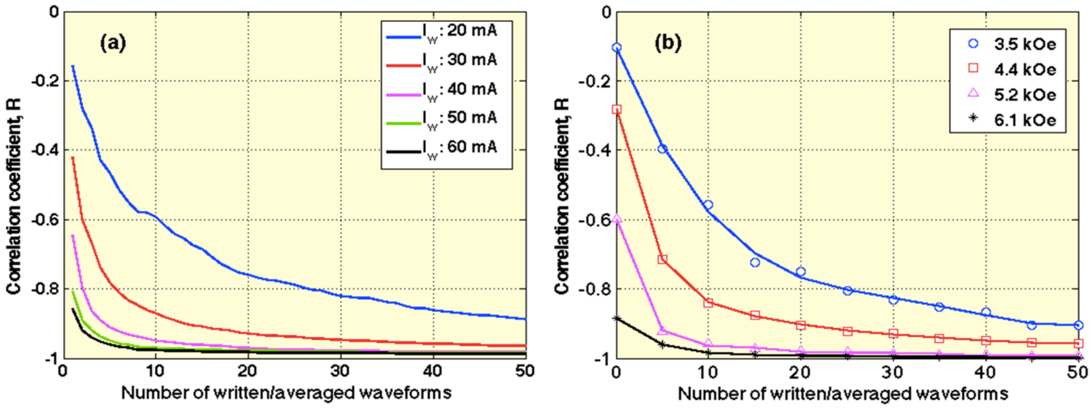

Figure 4.38 Correlation coefficient versus number of written / averaged waveforms with different head field amplitudes. The left and right graphs are generated by spin stand testing (left) and micromagnetic simulation (right), respectively with the same settings.

With the technique described above, the correlation coefficient has been investigated as a function of the written / averaged waveforms number with various head field amplitudes shown in Figure 4.38. Both spin stand testing (left graph) and micromagnetic modeling (right graph) with same settings are conducted. Here it is assumed that in the spin stand testing, the head field amplitude is linearly proportional to the writing current. For all the curves shown here, as the number of waveforms increases, the correlation coefficient gradually approaches to -1, which suggests more and more symmetrical behavior. Additionally, for the case of higher head field, the correlation coefficient with / without averaging is always relatively lower. This is because the higher head field better maintains the spin orientation against the thermal agitation during writing and less randomness is induced. Meanwhile, it can be noticed that results via both the spin stand testing and micromagnetic simulation match pretty well, which indicates the simulation captures the primary characteristics of recording system.

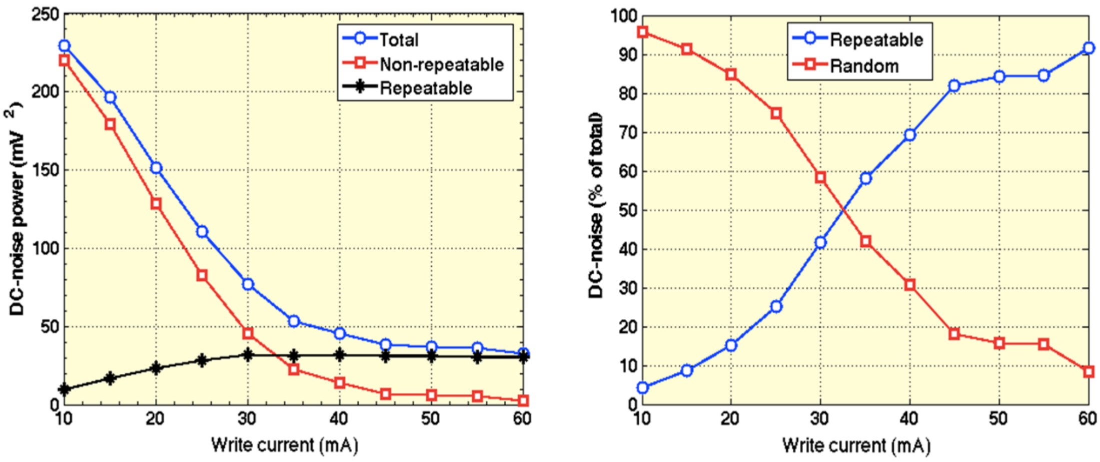

Figure 4.39 DC noise power versus write current (left) and relative weight of repeatable and random noise versus write current (right) [143].

Now that the randomness of the signal could be removed by averaging the accumulated waveforms, it would be interesting to analyze the relative weight of the random noise. In Figure 4.39, the total noise power, non-repeatable noise power, and repeatable noise power are plotted together versus write current. Specifically, the total noise power is calculated from the raw waveform. After sufficient averaging (when the average waveforms are already symmetrical), the noise power is calculated for repeatable noise power. By subtracting repeatable noise power from total noise power, the non-repeatable or random noise power could be obtained. Repeating this process at different write current, the left graph could be plotted. The results indicate that as write current increases, the total noise power gradually decreases. This could be understood since the incomplete switching is greatly suppressed with higher head field. It is also shown via the decreasing of the non-repeatable noise power. While for the repeatable noise, it is almost constant except a slight increasing at low field. This could be due to the existence of the multi-variant grains, which show more mixed behavior. With this result, the relative weight of repeatable and non-repeatable noise power could be generated by dividing the total noise power as shown in the right graph. As indicated by results, the non-repeatable noise component quickly decreases with higher head field, while the repeatable noise component starts to become dominant. Considering that there is an optimal head field value for practical recording, this type of analysis could tell the corresponding relative weight of these two noises. As the non-repeatable noise is primarily caused by the writing process, the system design and setting could be tuned to better enhance the SNR. For the repeatable noise, it is mainly caused by the media defects and should be addressed by the optimization of media fabrication process.

From this section, the relative weight of the incomplete switching noise and the embedded medium defect noise are analyzed via the correlation coefficient of opposite average DC writing waveforms. The technique is effective to remove the random noise caused by incomplete switching, which keeps the embedded noise. Recent recording characterization tends to have significant DC noise, which may be caused by either the incomplete switching or the embedded noise. In practical design, the technique can be applied in spin stand testing, so that the major noise can be identified. If the noise is mainly from the writing, additional RTW analysis could help confirm where the specific system stands. Then the other system aspects could be manipulated to approach the ideal RTW. As the incomplete switching is due to the limited RTW, to lower thermal gradient, to lower H_k, enhance M_s, to slow down the velocity, to increase the head field and so on may help better saturate the magnetization of grains. Whereas if the noise is mainly from the embedded noise, the medium quality has to be increased and the fabrication process needs further improvement. As mentioned that the grain boundary of the seed layer may be suspected of causing the multi-variant or other defect grains of FePt. Using single crystal MgO substrate may remove the MgO boundary and have superior FePt properties, but the cost would also greatly increase. For polycrystalline MgO, the following question would be to make sure the FePt grains grow one on one with respect to the MgO. If each FePt grain sits on one MgO grain, it would be necessary to scale down the MgO size simultaneously. On the other hand, if the bit patterned medium is utilized, the similar defects are expected. At this time, if one-on-one growth happens on the polycrystalline, the magnetic island position would have a lot of variation. Further balance on this needs exploration.

4.7 Conclusion

In this chapter, based upon the understanding of recording physics described in chapter 3, multiple previously known and newly discovered noise origins along with their noise mechanism and impact are analyzed and compared.

Specifically, the H_k variation manifests as the erasure of recorded bit as it causes the minimum energy barrier dispersion. While the system performance tightly correlates with the recording time window, T_c variation is able to change the RTW more significantly than H_k variation does. Therefore, the impact of T_c variation is more obvious than H_k variation. Even a few percent standard deviation of the T_c variation could cause a few dB drop of SNR, which can be caused with tens of H_k standard deviation. To control these two types of noise, medium with more uniform properties should be fabricated to narrow down the distributions. Another type of noise originates from the grain-to-grain heating capability variation. This one shows similar characteristics as the T_c does and also easily lowers the SNR with small variation. To control this, one has to work on the stability of laser, uniformity of medium, design of NFT and so on. On the other hand, the exchange coupling, which is generally considered as noise in conventional PMR, may have potential to enhance the recording. This is because the exchange helps make the adjacent spins tend to wobble coherently. Meanwhile, it is critical to ensure very narrow distribution of the oxide boundary thickness, since boundary thickness variation would easily lead to exchange coupling distribution and the temperature distribution. Both resulting noises could significantly degrade the recording quality. Besides these, as the defects embedded within the medium do behave as noise, certain technique could be applied to analyze the relative weight of the non-repeatable noise (primarily caused by incomplete switching) and the repeatable noise (embedded defects). This provides guidance for the direction of engineering, since the non-repeatable noise could be suppressed via better system design or settings, and the medium quality is mainly responsible for the repeatable noise.

5. Application of Theorem

With the fundamental understanding of the recording physics (chapter 3) and various noise origins and mechanisms (chapter 4), this chapter will give several experimental observations and application instances of the proposed theorem. The spin stand testing would be employed to validate multiple primary observations in previous micromagnetic simulations first. Then the recording time window analysis is applied for a generic design from industry to provide suggestions for modification. Regarding the medium properties, a home-made experimental platform is set up to evaluate recent medium samples from companies. Additionally, the transition curvature, a well-known issue, is investigated in terms of storage density impact. Utilizing the understanding of storage physics, a corresponding solution to transition curvature is also proposed for the first time.

5.1 Spin Stand Testing

5.1.1 Field Dependence

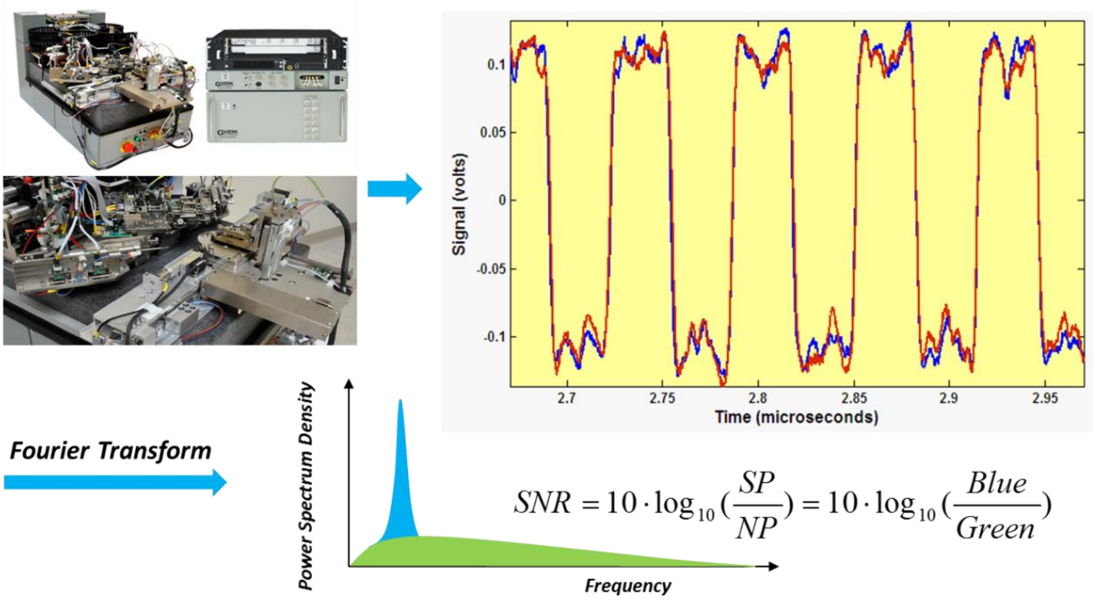

Figure 5.1 Procedure to obtain the recording SNR via spin stand testing [145].

In chapter 3, several representatives and fundamental phenomena are observed in the thermal coupled micromagnetic simulation, like incomplete switching, erase-after-write and so on. To experimentally validate these behaviors, the spin stand testing has been conducted in industrial labs of Western Digital.

Figure 5.1 shows the procedure to obtain the recording medium SNR via spin stand testing. To conduct an experimental comparative study, HAMR head gimbal assemblies (HGAs) and assorted HAMR media types were measured on a spin stand tester. After recording the 1T data pattern, the waveform was read back. The root-mean-square (RMS) signal at the recording frequency was taken as the signal power, while the other frequency components were regarded as noise after removing the higher-order harmonics of the signal. The logarithmic ratio of signal power S and noise power P, $10\log_{10}(S/P)$, gives SNR. It should be mentioned that the track width and head-media-spacing (HMS) were kept the same [146] by slightly tuning the laser power. The thermal gradient of various head / media combinations was also measured and found to be relatively constant. This suggests the thermal profiles are similar for all recording conditions.

In previous simulation results, the system SNR shows a strong correlation with the applied head field. At low fields, incomplete switching noise is dominant, since insufficient field is not able to fully maintain spin orientation during cooling. Consequently, a great amount of DC noise is induced. While at high fields, the predominant noise is erase-after-write. This occurs because the medium is exposed to the reversed head field for too long and the previously recorded bits are erased.

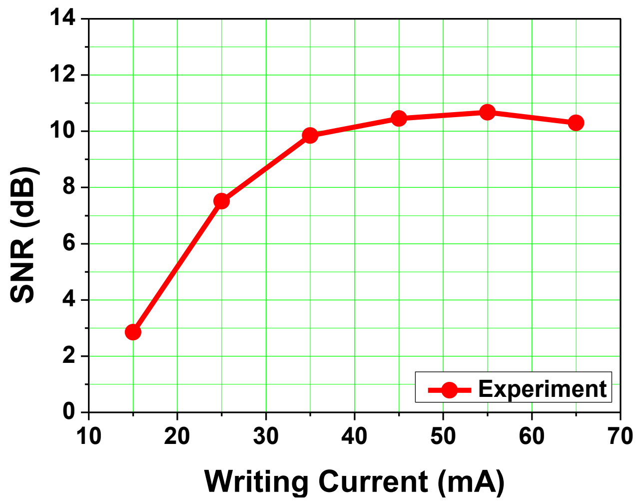

Figure 5.2 SNR versus writing current. At low current, media is poorly saturated. Beyond 55 mA, erasure starts to reduce SNR [147].

Figure 5.2 shows the SNR versus writing current. Similarly, we assume the head field is linearly proportional to the writing current [148]. The results indicate the SNR first quickly increases with writing current, and then saturates at around 55 mA. This is because incomplete switching noise is avoided with higher writing current and the media saturation is improved. When the current is further increased, the SNR starts to decrease gradually. In testing, although the writer current from the amplifier is maximized, the field generated is still insufficient [149], [85], to cause extreme erase-after-write. Additionally, other noise sources such as T_c variation, may make the curve flatter, as shown in modeling [150]. The curves observed for various heads and medium differ from each other somewhat, but the primary trends are similar.

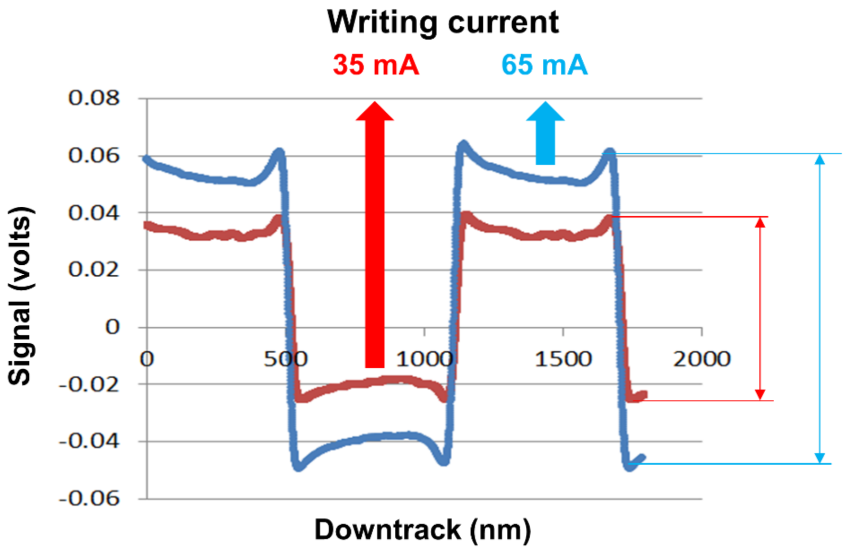

Figure 5.3 Read back signal level versus downtrack position using both low and high write currents for recording. The red trace was recorded at 35 mA while the blue trace was recorded at 65 mA.

To better observe the recording behavior in detail, waveforms written at low and high currents were captured as shown in Figure 5.3. The red trace here was recorded with lower current, 35 mA, while the blue trace was recorded with higher current, 65 mA. Both curves have similar shapes but the magnetization (signal) values are significantly different. It can be noticed that the zero-crossing of each curve is not located at 0 volts. This is because the reader has some nonlinear characteristics. As indicated by the arrows on the right high side, the range between the maximum and minimum level is defined as the saturation level. It is clearly shown that the case with higher writing current has a much higher saturation level. On the other hand, it should be mentioned that the concave shape of the signal is because the preamplifier used in measurements does not go to extremely low frequencies (DC). This ac-coupling results in a "boost" in the signal at the transition, followed by a rapid "droop" in the long-wavelength bit-cell, which makes the transition look high. Additionally, even with the concave shape of both curves, it can be noticed that the concave shape is asymmetrical, which is caused by the erase-after-write. And the erase-after-write for the higher write current is slightly more severe, while the concave shape for lower write current is relatively more symmetrical.

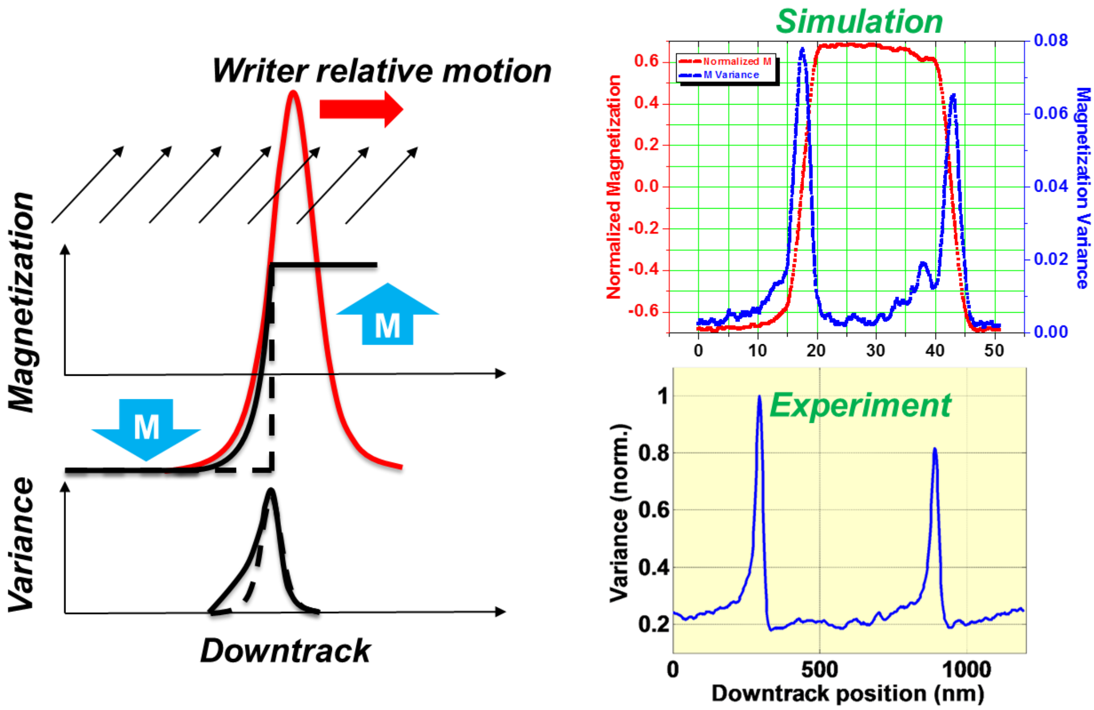

Figure 5.4 Schematic of the erase-after-write (left) and the signal variance from both micromagnetic simulation (top right) and spin stand testing (bottom right).

On the higher writing current side of Figure 5.2, erase-after-write is believed to be the dominant noise mechanism. As shown by the schematic on the left side in Figure 5.4, the writer is relatively moving towards the right direction. After completion of writing the first downwards bit, writer reverses the head field polarity and starts to record the second bit. However, at this moment the previous bit has not completely cooled down, and the reversed head field would partially erase the previous bit. To validate this prediction, in Figure 5.4, experimentally measured signal variance (bottom right) is plotted versus the down-track position in comparison with the simulation results (top right). In the simulation, the signal (red curve) has obvious degradation at the end of each bit, which is caused by erase-after-write. For the signal variance (blue curve), these two peaks sit at the transition positions and represent the transition jitter noise. Ideally, the transition jitter profiles should be symmetric, i.e. the variance peaks should be symmetric. However, here the front part of the variance peak expands and extends into the end of each bit, which suggests additional erasure induced noise component. In the experimental results, the signal variance shows a very similar behavior compared to the simulation. This is believed to be a clear footprint of the erase-after-write. As mentioned, the ac-coupling of the preamplifier makes the transition signal look relatively high and manifests less erasure effect. Instead, variance shows more clear erasure.

5.1.2 Velocity Effect

In the previous modeling, the system performance shows a strong correlation with recording time window (RTW). In the definition of RTW, tuning the disk rotational velocity can directly change the recording time window and consequently affect the system performance.

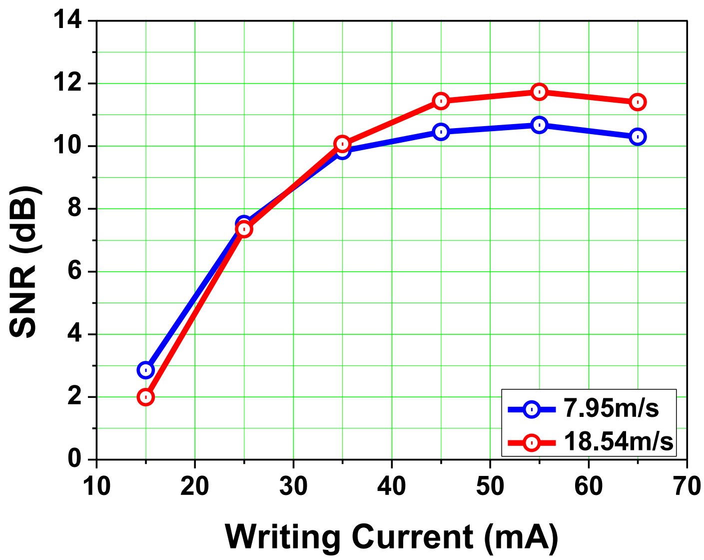

Figure 5.5 SNR versus write current at different head / media linear velocities, 7.95 m/s (blue) and 18.54 m/s(red), respectively.

Figure 5.5 shows the recording SNR versus write current at 7.95 m/s (blue) and 18.54 (red) linear velocity. 7.95 m/s and 18.54 m/s approximately correspond to 2700 rpm and 6500 rpm respectively for a 2-inch drive. Both curves shown here have similar write current dependence. The SNR first increases with write current, reaches an optimum and then gradually decreases at higher write current. At low write current, performance at lower velocity is better, while on the high write current side, the performance at high velocity is better. As pointed out before, the recording suffers from a limited recording time window so that the magnetization cannot be properly saturated and has primarily incomplete switching noise. Slower rotation of the disk gives a wider time window and relaxes the incomplete switching condition. On the high write current side, the recording is degraded due to the relatively long time window. Here higher velocity would effectively shrink the RTW and prevent the medium from being exposed to a reversed head field, giving higher SNR.

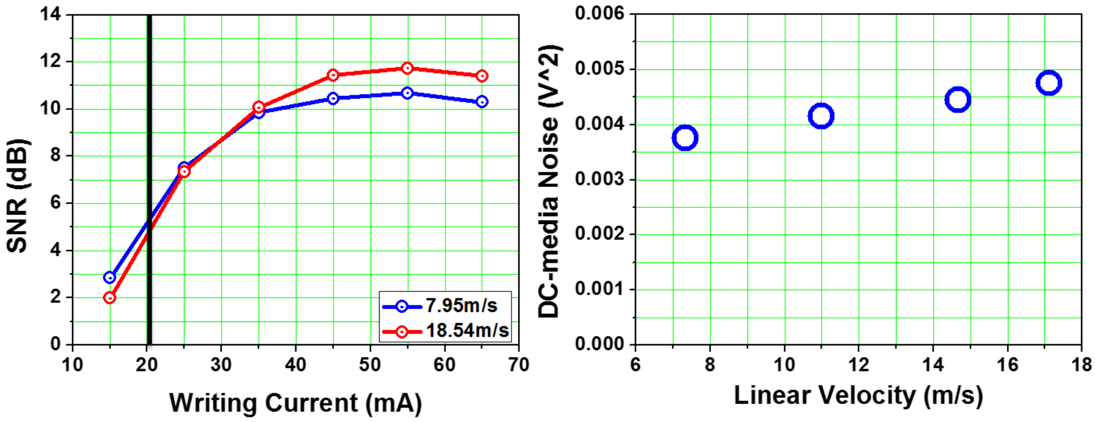

Figure 5.6 Recording SNR versus writing current and vertical line labels the 20 mA (left graph), where the DC noise is extracted for various disk velocities (right graph).

The components tested mainly show incomplete switching as the dominant noise mechanism. Here the write current is set to be 20 mA to measure recording characteristics at different velocities as shown in Figure 5.6. For this write current, the noise mainly manifests as the incomplete switching noise. This greatly affects the magnetization saturation level, which is proportional to the DC noise. Hence, in the right graph of Figure 5.6, the DC noise has been plotted as a function of the disk linear velocity. The results indicate that the DC noise increases with increasing velocity. This agrees with the left graph, since SNR is lower at higher linear velocities.

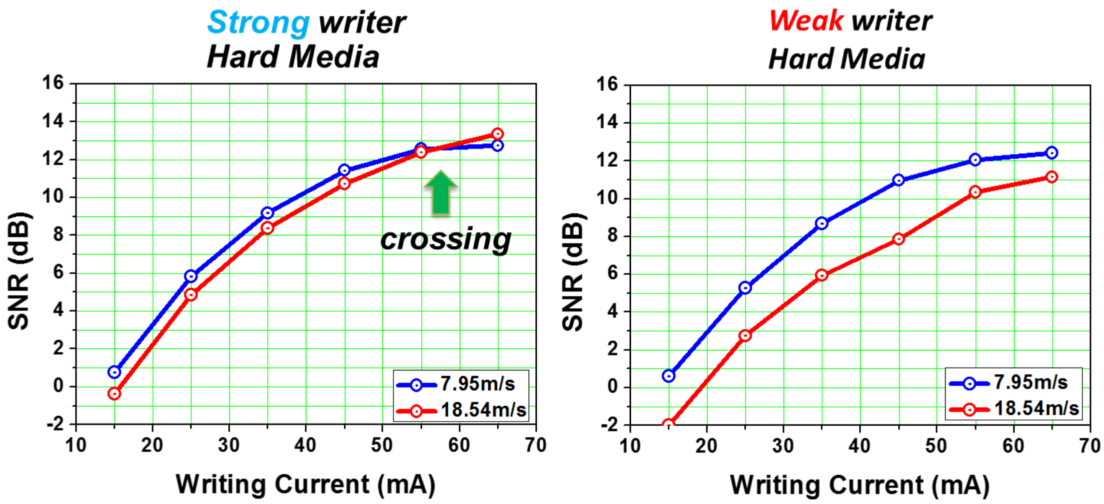

Figure 5.7 SNR versus write current at 7.95 m/s and 18.54 m/s linear velocities. The same hard media was used. The left graph used a strong writer while the right graph used a weaker writer.

Next, multiple recording components are tested and compared to understand optimization requirements. Figure 5.7 shows SNR of the same hard media using a strong writer and a weak writer. Here, hard media means the anisotropy field is relatively higher and the strong writer means the field generated is relatively higher. The results here show that the four curves all show similar trends and the incomplete switching noise dominates. It can be noted that the left graph with the strong writer has a crossing point between the curves with different velocities. The crossing point is close to the boundary between the incomplete switching dominant region and the erase-after-write dominant region. However, for the right graph, no crossing point is observed. Additionally, the spacing between the curves is larger in the right graph. These observations match up with the essence of different strengths of writers. With the same writing current, the field generated by the weaker writer is lower. Therefore, taking the left part of the left graph and scaling it laterally would lead to a graph similar to the right graph.

In Figure 5.8, the same strong writer has been employed while different recording medium are used. Similarly, the recording has been conducted at both 7.95 m/s and 18.54 m/s. The top graph is for hard media, while the bottom graph is for soft media. Here, soft media means the anisotropy field is relatively lower than that of the hard media. Again, the curves show similar trends. However, both graphs exhibit crossing points for curves measured at different velocities. For the right graph with soft media, the erase-after-write is more severe, so the crossing point is located at lower writing current. This is because the soft media has lower H_k and therefore smaller energy barriers to resist thermal erasure during the cooling process. Even relatively small magnetic field would lead to erase-after-write noise for this head / media combination.

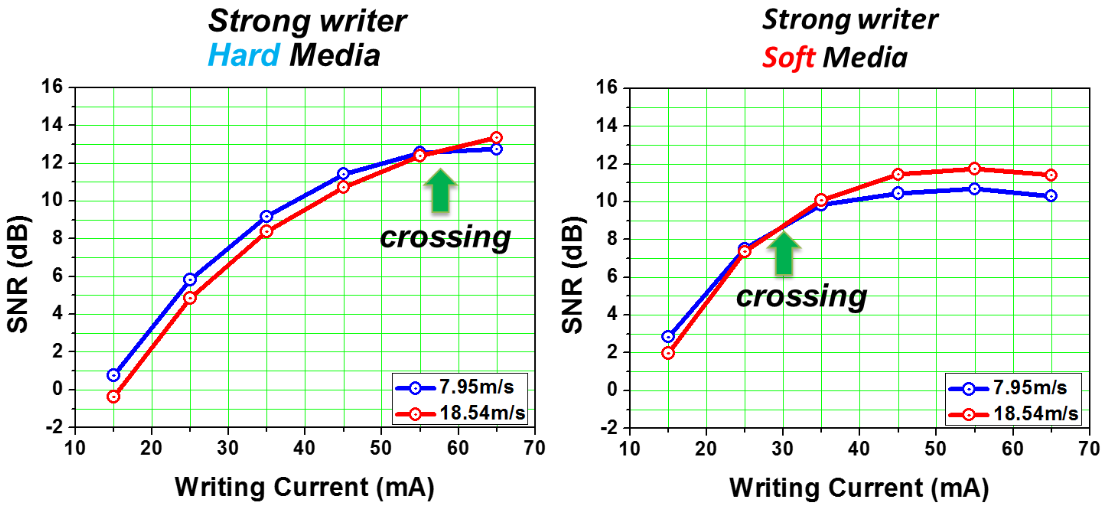

Figure 5.8 SNR versus write current at 7.95 m/s and 18.54 m/s. The same strong writer has been utilized. The left graph is for hard media while the right graph uses soft media.

5.1.3 Anisotropy Field H_k Effect

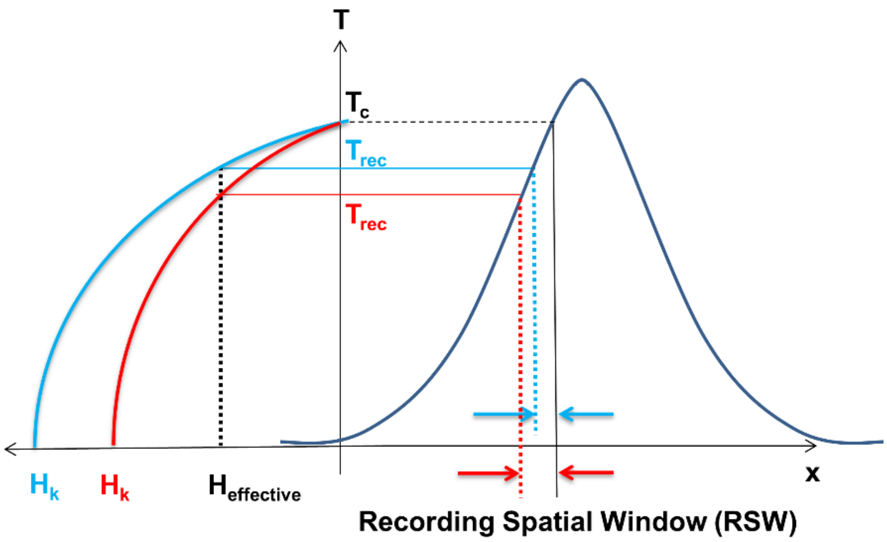

Figure 5.9 Schematic of the recording spatial window with soft media (lower H_k labeled by red color) and hard media (higher H_k labeled by blue color).

During the discussion of recording physics in chapter 3, the room temperature H_k

effect is described in 3.5. For review purpose, a schematic is shown in Figure 5.9 to illustrate the impact of media with low or high H_k value. The plot shows that with hard media of higher H_k value, the same effective head field would lead to higher recording temperature, which is closer to T_c. Projecting the T_{rec} and T_c onto the downtrack thermal profile would determine the downtrack coordinates, which define the recording spatial window (RSW) labeled by the arrows. The RTW for the hard media of higher H_k is correspondingly narrower and vice versa.

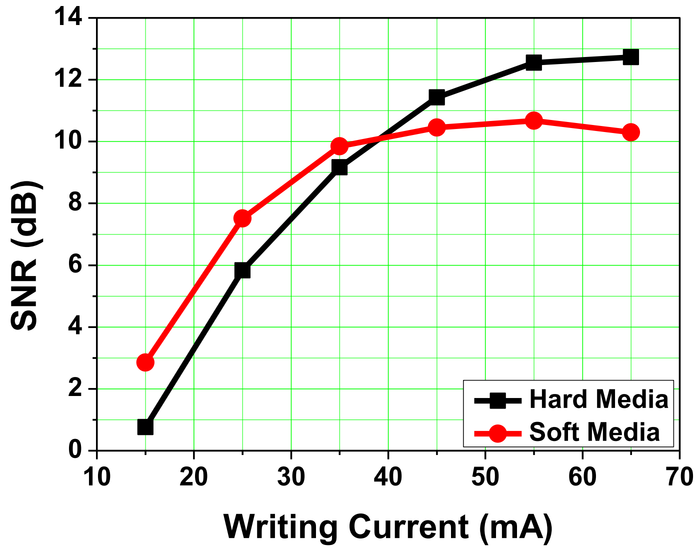

Figure 5.10 SNR versus write current for media with different anisotropy fields. The hard and soft media refer to high and low anisotropy field, respectively.

To better compare the hard and soft media types, the blue curves in Figure 5.8 are re-plotted in Figure 5.10. As is shown, on the lower write current side, the SNR is relatively higher for soft media. On the higher write current side, the SNR is relatively higher for hard media. This phenomenon can be explained in terms of the recording time window. As interpreted in the schematic of Figure 5.9, the hard media of higher H_k would have relatively shorter RSW and resulted recording time window (RTW). At the low write current side, the recording suffers from the incomplete switching caused by the limited RTW. Hard media would have more severe unsaturation due to its relatively shorter RTW. On the contrary, at the high write current side, the recording suffers from the erase-after-write caused by the redundant RTW. Hard media would have less noise since its relatively shorter RTW helps reduce the time that the media is exposed to erasure.

5.2 Industrial Head Field

In HAMR scheme, although the recording medium is heated over the Curie temperature during a recording process, adequate recording field amplitude is still required due to a relatively short time window for magnetization to reach saturation. Here a systematic micromagnetic analysis is described to depict recording performance for a generic industrial recording head design, in the absence of a medium soft under layer. The medium and recording condition are optimized under the insufficient head field resulted from this design [149].

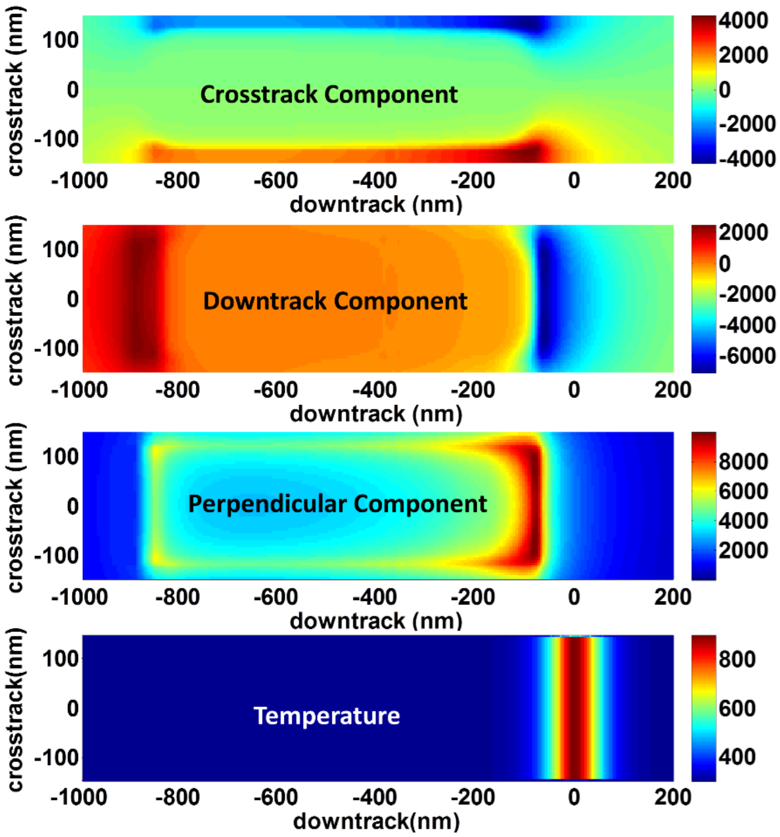

Figure 5.11 Crosstrack component, downtrack component, and perpendicular component of head field in a unit of Oe, along with the temperature profile in a unit of K.

In Figure 5.11, the crosstrack, downtrack, and perpendicular components of magnetic head field, respectively, are calculated by Finite-Element-Method (FEM) based on a generic design from Western Digital Corporation. Near where recording happens, the profile is quite uniform across the track. Therefore, a quasi-Gaussian thermal profile from COMSOL™ is also unified along the crosstrack direction, with peak temperature pinned at 900 K (fourth graph in Figure 5.11). The thermal gradient is around 9 K/nm if not mentioned. For all the simulations in this section, the medium is recorded at 1 MFCI and read at a width of six grains (approximately 42 nm).

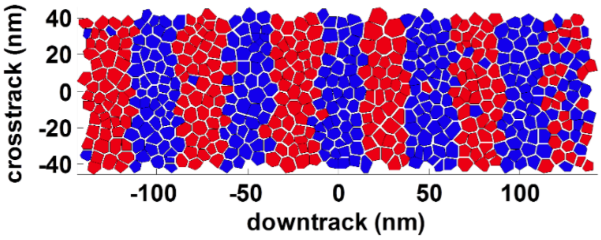

Figure 5.12 The magnetization pattern with default system design.

Using the specifications described above as the default settings, the recording simulation is conducted. The magnetization pattern is shown in Figure 5.12. Within the bits, the presence of a few un-switched grains can be noticed. To categorize the noise type, the dynamic recording process was captured. It is noticed that the noisy grains are formed during recording without after-write effect. Therefore, the noise seems very similar to incomplete switching noise.

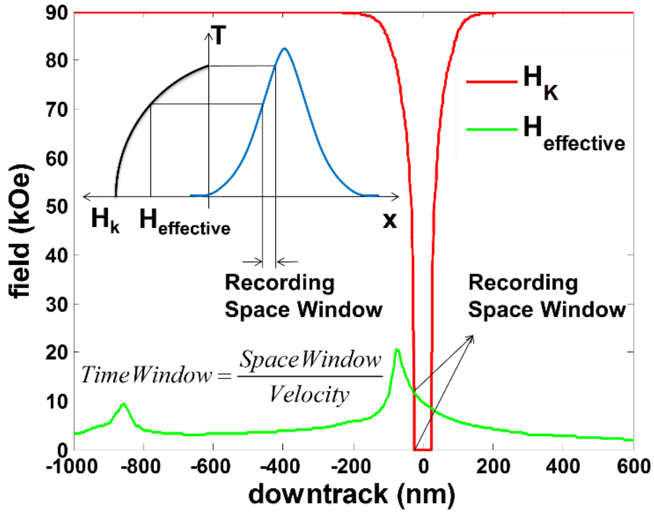

Figure 5.13 Definition of recording space window, RTW, and method to extract RTW from realistic field profiles.

Before further discussion, Figure 5.13 shows the method to extract the recording time window (RTW). Inset of Figure 5.13 is a schematic of recording space window (RSW). $H_{effective}$ is an effective field of head field, calculated by Stoner-Wohlfarth model.

With H_k vs. T curve, a temperature range can be determined. With a certain thermal profile, the temperature range leads to a spatial range, which is RSW. Dividing the RSW by velocity gives RTW. In the plot, the red and the green curves represent the H_k and $H_{effective}$ along downtrack, respectively. The downtrack positions of the two points labeled by the arrows thus define the RSW.

Now that the noise in this default design is caused by incomplete switching due to short RTW, in the following discussion, multiple aspects would be investigated to broaden RTW. Specifically, medium SNR is calculated versus space offset between NFT and writing pole / head field scale factor / disk rotational velocity / room temperature H_k / thermal gradient. Via the method above, the RTW of each data point is acquired. Hence, the medium SNR is plotted as a function of RTW for all the data points. The fitting curve of SNR vs. RTW with all data points is shown as the red curve in the insets.

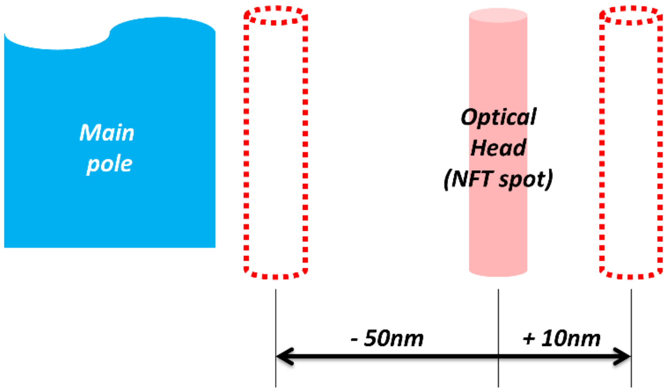

Figure 5.14 Schematic for -50 nm and +10 nm offset of the NFT position relative to writer main pole.

The magnetic field strength gradually decays as the evaluation point moves away from the writer main pole. Tuning the distance between the near-field transducer (NFT) and the writer main pole would also manipulate the magnetic head field strength. To illustrate this effect, the performance is calculated versus the NFT position offset. Figure 5.14 shows the schematic for the offset of NFT relative to writer main pole. -50 nm and +10 nm refer to closer or further to pole, respectively.

Figure 5.15 shows the medium SNR versus offset of distance between NFT and writing pole. With zero offset as default, the negative / positive offset means that NFT is closer to / further from writing pole, respectively. There is a drop in SNR when the offset changes from -50 nm to + 10 nm. This indicates that the head field would be stronger when the NFT gets closer to the writing pole. Hence, recording is enabled in a larger field range and RTW increases, which increases SNR. This is similar to the previous experimental observation in WD [85]. However, another potential issue is that the close spacing would degrade the thermal reliability of the system. The inset on the top right corner shows both the seven data points and the fitted curve mentioned above. When offset changes from -50 nm to +10 nm (from data #1 to data #7), RTW becomes smaller, which makes incomplete switching more severe.

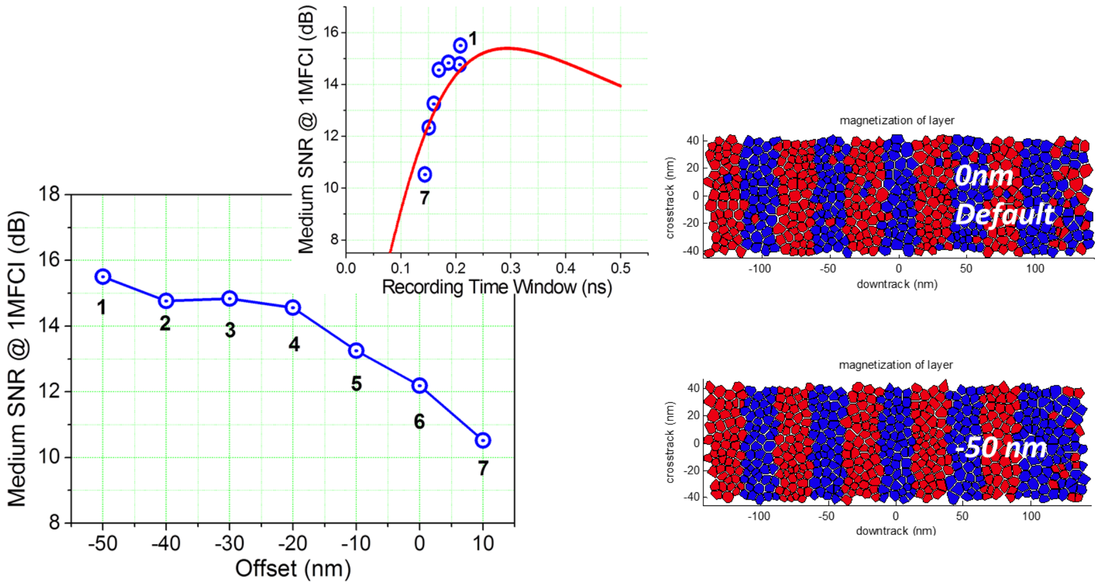

Figure 5.15 Medium SNR versus offset of spacing between NFT and writing pole. Top inset shows the same seven data points with fitted curve from all dataset. The magnetization patterns with default settings and -50 nm offset are shown on the right-hand side.

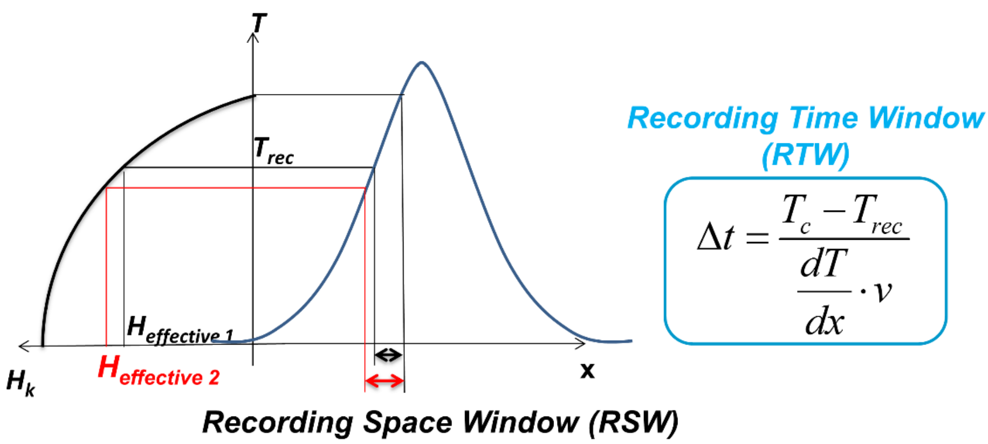

Figure 5.16 Schematic of the recording time window with different spacing between NFT and writer main pole. The red color refers to closer spacing, since it would provide higher head field.

Figure 5.16 shows the schematic of the recording time window with long (black) / short (red) distance between the NFT and the writer main pole. With closer distance, the head field felt by the medium would be consequently stronger. Therefore, the recording time window is further away from the T_c and the defined recording space window is wider. Now that the head field strength does affect the performance as expected, to manipulate the applied field magnitude as Figure 5.16, the head field could also be scaled up directly.

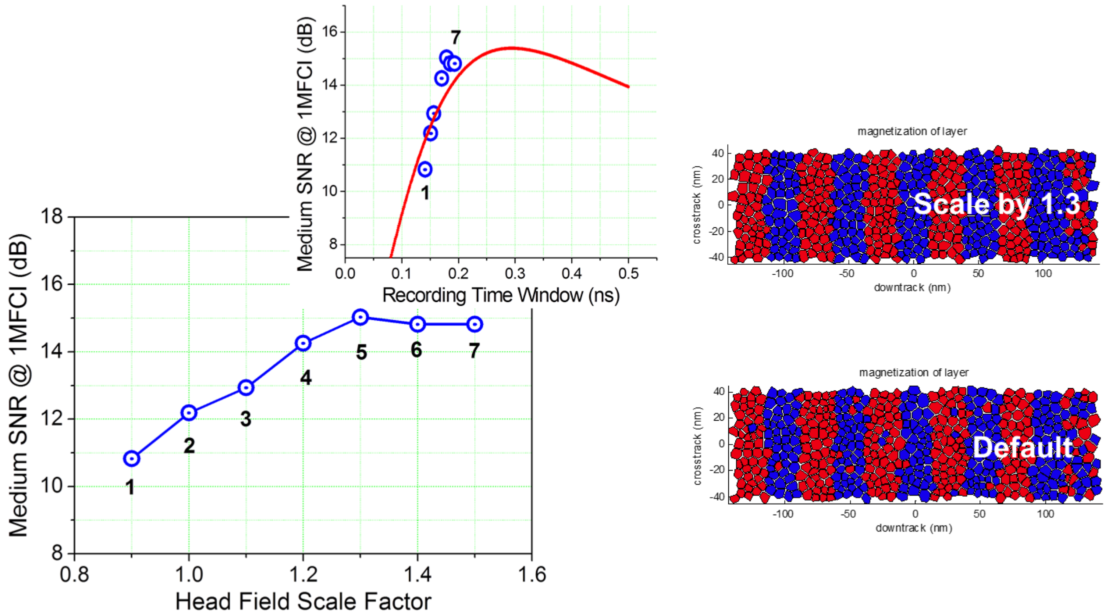

Figure 5.17 Medium SNR as a function of head field scale factor. Top inset shows the same seven data points with fitted curve from all dataset. The recording pattern with default setting and 1.3 scaling factor are shown on the right-hand side.

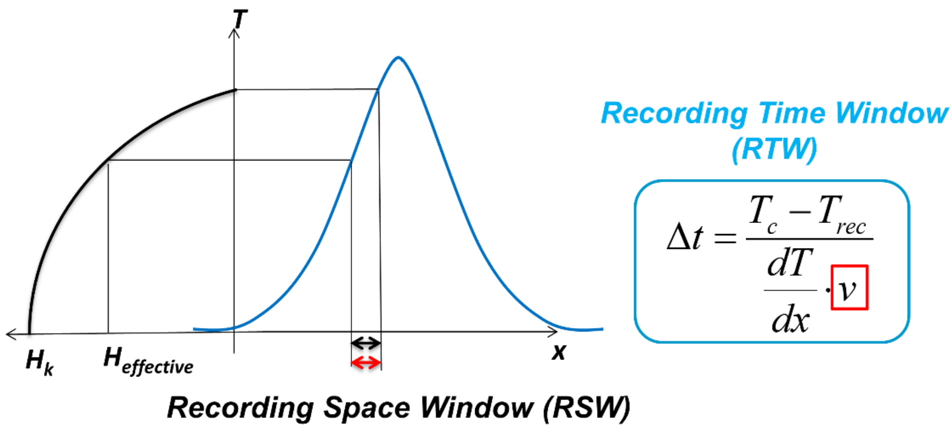

Figure 5.18 Schematic of the recording time window with different velocities.

Figure 5.17 shows the medium SNR versus head field scale factor ranging from 0.9 to 1.5. The SNR increases almost linearly until the scale factor reaches 1.3 and then saturates for higher scale factor. Similar to the situation where NFT is closer to writing pole, when head field is stronger, the recording process can happen at a larger field range and RTW would be larger as well. In the inset, when the scale factor changes from 0.9 to 1.5 (from data #1 to data #7), the RTW correspondingly increases and SNR climbs upward.

Another way to change the RTW is to change the disk rotational velocity. As shown in Figure 5.18, the recording space window is kept the same while the various velocity would help change RTW. Specifically, slower velocity would effectively widen the RTW so that the incomplete switching is relieved.

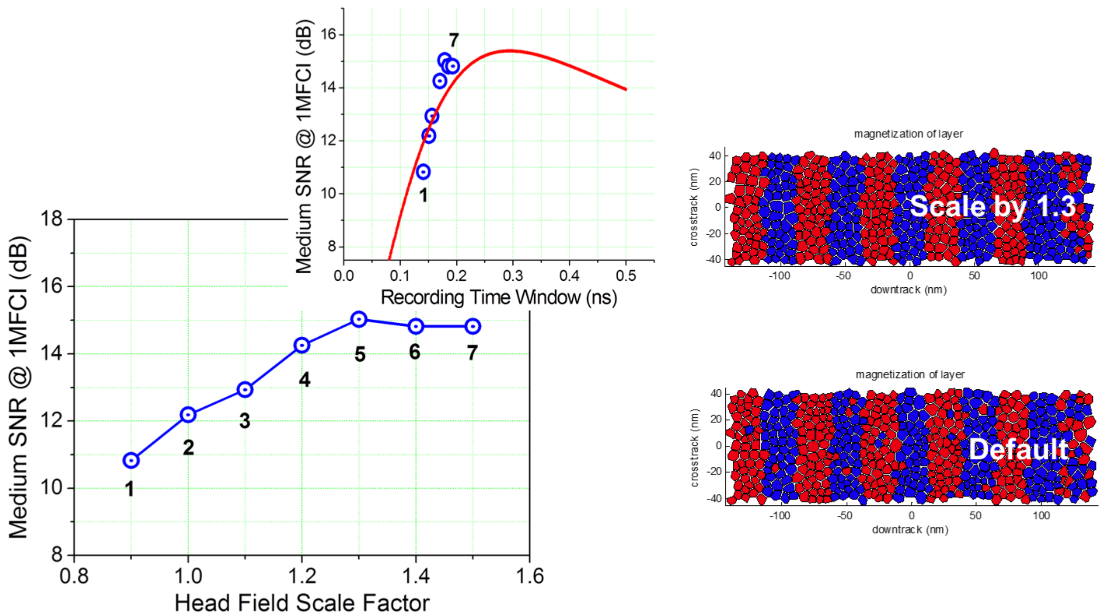

Figure 5.19 Medium SNR as a function of disk rotational velocity. Top right inset shows the same eight data points with fitted curve from all dataset.

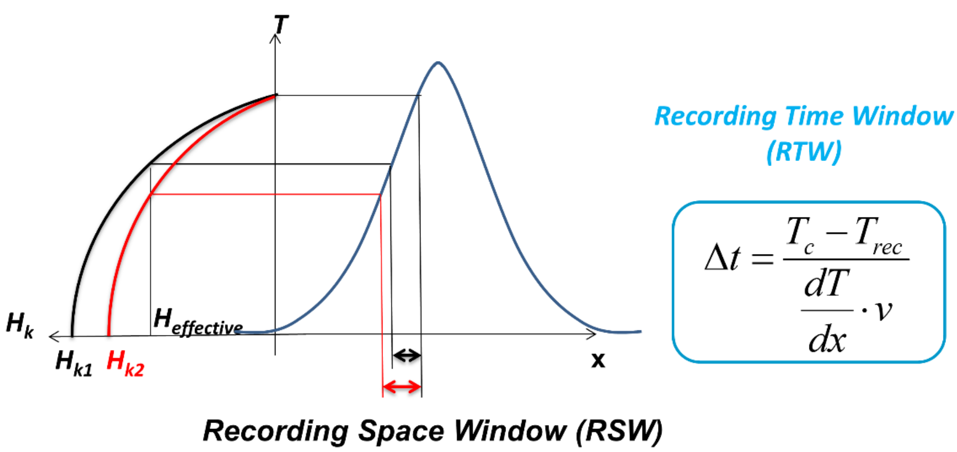

Figure 5.20 Schematic of the recording time window with different room temperature H_k values. The medium of lower H_k is labeled in red.

Figure 5.19 shows the medium SNR versus the disk rotational velocity, and the default velocity is 15 m/s, which is around 5600 RPM for a 2-inch disk. With velocity increasing from 5 m/s to 40 m/s (approximately from 1900 RPM to 15000 RPM), the SNR linearly decreases. This is because with the same RSW, faster velocity makes the RTW (RSW divided by velocity) narrower. Since the absence of SUL makes field insufficient, the RTW is already small. Higher velocity further decreases the RTW and the grains have even less time to be magnetized. In the inset, when velocity is tuned from 5 m/s to 40 m/s (from data #1 to data #8), the RTW approaches closer to zero and the SNR drops simultaneously.

It is shown that the field dependence of system performance is also greatly affected by the medium room temperature H_k, as shown in Figure 5.20. When the medium has relatively lower H_k, the same effective head field would give lower recording temperature. Consequently, the temperature range between the T_{rec} and the T_c would be broader, which also makes the RTW longer.

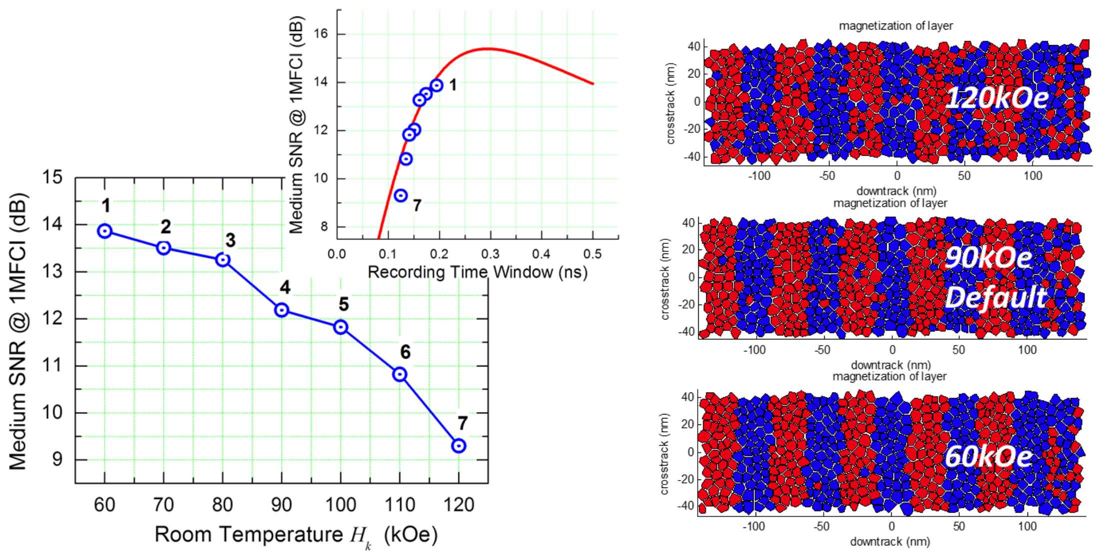

Figure 5.21 Medium SNR as a function of room temperature H_k. Top inset shows the same seven data points with fitted curve from all dataset. The recording patterns with 120 kOe, default settings, and 60 kOe are shown on the right-hand side.

Figure 5.21 shows the medium SNR versus room temperature H_k. With H_k increasing from 60 kOe to 120 kOe, the medium SNR monotonically decreases. Compared to default 90 kOe H_k, higher H_k means the same head field is only able to record when temperature is really close to T_c. Hence, the RTW would be even smaller, which aggravates incomplete switching. On the contrary, lower H_k provides wider RTW and more grains would be magnetized completely. Therefore, adequate H_k is important in this head design, since too high H_k narrows RTW and makes incomplete switching worse. In the inset, when H_k rises from 60 kOe to 120 kOe (from data #1 to data #7), RTW reduces and SNR becomes lower.

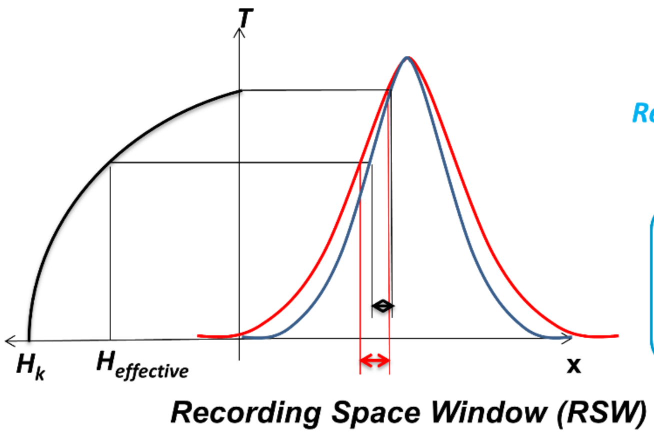

Figure 5.22 Schematic of the recording time window with different thermal gradient values. The lower thermal gradient case is labeled with red color.

Additionally, as shown in the schematic of the different thermal gradients in Figure 5.22, with shallower thermal gradient, the same temperature range between T_{rec} and T_c would give wider space range along downtrack. Therefore, lowering thermal gradient would effectively broaden the RTW.

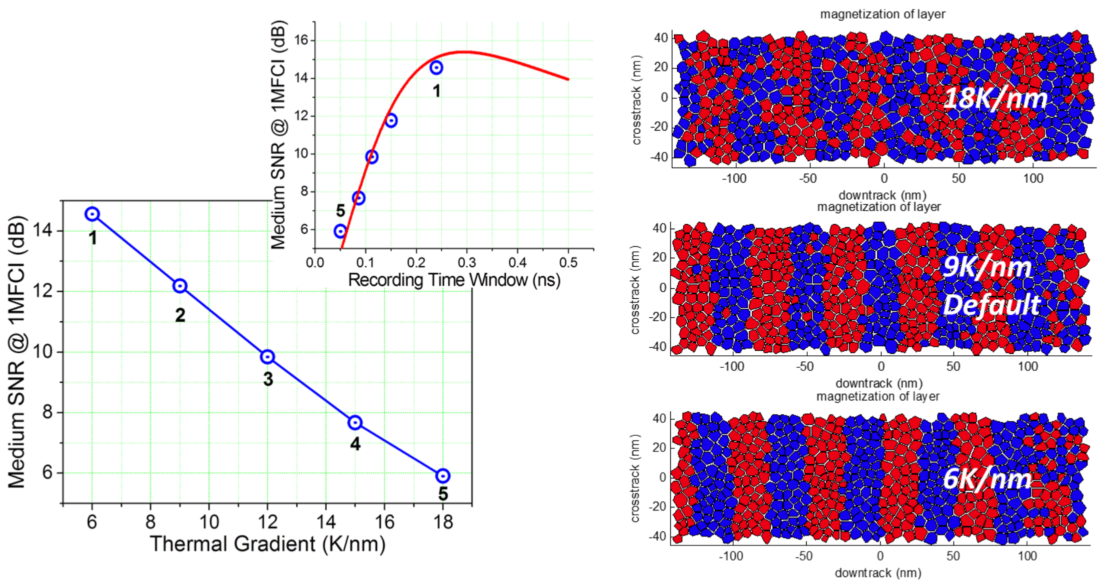

Figure 5.23 Medium SNR as a function of thermal gradient. Top right inset shows the same five data points with fitted curve from all dataset.

Figure 5.23 shows the medium SNR versus the thermal gradient (TG). The SNR drops linearly when the TG changes from 6 K/nm to 18 K/nm. This is because with higher TG, the medium H_k would recover more quickly during cooling and makes the RTW shorter. Compared with default 9 K/nm TG, 6 K/nm would help improve the SNR, since broader RTW is provided. It should be noted that for this design, due to the insufficient head field, the lower TG helps broaden the narrow RTW. But if sufficient head field is provided, the higher TG still leads to better performance [104]. In the inset, when the TG changes from 6 to 18 K/nm (from data #1 to data #5), the RTW drops, resulting in a decrease in SNR.

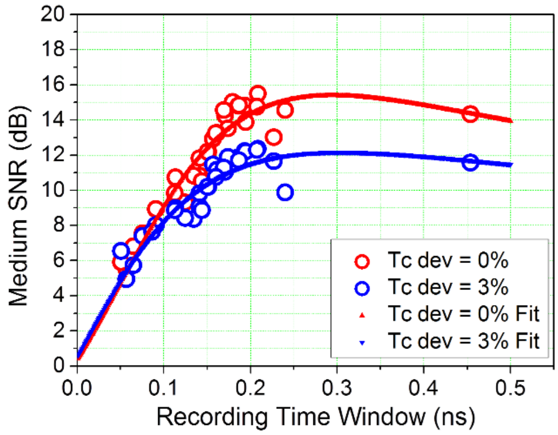

Figure 5.24 Medium SNR as a function of recording time window with or without 3% T_c variation.

As pointed out by previous discussion, the T_c distribution is potentially a critical noise source for ultra-high density recording. Figure 5.24 shows the medium SNR as a function of the RTW with and without 3% T_c variation. The hollow circles are the simulation data points, while the solid lines show the results from fitting. These data points are the same ones shown in the previous figures in this section. The results here show that the SNR first increases with the RTW, peaks at a certain RTW and then gradually decreases with an increasing RTW. The increase of the SNR is due to the alleviation of incomplete switching, while the decrease of the SNR is due to the aggravation of erase-after-write. The combinational effect of both leads to the peak of the SNR. Meanwhile, it could be noticed that the data points mainly concentrate near low RTW side, which suggests insufficient field is the primary issue for this specific design without SUL. The results also indicate that at the low RTW side, T_c variation makes a small difference of SNR. But when the SNR saturates, even 3% T_c variation causes nearly 3 dB SNR reduction. Recent measurement [130], [131] indicates 4% T_c variation in current medium. Additionally, when the T_c variation comes into the picture, the field dependence of the recording quality is likely to be weakened. It should be mentioned that the red fitting curve here is the same one in all the previous insets in this section.

5.3 Medium Properties

In previous discussion of both the recording physics and the noise origins, it has been seen that the medium properties have a significant impact. In this section, the experimental methodology to measure T_c distribution as well as H_k temperature dependence will be introduced.

5.3.1 Experiment Setup

To realize relevant measurement, Zhengkun Dai in our group, spent great efforts to set up the pump-probe platform to characterize the prototype HAMR medium. Corresponding micromagnetic simulations are also conducted to provide understanding and insight in accompany with experiments [132].

The pump-probe technique has been utilized to extract standard deviation of T_c from the switching probability versus medium temperature [130]. Here a similar technique is applied with an addition of scanning the applied external field $H_{external}$, so that $H_k(T)$ near T_c could be measured. In the pump-probe method, the medium temperature increase above room temperature is proportional to laser pulse energy [130]. In the experiment, the full width at half maximum (FWHM) of pump pulse is 12 ns. Hence, short dwell time at high temperature assures that the spins are switched by magnetic field $H_{external}$ rather than by thermal decay. Additional continuous He-Ne laser is used to detect the switching probability (normalized by saturation magnetization level) by polar magneto-optic Kerr effect (MOKE). The media is heated up by pump pulse and then cooled down to room temperature. The $H_{external}$ is always on during this process.

This process is repeated with different pump pulse energy (different medium temperatures), so that the switching probability versus the switching temperature T_s is obtained. Assuming the switching temperature distribution is Gaussian, by fitting, the corresponding standard deviation of switching temperature, σ_{T_s} is obtained along with the average switching temperature $<T_s>$, which corresponds to 50% switching probability. When $H_{external}$ is zero, $<T_s>$ equals to average T_c of all grains and σ_{T_s} equals to σ_{T_c}. When the $H_{external}$ is nonzero, the measured $<T_s>$ is the temperature corresponding to this specific H_k value. After repetition of this nonzero $H_{exeternal}$ measurement, the H_k versus T curve could be obtained.

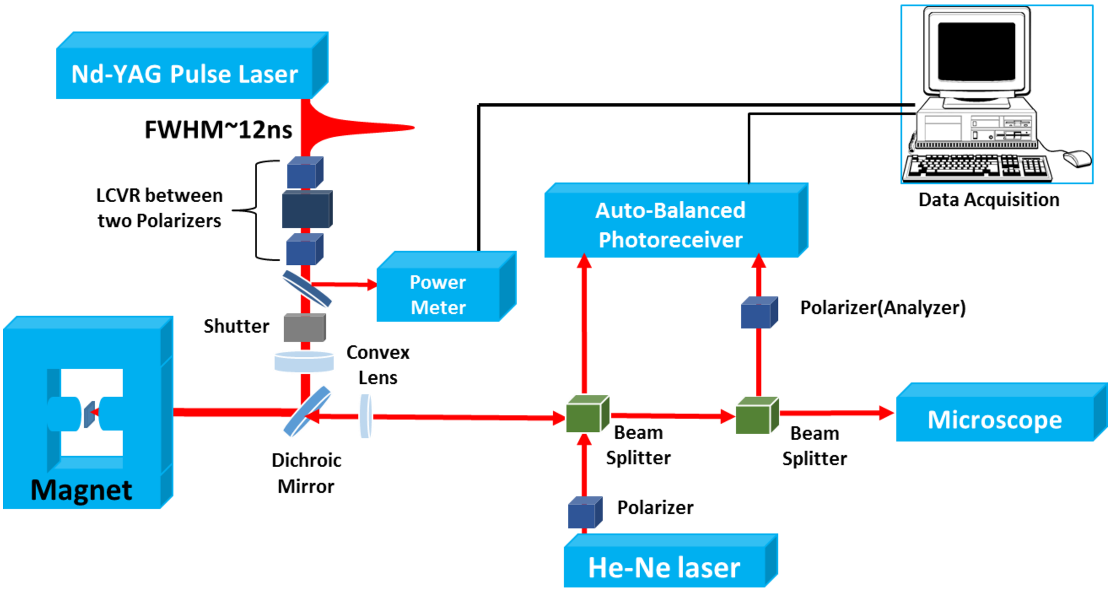

Figure 5.25 Optical diagram of the experiment setup (Courtesy of Zhengkun Dai).

As shown in the Figure 5.25, a 1064 nm wavelength Q-switched pulsed Nd-YAG laser from Spectra Physics is used. The FWHM and repetition rate are set to be 12 ns and 10 Hz, respectively. To maintain the pulse energy stability, the laser is operated at maximum output power with a free-running pulse train. The variable pulse energy control is achieved by placing a liquid crystal variable retarder (LCVR) between two polarizers. The pulse energy is monitored by a power meter after sampling the pulse train by a 50:50 beam splitter. The pulse energy can be varied from 50 μJ to 300 μJ, the standard deviation of measured pulse energy is less than 1 μJ. Single pulse is selected by a fast shutter synchronized to the Q-switch trigger of Nd-YAG laser. Neutral density filter is inserted to further attenuate the pulse energy by 90%. An auto-balanced detection scheme is used in probe laser line to reduce laser intensity noise [151]. Pump beam and probe beam are separately focused by two convex lenses and combined by a dichromic mirror, which allows easy adjustment of spot size ratio. A white light is also introduced into the optical path to check the beam alignment by microscope. According to the measurement with laser beam profilometer, the diameter of the probe laser spot is around 55 μm ($1/e^2$ diameter). The diameter of the pump laser spot is estimated from the damage pattern on thin film via microscope observation. The spot size ratio of the pump / probe laser is adjusted to be above 10:1, which assures the heating is uniform.

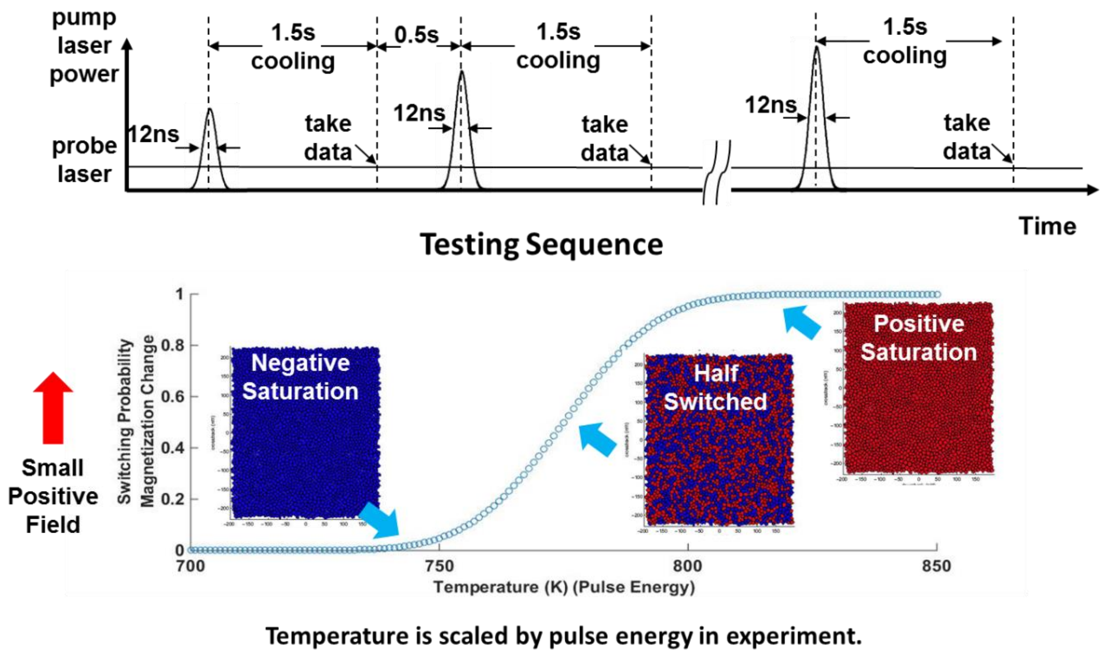

Figure 5.26 Heating and measurement procedure. The FWHM of pump laser is 12 ns. The top and bottom graphs are the testing sequence and the corresponding simulated sample patterns, respectively. The period of pulses is 2 s and the measurement is taken 1.5 s later than heating saturates. (Courtesy of Zhengkun Dai.)

Figure 5.26 shows the typical testing sequence (upper) and the switching procedure (lower) of the samples along with the simulated magnetization state. As is shown, the pump pulse width is 12 ns with a period of 2 s. At 1.5 s after each pulse, the magnetization level is measured. As the pulse power linearly increases with each pulse, the magnetic grains (initially saturated downward) would gradually switch and eventually be saturated upward. During heating, the sample temperature is proportional to the heating laser power. Therefore, the switching magnetization level change (equals to switching probability after normalization with saturation level) can be plotted versus heating temperature as shown in the lower graph. At the beginning, the sample is saturated downward with all negative magnetization. As temperature increases, magnetization gradually increases. At the middle point, the sample is half positively (red) and half negatively (blue) magnetized as the middle pattern. When temperature is sufficiently high, the sample is completely positively magnetized.

5.3.2 T_c Variation

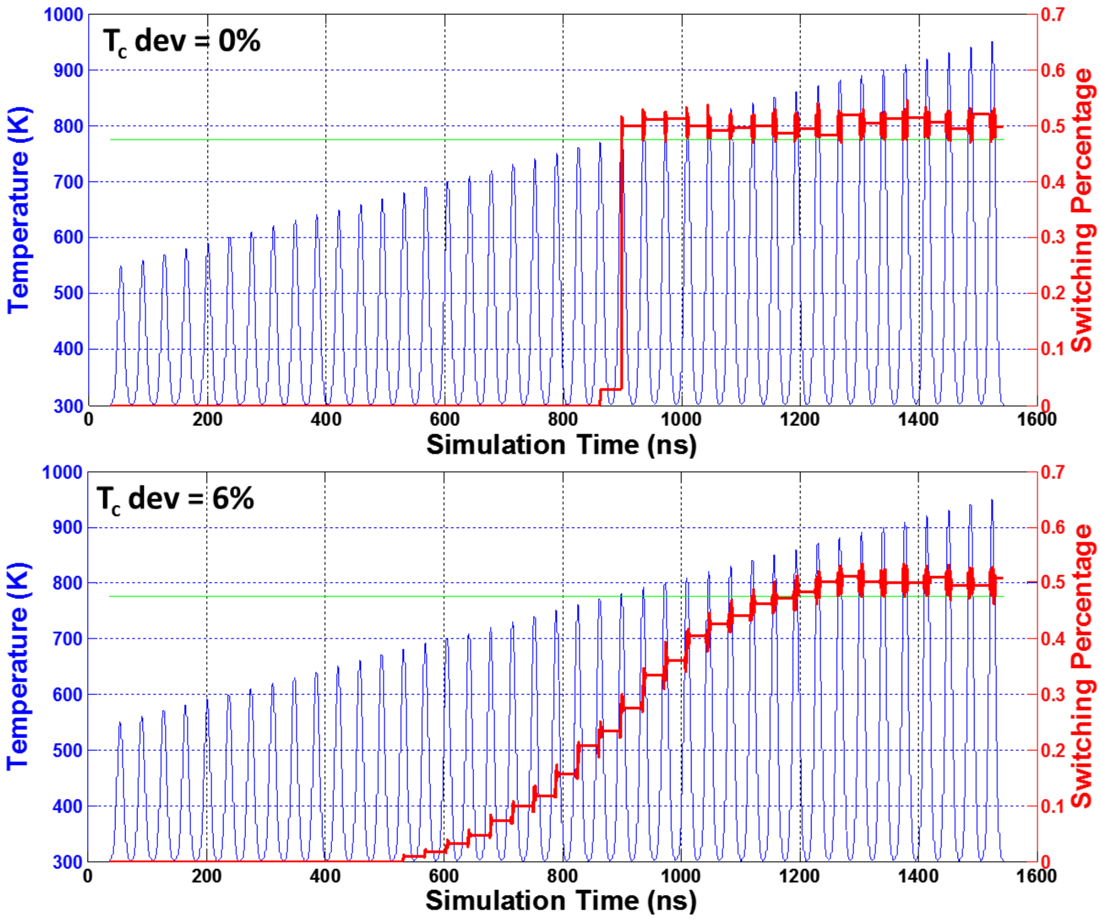

Figure 5.27 Simulated temperature (blue) and switching percentage (magnetization change normalized by saturation level, red) versus simulation time with 0% (upper) or 6% T_c (lower) variation. The FWHM of consequent pulses is 12.5 ns. Due to real time to simulate is relatively long, the period of pulses are shrunk, which should not change the results. The green horizontal line is the Curie temperature of 775 K.

To validate this methodology, thermal coupled micromagnetic simulation is conducted with the same specification. Figure 5.27 shows the sample temperature (blue) and switching percentage (magnetization change normalized by saturation level, red) as a function of the simulation time with 0% (upper) or 6% T_c (lower) variation. For guidance, the Curie temperature of 775 K is plotted with a green horizontal line. As is shown, the temperature is gradually increasing for consequent pulses and the switching percentage curve is of "S" shape. The switching percentage saturates at 0.5, since when at high temperature, the sample is thermally randomized with grains magnetized half down and half up. For both cases, when switching percentage is 0.25, the corresponding pulse peak temperature is around 775 K, which is the mean Curie temperature. For the case without the T_c variation, the switching curve is like a step function, which suggests at the moment when temperature reaches T_c, all the grains would switch. While for the case with 6% T_c variation, the switching curve is obviously laterally stretched. This suggests some grains switch at temperatures lower than T_c, while some grains would switch until temperatures are far beyond T_c.

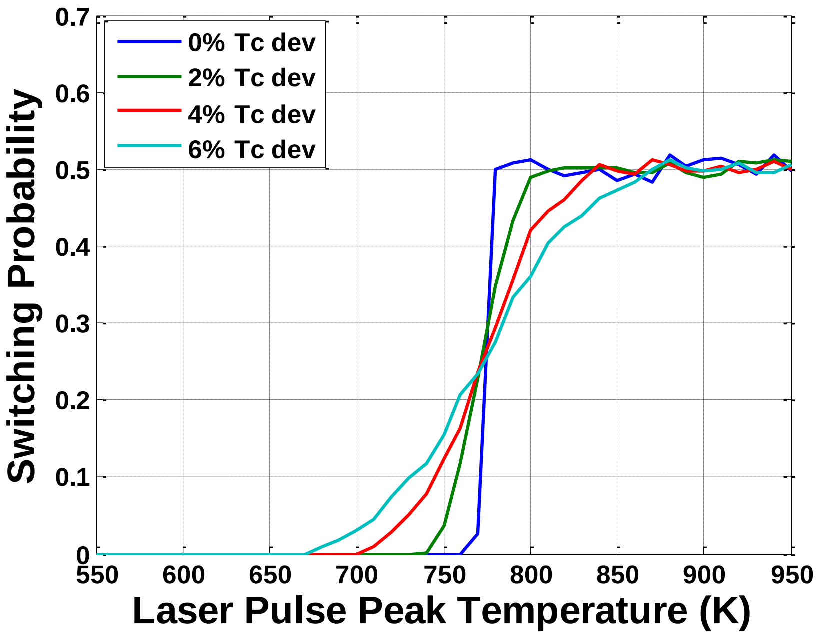

Figure 5.28 Simulated switching probability versus pulse peak temperature for recent FePt industrial medium samples with various T_c distributions.

By taking the switching percentage and the corresponding pulse peak temperature, the data points are replotted into Figure 5.28 illustrating cases with different T_c variations. The results clearly show that with the wider T_c distribution, the switching curve is more stretched, which suggests a one-to-one relation between the switching curve and the T_c distribution.

Assuming the T_c distribution is Gaussian, the switching curves in 5.28 would be the cumulative density function of the distribution. Therefore, differentiation of these curves would generate the probability density function as the histogram in Figure 5.29. Fitting a Gaussian function to it would generate the mean value and the standard deviation of the switching temperature. As mentioned before, when the $H_{external}$ is zero, the resulted average switching temperature is the mean T_c and the standard deviation of the switching temperature distribution is the T_c standard deviation. As labeled at the top of each graph in Figure 5.29, the measured T_c values and corresponding standard deviations match up with the settings. These results indicate that the model is consistent and this methodology described above is validated.

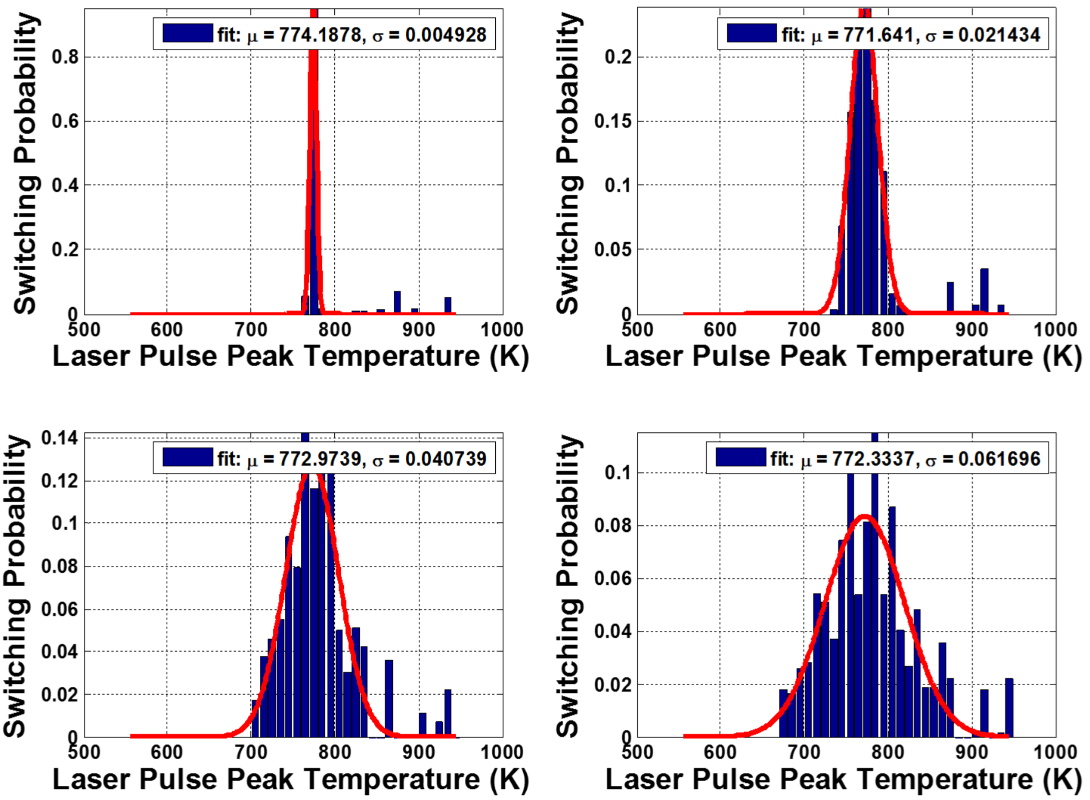

Figure 5.29 Simulated histogram and Gaussian fitting (mean value and standard deviation are labeled at the top of each graph) for samples with various T_c distributions.

With the experiment platform built up and the methodology described, the measurement is conducted with recent recording medium samples from two different companies. The experimental observations and their fitting analyses are shown together in Figure 5.30. The experimental data points are shown with the scatter symbols. By fitting with Gaussian cumulative density function, the solid curves are obtained, which show similar "S" shape as previous simulation results. Then both solid curves are differentiated with respect to the pulse energy. Hence, the probability density function could be obtained. Since the pulse energy is linearly proportional to the sample temperature, the parameters of the energy distribution could be converted with the formulas shown in the figure. The results indicate that these two measured samples have 5.2% and 9.6% T_c standard deviation, respectively. Compared to the recent work [131] to measure T_c distribution, the value here is slightly larger. The potential reasons may be because the heating is not completely uniform (which could be noticed by checking with profilometer) or the medium are not the latest ones.

$$\sigma_E \ to\ \sigma_{T_c} \ Conversion: \frac{\sigma_{T_c}}{\overline{T_c}} = \sigma_E \frac{\overline{T_c} - T_{Room}}{\overline{T_c}}$$

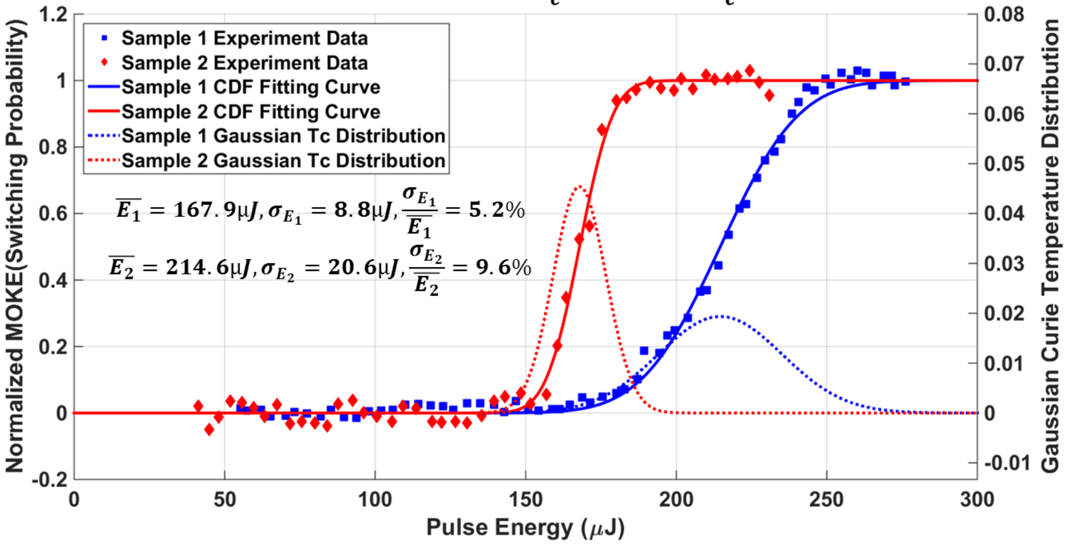

Figure 5.30 Experimental normalized MOKE (switching probability) and Curie temperature distribution of recent recording medium samples from two different companies.

5.3.3 H_k vs. T

In the previous discussion of this section, the $H_{external}$ has been excluded. As shown in Figure 5.31, when the $H_{external}$ is nonzero, the switching curve could be shifted. Similarly, the micromagnetic simulation is conducted to quantitatively analyze this process. The results here show that when the $H_{external}$ = 0 kOe, the switching happens at the moment when the pulse temperature is Curie temperature. While when the $H_{external}$

is nonzero, the red switching curve significantly shifts towards the left side, where the pulse peak temperature is much lower. Therefore, with nonzero external field, the switching could happen at a lower temperature. Assuming the effective field of the $H_{external}$ gives the H_k, the H_k versus T curve could be reconstructed via repetition of this procedure. It should also be noted that with zero $H_{external}$, the saturation is 0.5 due to thermal randomization. But when the $H_{external}$ is nonzero, the saturation would be 1 since the field would help guide and maintain the spin orientation during cooling.

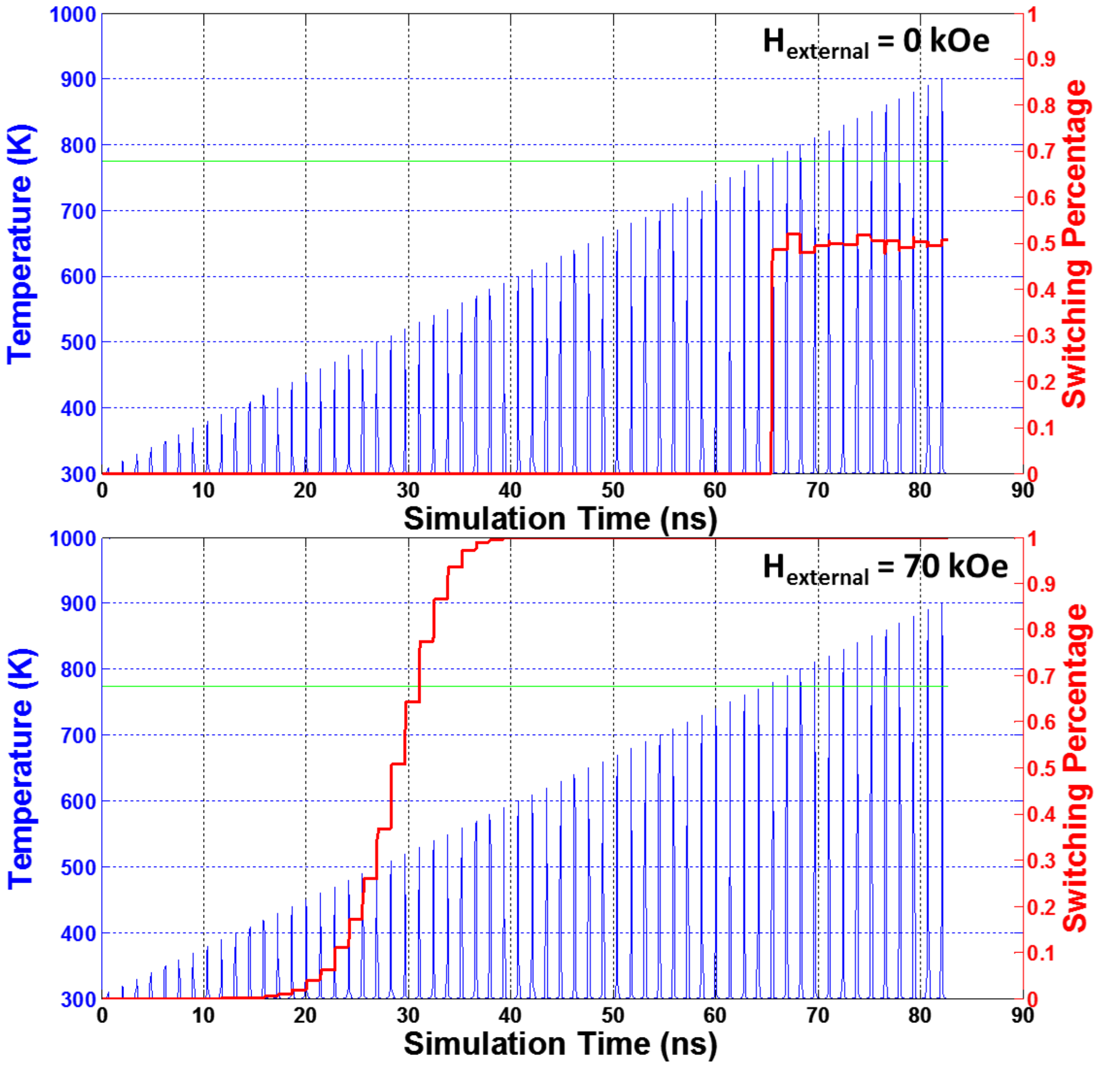

Figure 5.31 Simulated sample temperature and switching percentage as a function of the simulation time with 0 or 70 kOe external upward field. For both cases, 0% T_c variation is assumed. To avoid thermal decay, the FWHM of pulse is set to be extremely short. The green line is the Curie temperature.

To validate this, micromagnetic simulation with the process above with different $H_{external}$, is conducted and the obtained results are shown in Figure 5.32. Both the pre-settings (smooth curves) and the simulated results (curves with symbols) are shown together for the purpose of comparison. Meanwhile, the cases with n = 2.0 and n = 3.0 are both considered, where larger index n makes the H_k vs. T curve shallower with lower dH_k/dT near T_c. The results show that the general trend of curves is properly described by the simulation with some deviations. The match is close, especially when the temperature is relatively closer to T_c, while the deviation is more severe when the temperature is further away from T_c. This may be because with an extremely high field, the simulation becomes unstable even with slight thermal agitation. Moreover, shorter pulse width would help enhance the measurement accuracy of for this technique.

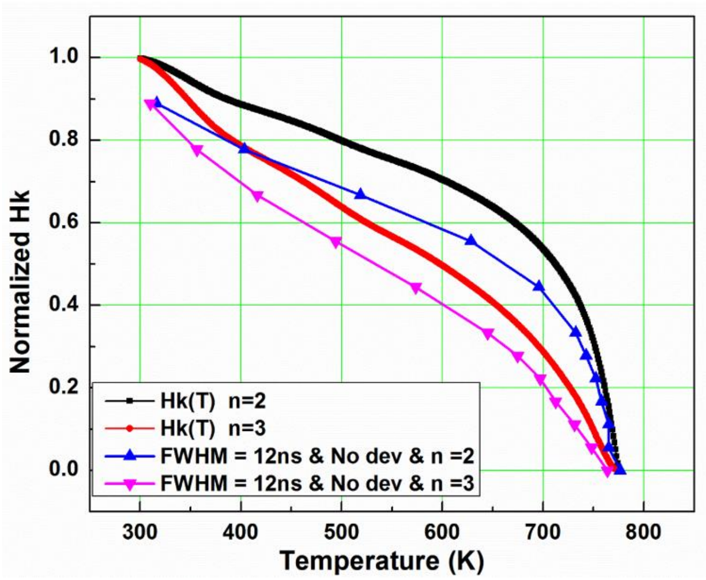

Figure 5.32 H_k vs. T curve in the pre-setting and the obtained data via the process described with various $H_{external}$ for n = 2.0 and n = 3.0 cases. The smooth solid lines are the pre-settings, while the curves with symbols are the calculated results. Meanwhile, case with larger index n is shallower with smaller dH_k/dT.

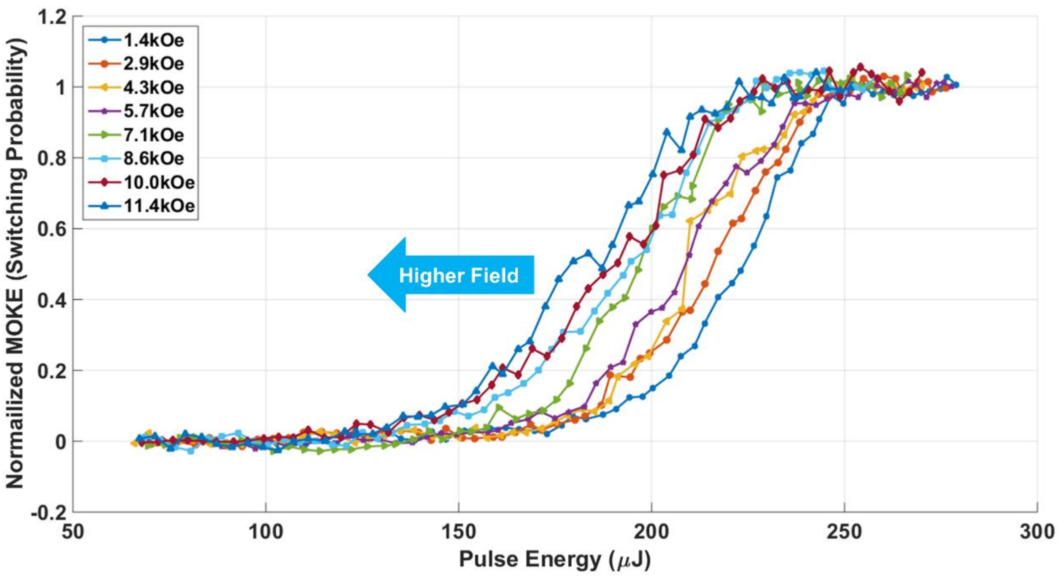

Figure 5.33 Experimental switching probability versus pulse energy under various external magnetic field.

After the validation of the methodology via micromagnetic simulation, the experimental measurement is conducted and the obtained results are shown in Figure 5.33. As shown, the curves with various $H_{external}$ all show "S" shape, where the switching is gradually more and more complete as the pulse energy increases. Meanwhile, when the $H_{external}$ is higher, the switching shifts to lower pulse energy value.

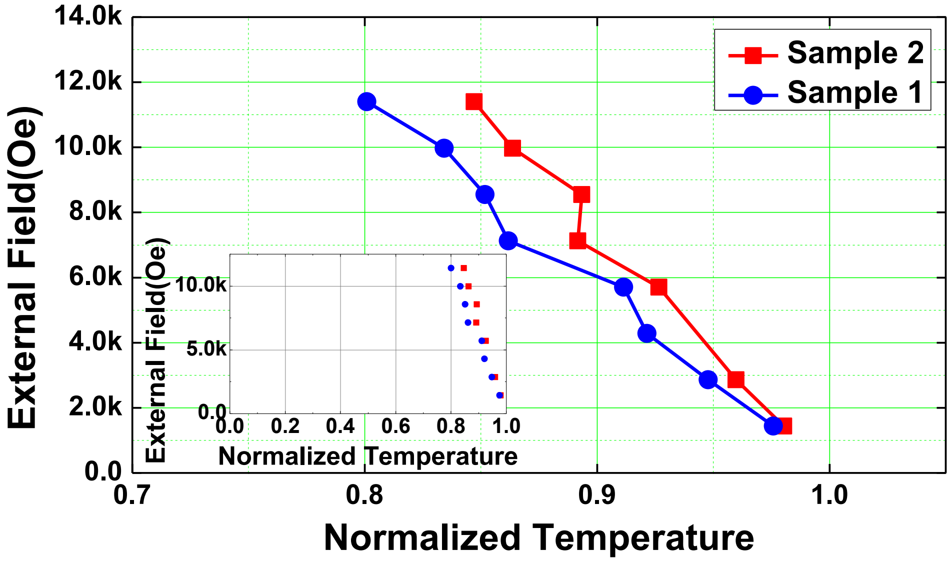

Figure 5.34 Experimental H_k versus T curve for two measured recording medium samples.

Replotting all the $H_{external}$ and corresponding switching temperature (normalized and scaled from pulse energy) would lead to the H_k vs. T curve as shown in Figure 5.34. As shown, with temperature decreasing, the H_k gradually starts to recover. Assuming a T_c of 775 K, the measurement gives around 200 - 300 Oe/K dH_k/dT, which is closer to the n = 3.0 case for H_k vs. T curve.

5.4 Transition Curvature

In the HAMR scheme, the thermal profile in recording medium, generated by plasmonically excited near field transducer (NFT), is often rounded in the medium plane [84], [96]. Such rounded thermal profiles with present writer head designs always create transitions with significant curvature [22], [23], [40], [152]. Transition curvature, resulted from a curved thermal profile in the medium, presents a severe limitation of achievable area density capability. In this section, the impact of curved transitions yielded by circular thermal profile is presented. Based on this understanding, a solution that rectifies the transition curvature and creates straightened transition front has been proposed. The analysis shows that recording with the solution that yields straightened transitions could result in a linear density increasing by 50%, while maintaining the same signal-to-noise ratio.

5.4.1 Curvature Impact

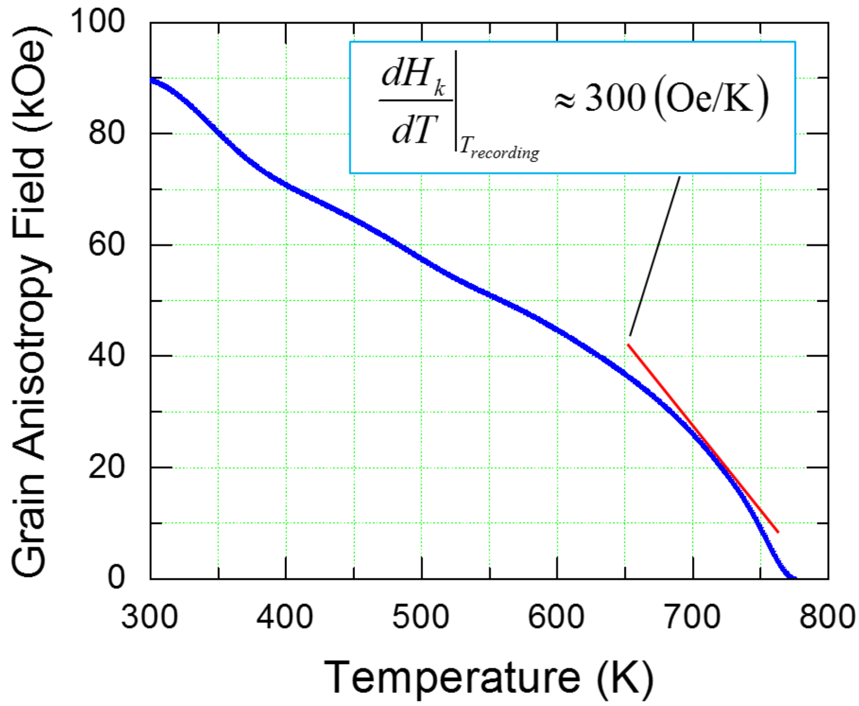

Figure 5.35 Anisotropy field H_k versus temperature T curve, where the dH_k/dT near T_c is around 300 Oe/K. This is for medium [86] **scaled with index n = 3.0.**

In this section, the medium has a mean room-temperature perpendicular anisotropy field of $H_k(RT)$ = 90 kOe and a mean saturation magnetization M_s = 900 emu/cc. The mean Curie temperature is 775 K. The complete temperature dependence of the grain anisotropy field is shown in Figure 5.35, where n = 3.0 with $M_s(T)$ taken from [86].

In order to study the impact of the transition curvature, two types of thermal profiles are assumed as shown in Figure 5.36: One is a squared thermal profile with straight thermal contour across the track width. At any crosstrack position within the written track width, the downtrack thermal profile is the same Gaussian distribution with a thermal gradient TG = 6 K/nm near the recording temperature, or the freezing temperature. The other is a perfectly circular thermal profile which is the same Gaussian distribution as in the above case with complete circular symmetry. The peak temperature assumed is the same in both cases, which is 785 K. Both thermal profiles generate virtually the same erasure width as recording is simulated over a prior created "ideal" 1T wide-track transitions at a linear density of 500 KFCI.

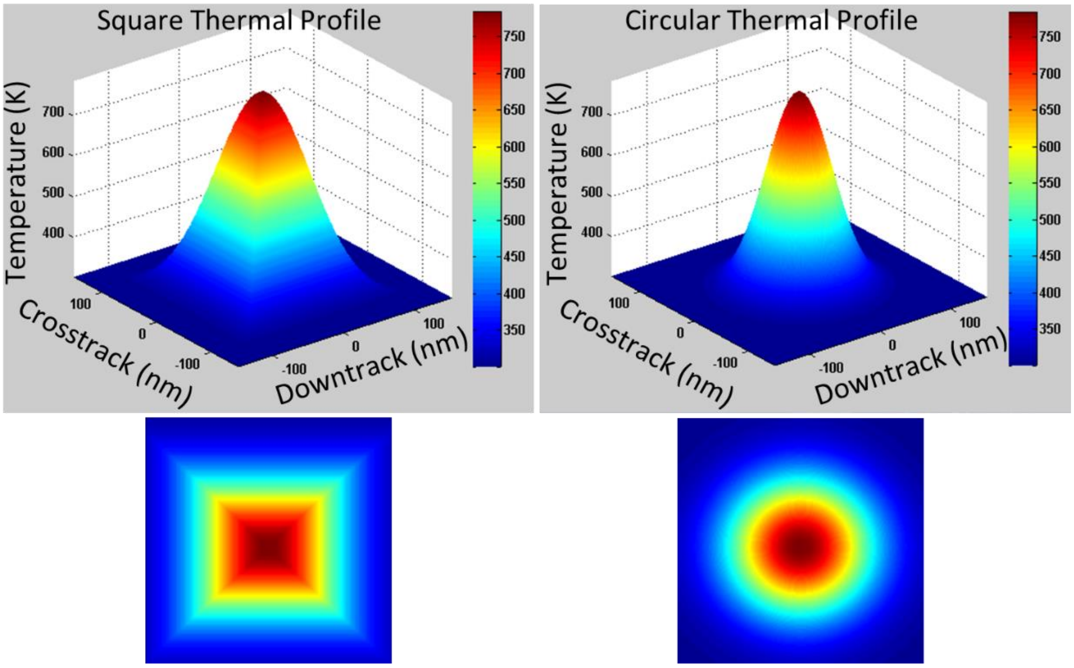

Figure 5.36 Square thermal profile (left column) and circular thermal profile with 6K/nm thermal gradient near recording temperature. The contour of recording temperature is of same width for both thermal profiles.

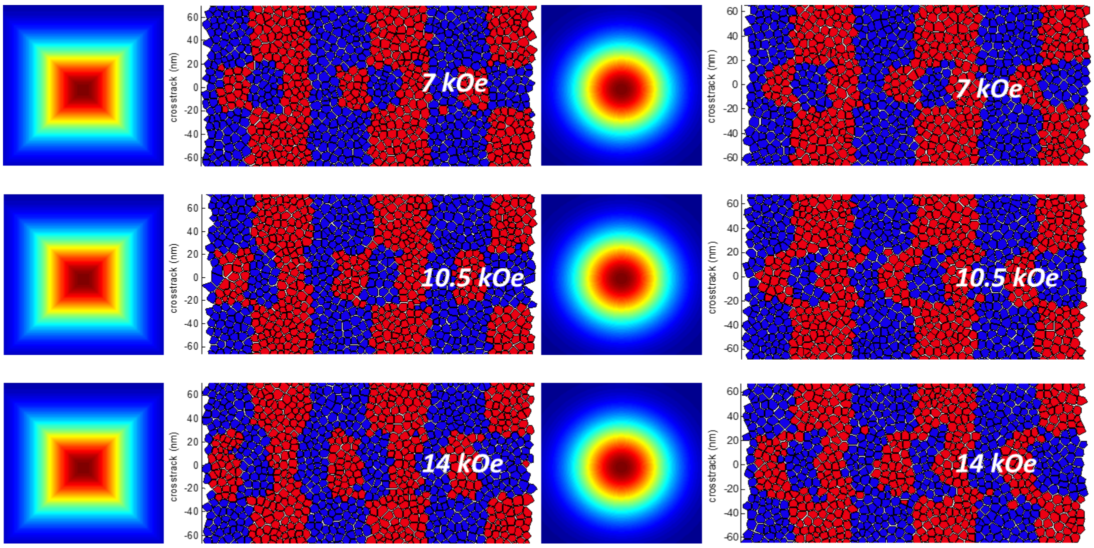

Figure 5.37 Simulated magnetization patterns with square (left) and circular (right) thermal profile of 6K/nm thermal gradient under various head field, 7, 10.5 and 14 kOe, respectively.

Firstly, the recording patterns at various applied head field with square (left column) / circular (right column) thermal profile are shown in Figure 5.37. For all the recording patterns in this figure, the uniform head field is applied. As designed, when the head field is 10.5 kOe, the track width is exactly 40 nm. As the field is 7 kOe, the track width would be much narrower, since the recording temperature is closer to the T_c. On the other hand, when the field is 14 kOe, the erase-after-write is obviously increased due to redundant RTW. Meanwhile, the curvature of the transitions created by the circular thermal profile is evident for all the cases, whereas the transition created by the square thermal profile shows straight transition front and relatively clean transition edges.

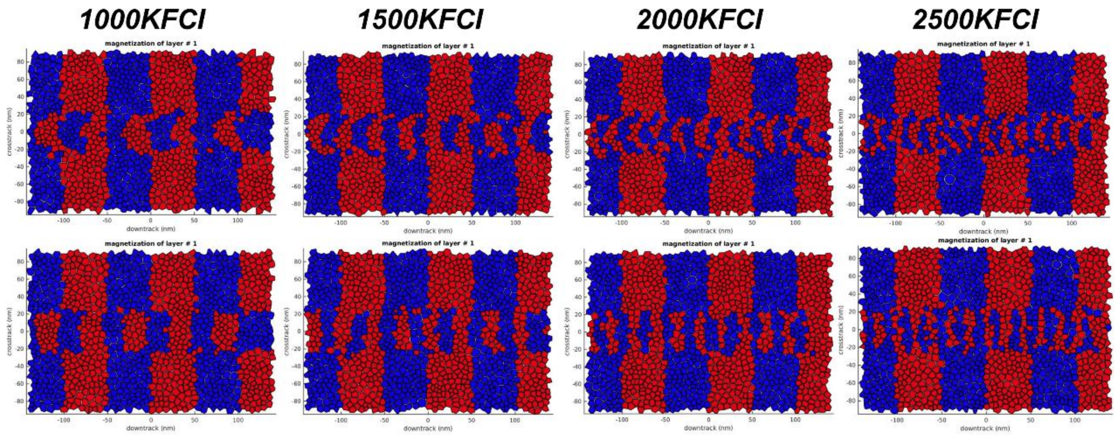

Figure 5.38 Magnetization patterns recorded using circular (upper row) or square (lower row) thermal profile with 6 K/nm thermal gradient under 10.5 kOe uniform head field.

To take into account the linear density impact, the recording with square / thermal profiles are also simulated and shown in Figure 5.38, where linear density ranges from 1 MFCI to 3 MFCI. As shown, when the linear density climbs up, the transitions get closer to each other and starts to have percolation, which greatly degrades the recording performance. Similar to Figure 5.37, the cases with the circular thermal profile have evident curved transition fronts. Additionally, the degradation of recording quality with circular thermal profile seems to be quicker and more significant.

To quantitatively analyze the linear density impact, a rectangular box of 40 nm in the crosstrack direction and 0.1 nm in the downtrack direction is utilized as the reader sensitivity function. The read-back waveforms are obtained for each simulated 1T transition sequences. Signal-to-noise ratio (SNR), are calculated for various linear densities [104] and plotted as a function of linear density for two types of thermal profiles in Figure 5.39. The straight-front transitions by the square thermal profile yield significantly higher SNR values than the curved transitions by the circular thermal profile, especially at high linear densities. If a minimum 1T SNR is required to be 7 dB, the straight transitions by the square thermal profile would offer a linear density 65% higher than the curved transitions by the circular thermal profile.

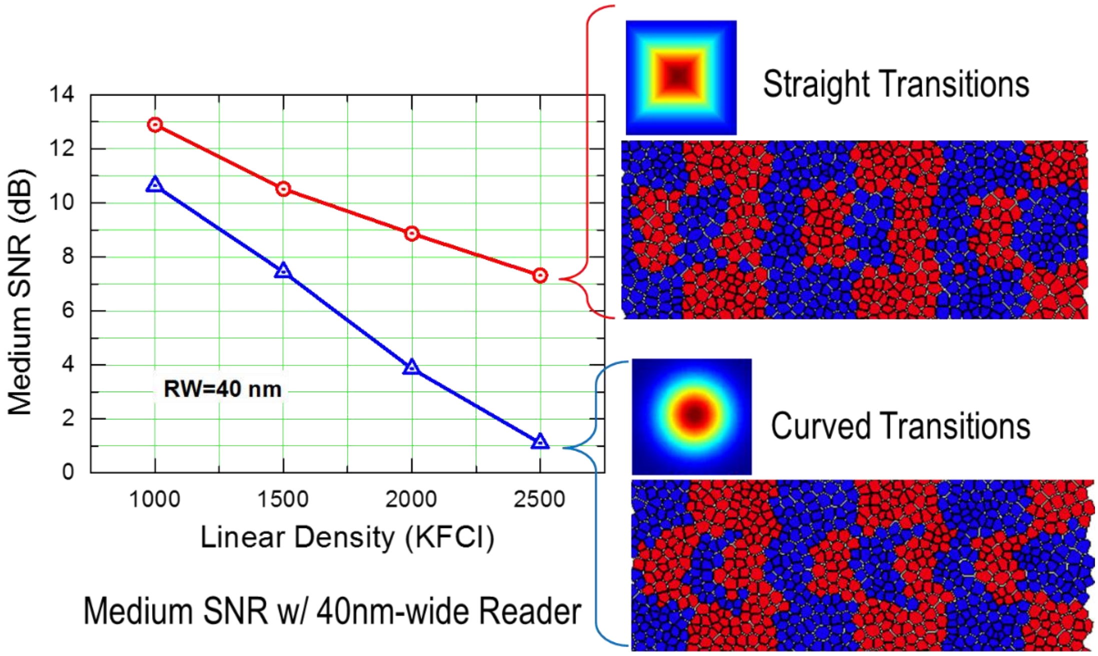

Figure 5.39 Calculated 1T SNR versus linear density with a read-width similar to the write width for the square (red) and the circular (blue) thermal profiles.

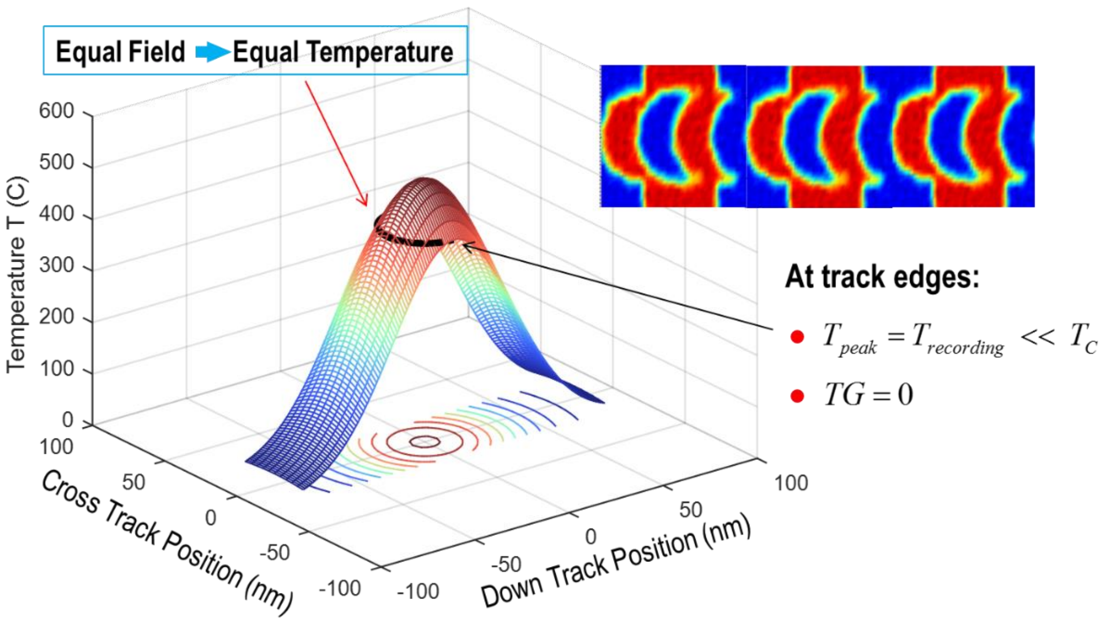

Figure 5.40 Circular thermal profile with uniform field yields quasi-circular transition fronts. At the track edges, the maximum temperature that the medium experiences is the same as the recording temperature and the thermal gradient is zero.

For the results shown in Figure 5.39, the SNR difference between the two cases includes both write and read effects, since the curved transitions generate downtrack phase shifts away from the track center, which would limit linear density capability. The rest of the section will only focus on the writing effect by introducing μ-read track analysis since the read effect due to the phase shift is obvious.

Figure 5.40 illustrates the reason for the curved transitions by the circular thermal profile. A spatial uniform write field means the transition front occurs at the same temperature, i.e. the recording temperature at which the magnetization freezes. For a circular thermal profile, the result is that transition fronts are basically half circles. It should also be noted that the maximum temperature that the medium experiences decreases at each crosstrack position further way from the track center. At the track edges, the maximum temperature is the same as the recording temperature, which is well below the Curie temperature. Such suboptimal recording condition could yield poorer transition quality near track edges.

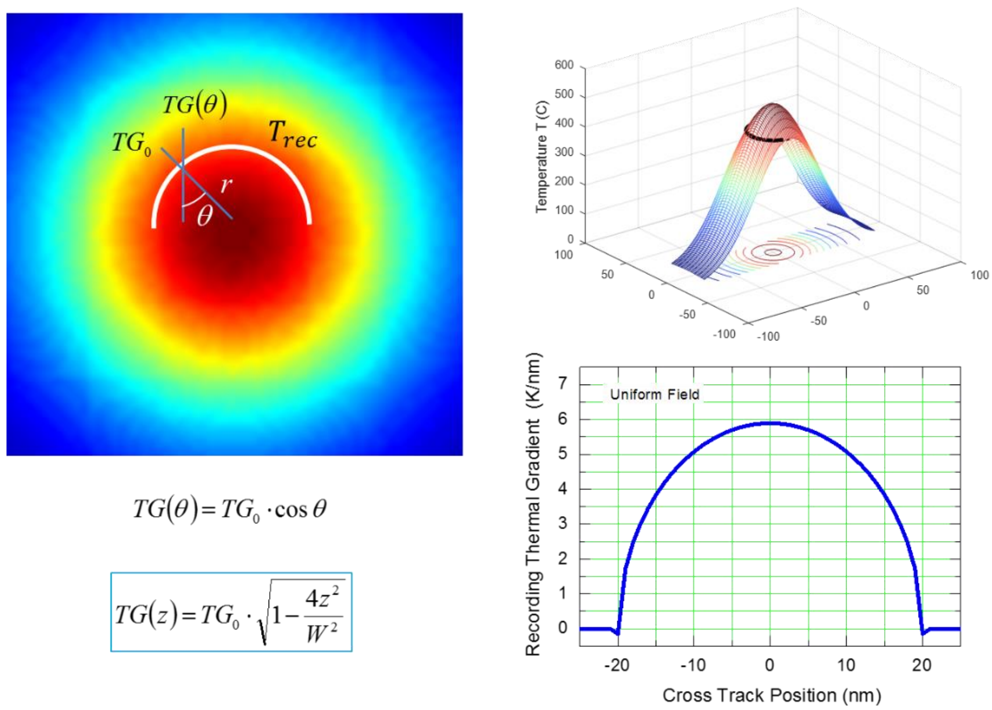

Figure 5.41 Illustration of thermal gradient (TG) reduction at position z away from track center. W is the track width and the calculated TG is plotted versus z in the bottom right graph.

Figure 5.41 illustrates the thermal gradient across the track at the recording temperature for circular thermal profile. As shown, the thermal gradient is the same in any radius direction. However, in recording, it is the downtrack thermal gradient that matters. It can be noted that the downtrack thermal gradient is the projection of the radius thermal gradient, which can be calculated by the formulas in the left bottom. The TG_0, z, and W are the radius thermal gradient, crosstrack position and track width, respectively. As shown in the right bottom graph, the TG would decay at positions away from the track center quickly. At track edge (z = W/2), the TG would vanish to zero.

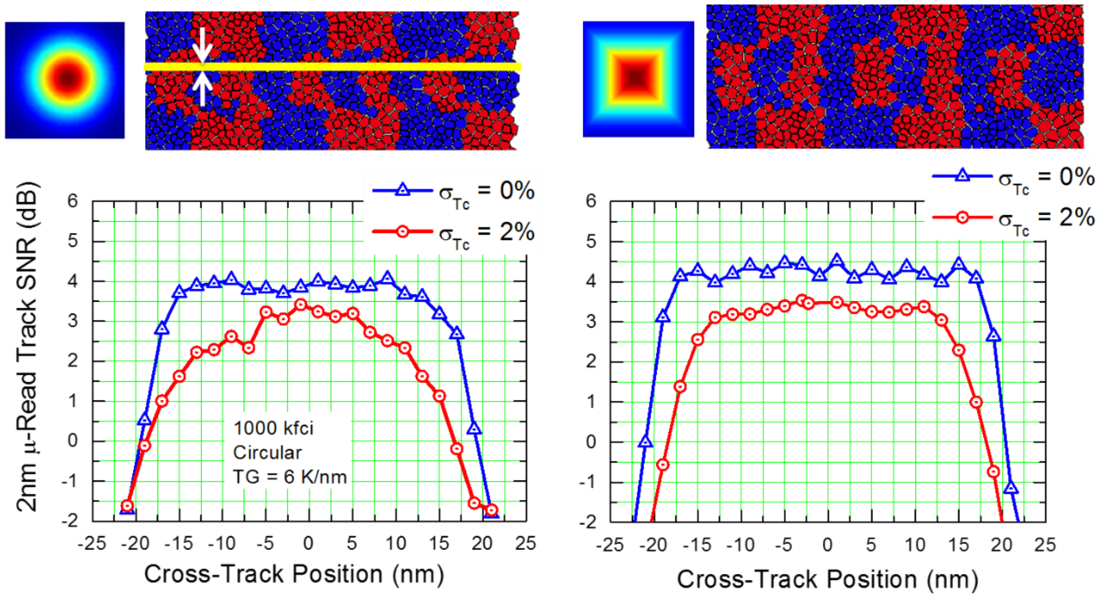

Figure 5.42 Calculated μ-track (read) SNR as a function of crosstrack position for circular (left) and square (right) thermal profiles. Two cases of grain-to-grain Curie temperature distributions with 0% (blue triangles) and 2% (red circles) are shown to illustrate the impact. The linear density here is 1000 KFCI. The yellow stripe is an example of μ-track to read.

In previous discussion of the Curie temperature distribution, it has been seen that higher TG would help suppress the SNR reduction due to T_c variation. Figure 5.42 presents the μ-track SNR, which is calculated using 2 nm x 2 nm box read sensitivity function convolving with the recording patterns, for both circular and square thermal profiles. For the case of the square thermal profile where the yielding transitions are straight, the reduction of the SNR due to the T_c variation is very similar across the track. While for the circular thermal profile, the SNR degradation is more severe at positions further away from track center.

Now that the T_c variation is significant in practical HAMR medium, especially as grain size of medium further scales down, maintaining sufficient TG would be very critical for high-density storage. Figure 5.43 shows the μ-track SNR versus crosstrack position for 2% T_c variation. The SNR is virtually unchanged across the track for the square thermal profile. But for the circular thermal profile, the SNR obviously decreases as the position deviates from the track center.

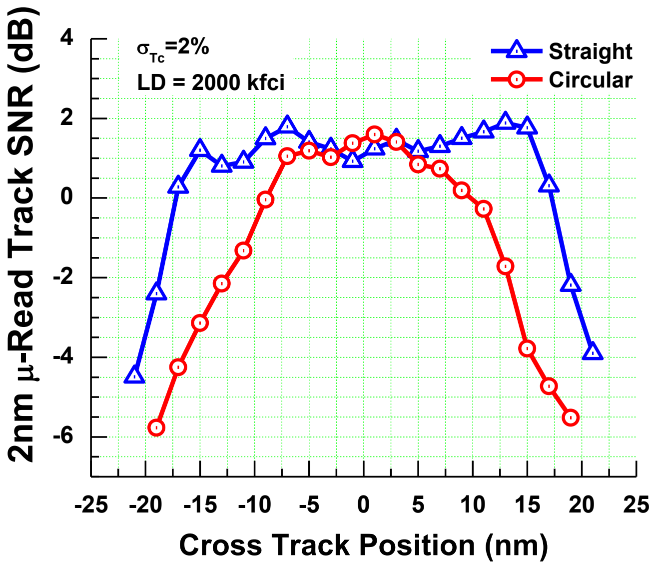

Figure 5.43 ***μ*-track SNR across track for square (blue triangles) and circular (red circles) thermal profiles.**

For the circular thermal profile, the TG degradation away from the track center is not only an important factor limiting the linear density capability, but also a critical factor limiting track density capability. The flat SNR region in the SNR across the track is less than 1/3 of the track width. Reducing track width would further reduce the portion of the flat region, which would cause severe SNR reduction.

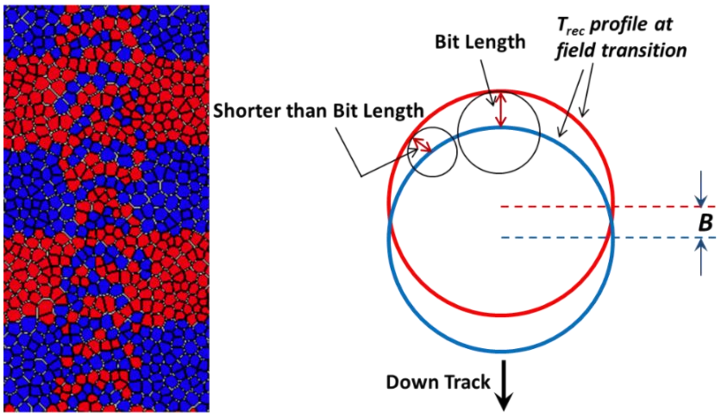

Figure 5.44 Schematic of the enhanced erase-after-write for circular thermal profile due to the reduction of the distance between the previously created transition front and the current thermal contour of recording temperature at crosstrack position away from the track center. A typical recording pattern is shown on the left, which shows evident erasure near the track edges.

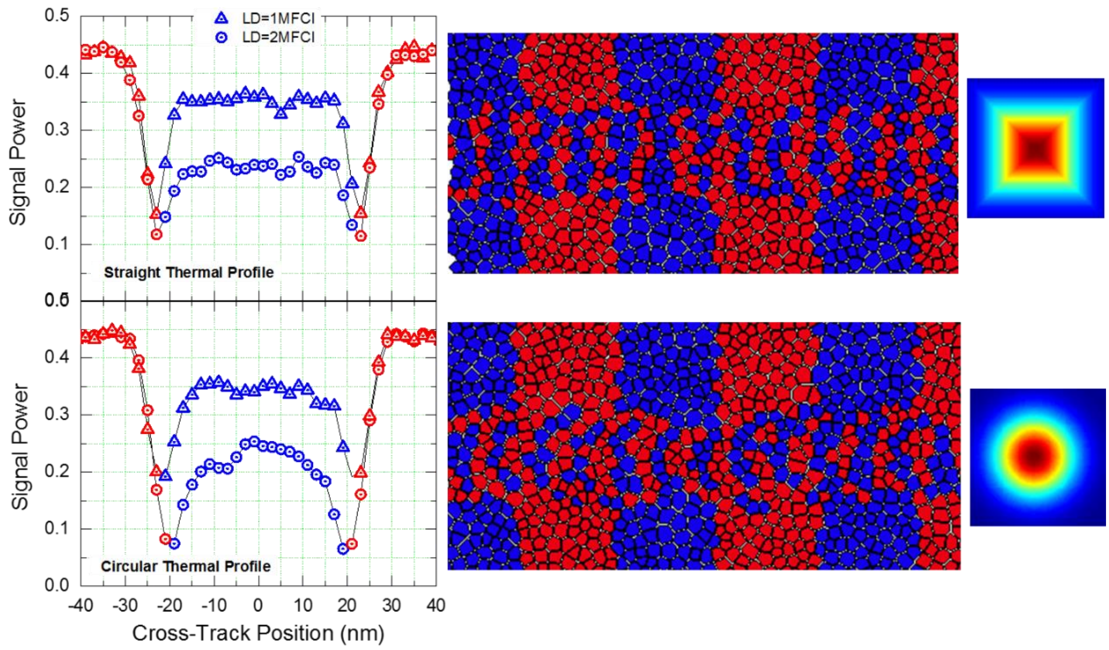

Figure 5.45 **μ-track signal power with square (top) and circular (bottom) thermal profiles at 1 MFCI and 2 MFCI. The T_c distribution here is assumed to be zero.**

Meanwhile, at high linear density, a circular thermal profile could yield additional degradation on transition quality. As illustrated in Figure 5.44, the shorter distance between the thermal contour of recording temperature and the previously created transition front becomes actually shorter than bit length at a position away from the track center. Compared with the square thermal profile case, the erase-after-write tends to be enhanced and occur at lower linear densities. Figure 5.45 shows the μ-track signal power at two different linear densities for two types of thermal profiles. It should be noted that here zero T_c variation is assumed. For the square thermal profile case, the signal power is similar across the track. Whereas for the circular thermal profile case, the signal power is reducing more severely as the crosstrack position is moving further away from the track center. The impact on the signal power clearly demonstrates the edge erasure effect illustrated in Figure 5.44. However, the edge erasure effect also enhances medium noise. Figure 5.46 presents the μ-track SNR versus crosstrack position. Away from the track center, the SNR reduction is much more severe in the case of the circular thermal profiles than in the square thermal profile case. At 2 MFCI linear density, the SNR profile is almost triangular across track for circular thermal profile, while that for square thermal profile still remains the trapezoidal shape similar to lower linear density,

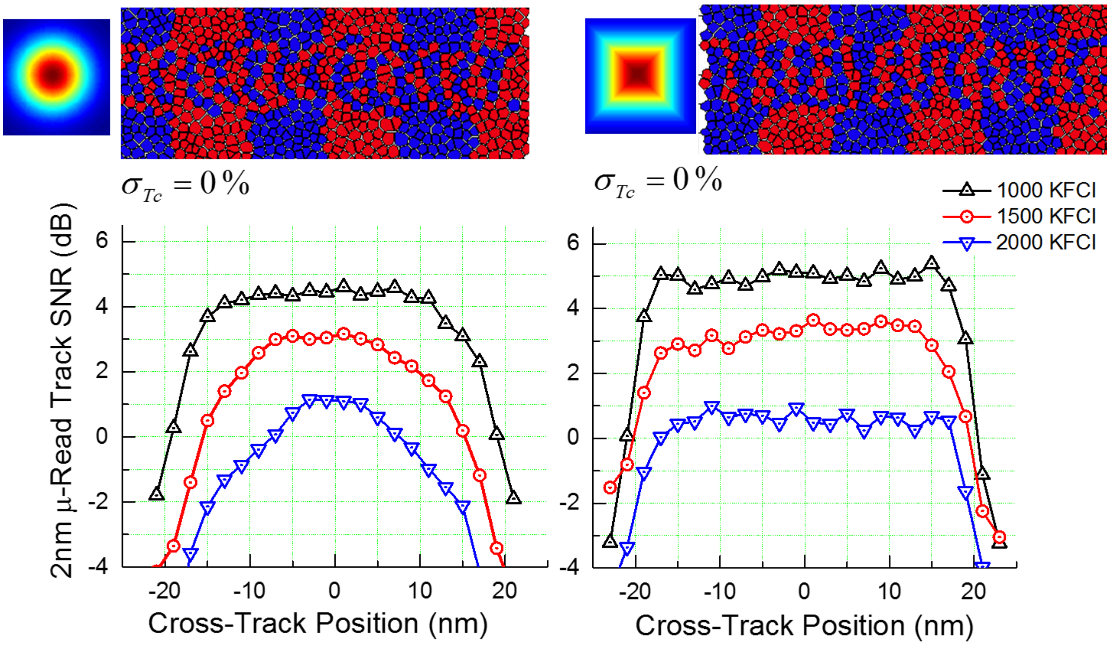

Figure 5.46 ***μ*-track SNR versus crosstrack position for recording with circular (left) square (right) thermal profiles. No T_c distribution is assumed here.**

In summary, the write impact of the circular thermal profile, which generates curved transitions, is substantial at high linear and high track densities. Three primary factors which significantly affect the quality of the recording transitions have been identified: (1) Suboptimal peak temperature at crosstrack positions away from the track center; (2) thermal gradient degradation at crosstrack position away from the track center; and (3) enhanced erase-after-write at crosstrack positions away from the track center. In order to achieve high areal density capability for HAMR, it is absolutely critical to eliminate the transition curvature.

5.4.2 Curvature Solution

In this section, the same circular thermal profile described and used in the previous section, will be used ONLY if not mentioned specifically. Via the understanding of the recording physics, a potential solution will be given to alleviate or even completely eliminate the transition curvature issue.

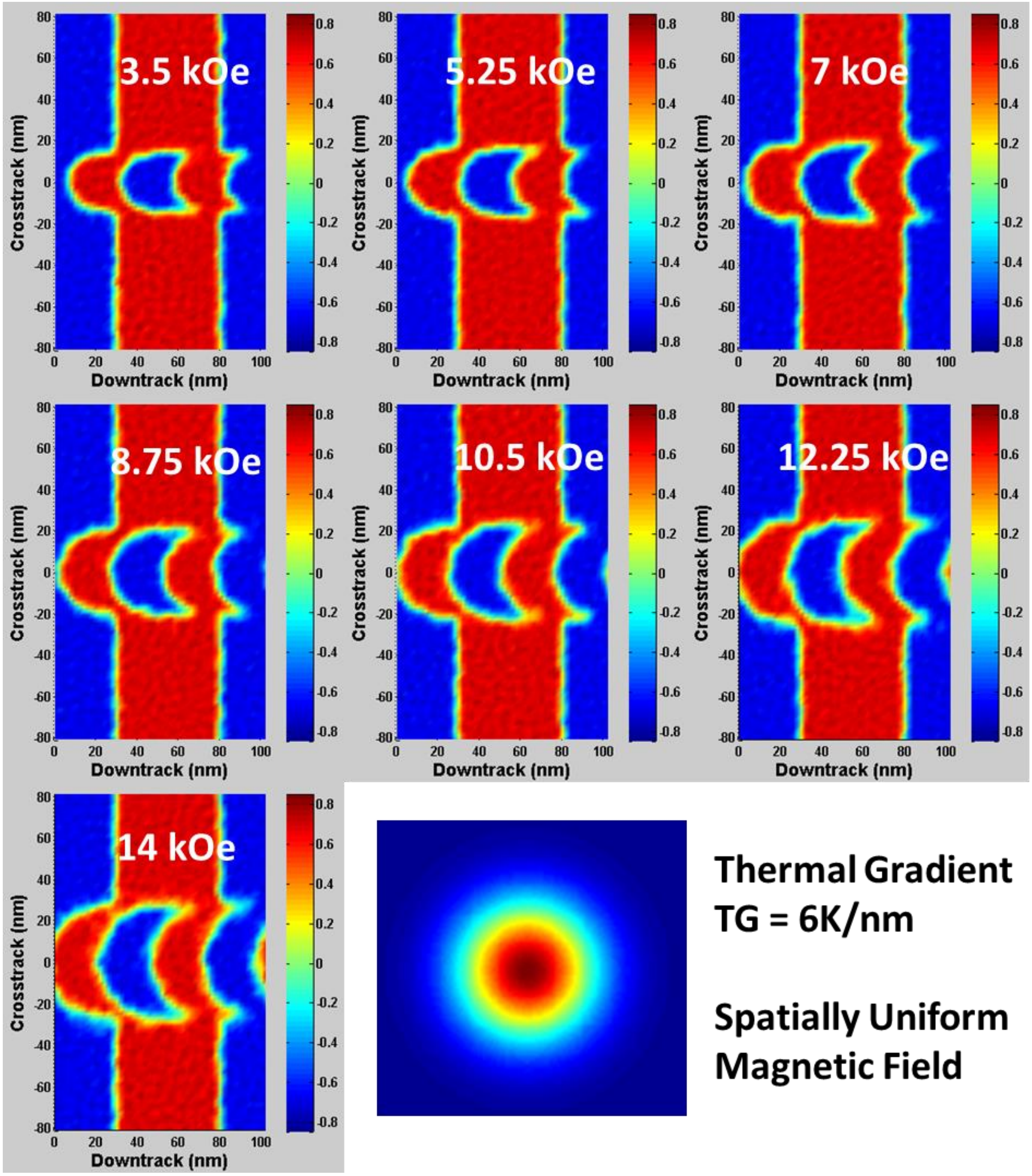

Figure 5.47 Recording magnetization patterns with the circular thermal profile under various spatially uniform head field. The thermal gradient is 6 K/nm.

First, the recorded transitions written with the circular thermal profile are generated under various uniform head field values as shown in Figure 5.47. The results indicate that as the field amplitude increases, transition front with bigger half circles would essentially be created. Besides, the transition front is also shifting towards to left direction in this specific situation. In the modeling, the writer is moving relatively to the right direction.

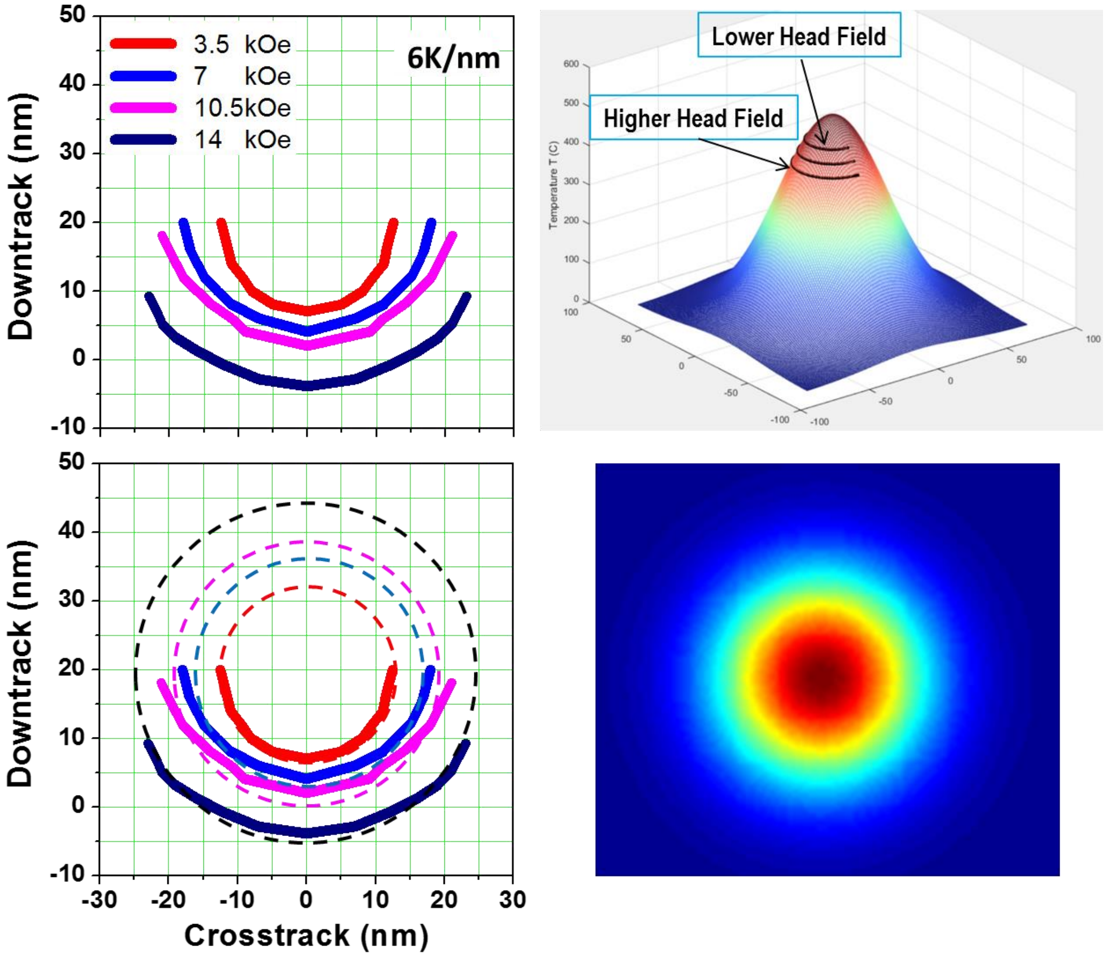

Figure 5.48 Transition front at various head field amplitudes (top left); Recording temperature contour with lower / higher head field (top right); transition fronts compared with the temperature contour (bottom left) of circular thermal profile (bottom right).

To better illustrate the reason for the transition shifting, the transition fronts recorded with various field amplitudes are plotted together in the top left graph of Figure 5.48. For the case with stronger head field, the radius of the transition front is evidently larger. In the top right graph, the recording temperature contours of lower or higher head field are labeled. Since strong head field enables recording at a temperature much lower than T_c, the resulted T_{rec} contour is much larger. Therefore, the corresponding transition front is of larger half circle. To justify the circular shape of the transition front, the dash lines are the temperature contour from the circular thermal profile in the bottom right graph. It can be noted that the shapes of the transition front at various field amplitudes closely match the contours.

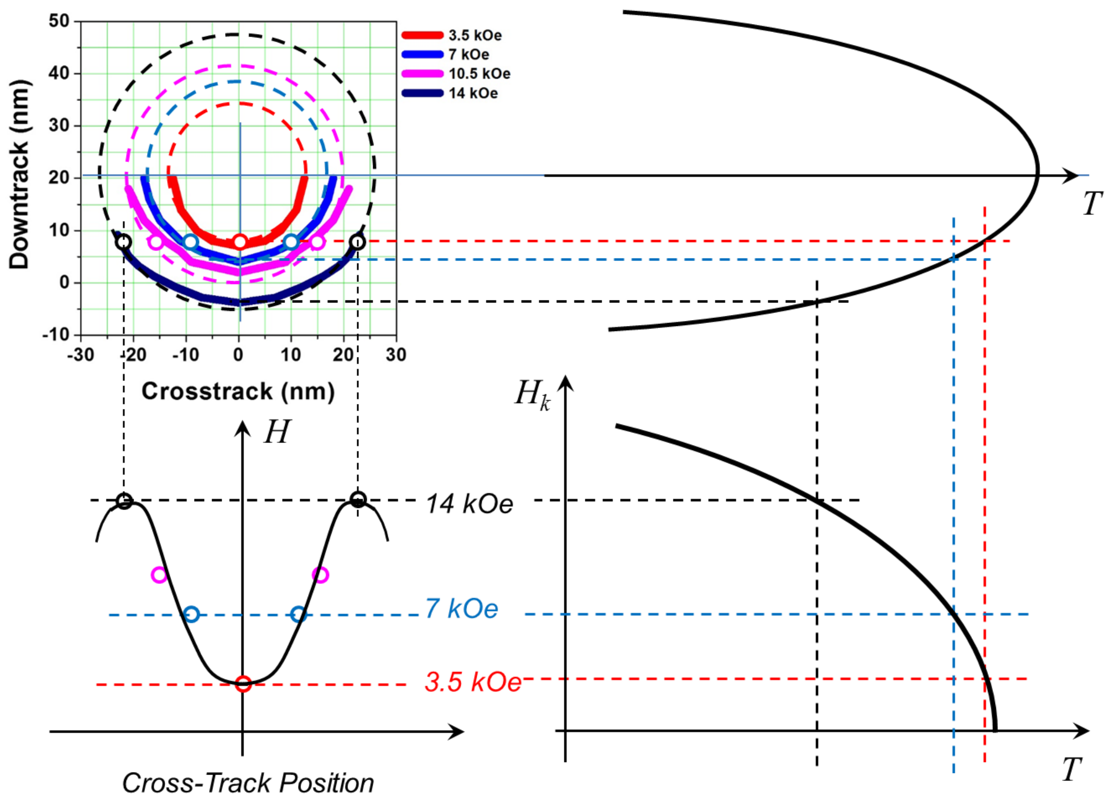

Figure 5.49 Illustration of procedure to generate crosstrack varying head field, which can yield a straight transition front and eliminate transition curvature.

Now that different head field amplitudes correspond to different transition circles, it becomes possible to create a straight transition front by varying the head field magnitude across the track. The Figure 5.49 shows the correlation between the transition fronts at various head field amplitudes, downtrack thermal profile, H_k vs. T curve and desired crosstrack varying head field profile. By writing with various uniform field magnitudes, a series of transition fonts can be defined. On one hand, the crosstrack positions (dots in top left graph) correlate with recording temperature of the thermal profile. On the other hand, the recording temperature could be projected onto the H_k vs. T curve to get the H_k. Therefore, the crosstrack varying field can be constructed.

In Figure 5.50, the same magnetization patterns shown previously are presented with additional labeling. The vertical line in each graph is determined by the downtrack position of the 1st bit transition front when field is 3.5 kOe. Using this vertical line, the intersection points (labeled by the white solid dots) could be found for each case with a different head field amplitude. It can be noted that since the transition moves to the left as the field increases, the intersection points would be further away from the track center. Later small portion of each transition here would form straightened transition.

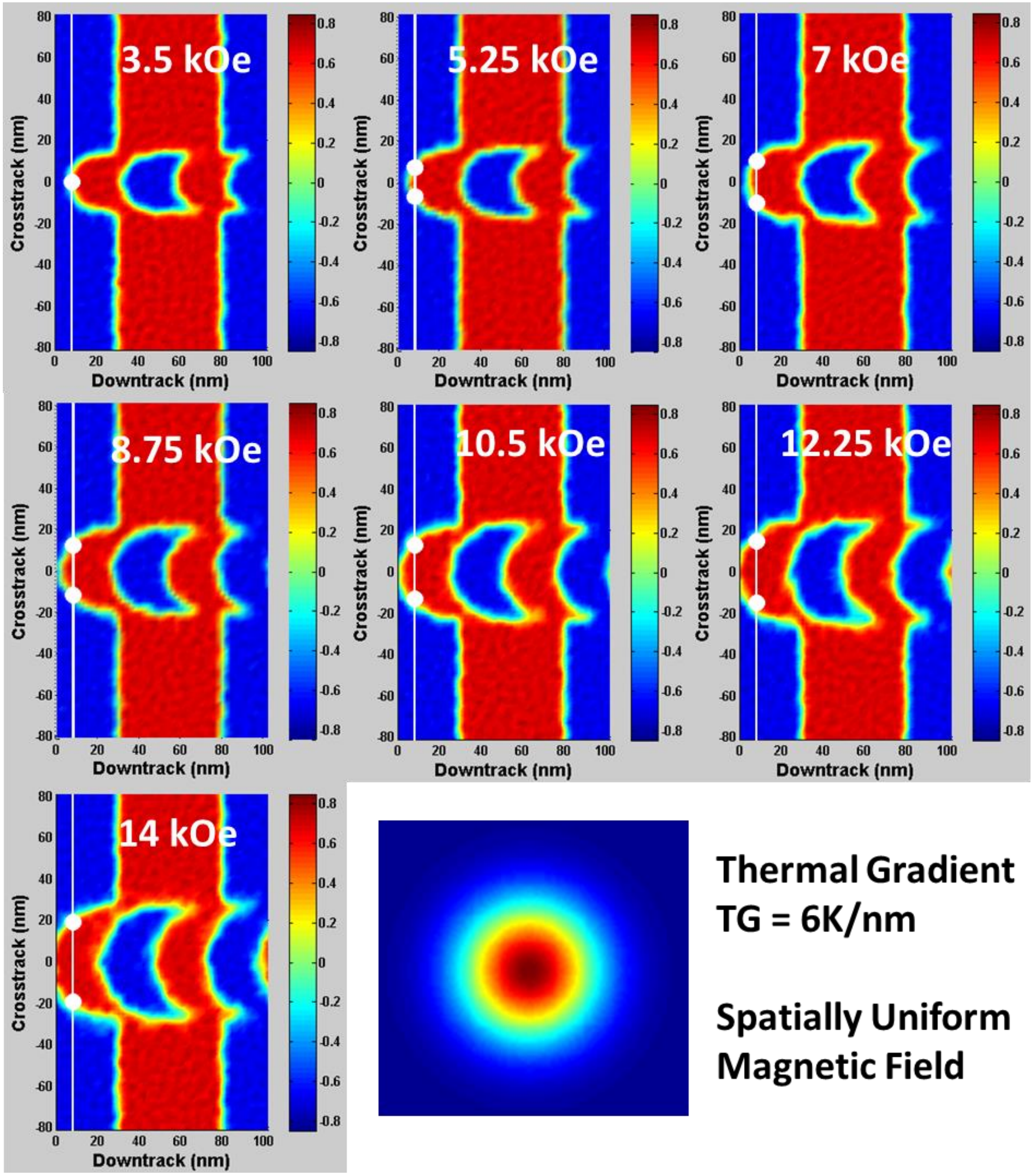

Figure 5.50 Magnetization patterns created with various head field amplitudes. The vertical line is determined by the downtrack position of 1st bit at track center when field is 3.5 kOe. The intersection points are labeled with white solid dots in each graph.

Next, in Figure 5.51, the head field values and corresponding crosstrack position of intersection points are plotted to generate the crosstrack varying head field (top right graph). For purpose of comparison, the uniform field profile is shown in top left graph. Using these two types of head field profile, the recording simulation is conducted with same medium and the representative magnetization patterns are shown below. The transition sequences written with the crosstrack varying field are clearly straightened with curvature completely eliminated.

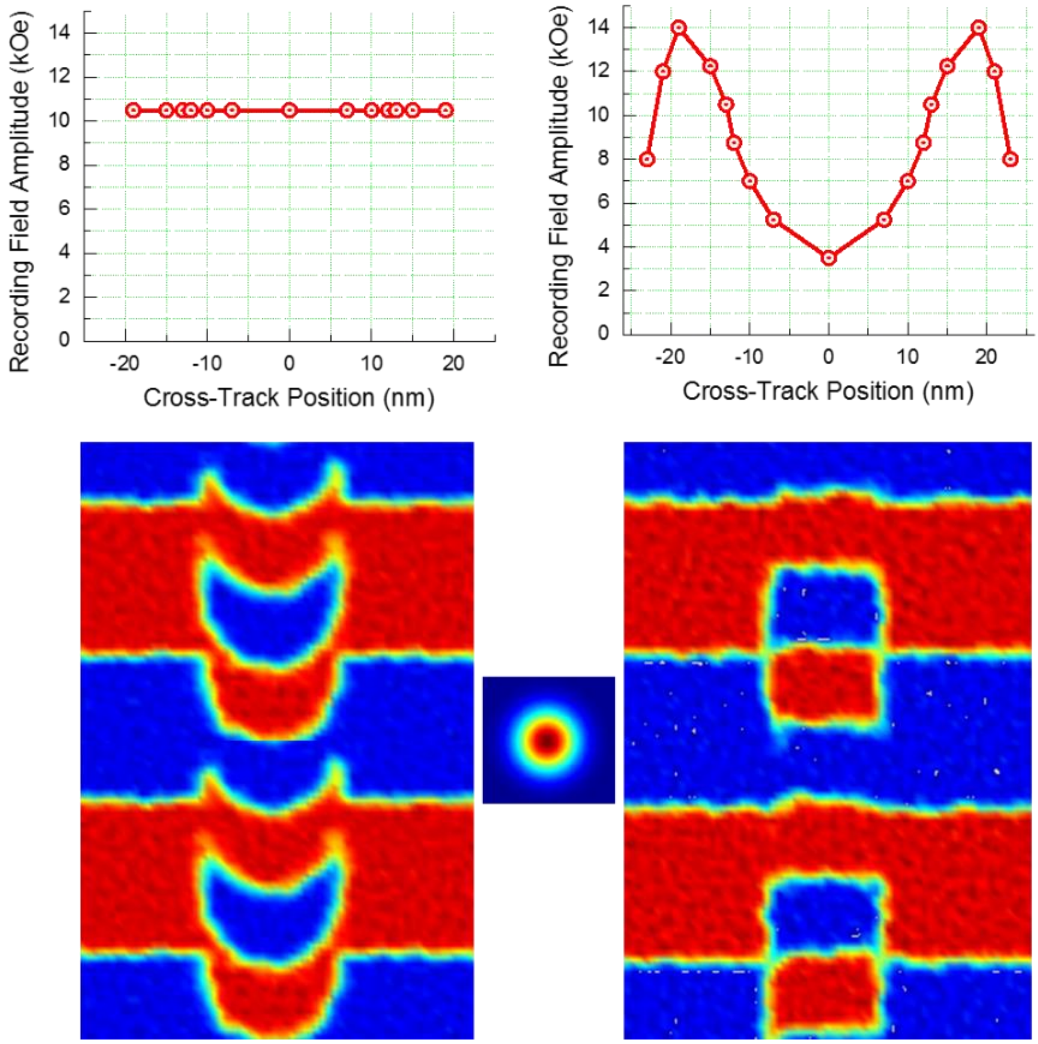

Figure 5.51 Uniform head field (top left) and constructed crosstrack varying head field (top right), along with the corresponding recording patterns shown below. The same circular thermal profile (bottom middle) is used for both cases.

To better optimize the recording performance in finer granularity, the μ-track SNR is evaluated versus applied uniform head field, as shown in Figure 5.52. The results indicate that the recording saturates at lower field when the crosstrack position is near the center of track. Whereas, the optimal head field gradually increases when the crosstrack position deviates away from the track center. It is potentially because the suboptimal heating near the track edges. This observation also suggests that the crosstrack varying field profile obtained previously properly takes advantage of this optimal field change versus crosstrack positions.

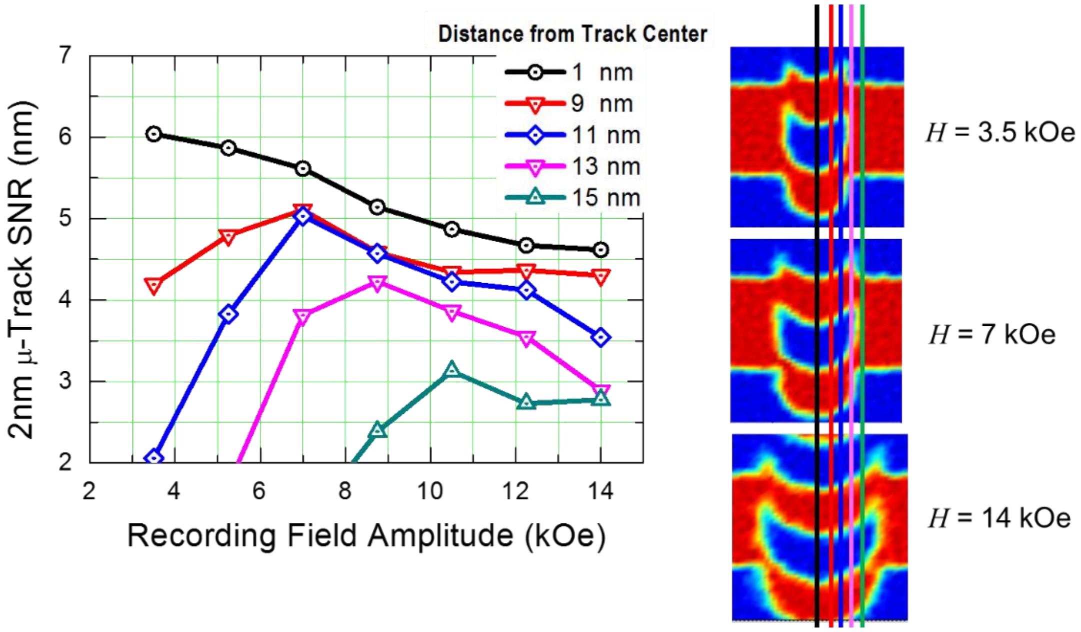

Figure 5.52 ***μ*-track SNR versus uniform head field amplitude at different crosstrack positions away from the track center. The typical recording patterns are shown on the right.**

To quantitatively compare, the μ-track reading SNR for crosstrack varying field, different uniform field cases are plotted as a function of crosstrack position in Figure 5.53. The results indicate that the SNR would remain relatively decent within the track width, when the crosstrack varying head field is utilized. In comparison, the cases with the uniform field, the curved transitions would have obvious SNR reduction and decreases much faster when it is position closer to the track edges.

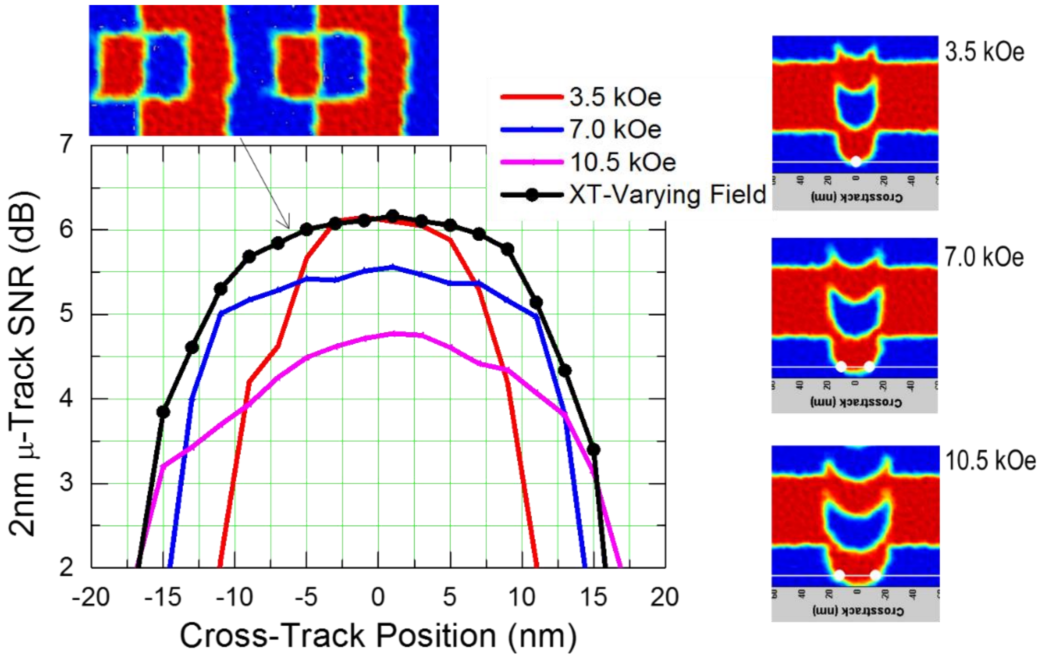

Figure 5.53 ***μ*-track SNR for crosstrack varying head field and different uniform head field. The typical recording patterns are shown on the right hand side.**

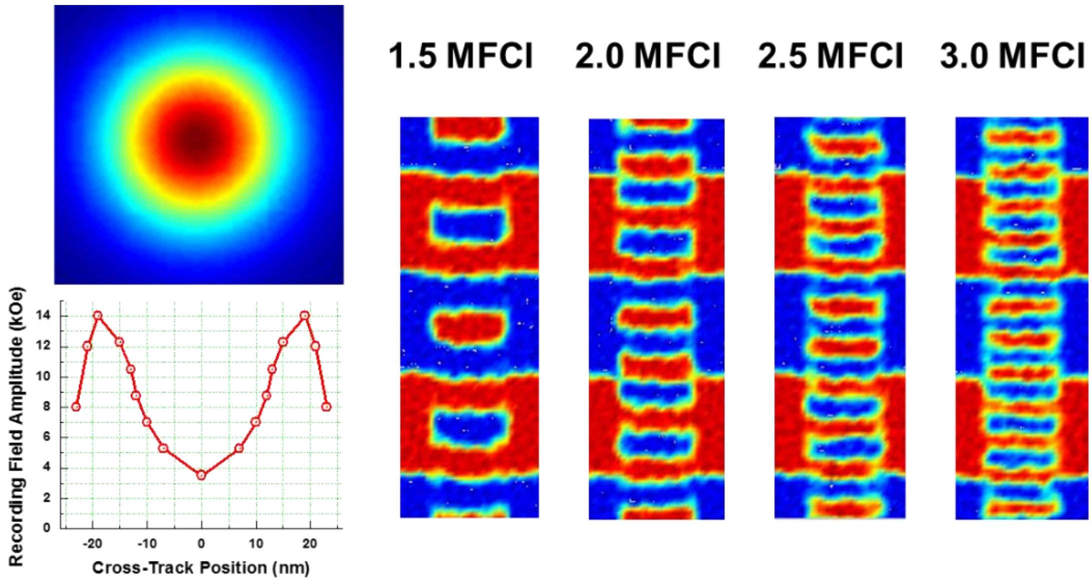

Figure 5.54 Averaged 1T transition sequences at various linear densities, recorded with a crosstrack varying write head field (left bottom) and the circular thermal profile (left top).

Figure 5.54 shows the averaged transition sequences at various linear densities, recorded with the same crosstrack varying field. Transitions are still clearly well-defined at 3 MFCI linear density. By quickly dropping the field amplitude, the track width can be defined by crosstrack field profile instead of thermal gradient. These results demonstrate the viability of this technique at different storage densities. The advantage of this approach will be further elucidated later.

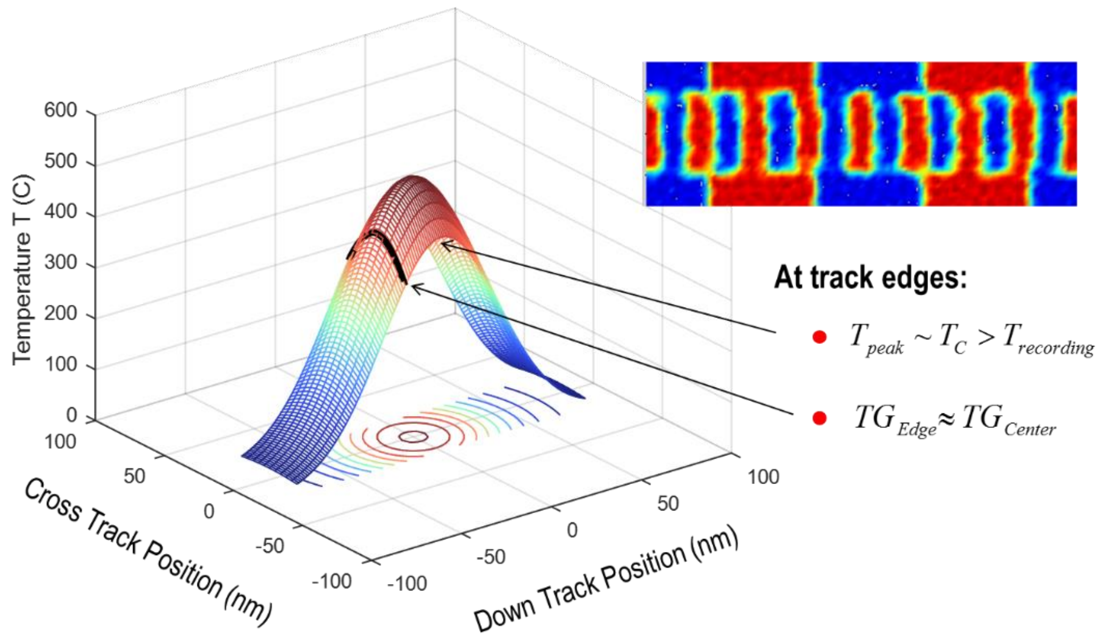

Figure 5.55 Illustration of the improved recording conditions with the crosstrack varying write field. The black curve indicates the location of the transition on the surface of the circular thermal profile.

The straightened transition front by varying the head field along the crosstrack position brings many improved recording conditions, as many can be illustrated in the Figure 5.55. The black curve on the surface of the circular thermal profile indicates the location of the transition when it is first created. First, it should be noted that since the width is now determined by the write field instead, the peak temperature at the track edges can be significantly higher than the recording temperature. Hence, the peak temperature can be slightly raised up to ensure the thermal gradient across the track width will be sufficiently high without significant degradation near the track edges. Moreover, the RTW can be very similar and optimal recording conditions can be maintained across the track.

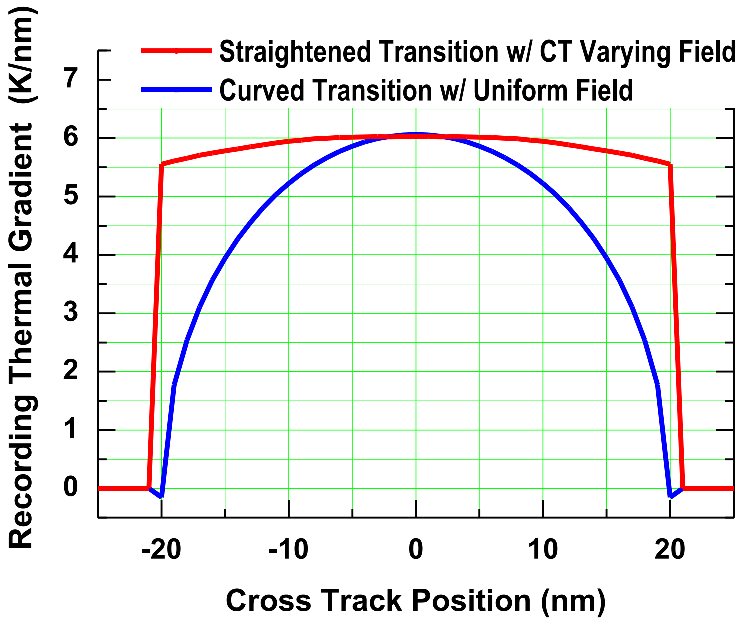

Figure 5.56 Thermal gradient across track at the recording temperature for the case of crosstrack varying field (red) and the uniform field (blue).

Figure 5.56 presents the thermal gradient at the recording temperature at different crosstrack positions for straightened transitions generated by crosstrack varying field (red) and the curved transitions generated by uniform field (blue). With the crosstrack varying field, the thermal gradient is almost constant across the track width, unlike the uniform field case where the thermal gradient quickly drops as moving away from the track center.

Figure 5.57 shows the full track width 1T SNR as a function of linear density. The case with crosstrack varying field under circular thermal profile shows similar, actually slightly better, performance than that of the case with uniform field and the square thermal profile. While the case with uniform head field and circular thermal profile has much lower SNR than the previous two cases. These results show that creating an appropriate crosstrack varying head field, with the circular thermal profile, greatly enhances the performance. The upgraded area density capability can at least match that of an ideal thermal profile with square temperature contour.

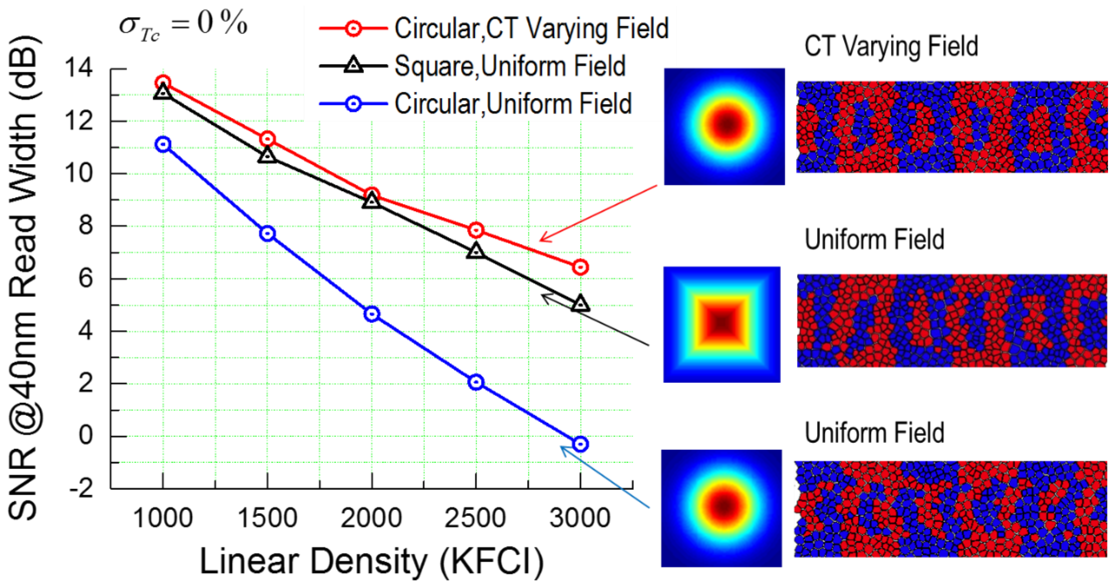

Figure 5.57 Full track 1T SNR vs. linear density for the circular thermal profile with the crosstrack varying head field (red circles) and spatial uniform head field (blue). The corresponding results for the square thermal profile case (black triangles) are shown for comparison.

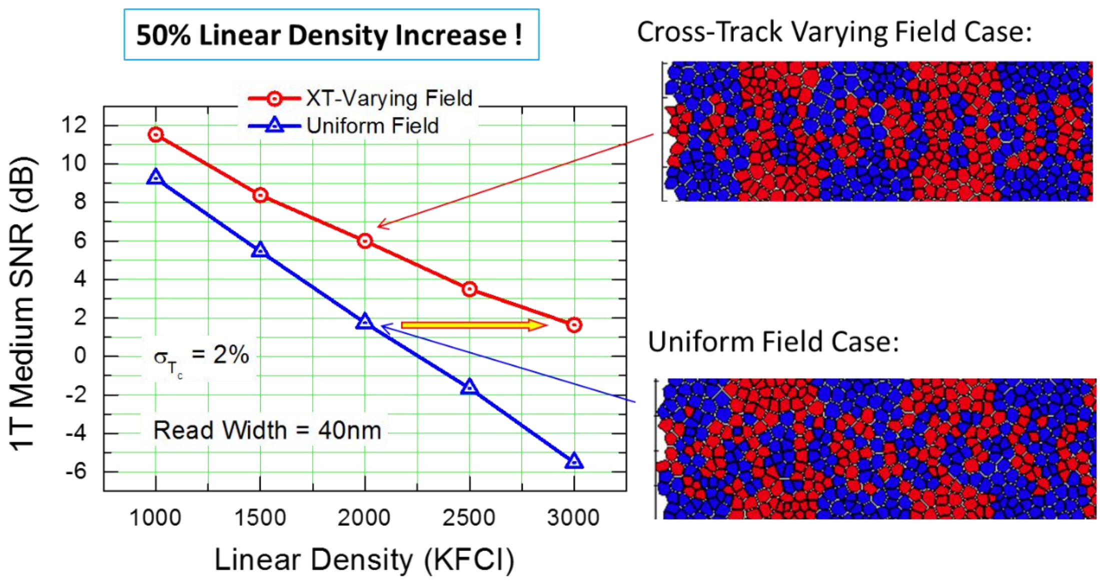

Figure 5.58 SNR comparison between the crosstrack varying field and the uniform field with circular thermal profile. 2% T_c variation is assumed to better match with a practical situation.

In a practical situation, the HAMR media tends to have nonzero grain-to-grain Curie temperature dispersion. The enhancement of the thermal gradient with the crosstrack varying field, in the case of circular thermal profile, yield significantly better SNR performance as shown in Figure 5.58. Here the standard deviation of Curie temperature distribution is set to be 2% [153]. If the minimum 1T SNR is required to be 2 dB, with the crosstrack varying write field, the increase of linear density can be at least 50%, from 2 MFCI to 3 MFCI.

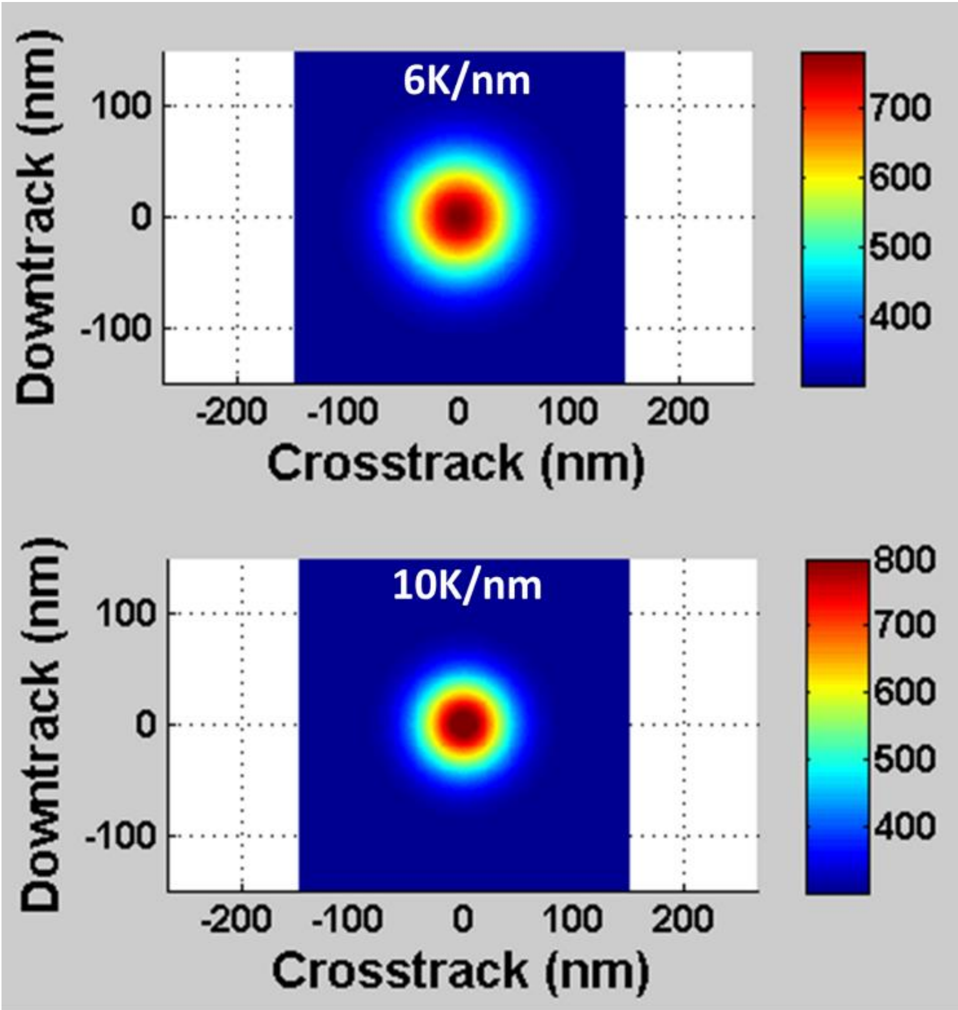

Figure 5.59 Circular thermal profiles with 6 K/nm (top) and 10 K/nm (bottom).

Furthermore, this technique is expected to be viable for different thermal profiles. Figure 5.59 shows the circular thermal profiles with different thermal gradient, 6 K/nm (top, the same thermal profile used in previous sections) and 10 K/nm (bottom), respectively. It can be noticed that the same temperature contour is smaller for the higher thermal gradient case.

Using the procedure described previously, the crosstrack varying field has been constructed separately for thermal profiles with different thermal gradients, as shown in Figure 5.60. For both cases, the field is relatively weaker near the track center and quickly grows stronger as the crosstrack position is moving away further from the track center. It can be noted that the crosstrack field slope is higher for the higher thermal gradient case.

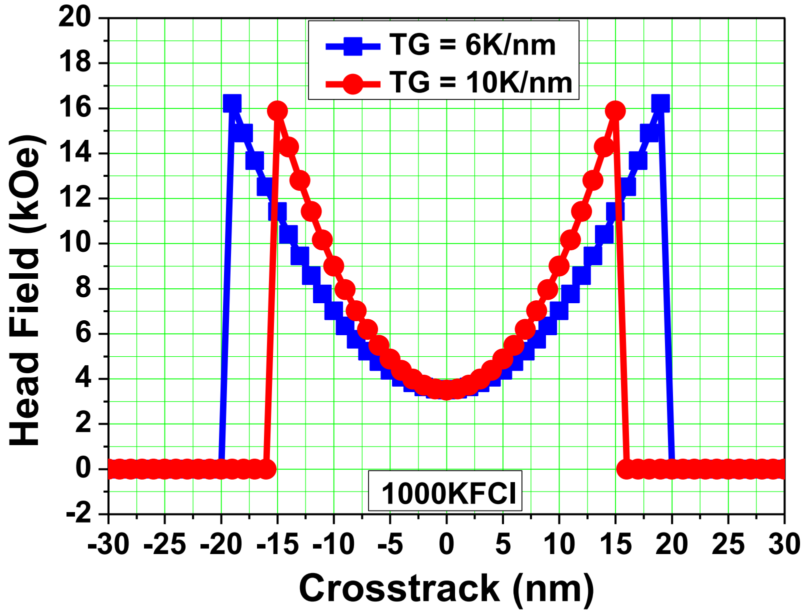

Figure 5.60 Crosstrack varying field for thermal profiles with different thermal gradient values.

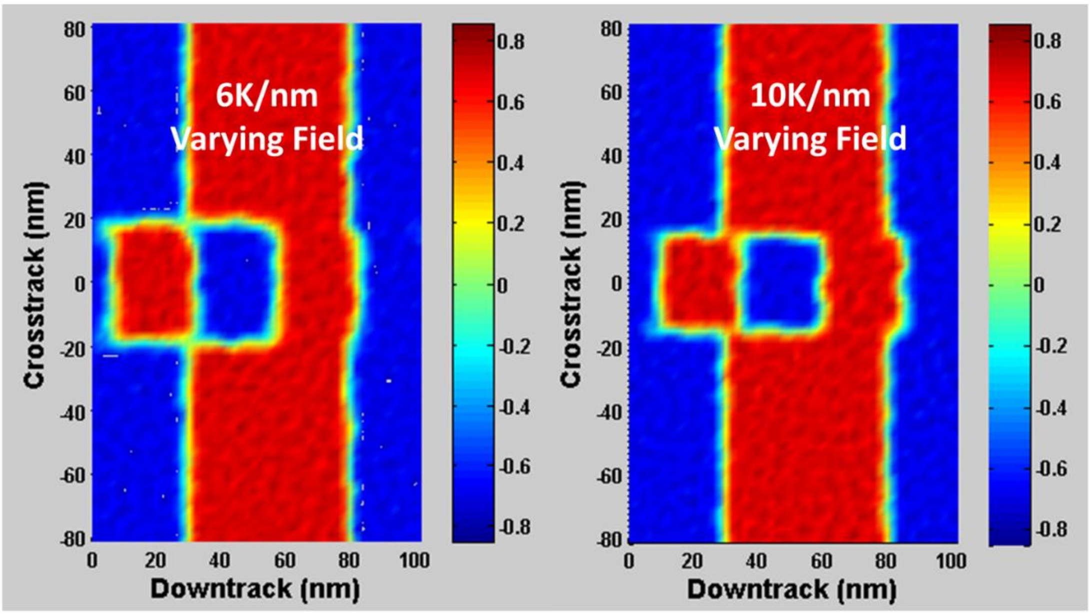

Figure 5.61 Magnetization patterns with the crosstrack varying field paired with the corresponding thermal profile of different thermal gradients, 6 K/nm (left) and 10 K/nm (right).

With the crosstrack varying field constructed, the recording simulations have been conducted and the consequent magnetization patterns are shown in Figure 5.61. The results indicate that for both cases, the recorded transitions have straightened fronts, with the curvature eliminated completely. This technique is general for thermal profiles with different degrees of curvature.

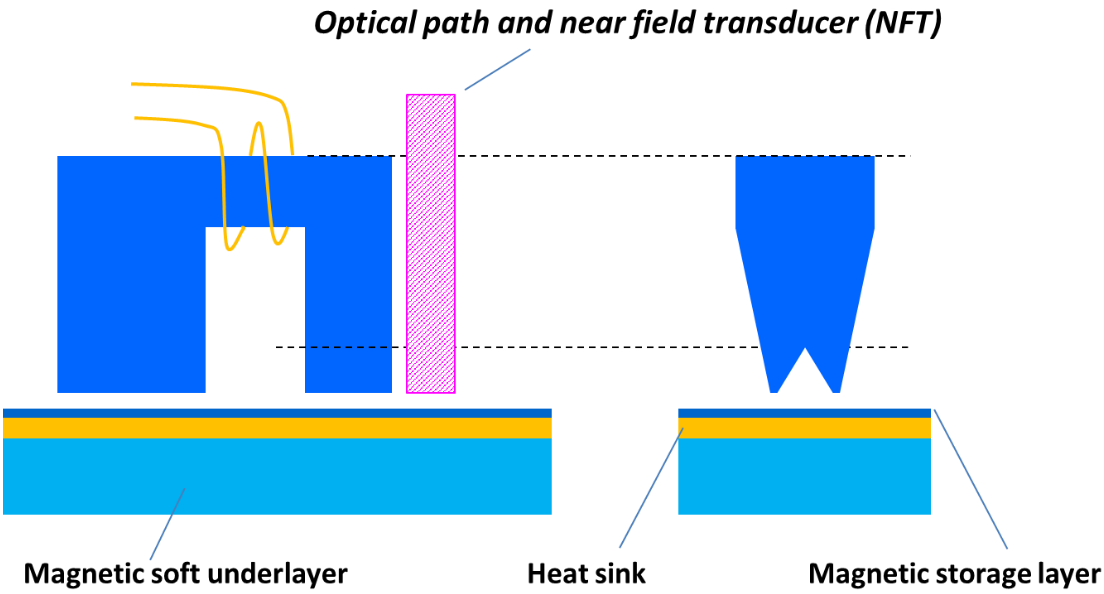

Figure 5.62 Schematic of a proposed writer shape with a triangular groove underneath.

Now that the crosstrack varying field is validated to correct the transition curvature, generating head field profiles will be discussed next. Figure 5.62 shows a schematic of a proposed writer pole shape. As is shown, there is a triangular groove underneath the writer main pole. This feature is expected to provide weaker field at the center, while the field gradually increases at the position further away from the track center. The tapering at the edges are supposed to make the field decay quickly at the track edge so that the narrow track width could be defined. The practical design could vary, with the essence being kept.

To validate the field profile, a simplified writer pole with triangular groove is simulated with the Finite-Element-Method (FEM) using COMSOL^{TM} multiphysics package. The meshing and zoomed in details are shown in the Figure 5.63. The meshing is set to be adaptive, where smaller mesh cells are located near some fine features of design, like the main pole tips and so on. This would deliver smoother results and ensure calculation precision.

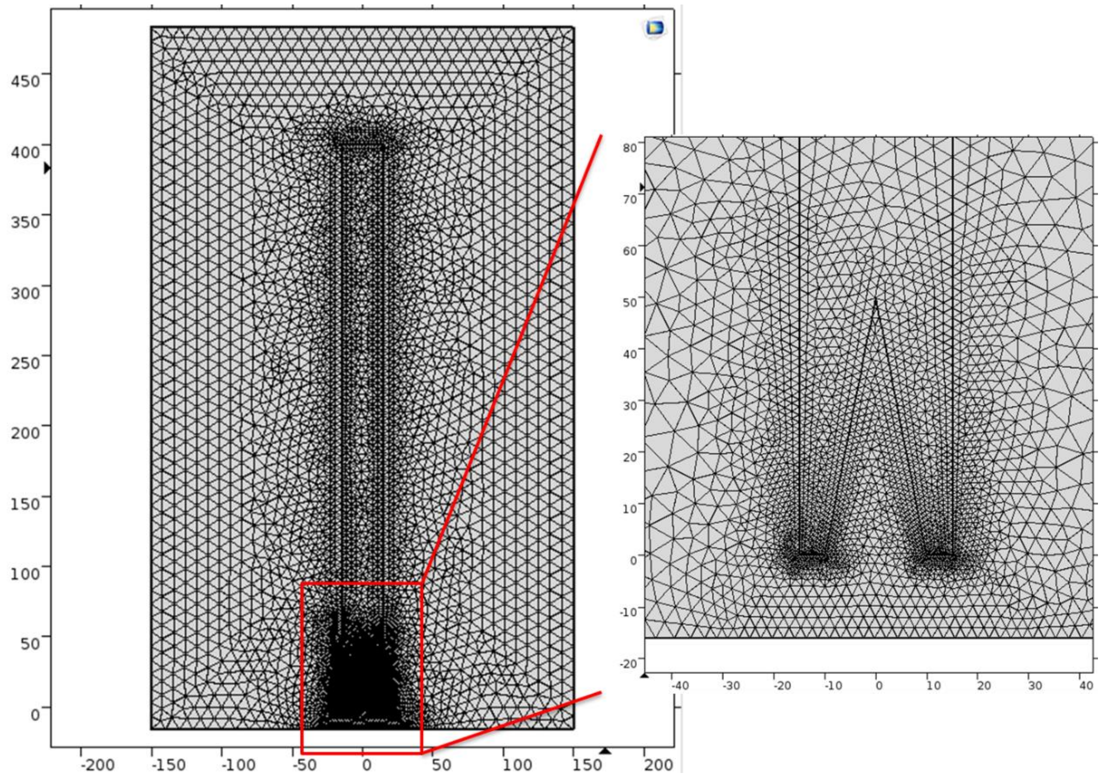

Figure 5.63 Meshing of a simplified writer main pole structure in the COMSOL™ Multiphysics simulator. Adaptive meshing is utilized and the numbers are in unit of nm.

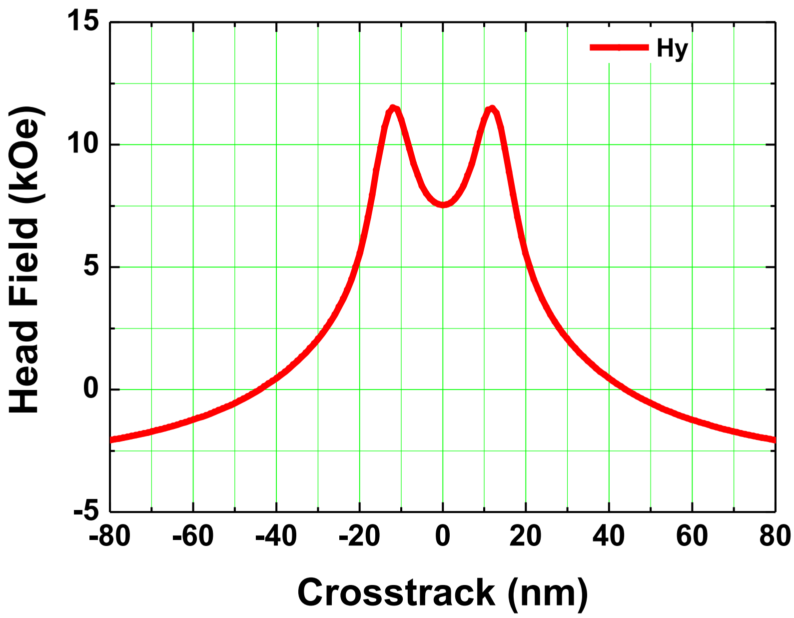

Figure 5.64 Perpendicular component of the head field across the track calculated with FEM.

The calculated perpendicular component of the head field is plotted in the Figure 5.64. Similar to the desired head field profile, the head value is relatively low at the track center and quickly increases as the position deviates away from the track center. Although there exists some deviation, with more detailed engineering, the generated head field profile is expected to match up with the necessary field profile to rectify the transition curvature.

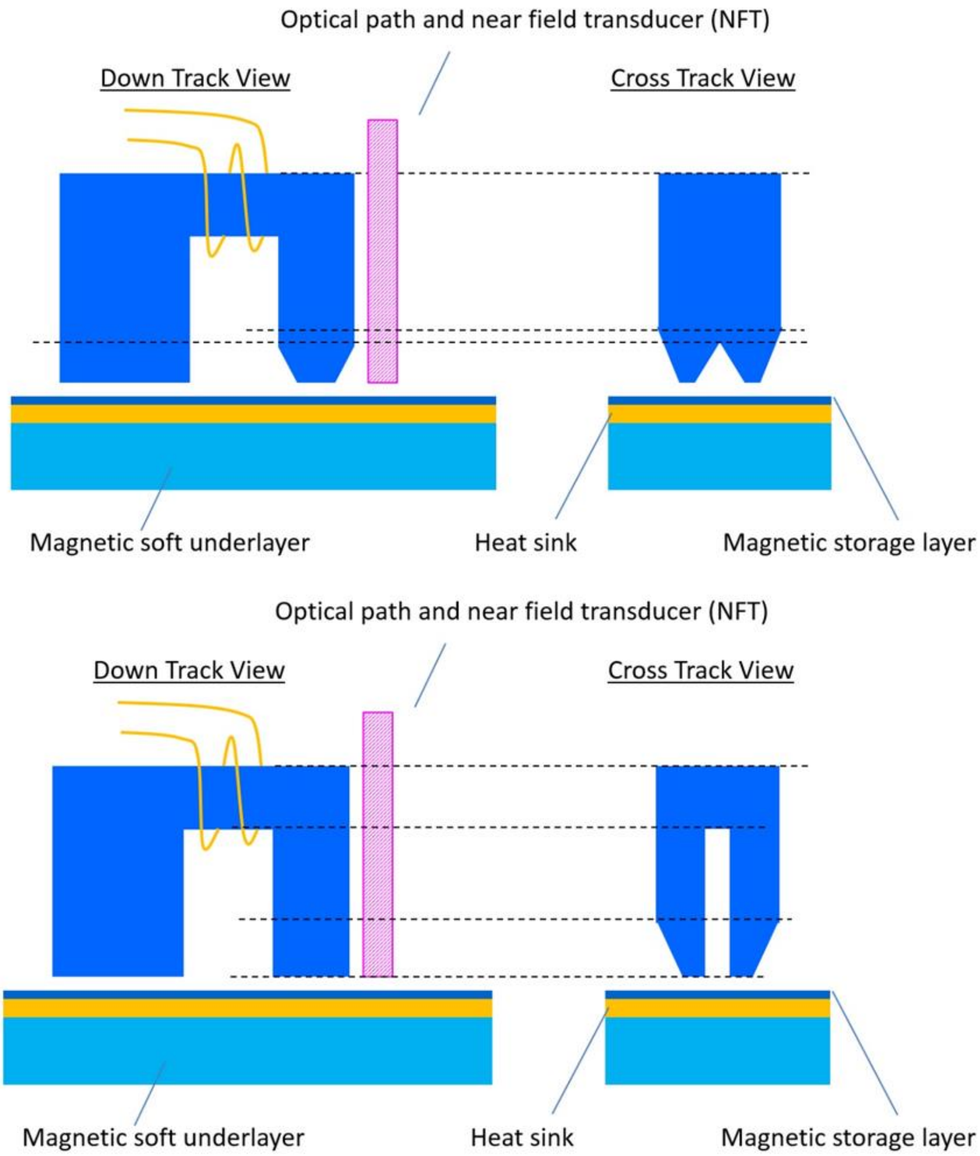

Figure 5.65 Additional possible features to enhance the head field profiles. The top graph has tapering along downtrack direction to enhance flux concentration and tune the field angle. The lower graph has vertical slot of main pole to enhance the field slope and amplitude as well.

Figure 5.65 shows some possible variation of the design to better improve the head field profile. The top graph illustrates the tapering of the main pole along the downtrack direction, which would help concentrate the magnetic flux and provide proper field angle. The tapering does not have to be on both sides and can be made for one side only. The lower graph shows a vertical slot. This may help enhance the crosstrack field slope and enhance the field amplitude as well.

5.5 Conclusion

Based upon the fundamental understanding of the storage physics and noise mechanism discussed in previous chapters, the proposed recording theorem has been applied in experiments and realistic design.

With the spin stand testing, the incomplete switching and erase-after-write noise mechanism are observed. To prove the concept of recording time window, the velocity effect and the anisotropy field impact are both investigated, and the findings match up with theoretical expectation and micromagnetic simulation.

Considering the realistic writer design could vary in many aspects, an instance is given to analyze the entire recording system in terms of RTW. This type of analysis suggests where this design sits, like short of RTW or having redundant RTW. This is critical since it tells the direction to modify the system specification, so that the optimal RTW can be achieved.

As multiple noise origins have been analyzed or first proposed in previous discussion, systematic modeling is also conducted to validate experimental testing methodology and understand the testing results. In collaboration with the experiments, the Curie temperature distribution and the temperature dependence of the H_k are both obtained, which greatly affect the recording quality.

Besides, transition curvature, a well-known and long existing issue has been investigated. The impact on the recording density is analyzed with carefully engineered square and circular thermal profiles. Due to the significant impact of the transition curvature, a practical solution is proposed for the first time, based upon the understanding of storage physics. A technique is introduced to generate thermal guided writer field design, which can be paired up with the curved thermal profile. With this novel design, the linear density increase can be at least 50%!

The results in this chapter not only experimentally validate the series of theorem proposed in this thesis, but also provide practical guidance and novel solution for real recording system design.

6. Summary

Heat-Assisted Magnetic Recording has been widely considered as the leading candidate for the next generation of hard disk drive technology. Several progressive industrial demos [24], [73] have been given during prestigious conferences. In this Ph.D. thesis work, in order to better master the HAMR potential, a systematic thermal coupled micromagnetic study has been conducted to understand the recording physics and noise mechanism.

At the very beginning, to capture and simulate the FePt spin magnetic dynamics, great efforts have been devoted to understanding and applying the Landau-Lifshitz-Bloch (so-called LLB) equation to upgrade the model. With the newly developed model, the shrinking and recovering of magnetization can be better described. The temperature dependence of the damping and the effective field are taken into account. Ultra-fast magnetization reversal is also described more properly in this scenario. During the same period of time, ultra-fast magnetic dynamics gradually becomes a hot topic in fundamental condensed matter physics research. This thesis is believed to be one of the pioneering work with LLB equation to study HAMR recording physics and noise mechanism.

In HAMR scheme, despite certain variations, the incomplete switching and erase-after-write phenomena are discovered to be general in different system specifications. The combinational effect of these two noise sources leads to the obvious head field dependence of recording performance, especially for smaller grains. This behavior is essentially caused by the thermal agitation originated from the fluctuation-dissipation theorem. Due to the thermally induced noise, the real performance gradually deviates from the expected performance, when medium with smaller grains are utilized. Through the study, it is discovered that the system performance strongly correlates with a newly proposed concept, recording time window (RTW). To validate the concept of RTW, the disk rotational velocity has been tuned to check the impact. This concept and understanding have also been applied to properly interpret nearly all the primary observations and behaviors, which shows the elegant facet of this theorem. Therefore, although there are many aspects of system parameters, such as thermal, magnetic, mechanical and so on, the system designs could be translated into the same term, RTW. This allows better optimization and provides guidance for the modification direction of parameters. According to the realistic requirement, several parameters could be tuned to provide the ideal RTW and fully take advantage of HAMR potential. For instance, higher thermal gradient and higher room temperature anisotropy field H_k have been shown to help enhance the recording writing quality and avoid the erase-after-write induced noise.

Since there exists a strong correlation between the system performance and the RTW, the parameters that could easily change the RTW are supposed to affect the system more significantly. Motivated by this deduction, multiple pre-known or unknown noise sources are analyzed or discovered. Their noise mechanisms are also investigated in details. The well-known H_k distribution is first revisited, although it also exists in the conventional perpendicular magnetic recording. For HAMR application, this type of noise is of slightly less impact, since the effective field gradient (product of dH_k/dT and dT/dx) could be much higher. But H_k variation could cause severe erase-after-write, as the H_k distribution can lead to the minimum energy barrier dispersion during the cooling process. It is true that the optimal field could be selected to avoid a great amount of erase-after-write, narrow H_k distribution would be necessary for ultra-high density storage. Next, considering that the T_c is a parameter in the definition of the RTW, the T_c variation is studied. It turns out that the SNR could reduce significantly even with a few percent of T_c variation. It is also found that the T_c variation could make the transition to form at different downtrack locations, which is considered as transition jitter. To realize 4 Tbit/in^2, the ASTC meeting [101] suggests 2% T_c variation after the T_c distribution impact is discovered during this thesis work. Similar to the discovery of T_c variation, the thermal gradient is another parameter in the RTW. This motivated the study of grain-to-grain heating variation. Different from the T_c variation which is primarily caused by the medium fabrication, the heating variation could be induced by both the medium and the writer properties, like grain geometry, grain-boundary contact, NFT field uniformity and so on. But it is interesting to notice that the T variation shows a huge impact on recording, similar to that of T_c variation. On the other hand, the exchange coupling, a well know noise source, is analyzed. It is found that the uniform and adequate exchange strength may help suppress recording noise. While the exchange coupling distribution is always detrimental to recording quality. Apart from these, a technique is discussed to evaluate the relative weight of the deterministic noise (embedded noise, like in-plane grain) and incomplete switching. This allows people to better target the noise source, since the embedded noise mainly comes from the medium fabrication and the random noise could be effectively avoided with better system design.

With these understandings of the recording physics and noise origins, this set of theorem has been applied to several realistic experiments and system designs. To validate the theorem, the spin stand testing is employed to observe the primary phenomena, like incomplete switching and erase-after-write. The read back signal shows very similar behaviors as the model predicted. Regarding the field dependence, the recording is conducted with various write currents and shows a similar trend as modeling does. By tuning the disk rotation velocity and comparing different medium / writer components, the performance change matches up with the theorem predictions properly. Better understanding is supposed to guide the design. Field profiles generated with a generic writer design is taken from Western Digital. Via the RTW analysis, the insufficient field has been identified to be a primary concern. It is suggested the soft underlayer be inserted into the medium and the writer field strength be enhanced as well. Furthermore, the dispersion of the medium properties greatly impacts the performance. Measurement methodology has been checked via modeling, in collaboration with experiments. Not only is the T_c variation extracted from the industrial medium samples, but also the temperature dependence of anisotropy field is constructed. What is more, the transition front curvature is well known to degrade recording. Intensive study has been conducted to analyze the impact of transition curvature. Utilizing the recording understanding, an innovative technique has been proposed to realize thermal guided writer field design. The resulted crosstrack varying field manages to deliver straightened transitions with curvature completely eliminated. For certain requirement of the SNR, the increase of linear density could be more than 50%!

At this moment, there are still quite a few challenges to conquer. But with this thesis work, hopefully, the realization and commercialization of HAMR storage will be around the corner.

Reference

[1] P. Zikopoulos, D. DeRoos, C. Bienko, R. Buglio, and M. Andrews, *Big Data Beyond the Hype*, vol. 44, no. 8. 2015.

[2] J. Melorose, R. Perroy, and S. Careas, *Harness the Power of Big Data*, vol. 1. 2015.

[3] T. Rausch, E. Gage, and J. Dykes, “Ultrafast Magnetism I,” *Ultrafast Magn. I*, vol. 159, pp. 200–202, 2015.

[4] S. Iwasaki, “Perpendicular Magnetic Recording,” *IEEE Trans. Magn.*, vol. 16, no. 1, pp. 71–76, 1980.

[5] S. Iwasaki, “Perpendicular magnetic recording - Evolution and future,” *Magn. IEEE Trans.*, vol. 20, no. 5, pp. 657–662, 1984.

[6] L. Team, A. Alstrin, T. Goker, M. Lantz, J. Mcallister, H. P. Enterprise, G. Spratt, and H. P. Enterprise, “2.0 technology roadmap 2.0 participants,” no. December, pp. 1–21, 2015.

[7] B. Marchon, T. Pitchford, Y. T. Hsia, and S. Gangopadhyay, “The head-disk interface roadmap to an areal density of 4 Tbit/in 2,” *Adv. Tribol.*, vol. 2013, no. Figure 2, 2013.

[8] P. Brace, “Designing Efficient Storage Systems,” in *Flash Memory Summit*, 2016.

[9] T. international D. D. E. and M. Association, “ASTC-Technology-Roadmap-2014-v8.” 2016.

[10] H. J. Richter, “The transition from longitudinal to perpendicular recording,” *J. Phys. D. Appl. Phys.*, vol. 40, pp. R149–R177, 2007.

[11] J.-G. Zhu, “New heights for hard disk drives,” *Mater. Today*, vol. 6, no. 7–8, pp. 22–31, 2003.

[12] E. A. Dobisz, Z. Z. Bandić, T. W. Wu, and T. Albrecht, “Patterned media: Nanofabrication challenges of future disk drives,” *Proc. IEEE*, vol. 96, no. 11, pp. 1836–1846, 2008.

[13] M. H. Kryder, “After Hard Drives—What Comes Next?,” *IEEE Trans. Magn.*, vol. 45, no. 10, pp. 3406–3413, Oct. 2009.

[14] S. H. Charap, Pu-Ling Lu, and Yanjun He, “Thermal stability of recorded information at high densities,” *IEEE Trans. Magn.*, vol. 33, no. 1, pp. 978–983, 1997.

[15] D. Z. Bai and J. G. Zhu, “Micromagnetics of perpendicular write heads with extremely small pole tip dimensions,” *J. Appl. Phys.*, vol. 91, no. 10 I, pp. 6833–6835, 2002.

[16] M. H. Kryder and R. W. Gustafson, “High-density perpendicular recording - Advances, issues, and extensibility,” *J. Magn. Magn. Mater.*, vol. 287, no. SPEC. ISS., pp. 449–458, 2005.

[17] M. Mallary, A. Torabi, and M. Benakli, “One terabit per square inch perpendicular recording conceptual design,” *IEEE Trans. Magn.*, vol. 38, no. 4 I, pp. 1719–1724, 2002.

[18] B. Marchon and T. Olson, “Magnetic spacing trends: From LMR to PMR and beyond,” *IEEE Trans. Magn.*, vol. 45, no. 10, pp. 3608–3611, 2009.

[19] B. M. H. Kryder, E. C. Gage, T. W. Mcdaniel, W. A. Challener, R. E. Rottmayer, G. Ju, Y. Hsia, and M. F. Erden, “Heat Assisted Magnetic Recording,” *Proc. IEEE*, vol. 96, no. 11, 2008.

[20] W. A. Challener, C. Peng, A. V. Itagi, D. Karns, W. Peng, Y. Peng, X. Yang, X. Zhu, N. J. Gokemeijer, Y.-T. Hsia, G. Ju, R. E. Rottmayer, M. A. Seigler, and E. C. Gage, “Heat-assisted magnetic recording by a near-field transducer with efficient optical energy transfer,” *Nat. Photonics*, vol. 3, no. 4, pp. 220–224, Mar. 2009.

[21] B. C. Stipe, T. C. Strand, C. C. Poon, H. Balamane, T. D. Boone, J. A. Katine, J.-L. Li, V. Rawat, H. Nemoto, A. Hirotsune, O. Hellwig, R. Ruiz, E. Dobisz, D. S. Kercher, N. Robertson, T. R. Albrecht, and B. D. Terris, “Magnetic recording at 1.5 Pb m−2 using an integrated plasmonic antenna,” *Nat. Photonics*, vol. 4, no. 7, pp. 484–488, May 2010.

[22] G. Ju, Y. Peng, E. K. C. Chang, Y. Ding, A. Q. Wu, X. Zhu, Y. Kubota, T. J. Klemmer, H. Amini, L. Gao, Z. Fan, T. Rausch, P. Subedi, M. Ma, S. Kalarickal, C. J. Rea, D. V. Dimitrov, P.-W. Huang, K. Wang, X. Chen, C. Peng, W. Chen, J. W. Dykes, M. A. Seigler, E. C. Gage, R. Chantrell, and J.-U. Thiele, “High Density Heat-Assisted Magnetic Recording Media and Advanced Characterization - Progress and Challenges,” *IEEE Trans. Magn.*, vol. 51, no. 11, pp. 1–9, 2015.

[23] C. Rea, M. Benakli, P. Subedi, R. Mendonsa, S. Kalarickal, J. Kiely, W. Chen, H. Zhou, S. Hernandez, Y. Peng, J. Thiele, A. Q. Wu, G. Ju, T. Rauch, K. Gao, M. Seigler, and E. Gage, “Writer and Reader Head-to-Media Spacing Sensitivity Assessment in HAMR,” *IEEE Trans. Magn.*, vol. 52, no. 2, 2016.

[24] A. Q. Wu, Y. Kubota, T. Klemmer, T. Rausch, C. Peng, Y. Peng, D. Karns, X. Zhu, Y. Ding, E. K. C. Chang, Y. Zhao, H. Zhou, K. Gao, J.-U. Thiele, M. Seigler, G. Ju, and E. Gage, “HAMR Areal Density Demonstration of 1+ Tbpsi on Spinstand,” *IEEE Trans. Magn.*, vol. 49, no. 2, pp. 779–782, Feb. 2013.

[25] J.-G. Zhu, X. Zhu, and Y. Tang, “Microwave Assisted Magnetic Recording,” *IEEE Trans. Magn.*, vol. 44, no. 1, pp. 125–131, Jan. 2008.

[26] J. Zhu and Y. Wang, “Torque Oscillator With Switchable Perpendicular Electrodes,” *Current*, vol. 46, no. 3, pp. 751–757, 2010.

[27] Y. Nozaki, M. Ohta, S. Taharazako, K. Tateishi, S. Yoshimura, and K. Matsuyama, “Magnetic force microscopy study of microwave-assisted magnetization reversal in submicron-scale ferromagnetic particles,” *Appl. Phys. Lett.*, vol. 91, no. 8, p. 82510, 2007.

[28] T. Tanaka, Y. Otsuka, Y. Furomoto, K. Matsuyama, and Y. Nozaki, “Selective magnetization switching with microwave assistance for three-dimensional magnetic recording,” *J. Appl. Phys.*, vol. 113, no. 14, p. 143908, 2013.

[29] H. Li, F. Hou, P. Li, and X. Yang, “Influences of switching field rise time on microwave-assisted magnetization reversal,” *IEEE Trans. Magn.*, vol. 47, no. 2 PART 1, pp. 355–358, 2011.

[30] T. R. Albrecht, H. Arora, V. Ayanoor-Vitikkate, J. M. Beaujour, D. Bedau, D. Berman, A. L. Bogdanov, Y. A. Chapuis, J. Cushen, E. E. Dobisz, G. Doerk, H. Gao, M. Grobis, B. Gurney, W. Hanson, O. Hellwig, T. Hirano, P. O. Jubert, D. Kercher, J. Lille, Z. Liu, C. M. Mate, Y. Obukhov, K. C. Patel, K. Rubin, R. Ruiz, M. Schabes, L. Wan, D. Weller, T. W. Wu, and E. Yang, “Bit-patterned magnetic recording: Theory, media fabrication, and recording performance,” *IEEE Trans. Magn.*, vol. 51, no. 5, 2015.

[31] C. Vogler, C. Abert, F. Bruckner, D. Suess, and D. Praetorius, “Areal density optimizations for heat-assisted-magnetic recording of high density bit-patterned media,” *arXiv:1512.03690 [cond-mat]*, vol. 223903, 2015.

[32] C. A. Ross, “Patterned Magnetic Recording Media,” *Annu. Rev. Mater. Res.*, vol. 31, no. 203–235, 2001.

[33] M. V. Lubarda, S. Li, B. Livshitz, E. E. Fullerton, and V. Lomakin, “Reversal in bit patterned media with vertical and lateral exchange,” *IEEE Trans. Magn.*, vol. 47, no. 1 PART 1, pp. 18–25, 2011.

[34] O. Hellwig, J. K. Bosworth, E. Dobisz, D. Kercher, T. Hauet, G. Zeltzer, J. D. Risner-Jamtgaard, D. Yaney, and R. Ruiz, “Bit patterned media based on block copolymer directed assembly with narrow magnetic switching field distribution,” *Appl. Phys. Lett.*, vol. 96, no. 5, pp. 17–20, 2010.

[35] V. Sundar, J. Zhu, D. E. Laughlin, and J. G. Zhu, “Novel scheme for producing nanoscale uniform grains based on templated two-phase growth,” *Nano Lett.*, vol. 14, no. 3, pp. 1609–1613, 2014.

[36] J. K. Cheng, C. T. Rettner, D. P. Sanders, H. C. Kim, and W. D. Hinsberg, “Dense self-assembly on sparse chemical patterns: Rectifying and multiplying lithographic patterns using block

copolymers," *Adv. Mater.*, vol. 20, no. 16, pp. 3155–3158, 2008.

[37] Q. Peng, Y. C. Tseng, S. B. Darling, and J. W. Elam, "A route to nanoscopic materials via sequential infiltration synthesis on block copolymer templates," *ACS Nano*, vol. 5, no. 6, pp. 4600–4606, 2011.

[38] R. Wood, M. Williams, A. Kavcic, and J. Miles, "The feasibility of magnetic recording at 10 terabits per square inch on conventional media," *IEEE Trans. Magn.*, vol. 45, no. 2, pp. 917–921, 2009.

[39] S. Greaves, Y. Kanai, and H. Muraoka, "Shingled recording for 2-3 Tbit/in2," *IEEE Trans. Magn.*, vol. 45, no. 10, pp. 3823–3829, 2009.

[40] Y. J. Chen, S. Member, S. H. Leong, B. X. Xu, and H. Z. Yang, "Challenges and implementation approaches of shingled heat assisted magnetic recording (HAMR) for 10 Tb / in 2 data storage," in *Magnetics Symposium 2014 - Celebrating 50th Anniversary of IEEE Magnetics Society (MSSC50)*, 2014, vol. 2014, pp. 1–2.

[41] F. Lim, B. Wilson, and R. Wood, "Analysis of shingle-write readback using magnetic-force microscopy," *IEEE Trans. Magn.*, vol. 46, no. 6, pp. 1548–1551, 2010.

[42] Y. Shiroishi, K. Fukuda, I. Tagawa, H. Iwasaki, S. Takenoiri, H. Tanaka, H. Mutoh, and N. Yoshikawa, "Future Options for HDD Storage," *IEEE Trans. Magn.*, vol. 45, no. 10, pp. 3816–3822, Oct. 2009.

[43] K. S. Chan, J. J. Miles, E. Hwang, B. V. K. Vijayakumar, J. Zhu, W. Lin, and R. Negi, "TDMR Platform Simulations and Experiments," vol. 45, no. 10, pp. 3837–3843, 2009.

[44] A. R. Krishnan, R. Radhakrishnan, B. Vasic, A. Kavcic, W. Ryan, and F. Erden, "2-D magnetic recording: Read channel modeling and detection," *IEEE Trans. Magn.*, vol. 45, no. 10, pp. 3830–3836, 2009.

[45] A. Kavcic, X. Huang, B. Vasic, W. Ryan, and M. F. Erden, "Channel modeling and capacity bounds for two-dimensional magnetic recording," *IEEE Trans. Magn.*, vol. 46, no. 3 PART 1, pp. 812–818, 2010.

[46] Y. Wang, M. F. Erden, and R. H. Victora, "Study of two-dimensional magnetic recording system including micromagnetic writer," *IEEE Trans. Magn.*, vol. 50, no. 11, 2014.

[47] M. R. Elidrissi, K. S. Chan, and Z. Yuan, "A study of SMR/TDMR with a double/triple reader head array and conventional read channels," *IEEE Trans. Magn.*, vol. 50, no. 3, pp. 24–30, 2014.

[48] Y. Wang, T. Maletzky, E. X. Jin, D. Zhou, J. Smyth, and M. Dovek, "Pulsed Thermally Assisted Magnetic Recording," *IEEE Trans. Magn.*, vol. 49, no. 2, pp. 739–743, Feb. 2013.

[49] B. X. Xu, Z. H. Cen, J. H. Goh, J. M. Li, Y. T. Toh, J. Zhang, K. D. Ye, and C. G. Quan, "Performance benefits from pulsed laser heating in heat assisted magnetic recording," *J. Appl. Phys.*, vol. 115, no. 17, pp. 2014–2017, 2014.

[50] B. Xu, H. Wang, Z. Cen, Z. Liu, K. Ye, H. Yang, J. Zhang, and J. Li, "Simulation Study of Pulse Laser Quality Effects on Recording Performances of Heat-Assisted Magnetic Recording by Short-Pulse Laser Heating," vol. 51, no. 11, 2015.

[51] H. J. Richter, G. Parker, M. Staffaroni, M. Grobis, and B. C. Stipe, "Heat assisted magnetic recording with laser pulsing," *IEEE Trans. Magn.*, vol. 50, no. 11, 2014.

[52] T. Rausch, A. S. Chu, P.-L. Lu, S. Puranam, D. Nagulapally, T. Lammers, J. W. Dykes, and E. C. Gage, "Recording Performance of a Pulsed HAMR Architecture," *IEEE Trans. Magn.*, vol. 51, no. 4, pp. 1–5, 2015.

[53] W. Li, "Acoustically Assisted Magnetic Recording," Oregon State University, 2015.

[54] W. Li, B. Buford, A. Jander, and P. Dhagat, "Acoustically assisted magnetic recording: A new

paradigm in magnetic data Storage," *IEEE Trans. Magn.*, vol. 50, no. 3, pp. 37–40, 2014.

[55] A. Khan, D. E. Nikonov, S. Manipatruni, T. Ghani, and I. A. Young, "Voltage induced magnetostrictive switching of nanomagnets: Strain assisted strain transfer torque random access memory," *Appl. Phys. Lett.*, vol. 104, no. 26, 2014.

[56] N. Nakamura, N. Yoshimura, H. Ogi, and M. Hirao, "Elastic constants of polycrystalline L10-FePt at high temperatures," *J. Appl. Phys.*, vol. 114, no. 9, pp. 2–6, 2013.

[57] D. E. Laughlin, K. Srinivasan, M. Tanase, and L. Wang, "Crystallographic aspects of L10 magnetic materials," *Scr. Mater.*, vol. 53, no. 4, pp. 383–388, 2005.

[58] B. R. H. Victora and X. Shen, "Exchange Coupled Composite Media," *Proc. IEEE*, vol. 96, no. 11, 2008.

[59] J. P. Wang, W. Shen, and S. Y. Hong, "Fabrication and Characterization of Exchange Coupled Composite Media," *Magn. IEEE Trans.*, vol. 43, no. 2, pp. 682–686, 2007.

[60] J. Wang, H. Sepehri-Amin, Y. K. Takahashi, S. Okamoto, S. Kasai, J. Y. Kim, T. Schrefl, and K. Hono, "Magnetization reversal of FePt based exchange coupled composite media," *Acta Mater.*, vol. 111, pp. 47–55, 2016.

[61] Z. Liu, Y. Jiao, and R. H. Victora, "Composite media for high density heat assisted magnetic recording," *Appl. Phys. Lett.*, vol. 108, no. 23, p. 232402, 2016.

[62] H. Wang, H. Zhao, T. Rahman, Y. Isowaki, Y. Kamata, T. Maeda, H. Hieda, A. Kikitsu, and J. P. Wang, "Fabrication and characterization of fept exchange coupled composite and graded bit patterned media," *IEEE Trans. Magn.*, vol. 49, no. 2, pp. 707–712, 2013.

[63] S. J. Greaves, H. Muraoka, and Y. Kanai, "Discrete track media for 600 Gbits/in2 recording," *J. Appl. Phys.*, vol. 99, no. 8, pp. 23–25, 2006.

[64] N. Toyoda, T. Hirota, I. Yamada, H. Yakushiji, T. Hinoue, T. Ono, and H. Matsumoto, "Fabrication of planarized discrete track media using gas cluster ion beams," *IEEE Trans. Magn.*, vol. 46, no. 6, pp. 1599–1602, 2010.

[65] T. Hinoue, T. Ono, H. Inaba, T. Iwane, H. Yakushiji, and A. Chayahara, "Fabrication of discrete track media by Cr ion implantation," *IEEE Trans. Magn.*, vol. 46, no. 6, pp. 1584–1586, 2010.

[66] M. T. Moneck, J. G. Zhu, X. Che, Y. Tang, H. J. Lee, S. Zhang, K. S. Moon, and N. Takahashi, "Fabrication of flyable perpendicular discrete track media," *IEEE Trans. Magn.*, vol. 43, no. 6, pp. 2127–2129, 2007.

[67] Y. Tang, X. Che, H. J. Lee, and J. Zhu, "Understanding Adjacent Track Erasure in Discrete Track Media," vol. 44, no. 12, pp. 4780–4783, 2008.

[68] G. W. Qin, Y. P. Ren, N. Xiao, B. Yang, L. Zuo, and K. Oikawa, "Development of high density magnetic recording media for hard disk drives: materials science issues and challenges," *Int. Mater. Rev.*, vol. 54, no. 3, pp. 157–179, 2009.

[69] J.-G. Zhu and Y. Tang, "A medium microstructure for high area density perpendicular recording," *J. Appl. Phys.*, vol. 99, no. 8, p. 08Q903, Apr. 2006.

[70] V. Neu, C. Schulze, M. Faustini, J. Lee, D. Makarov, D. Suess, S.-K. Kim, D. Grosso, L. Schultz, and M. Albrecht, "Probing the energy barriers and magnetization reversal processes of nanoperforated membrane based percolated media.," *Nanotechnology*, vol. 24, no. 14, p. 145702, 2013.

[71] S. Oikawa, T. Onitsuka, A. Takeo, and M. Takagishi, "Flat surface percolated perpendicular media with metal pinning sites," *IEEE Trans. Magn.*, vol. 48, no. 11, pp. 3192–3194, 2012.

[72] D. E. Laughlin, Y. Peng, Y. L. Qin, M. Lin, and J. G. Zhu, "Fabrication, microstructure, magnetic,

and recording properties of percolated perpendicular media," *IEEE Trans. Magn.*, vol. 43, no. 2, pp. 693–698, 2007.

[73] T. Rausch, J. D. Trantham, A. S. Chu, H. Dakroub, J. W. Riddering, C. P. Henry, J. D. Kiely, E. C. Gage, and J. W. Dykes, "HAMR Drive Performance and Integration Challenges," *IEEE Trans. Magn.*, vol. 49, no. 2, pp. 730–733, Feb. 2013.

[74] R. E. G. Bertero, M. Alex, B. Valcu, "HAMR Recording Challenges at High Linear Densities," in *2015 IEEE Magnetics Conference (INTERMAG)*, 2015, p. 2015.

[75] T. RAUSCH, J. D. TRANTHAM, A. S. CHU, H. DAKROUB, J. W. RIDDERING, C. P. HENRY, J. D. KIELY, E. C. GAGE, and J. W. DYKES, "HAMR Drive Performance and Integration Challenges," *IEEE Trans. Magn.*, vol. 49, no. 2, pp. 730–733.

[76] Y. Jiao, Z. Liu, and R. H. Victora, "Renormalized anisotropic exchange for representing heat assisted magnetic recording media," *J. Appl. Phys.*, vol. 117, no. 17, p. 17E317, 2015.

[77] R. F. L. Evans, W. J. Fan, P. Chureemart, T. a Ostler, M. O. a Ellis, and R. W. Chantrell, "Atomistic spin model simulations of magnetic nanomaterials.," *J. Phys. Condens. Matter*, vol. 26, no. 10, p. 103202, 2014.

[78] W. Wang, M. Albert, M. Beg, M. A. Bisotti, D. Chernyshenko, D. Cort??s-Ortu??o, I. Hawke, and H. Fangohr, "Magnon-driven domain-wall motion with the Dzyaloshinskii-Moriya interaction," *Phys. Rev. Lett.*, vol. 114, no. 8, pp. 1–5, 2015.

[79] D. A. Garanin, "Fokker-Planck and Landau-Lifshitz-Bloch equations for classical ferromagnets," vol. 55, no. 5, pp. 3050–3057, 1997.

[80] U. Nowak, R. W. Chantrell, and D. Garanin, "Dynamic approach for micromagnetics close to the Curie temperature," *Phys. Rev. B*, vol. 74, no. 2006, pp. 1–5, 2009.

[81] D. Wei, S. Wang, Z. Ding, and K.-Z. Gao, "Micromagnetics of Ferromagnetic Nano-Devices Using the Fast Fourier Transform Method," *IEEE Trans. Magn.*, vol. 45, no. 8, pp. 3035–3045, Aug. 2009.

[82] R. F. Evans, D. Hinzke, U. Atxitia, U. Nowak, R. Chantrell, and O. Chubykalo-Fesenko, "Stochastic form of the Landau-Lifshitz-Bloch equation," *Phys. Rev. B*, vol. 85, no. 1, pp. 1–9, Jan. 2012.

[83] X. Xu, N. Zhou, Y. Li, and L. Traverso, "Optical and Thermal Behaviors of Plasmonic Bowtie Aperture and Its NSOM Characterization for Heat-Assisted Magnetic Recording," *Ieee Trans. Magn.*, vol. 52, no. 2, 2016.

[84] N. Zhou, X. Xu, A. T. Hammack, B. C. Stipe, K. Gao, W. Scholz, and E. C. Gage, "Plasmonic near-field transducer for heat-assisted magnetic recording," *Nanophotonics*, vol. 3, no. 3, pp. 141–155, 2014.

[85] A. Michael, G. Matt, A. Antony, M. Michael, and W. Xiao, "Heat Assisted Magnetic Recording Physics and Integration Challenges," in *TMRC - B1*, 2012.

[86] J.-U. Thiele, K. R. Coffey, M. F. Toney, J. a. Hedstrom, and a. J. Kellock, "Temperature dependent magnetic properties of highly chemically ordered Fe[sub 55−x]Ni[sub x]Pt[sub 45]L1[sub 0] films," *J. Appl. Phys.*, vol. 91, no. 10, p. 6595, 2002.

[87] B. D. Lubachevsky and F. H. Stillinger, "Geometric properties of random disk packings," *J. Stat. Phys.*, vol. 60, no. 5–6, pp. 561–583, 1990.

[88] Y. Wang and J. Zhu, "Simulation of Realistic Particle Packing and Impact on High-Density Tape Recording," *IEEE Trans. Magn.*, vol. 45, no. 10, pp. 3737–3740, 2009.

[89] O. Mosendz, S. Pisana, J. W. Reiner, B. Stipe, and D. Weller, "Ultra-high coercivity small-grain FePt media for thermally assisted recording (invited)," *J. Appl. Phys.*, vol. 111, no. 7, 2012.

[90] J. G. Klemmer Timothy, Peng Yingguo, Wu Xiaowei, "Materials Processing for High Anisotropy

L10 Granular Media," *IEEE Trans. Magn.*, vol. 45, no. 2, p. 845-, 2009.

[91] L. Zhang, Y. K. Takahashi, A. Perumal, and K. Hono, "L10-ordered high coercivity (FePt)AgC granular thin films for perpendicular recording," *J. Magn. Magn. Mater.*, vol. 322, no. 18, pp. 2658–2664, 2010.

[92] J. Thiele, K. R. Coffey, M. F. Toney, J. A. Hedstrom, and A. J. Kellock, "Temperature dependent magnetic properties of highly chemically ordered Fe55 − xNixPt45L10 films," *J. Appl. Phys.*, vol. 6595, no. 2002, 2012.

[93] W. F. Brown, "Thermal fluctuations of a single-domain particle," *Phys. Rev.*, vol. 130, no. 5, pp. 1677–1686, 1963.

[94] J. Fidler and T. Schrefl, "Micromagnetic modelling - the current state of the art," *J. Phys. D. Appl. Phys.*, vol. 33, no. 15, pp. R135–R156, 2000.

[95] J. G. Zhu, "Thermal magnetic noise and spectra in spin valve heads," *J. Appl. Phys.*, vol. 91, no. 10 I, pp. 7273–7275, 2002.

[96] J. Gosciniak, M. Mooney, M. Gubbins, and B. Corbett, "Novel droplet near-field transducer for heat-assisted magnetic recording," *Nanophotonics*, vol. 4, no. 1, pp. 503–510, 2015.

[97] Y. Wang and J.-G. Zhu, "Understanding field angle for heat assisted magnetic recording via dynamic modeling," *J. Appl. Phys.*, vol. 109, no. 7, p. 07B706, 2011.

[98] M. Recording, H. J. Richter, C. C. C. Poon, G. Parker, M. Staffaroni, O. Mosendz, R. Zakai, B. C. Stipe, and M. Recording, "Direct measurement of the thermal gradient in heat assisted magnetic recording," *Magn. IEEE …*, vol. 49, no. 10, pp. 5378–5381, 2013.

[99] J. Hohlfeld, X. Zheng, and M. Benakli, "Measuring temperature and field profiles in heat assisted magnetic recording," *J. Appl. Phys.*, vol. 118, no. 6, p. 64501, 2015.

[100] Y. Kim, A. Gupta, B. Urgaonkar, P. Berman, and A. Sivasubramaniam, "HybridStore: A cost-efficient, high-performance storage system combining SSDs and HDDs," *IEEE Int. Work. Model. Anal. Simul. Comput. Telecommun. Syst. - Proc.*, pp. 227–236, 2011.

[101] D. Weller, G. Parker, O. Mosendz, E. Champion, B. Stipe, X. Wang, T. Klemmer, G. Ju, and A. Ajan, "A HAMR Media Technology Roadmap to an Areal Density of 4 Tb/in^2," *IEEE Trans. Magn.*, vol. 50, no. 1, pp. 1–1, 2013.

[102] P. W. Huang and R. H. Victora, "Approaching the grain-size limit for jitter using FeRh/FePt in heat-assisted magnetic recording," *IEEE Trans. Magn.*, vol. 50, no. 11, 2014.

[103] C. Vogler, C. Abert, F. Bruckner, D. Suess, and D. Praetorius, "Basic noise mechanisms of heat-assisted-magnetic recording," pp. 1–7, 2016.

[104] J.-G. Zhu and H. Li, "Understanding Signal and Noise in Heat Assisted Magnetic Recording," *IEEE Trans. Magn.*, vol. 49, no. 2, pp. 765–772, Feb. 2013.

[105] J.-G. Zhu and H. Li, "Understand SNR limit and area density capability in HAMR."

[106] Y. Hsu, V. Nikitin, D. Hsiao, J. Chen, Y. Zheng, A. Pentek, J. Loo, M. Jiang, S. Yuan, M. Alex, Y. Luo, M. Salo, T. Okada, Y. Maruyama, and K. Mitsuoka, "Challenges for perpendicular write heads at high recording density," *IEEE Trans. Magn.*, vol. 43, no. 2, pp. 605–608, 2007.

[107] K. Takano, L. Guan, Y. Zhou, Y. Liu, J. Smyth, and M. Dovek, "Micromagnetic simulation of various pole-tip design perpendicular magnetic recording heads," *J. Appl. Phys.*, vol. 105, no. 7, pp. 2–5, 2009.

[108] G. D. C. Cullity D. B., *Introduction to Magnetic Materials*. Wiley-IEEE Press; 2 edition, 2008.

[109] T. W. McDaniel, "Application of Landau-Lifshitz-Bloch dynamics to grain switching in heat-assisted magnetic recording," *J. Appl. Phys.*, vol. 112, no. 1, p. 13914, 2012.

[110] J. Zheng and D. B. Bogy, “A numerical investigation of different touchdown patterns of thermal-flying-height-control sliders,” *Microsyst. Technol.*, vol. 19, no. 9–10, pp. 1377–1381, 2013.

[111] X. Shaomin and D. B. Bogy, “Flying Height Modulation for a Dual Thermal Protrusion Slider in Heat Assisted Magnetic Recording (HAMR),” *IEEE Trans. Magn.*, vol. 49, no. 10, pp. 5222–5226, Oct. 2013.

[112] H. Li and S. Shen, “Slit design for the thermal flying height control slider,” pp. 1535–1539, 2014.

[113] D. Li, M. Staffaroni, E. Schreck, and B. Stipe, “A new AFM-based technique to detect the NFT protrusion on HAMR head,” *IEEE Trans. Magn.*, vol. 49, no. 7, pp. 3576–3579, 2013.

[114] K.-S. Park, J. Choi, Y.-P. Park, and N.-C. Park, “Thermal Deformation of Thermally Assisted Magnetic Recording Head in Binary Gas Mixture at Various Temperatures,” *IEEE Trans. Magn.*, vol. 49, no. 6, pp. 2671–2676, 2013.

[115] S. N. Piramanayagam, “Perpendicular recording media for hard disk drives,” *J. Appl. Phys.*, vol. 102, no. 1, 2007.

[116] B. S. D. C. S. Varaprasad, J. Wang, T. Shiroyama, Y. K. Takahashi, and K. Hono, “Columnar Structure in FePt–C Granular Media for Heat-Assisted Magnetic Recording,” *IEEE Trans. Magn.*, vol. 51, no. 11, pp. 1–4, 2015.

[117] M. Ohtake, S. Ouchi, F. Kirino, and M. Futamoto, “L1 0 ordered phase formation in FePt, FePd, CoPt, and CoPd alloy thin films epitaxially grown on MgO(001) single-crystal substrates,” *J. Appl. Phys.*, vol. 111, no. 7, pp. 2014–2017, 2012.

[118] H. Ho, J. Zhu, A. Kulovits, D. E. Laughlin, and J. G. Zhu, “Quantitative transmission electron microscopy analysis of multi-variant grains in present L10-FePt based heat assisted magnetic recording media,” *J. Appl. Phys.*, vol. 116, no. 19, 2014.

[119] H. Pandey, J. Wang, T. Shiroyama, B. S. D. C. S. Varaprasad, H. Sepehri-Amin, Y. K. Takahashi, A. Perumal, and K. Hono, “Structure optimization of FePt-C nanogranular films for heat assisted magnetic recording media,” *Magn. IEEE Trans.*, vol. in press, no. October, p. DOI:10.1109/TMAG.2015.2477313, 2015.

[120] S. Kang, Z. Jia, S. Shi, D. E. Nikles, and J. W. Harrell, “Easy axis alignment of chemically partially ordered FePt nanoparticles,” *Appl. Phys. Lett.*, vol. 86, no. 6, pp. 1–3, 2005.

[121] S. Chikazumi, *Physics of Ferromagnetism*, vol. 53, no. 9. Oxford Science Publications, 1996.

[122] J.-G. (Jimmy) Zhu and H. Li, “Medium Optimization for Lowering Head Field and Heating Requirements in Heat-Assisted Magnetic Recording,” vol. 6, pp. 8–11, 2015.

[123] V. Sundar, “Templated Growth of Magnetic Recording Media,” Carngie Mellon University, 2015.

[124] S. Wicht, V. Neu, L. Schultz, D. Weller, O. Mosendz, G. Parker, S. Pisana, and B. Rellinghaus, “Atomic resolution structure-property relation in highly anisotropic granular FePt-C films with near-Stoner-Wohlfarth behaviour,” *J. Appl. Phys.*, vol. 114, no. 6, pp. 0–8, 2013.

[125] M. Mizuguchi, T. Sakurada, T. Y. Tashiro, K. Sato, T. J. Konno, and K. Takanashi, “Fabrication of highly L10-ordered FePt thin films by low-temperature rapid thermal annealing,” *APL Mater.*, vol. 1, no. 3, pp. 0–7, 2013.

[126] M. Albrecht and C. Brombacher, “Rapid thermal annealing of FePt thin films,” *Phys. Status Solidi*, vol. 210, no. 7, pp. 1272–1281, 2013.

[127] M. C. Traub, W. Longsine, and V. N. Truskett, “Advances in Nanoimprint Lithography,” *Annu. Rev. Chem. Biomol. Eng.*, vol. 7, no. March, pp. 1–22, 2016.

[128] H. Li and J.-G. Zhu, “The Role of Media Property Distribution in HAMR SNR,” *IEEE Trans. Magn.*, vol. 49, no. 7, pp. 3568–3571, 2013.

[129] H. Li and J.-G. Zhu, “Understanding the impact of Tc and Hk variation on signal-to-noise ratio in heat-assisted magnetic recording,” *J. Appl. Phys.*, vol. 115, no. 17, p. 17B744, May 2014.

[130] S. Pisana, S. Jain, J. W. Reiner, G. J. Parker, C. C. Poon, O. Hellwig, and B. C. Stipe, “Measurement of the Curie temperature distribution in FePt granular magnetic media,” *Appl. Phys. Lett.*, vol. 104, no. 16, p. 162407, Apr. 2014.

[131] A. Chernyshov, T. Le, B. Livshitz, O. Mryasov, C. Miller, R. Acharya, and D. Treves, “Measurement of Curie temperature distribution relevant to heat assisted magnetic recording,” *J. Appl. Phys.*, vol. 117, no. 17, 2015.

[132] Z. Dai, H. Li, and J. Zhu, “Measuring Temperature Dependence of Anisotropy Field in Heat Assisted Magnetic Recording Media by Pump-Probe Method,” *IEEE Trans. Magn.*, vol. 9464, no. c, pp. 1–1, 2016.

[133] O. Hovorka, S. Devos, Q. Coopman, W. J. Fan, C. J. Aas, R. F. L. Evans, X. Chen, G. Ju, and R. W. Chantrell, “The Curie temperature distribution of FePt granular magnetic recording media,” *Appl. Phys. Lett.*, vol. 101, no. 5, p. 52406, 2012.

[134] H. Ho, A. A. Sharma, W. L. Ong, J. A. Malen, J. A. Bain, and J. G. Zhu, “Experimental estimates of in-plane thermal conductivity in FePt-C granular thin film heat assisted magnetic recording media using a model layered system,” *Appl. Phys. Lett.*, vol. 103, no. 13, pp. 3–7, 2013.

[135] J.-G. (Jimmy) Zhu and H. Li, “Signal-to-noise ratio impact of grain-to-grain heating variation in heat assisted magnetic recording,” *J. Appl. Phys.*, vol. 115, no. 17, p. 17B747, May 2014.

[136] S. Jain, S. H. Wee, O. Hellwig, and S. Pisana, “Investigating temperature distributions in granular FePt media for Heat-Assisted Magnetic Recording (HAMR),” in *13th Joint MMM-Intermag Conference*, 2016.

[137] J. A. Schuller, E. S. Barnard, W. Cai, Y. C. Jun, J. S. White, and M. L. Brongersma, “Plasmonics for extreme light concentration and manipulation.,” *Nat. Mater.*, vol. 9, no. 3, pp. 193–204, 2010.

[138] N. Liu, J. Zheng, and D. B. Bogy, “Thermal flying-height control sliders in air-helium gas mixtures,” *IEEE Trans. Magn.*, vol. 47, no. 1 PART 1, pp. 100–104, 2011.

[139] J. Yang, C. P. H. Tan, and E. H. Ong, “Thermal analysis of helium-filled enterprise disk drive,” *Microsyst. Technol.*, vol. 16, no. 10, pp. 1699–1704, 2010.

[140] N. . Dwivedi, N. . Satyanarayana, R. J. . Yeo, H. . Xu, K. . Ping Loh, S. . Tripathy, and C. S. . Bhatia, “Ultrathin carbon with interspersed graphene/fullerene-like nanostructures: A durable protective overcoat for high density magnetic storage,” *Sci. Rep.*, vol. 5, no. May, pp. 1–16, 2015.

[141] V. Sokalski, D. E. Laughlin, and J. Zhu, “Experimental modeling of intergranular exchange coupling for perpendicular thin film media,” *Appl. Phys. Lett.*, pp. 2–4, 2009.

[142] Y. Wang and J. Zhu, “Dual Easy Axes Effect on Nanosized Near-Spherical Particles for Advanced Tape Storage,” vol. 44, no. 11, pp. 3557–3560, 2008.

[143] M. Alex, H. Li, G. Bertero, and J. G. Zhu, “Distinguishing Random and Spatially Deterministic Noise Components in Heat Assisted Magnetic Recording,” *IEEE Trans. Magn.*, vol. PP, no. 99, p. 1, 2016.

[144] J. R. Hoinville, R. S. Indeck, and M. W. Muller, “Spatial Noise Phenomena of Longitudinal Magnetic Recording Media,” *IEEE Trans. Magn.*, vol. 28, no. 6, pp. 3398–3406, 1992.

[145] H. Li, M. Alex, and J. Zhu, “Comparative study of micromagnetic modeling and experiment in heat-assisted magnetic recording,” *IEEE Int. Magn. Conf. Dig.*, 2015.

[146] B. X. Xu, H. X. Yuan, J. Zhang, J. P. Yang, R. Ji, and T. C. Chong, “Thermal effect on slider flight height in heat assisted magnetic recording,” *J. Appl. Phys.*, vol. 103, no. 7, pp. 101–104, 2008.

[147] H. Li, M. Alex, and J. G. J. Zhu, “HAMR Noise Mechanism Study with Spin-Stand Testing,” *IEEE Trans. Magn.*, vol. 51, no. 11, 2015.

[148] Z. Li, D. Z. Bai, T. Pan, D. Han, F. Liu, S. Li, and S. Yuan, “Write Field Dynamics in the Presence of Antiferromagnetic Coupling of Writer Pole,” *IEEE Trans. Magn.*, vol. 49, no. 7, pp. 3725–3728, 2013.

[149] H. Li, B. Johnson, M. Morelli, M. Gibbons, and J.-G. (Jimmy) Zhu, “Analysis of signal-to-noise ratio impact in heat assisted magnetic recording under insufficient head field,” *J. Appl. Phys.*, vol. 117, no. 17, p. 17D133, 2015.

[150] J. G. Zhu and H. Li, “SNR impact of noise by different origins in FePt-L10 HAMR Media,” *IEEE Trans. Magn.*, vol. 51, no. 4, 2015.

[151] Y. Halahovets, P. Siffalovic, M. Jergel, R. Senderak, E. Majkova, S. Luby, I. Kostic, B. Szymanski, and F. Stobiecki, “Scanning magneto-optical Kerr microscope with auto-balanced detection scheme,” *Rev. Sci. Instrum.*, vol. 82, no. 8, 2011.

[152] S. Greaves, Y. Kanai, and H. Muraoka, “Magnetization Switching in Energy Assisted Recording,” *IEEE Trans. Magn.*, vol. 48, no. 5, pp. 1794–1800, May 2012.

[153] D. Weller, G. Parker, O. Mosendz, E. Champion, B. Stipe, X. Wang, T. Klemmer, G. Ju, and A. Ajan, “A HAMR Media Technology Roadmap to an Areal Density of 4 Tb/in^2,” *IEEE Trans. Magn.*, vol. PP, no. 99, pp. 1–1, 2013.

Publication List

[1] Jian-Gang Zhu, ***Hai Li***, "Write Field Design for Transition Curvature Straightening and SNR Enhancement in Heat-Assisted Magnetic Recording," *61st Annual Conference on Magnetism and Magnetic Materials (MMM) Abstract*, 2016 (Accepted)

[2] Jian-Gang Zhu, ***Hai Li***, "Rectifying Transition Curvature in Heat-Assisted Magnetic Recording," *IEEE Trans. Magn.*, 2016 (submitted) (**INVITED**)

[3] Michael Alex, ***Hai Li***, G. Bertero, Jian-Gang Zhu, "Distinguishing Random and Spatially Deterministic Noise Components in Heat Assisted Magnetic Recording", *IEEE Trans. Magn.*, Vol. PP, No. 99, 2016

[4] Zhengkun Dai, ***Hai Li***, Jian-Gang Zhu, "Measuring Temperature Dependence of Anisotropy Fields in HAMR Media by Pump-Probe Method', *IEEE Trans. Magn.*, Vol. PP, No. 99, 2016

[5] ***Hai Li***, Michael Alex, Jian-Gang Zhu, "HAMR Noise Mechanism Study with Spin Stand Testing," *IEEE Trans. Magn.*, Vol. PP, No. 99, 2015

[6] Jian-Gang Zhu, ***Hai Li***, "Medium Optimization for Lowering Head Field and Heating Requirements in Heat-Assisted Magnetic Recording," *IEEE Magn. Lett.*, Vol. 6, 2015

[7] ***Hai Li***, Brad Johnson, Michael Morelli, Matt Gibbons and Jian-Gang Zhu, "Analysis of SNR Impact in Heat Assisted Magnetic Recording Under Insufficient Head Field," *J. Appl. Phys.*, 117, 17D133 (2015)

[8] Jian-Gang Zhu, ***Hai Li***, "SNR Impact of Noise by Different Origins in FePt-$L1_0$ HAMR Media," *IEEE Trans. Magn.*, Vol. 51, No. 4, 2015 (**INVITED**)

[9] Jian-Gang Zhu, ***Hai Li***, "Origins of Medium Noise and Their Characteristics in Heat Assisted Magnetic Recording," *IEEE INTERMAG Digest*, 2014 (**INVITED**)

[10] ***Hai Li***, Jian-Gang Zhu, "Understanding the Impact of T_c and H_k Variation on SNR in Heat-Assisted Magnetic Recording," *J. Appl. Phys.*, 115, 17B744 (2014)

[11] Jian-Gang Zhu, ***Hai Li***, "SNR Impact of Grain-to-Grain Heating Variation in Heat Assisted Magnetic Recording," *J. Appl. Phys.*, 115, 17B747 (2014)

[12] ***Hai Li***, Jian-Gang Zhu, "The Role of Media Property Distribution in HAMR SNR," *IEEE Trans. Magn.*, Vol. 49, No. 7, 2013

[13] Jian-Gang Zhu, ***Hai Li***, "Understanding Signal and Noise in Heat Assisted Magnetic Recording," *IEEE Trans. Magn.*, Vol. 49, No. 2, 2013 (**INVITED**)

[14] Jian-Gang Zhu, ***Hai Li***, "Understand SNR Limit and Area Density Capability in HAMR," *Asia Pacific Magnetic Recording Conference (APMRC) Digest,* 2012 (**INVITED**)